Fondo Sociale Europeo - FSE
Programma Operativo Nazionale 2000/06
"Ricerca, Sviluppo tecnologico ed Alta Formazione
nelle regioni dell'Obiettivo 1" - Misura 1.1 (F.S.E)

University of Calabria

Ph.D. Course in Chemical Engineering and Materials

Thesis

PROCESS INTENSIFICATION: INTEGRATED MEMBRANE OPERATIONS FOR BRACKISH AND SEAWATER DESALINATION

Settore Scientifico Disciplinare CHIM07 – Fondamenti Chimici delle Tecnologie

Supervisor

Ch.mo Prof. Enrico DRIOLI

Dr. Ing. Efrem Curcio

PhD Student

Sulaiman AL-OBAIDANI
Ciclo XXI

PhD Coordinator

Ch.mo Prof. Raffaele MOLINARI

A.A. 2007-2008

To my Family

" وَجَعَلْنَا مِنَ الْمَاءِ كُلَّ شَيْءٍ حَيٍّ "

القرآن الكريم سورة الأنبياء الآية 30

"Dall'acqua traemmo ogni essere vivente."

Nobile Corano Surat Al Anbia (I Profeti) XXI Verse 30

"We made from water every living thing"

The Noble Qura'n Surat Al Anbia (The Profits) 21 Verse 30

ABSTRACT

The present research study is focusing on the evaluation of the integrated membrane system which merges the membrane contactor technology such as gas-liquid membrane contactors (GLMC) and membrane distillation /crystallization (MD/MDC) with the conventional pressure-driven membrane operations such as micrfiltration/ultrafiltration (MF/UF), nanofiltration (NF) and reverses osmosis (RO) within the logic of Process Intensification (PI) strategies in order to redesign the desalination plants to be cheaper, safer and sustainable. The importance of applying the PI strategies in the desalination industry is presented in chapter 1. In addition, this chapter gives the research project objectives and activities.

The optimization and the feasibility of using the GLMC in the proposed integrated membrane system were discussed in chapter 2. Simulation model for the GLMC was implemented by computer and the results were verified by experimental tests. The results showed that there was a good agreement between the simulation and experimental results with less than 10% differences. In terms of CO_2 transfer rate, the results showed that higher transfer rates were obtained at higher liquid flow rates and higher pH values due to lower mass transfer resistance and higher reaction rates, respectively. The feasibly study showed that using GLMC is more economically feasible since the cost of the NaOH used in the GLMC after reacting with CO_2 to produce Na_2CO_3 was less than the cost of using Na_2CO_3 directly from the market in order to precipitate Ca^{+2} as $CaCO_3$. Moreover, the GLMC will contribute to the reduction of CO_2 emission from desalination plants and reduce their environmental impact.

Since so far there are no membrane modules especially made for MD, the aim of this study was to provide optimization guidelines for materials and methods for using MD in desalination. Therefore, in chapter 3, comprehensive theoretical analysis have been carried out and simulation model was developed to describe the mass flux and heat efficiency in MD processes considering transport phenomena, membrane structural properties and most sensitive process parameters, with the aim to investigate the effects of the membrane properties on the MD performance and to set some criterions to optimize these properties in order to obtain the best performance. Experimental tests were conducted in order to validate the results obtained by the computer simulation and the results showed that the computer simulations were able to estimate the MD performance with errors not exceeding 5%. The results showed that an increase of the temperature gradient resulted in the enhancement of both transmembrane flux and thermal efficiency. On the other hand, feed concentration had low effects in flux reduction even at high values close to saturation which contribute to only 30-50% flux reduction. This makes the MD

process attractive technique for seawater desalination especially when integrated with RO in the logic of the ZLD concept and satisfying the process intensification goals. The investigation of the effects of membrane properties confirmed that better MD performance was achieved when using polymeric membranes characterized by low thermal conductivity (flux and thermal efficiency declined by 26% and 50%, respectively, when increasing thermal conductivity from 0.1 to 0.5 W/m K), lower thickness (increasing the membrane thickness from 0.25 to 1.55 mm resulted in a flux decay of about 70% without a significant improvement in thermal efficiency), and high porosity. The investigation of the complex correlations between physico-chemical properties of the membrane and MD performance confirms the need for a customized hardware, i.e. high porosity hydrophobic membranes with appropriate thickness and made by low-heat conductive polymers in order to reduce the amount of wasted energy.

The basic mechanisms and kinetics of crystallization were considered in chapter 4 in order to accomplish the modeling and simulation for the membrane crystallizers. The computer simulation of the MDC was similar to the one of the MD presented in chapter 3 with addition of crystallization kinetics calculation. The simulation model was used in parallel with the experimental tests in order to improve the design and performance of the crystallizers. The results showed that it was possible to obtain NaCl crystals from the NF retentate at a good quality and narrow crystal size distribution (CSD). The effects of the concentration polarization in the transmembrane flux were very limited; however, there was an unexpected flux decline after the formation of the crystals in the system. This was due to the deposition of the salts crystals on the membrane surface which caused pore blockage and hence flux drop. The design improvement of the MDC suggested to introduce another opening at the bottom of the crystallizer tank for removing crystals, and to install a filter in the suction side of the feed pump in order to avoid crystals for recirculation inside the membrane module with the feed.

Exergy analysis, economical investigation and sensitivity study were carried out in chapter 5 to evaluate the feasibility of the integrated membrane system. The exergy analysis showed that the highest work input was for the plant which involved the pressure-driven membranes UF-NF-RO due to the high pumping and pressurizing energy requirement especially in NF and RO pumps. On the other hand, the highest heat energy input was associated with the membrane distillation plant as a stand alone process. The exergy efficiency was generally higher in case of pressure-driven operations than thermal processes. In addition, the performance of plants with energy and heat recovery systems was always better than the ones without energy and heat recovery systems.

Economical study and cost evaluation for several configurations showed that the lowest total water costs were 0.51 and 0.29 $/m^3$ when using UF-RO

plant with energy recovery system for seawater and brackish water desalination, respectively. In case of the integrated system which contained both pressure and thermal processes, the best combination was obtained when using the pressure-driven membranes combined with a membrane crystallization unit operating on the NF concentrated stream and a membrane distillation unit operating on the RO brine stream. The total water cost in this case was 1.27 $/m^3$ and 1.10 $/m^3$ for seawater and brackish water, respectively. Moreover, the combination of membrane crystallization units is very attractive especially if the salt crystals produced by the crystallization process are considered. This means that the desalination plant will produce both water and salt crystals. In this case, the price of the salts can cover the whole expenses of the desalination process. Besides, the problems related to brine disposal were minimized when using the integrated membrane system.

The sensitivity analysis revealed that the pressure-driven membrane operations were very sensitive to the feed concentration and the cost of electricity. On the other hand, MD processes were not sensitive to the variation on the feed concentration or the electricity costs. The most sensitive parameter in the total water cost of the MD plant was the cost of steam which contributed to values as high as high as 11.4% in case of MD without heat recovery system. The best tolerance to the variation of these parameters was obtained when using the integrated membrane system of pressure-driven membranes and MD/MDC processes.

The realization of the semi-pilot plant of the integrated membrane system was covered in chapter 6. The semi-pilot plant of the integrated membrane system was designed and assembled based on the results obtained by the computer simulations and the preliminary experiments done for each unit individually in the previous chapters. It consisted of UF-NF-RO as the pressure-driven membrane operations with the GLMC for Ca^{+2} precipitation and an MDC unit which can be operated as an MD or as a membrane crystallizer. The semi-pilot desalination plant of the integrated membrane system was operated using synthetic and real seawater in order to confirm the performance and process stability. The transmembrane flux was stable during the operation. The MDC was able to produce salt crystals from the NF retentate and the RO brine streams. The CSD of the crystals obtained by the MDC operating on the RO brine showed sharper distribution trends than the ones obtained from the MDC when operating on the NF retentate. In addition, the MD unit was operated as a stand-alone desalination process using real seawater and the results showed that it was stable and the membrane did not loss its hydrophobicity during the operation.

SOMMARIO

Il presente studio è incentrato sulla valutazione del sistema integrato a membrana in cui la tecnologia dei contattori a membrana (tipo i contattori gas-liquido (GLMC) e la distillazione/cristallizzazione a membrana (MD/MDC)) viene combinata con le operazioni convenzionali a membrana indotti dalla pressione (come la microfiltrazione/ultrafiltrazione (MF/UF), nanofiltrazione (NF) e l'osmosi inversa (RO)) nella logica della Intensificazione del Processo (PI) al fine di ridisegnare gli impianti di desalinazione per essere più convenienti, sicuri e sostenibili. L'importanza di applicare le strategie del PI nella dissalazione industriale è presentata nel capitolo 1 del presente lavoro. Questo capitolo fornisce inoltre gli obiettivi e le attività del progetto di ricerca.

L'ottimizzazione e la possibilità di utilizzare i GLMC nel proposto sistema integrato a membrana sono stati discussi nel capitolo 2. La simulazione del GLMC è stato effettuato tramite calcolatore e i risultati sono stati verificati tramite prove sperimentali. I risultati hanno dimostrato che vi è stato buon accordo tra la simulazione e risultati sperimentali con differenze inferiori al 10%. In termini di velocità di trasferimento di CO_2, i risultati ottenuti hanno mostrato che le velocità più elevate si hanno per portate di liquido alte e ad alti valori di pH a causa, rispettivamente, della minore resistenza al trasferimento di materia e alla maggiore velocità di reazione. Lo studio condotto ha mostrato che l'uso del GLMC è più economicamente conveniente in quanto, il costo per l'NaOH da utilizzare nel GLMC per produrre Na_2CO_3 è inferiore al costo che si avrebbe se l'Na_2CO_3 fosse acquistato tal quale dal mercato. Inoltre, il GLMC contribuirà alla riduzione delle emissioni di CO_2 dagli impianti di desalinazione e ridurrà il loro impatto ambientale.

Poiché finora non vi sono moduli a membrana appositamente realizzati per la MD, l'obiettivo di questo studio era quello di fornire le linee guida per l'ottimizzazione dei materiali e dei metodi per utilizzare la MD nella dissalazione. Pertanto, nel capitolo 3, sono state effettuate approfondite analisi teoriche ed è stato inoltre sviluppato un modello di simulazione per descrivere il flusso di materia e l'efficienza termica nel processo di MD considerando i fenomeni di trasporto, le proprietà strutturali della membrana e i parametri più sensibili del processo, con l'obiettivo di indagare gli effetti delle proprietà della membrana sul rendimento del processo di MD e di fissare alcuni criteri per ottimizzare queste proprietà al fine di ottenere le migliori prestazioni. Prove sperimentali sono state condotte al fine di convalidare i risultati ottenuti tramite la simulazione al computer ed i risultati hanno mostrato che le simulazioni al computer sono state in grado di stimare il rendimento della MD con errori non superiori al 5%. I risultati hanno dimostrato che un aumento del gradiente di temperatura ha portato all'accrescimento sia del flusso transmembrana che dell'efficienza termica. D'altro canto, la concentrazione dell'alimentazione ha un effetto inferiore sulla riduzione del flusso anche a valori elevati vicino alla saturazione, e contribuiscono a solo il 30-50% di riduzione di flusso. Questo rende il processo di MD una tecnica interessante per la dissalazione

dell'acqua di mare, in particolare quando integrata con la RO nella logica del ZLD per soddisfare gli obiettivi della Intensificazione del Processo. L'indagine degli effetti delle proprietà della membrana hanno confermato che la MD mostra un migliore rendimento quando si utilizzano membrane polimeriche caratterizzate da una bassa conducibilità termica (flusso ed efficienza termica sono diminuiti, rispettivamente, del 26% e 50%, quando la conducibilità termica aumenta da 0,1 a 0,5 W/m K), da un più basso spessore (aumentando lo spessore della membrana da 0,25 a 1,55 millimetri si ha un decadimento di flusso di circa il 70% senza un significativo miglioramento nel rendimento termico), e da alta porosità. L'analisi delle complesse relazioni tra le proprietà fisico-chimiche della membrana e le prestazioni della MD conferma la necessità di realizzare membrane caratterizzate da un ben preciso hardware, vale a dire membrane idrofobe ad alta porosità con spessore adeguato e costruite con polimeri caratterizzati da coefficienti di conduttività bassi al fine di ridurre la quantità di energia dissipata.

I meccanismi di base e le cinetiche di cristallizzazione sono state prese in considerazione nel capitolo 4, al fine di realizzare la modellazione e la simulazione dei cristallizzatori a membrana. La simulazione al computer del MDC è stata simile a quella della MD presentata nel capitolo 3 con l'aggiunta del calcolo delle cinetiche di cristallizzazione. Il modello di simulazione è stato utilizzato in parallelo con le prove sperimentali al fine di migliorare la progettazione e l'esecuzione dei cristallizzatori. I risultati hanno mostrato che era possibile ottenere cristalli di NaCl di buona qualità dal retentato della NF e distribuzione delle dimensioni dei cristalli (CSD) strette. Gli effetti della polarizzazione per concentrazione nel flusso transmembrana sono stati molto limitati; tuttavia, vi è stato un inatteso calo del flusso dopo la formazione di cristalli nel sistema. Ciò è dovuto alla deposizione di cristalli sulla superficie della membrana che ha causato il blocco dei pori e, quindi, la caduta del flusso. Per migliorare il MDC si è pensato di introdurre un altra apertura al fondo del serbatoio di cristallizzazione per la rimozione di cristalli, e di installare un filtro nel lato di aspirazione della pompa di alimentazione, al fine di evitare il ricircolo dei cristalli all'interno del modulo a membrana con l'alimentazione.

L'analisi exergetica, l'indagine economica e lo studio di sensitività sono stati effettuati nel capitolo 5 per valutare la fattibilità del sistema integrato a membrana. L'analisi exergetica ha mostrato che il maggiore lavoro in ingresso si aveva nell'impianto con le unità di UF-NF-RO a causa degli elevati consumi energetici delle pompe, soprattutto per la NF e RO. D'altro canto, il maggiore consumo termico si ha nell'impianto con la sola unità di distillazione a membrana. L'efficienza exergetica era generalmente più elevata nel caso di operazioni a membrana indotti dalla pressione di quella dei processi termici. In aggiunta, le prestazioni degli impianti con sistemi di recupero di energia e di calore erano sempre migliori di quelli senza sistemi di recupero.

L'analisi economica e la valutazione dei costi per diverse configurazioni ha mostrato che i più bassi costi totali dell'acqua erano 0,51 e 0,29 $/m^3 quando si

utilizza l'impianto UF-RO con sistema di recupero di energia per la dissalazione dell'acqua salina e salmastra, rispettivamente. Nel caso del sistema integrato che conteneva contemporaneamente processi termici e indotti dalla pressione, la migliore combinazione è stata ottenuta quando si utilizza i processi a membrane indotti dalla pressione con cristallizzatore a membrana operante sul concentrato della NF e distillazione a membrana operante su quello della RO. Il costo totale dell'acqua in questo caso è stato \$ 1,27/m^3 e \$ 1,10/m^3 per acqua di mare e salmastra, rispettivamente. Inoltre, la combinazione di unità di cristallizzazione a membrana è molto interessante, soprattutto se vengono considerati i cristalli prodotti dal processo di cristallizzazione. Ciò significa che l'impianto di dissalazione produrrà sia acqua che cristalli. In questo caso, il prezzo dei sali può coprire le spese di tutto il processo di desalinizzazione. Inoltre, i problemi legati allo smaltimento del brine sono stati ridotti al minimo quando si utilizza il sistema integrato a membrana.

L'analisi di sensitività ha rivelato che, le operazioni a membrana indotte dalla pressione sono molto sensibili alla concentrazione dell'alimentazione e al costo dell'elettricità, cosa che invece non accade nel caso della MD. Il costo totale dell'acqua nell'impianto MD è risultato essere invece molto sensibile al variare del costo del vapore, che rappresenta l'11.4% del costo totale nel caso in cui la MD opera senza sistema di recupero del calore. Una minore sensibilità alla variazione di questi parametri è stata ottenuta quando si utilizza il sistema integrato con unità a membrana indotte dalla pressione e processi MD/MDC.

La realizzazione dell'impianto semi-pilota del sistema integrato di membrana è stato descritto nel capitolo 6. Tale impianto è stato progettato e assemblato sulla base dei risultati ottenuti dalle simulazioni al computer e dai preliminari esperimenti eseguiti singolarmente in ciascuna unità e descritti nei capitoli precedenti. Esso è consistito da UF-NF-RO come processi a membrana indotti dalla pressione assieme a unità di GLMC, per la precipitazione del Ca^{+2}, e di MDC da utilizzare come MD o come cristallizzazione a membrana. L'impianto semi-pilota integrato di dissalazione, è stato utilizzato sia con acqua di mare sintetica che reale, al fine di confermare le prestazioni e la stabilità del processo. Il flusso transmembrana è rimasto stabile durante il funzionamento. Il MDC è stato in grado di produrre sali dal retentato della NF e della RO. La CSD dei cristalli ottenuti dalla operazione di MDC sul retentato della RO ha mostrato distribuzioni più strette di quelle ottenute sottoponendo a cristallizzazione il retentato della NF. Inoltre, la MD è stata anche utilizzata da sola, ovvero come processo unico, per la dissalzione dell'acqua di mare reale ed i risultati hanno mostrato che essa è rimasta stabile e cha la membrana non ha subito perdite di idrofobicità durante l'operazione.

CONTENTS

LIST OF TABLES

LIST OF FIGURES

CHAPTER 1
PROCESS INTENSIFICATION FOR DESALINATION

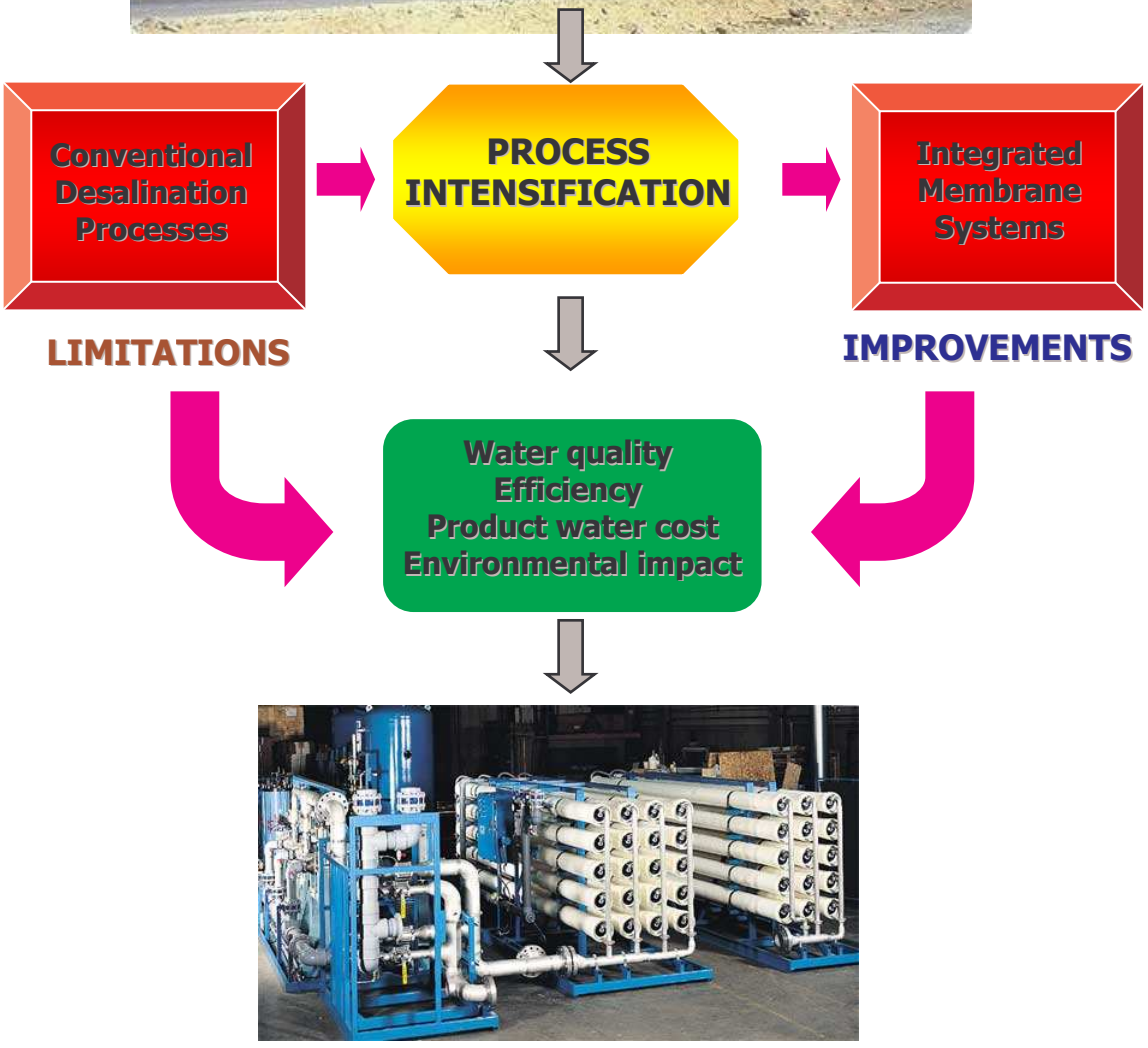

Summary

This is the first chapter in the thesis which includes some introductory information about the process intensification strategies and benefits. It also shows the importance of membrane science and technology in satisfying the process intensification goals in desalination industry. It ends up by stating the research project objectives and activities.

1.1 Process intensification (PI)

Over the last two decades, different definitions of this term were published. Cross and Ramshaw defined PI as follows: "Process intensification is a term used to describe the strategy of reducing the size of chemical plant needed to achieve a given production objective"[1]. Stankiewicz and Moulijn [2] proposed the following definition: "Process intensification consists of the development of novel apparatuses and techniques that, compared to those commonly used today, are expected to bring dramatic improvements in manufacturing and processing, substantially decreasing equipment-size/production-capacity ratio, energy consumption, or waste production, and ultimately resulting in cheaper, sustainable technologies". They also provided a description of the PI toolbox which contained two dimensions namely, equipment and processing methods. From business point of view, the BHR Group defined PI as [3]: "Process Intensification (PI) is a revolutionary approach to process and plant design, development and implementation. Providing a chemical process with the precise environment it needs to flourish results in better products, and processes which are safer, cleaner, smaller - and cheaper. PI does not just replace old, inefficient plant with new, intensified equipment. It can challenge business models, opening up opportunities for new patentable products and process chemistry and change to just-in-time or distributed manufacture".

As realized from the above definitions, PI is the development of innovative apparatuses, techniques and methodologies that offer a drastic improvement in the manufacturing and processing, and substantially increasing

the process efficiency, reducing equipment size and reducing energy consumption, and minimizing the environmental impact by recycling waste, reduce waste formation, reduce hazardous materials and reduce raw material utilization. Ultimately it leads to cheaper, safer and sustainable technique as demonstrated in Figure 1.1.

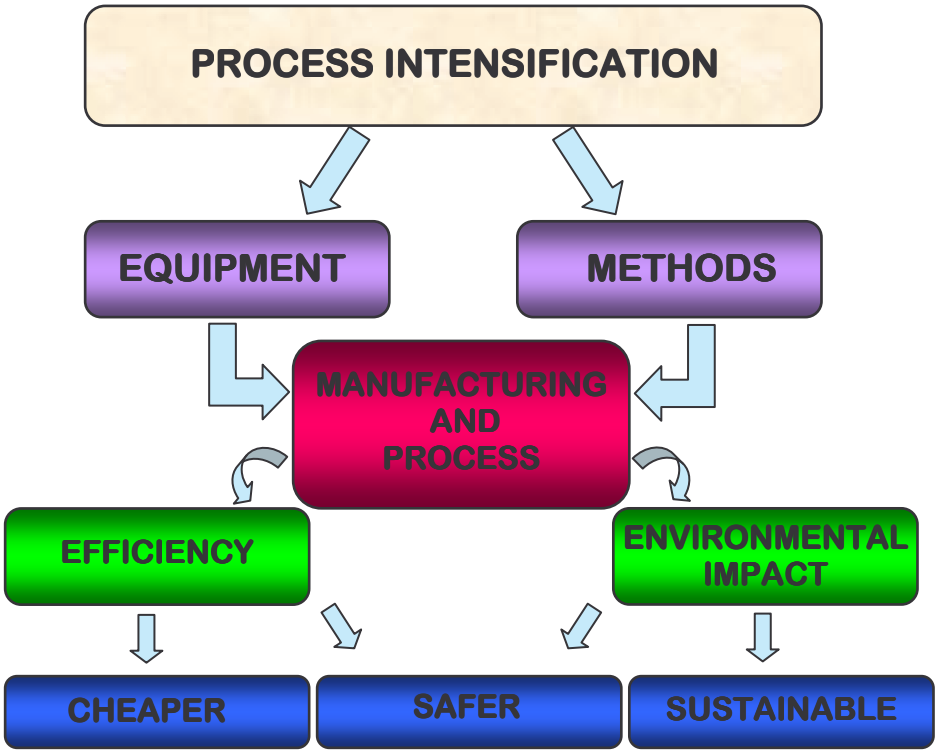

Figure 1.1 Schematic demonstration of the PI

Apparently, the philosophy of the PI has been characterized by four words: smaller, cheaper, safer and cleaner. The PI leads to substantially cheaper processes particularly in terms of land costs (higher production per unit area), investment costs (compact equipment and integrated processing units which reduce civil work), costs of raw materials (due to higher yields and selectivities), costs of energy (due higher energy efficiency), and costs of waste (less waste generation). Indeed, equipment size, land use costs, and process safety are among the most important PI motivations [4]. In this sense, several years ago DSM published a picture symbolizing its own vision of process intensification

[5], in which skyscraping distillation towers of the naphtha-cracking unit were replaced by a compact, clean, and tidy indoor plant as shown in Figure 1.2.

Figure 1.2 The DSM vision for the PI

Satisfying the increasing demand for raw materials, energy and product under the constraints of sustainable development and environment protection is challenging the chemical and process engineering. However, PI has provided a pathway to maintain sustainability of the chemical and process engineering through the rational integration and implementation of new industrial, economical, environmental and social strategies. PI involves the design of novel equipment based on scientific principles and new production methods which leads to more or less complex technologies that replace conventional equipment or processes with ones that are smaller, cheaper and more efficient; or that combine multiple operations into a single apparatus or into fewer devices [6].

1.2 The role of membrane science and technology in satisfying the PI targets

Membrane science and technology is expected to give a substantial contribution to satisfy the process intensification goal to develop substantially pathways, thus providing reliable options for both industrial growth and environmental protection. In fact, membrane technology can be the key factor in

the rationalization of the process intensification due to their characteristics of high efficiency, operational simplicity, high selectivity and permeability for mass transfer of specific compounds, compatibility of different membrane operation to work in an integrated system, low energy requirement, operational stability, environmental compatibility, easy control and scale up and large flexibility [7].

Membrane technology has been applied in many scientific and industrial fields. Essentially, membrane technology succeeded in biochemical applications (such as artificial kidneys and livers, extracorporeal blood oxygenators and dialysis), food processing and water treatment and desalination [8]. This study will mainly focus on the application of membrane technology in the water desalination industry aiming to meet the PI requirements.

1.3 Application of membrane technology and PI in desalination

Desalination processes were developed to obtain fresh water from the earth's inexhaustible supply of seawater. The two most successful commercial water desalination techniques involve thermal and membrane separation methods. Thermal separation processes include multi stage flash (MSF), multi effect evaporation (MEE) / multi effect distillation (MED), vapor compression (VC) and solar desalination. Membrane separation processes include reverses osmosis (RO) and electro-dialysis (ED). Among these different technologies available, MSF distillation and RO dominate the existing plants [9].

Water shortage problem is now becoming more and more evident worldwide due to the limited water resources and increased population growth. Rational utilization and sustainable water resources management in combination with waste water treatment and developing high efficiency desalination technologies are the only solutions to face water shortage problem [10]. Therefore, desalination is no longer a marginal water resource for municipal and industrial use as in some countries like as Qatar, Saudi Arabia and Kuwait. Two-

third of the world's desalination plants are located in Gulf Cooperation Council (GCC) countries: Saudi Arabia, Kuwait, Qatar, Bahrain, UAE, and Oman [9].

Currently, reverse osmosis (RO) is one of the most prevalent technologies for seawater desalination. However, a crucial drawback of RO membranes is their weakness against fouling due to the presence of colloidal, particulate, dissolved organics and inorganic matter in feed water, as well as biological growth in the RO system. Therefore, it is required to install a pretreatment step for the feed water before going to the RO unit. The conventional pre-treatment were based on mechanical treatment (media filters, cartridge filters) followed by extensive chemical treatment like flocculation, coagulation, acid treatment and disinfection. The main problems in using the conventional pretreatment is that it does not represent a complete barrier to colloids and suspended particles and produces unsteady feed water quality and quantity [11]. In addition, this pretreatment is known to be complex, labor intensive and space consuming [12]. Furthermore, it consumes large amount of chemicals which are used for coagulant dosages to provide surface charge neutralization, chlorination to limit biological growth, and flocculation-sedimentation sequences. Similar technology used to treat waste water was found 500 years ago in the Agricola's book De Re Metallica (1556) [7] indicating that the hardware remained unchanged as shown in Figure 1.3.

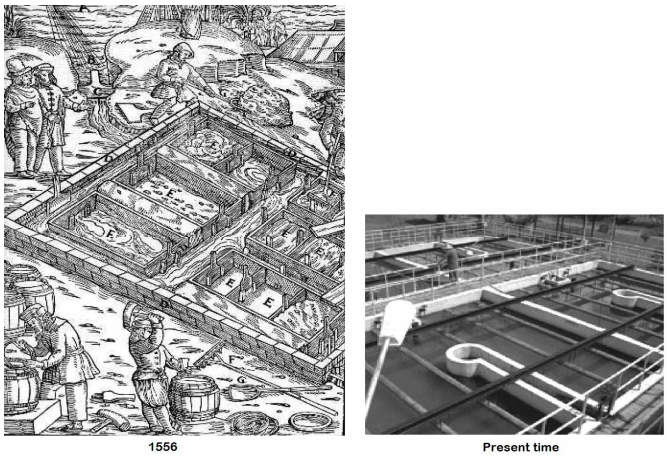

Figure 1.3 Comparison of technologies used for waste water treatment

1.3.1 Integrated pressure-driven membranes system

Integrating the various pressure-driven membrane operations in one system is the first step towards satisfying the PI obligation. In fact, pressure-driven membranes such as microfiltration (MF) and ultrafiltration (UF) are the new trends in designing the pretreatment systems for desalination plants and they can be used as a substitute for the conventional pretreatment technologies. MF can remove suspended solids and lower the silt density index (SDI) while in UF, not only suspended solids and large bacteria are retained, but also (dissolved) macromolecules, colloids and small bacteria. MF and UF pretreatment leaded to a better control of membrane biofouling, increased the membrane lifetime, and limited the cleaning frequency of the plant. Furthermore, permeate fluxes measured at the successive high-pressure membrane filtration unit increase up to 30% [13], thus resulting in higher reliability and better overall economics of the desalination system. In RO desalination, the capital and operating costs are the major drivers for process selection and due to relatively low water recovery in RO plants, any cost saving incurred in the pretreatment system will strongly affect the cost of water produced. Actually, the MF/UF were predicted to contribute for about 10% reductions in the total water cost [13]. It has been reported that a reduction of 39% in the operating and maintenance costs can be achieved when replacing the conventional pretreatment with MF or UF. Besides, the elimination of flocculation, recarbonation, and filtration steps will decrease the power and chemical costs and reduce the plant space which leads to a significant reduction in the plant capital costs [14].

.

Moreover, nanofiltration (NF) is today used in softening, disinfection, and removal of organic materials and metals. The installation of NF as a pretreatment will lead to a breakthrough in the application of RO due to its capability of effectively removing dissolved organic compounds, scale forming hardness ions, and bivalent ions. As consequence, the osmotic pressure of RO

feed and retentate streams is decreased, thus allowing the system to operate at high water recovery factors (70%) with minor scaling problems [15].

At this stage, the integrated pressure-driven membrane (MF/UF-NF-RO) system is characterized by global water recovery factors up to 50%, energy saving of 25-30%, less consumption of chemicals and additives, smaller land space, and less amount of discharged wastes [16, 17].

Despite the fact that the utilization of RO in combination with other pressure-driven membrane operations such as MF, UF and NF has led fundamental contribution in terms of overall process economics, some critical developments are still necessary in order to accomplish possible improvements in the process efficiency (increase recovery), operational stability (reduce fouling and scaling problems), environmental impact (reduce brine disposal), water quality (remove harmful substances) and costs. In particular, cost effective and environmentally sensitive concentrate management is today recognized as a significant obstacle to extensive implementation of desalination technologies. Considering a typical RO desalination plant with water recovery factor of 45–60% (seawater) or 75–85% (brackish water), this would result in a significant excess of high concentrated solutions to be disposed-off. At present, the most frequent disposal practice for brines is a direct discharge into lakes, lagoons, rivers, ocean and sanitary drains. However, the requirements of more and more rigid environmental protection regulations will stop this low-cost brine disposal in the near future [18].

As a result of the significant impact of desalination plants on the environment, the requirements for concentrate management tight up: brine disposal minimization and zero liquid discharge (ZLD) are the demanding targets for several applications. In the last years, several process engineering strategies have been implemented in order to accomplish the concept of the ZLD in seawater desalination [19].

1.3.2 Innovative membrane contactors technology and their potential of integration

Gas-liquid membrane contactors (GLMC) are an emerging technology in which the hollow fiber porous membranes are used as a tool for inter-phase mass transfer. They are able to immobilize the gas-liquid interface at the membrane pores due to the hydrophobic nature of the membrane itself, and to create a large contact area that activates stripping or absorption processes. The surface/volume ratio in membrane hollow fibers is one order of magnitude higher than the conventional separators and therefore GLMC offers additional advantages of higher liquid mass transfer coefficients, simple and flexible design procedures, and the nonexistence of fluid dynamic limitations (flooding) [20]. GLMC allows an adequate control of dissolved gas composition against corrosion and depletion of the water quality. Moreover, the reactive transfer of CO_2 allows to control the simultaneous precipitation equilibrium of inorganic salts, acting on the pH of the solution [21]. Hence, the GLMC's are employed as pretreatment to prevent scaling and as post-treatment to improve the water quality.

Membrane distillation/crystallization (MD/MC) is a well-known methodology having great potential as evaporation process carried out at relatively low temperature by using microporous hydrophobic membranes. The hydrophobic nature of the membrane prevents the mass transfer of the liquid phase and creates a vapour-liquid interface at the pore entrance. Here, volatile compounds evaporate, diffuse and/or convect across the membrane pores, and are condensed and/or removed on the opposite side (permeate or distillate) of the system. The driving force is the partial pressure difference created by the temperature difference between the two phases which allows theoretically the complete rejection of non-volatile solutes. Lower temperatures and pressures with respect to those usually used in conventional distillation columns are generally sufficient to establish a quite interesting transmembrane flux (1-20

kg/m^{2}h), with consequent reduction of energy costs and mechanical requirements of the membranes [22]. Typical feed temperatures vary in the range of 30-60 °C, thus permitting the efficient recycle of low-grade or waste heat streams, as well as the use of alternative energy sources (solar, wind or geothermal). In addition, the possibility to use plastic equipments also reduces or avoids corrosion problems. If compared with RO, MD does not suffer limitations arising from concentration polarization phenomenon and can be preferentially employed whenever high permeate recovery factors are requested [22]. MD is characterized by production of high purity distillate, reduced sensitivity to fouling and absence of concentration polarization phenomena, and high flexibility.

Membrane crystallization (MC) has been recently proposed as one of the most interesting and promising extension of the MD concept in which solutions are concentrated above their saturation limit and achieve a metastable state (supersaturation) in which crystals nucleate and grow [23]. MC, therefore, represent an additional option for realizing integrated membrane desalination systems.

MD/MC units also offer the attractive opportunity to be integrated in water treatment cycles. In this respect, an MD unit, operating on the brine of a RO plant, allows to reach higher recovery factor in a seawater desalination application with respect to a single RO stage. Drioli et al. [24] obtained a total fresh water factor recovery of about 88% (40% for the RO unit and 77% for the MD stage) by operating an MD unit on the retentate of a SWRO plant with a considerable reduction in the quantity of brine produced. Additionally, the use of MC allows the recovery of NaCl and MgSO4.7H2O from brines. The overall water recovery of the integrated system can be increased up to values approaching 95% [25]. GLMC is employed in order to promote reactive transfer of CO_2 into the concentrate stream and to control the ionic strength during $CaCO_3$ precipitation.

There are some very interesting opportunities to integrate different membrane operations into industrial processes and so achieve the overall benefits of PI. In this context, the combination of the conventional pressure-driven membrane operations such as MF, NF and RO with the membrane contactors technology such as gas-liquid membrane contactors (GLMC) and membrane distillation/crystallization processes (MD/MC) is expected to offer alternative design-pathways for improving water quality and brine management. The integration of different membrane units will fulfil the PI strategy and will represent an interesting way for achieving the ZLD goal due to the possibility of overcoming the limits of the single units and, thus, to improve the performance of the overall operation [26].

Although the combination of two or more conventional unit operations within one framework permits a high possibility of energy savings and/or capital investment reduction, it never means that the full potentials can be simply achieved with an arbitrary combination of all the conventional unit operations considered. It might lead to more challenging problem in process operation than the conventional design philosophy due to the intensified internal mass and energy integration. Hence, a matter of serious concern in process intensification is the occurrence of complicated process dynamics and the introduction of great difficulties to process operation. Consequently, it is required to identify the process dynamics and operation at early stage of the process development in order to avoid such problems. In addition, it should be indicated that the way to combine all the conventional unit operations involved could actually have a strong effect upon the process dynamics and controllability. Due to the strong interactions between internal mass integration and energy integration, a careful trade-off has to be implemented in process development [27].

1.4 Objectives

The primary objective of this research is to study the combination of the membrane contactors technology with the pressure driven membranes in order to completely redesign the water desalination plants. The research project focuses on the elaboration of an innovative technological approach in order to:

- Improve the efficiency of membrane desalination systems by combining the single membrane units in a globally optimized and compact integrated membrane desalination system and processing NF/RO retentate by MD/MC units in order to increase the overall recovery factor (up to 95%) and to decrease the concentrated wastes.
- Produce water with good quality by remove a wider range of contaminants (including boron) by using evaporative membrane units able to reach 100% retention of solutes, colloids, non-volatile organic contaminants etc.
- Keep water affordable by decrease operating costs.
- Ensure sustainability of desalination plants by facing the brine disposal problem through processing superconcentrated streams in order to produce crystalline salts with high purity, controlled shape and crystal size distribution.

1.5 Project description

This research program will consider: (i) a theoretical part aiming to develop appropriate tools for the analysis and simulation of membrane contactors units and for predicting the effects of the main operative parameters on the performance of the single stage; (ii) an energy and exergy analysis of the integrated membrane desalination system for process optimization and diagnosis of inefficiencies; (iii) a cost analysis for evaluating the potential economics; (iv) an experimental phase, to carry out in parallel with the modelling activity, aiming to

confirm the reliability of the proposed approach; (v) the realization of a bench-scale integrated membrane desalination plant.

The project work is subdivided into the following tasks:

TASK 1. Modeling and optimization of the integrated membrane system

This study will be mainly on the modeling and optimization of the GLMC and the MD/MC units.

Task 1.1: Analysis and simulation of a GLMC unit

Research activities:

- Investigation of main process variables (temperature, pressure, gas and liquid flow rates, pH, structural properties of the membrane) on the gas transfer rate.
- Identification of the controlling resistance to mass the transport and optimization of the GLMC unit.

Task 1.2: Analysis and simulation of MD/MC units

Research activities:

- Solving mass and heat balances in order to predict the transmembrane flux as function of the operative variables and to control polarization phenomena.
- Identifying the fluid-dynamic threshold representing the transition from a regime with low diffusion rate to a regime with higher relative weight of interfacial kinetics, in order to limit the potential effect of impurity.
- Predicting crystal size distribution (CSD) according to Population-Balance equations and to characterize its dispersion value by the Coefficient of Variation (CV).

TASK 2. Energy and exergy analysis of the integrated membrane system

A comprehensive analysis based on the second law of thermodynamics will be carried out by considering entropy production, thermal, electrical and mechanical inputs to the integrated schemes. A literature survey will allow determining and/or updating substitution coefficient, energy sources conversion and efficiency. Inefficiency in integrated processes due to their intrinsic irreversibility will be identified, located and quantified in order to elaborate possible strategies for improving locally and globally the system design.

Energy and exergy analysis aims to compare the potentialities and performance of different integrated schemes in terms of energy demand and exergy efficiency. This analysis will represent a crucial tool for selecting the optimal schemes in order to realize a final prototype of integrated plant and successive adjustments of the operative conditions.

TASK 3. Cost analysis and sensitivity study of the integrated membrane system

In order to estimate the economic feasibility of the proposed integrated system, a cost analysis will be also carried out.

The economic evaluation will consider:

- The impact of additional membrane contactor units on the installation and operating costs as a result of an increased consumption of electric power, heating steam for thermally driven membrane operations (membrane distillation/crystallization), chemicals, membranes and maintenance.
- Influence of the increased water recovery ratio on the unit product cost.
- Potential economics of crystalline salts produced by membrane crystallization from brine.

A sensitivity study will investigate the effect of changing a single variable on the integrated system with the aim to optimize the process profitability. The major

operational parameters will be identified and related to the overall system performance.

TASK 4. Experimental tests on membrane contactor units

The experimental study will be carried out on GLMC and MD/MC units.

Task 4.1 Experimental tests on Gas-Liquid Membrane Contactor unit

The activities will focus on the study of CO_2 transfer from the liquid phase to the gas phase

Task 4.2 Experimental tests on Membrane Distillation/Crystallization unit

The experimental study on MD will consider the evaluation of distillate fluxes at different transmembrane temperatures and flow rates, the study of polarization phenomena and their detrimental effect on the overall efficiency of the unit, the stability of the hydrophobic character of the membrane in long-term operations, the water recovery factor. Experiments on MC will be devoted to identify the favorable operative conditions for obtaining a crystalline product with uniform size distribution and high purity, combined with appropriate quality of the water permeate and higher recovery factors approaching 90-95%.

The experimental activity will focus on:

- Study of the evaporation efficiency as function of energy input and trans-membrane flux of permeate. Optimization of the operative conditions and targets (transmembrane temperatures feed and permeate flow rates, longitudinal pressure drop, brine concentration and recovery factor).
- Evaluation of the stability (preservation of hydrophobic property) of MD/MC membrane modules against fouling, plugging, and caking.
- Analysis of the crystalline product in terms of shape, purity, crystal size distributions and yield.

TASK 5. Running a semi-pilot prototype of integrated membrane desalination system

The final goal is to integrate the various membrane operations, starting from UF-NF as pre-treatment for RO and membrane contactors devices in opportune configuration, and to define the strategies and protocols requested to operate the system at high recovery factors (>95%), for inducing selective formation of crystals from high concentrated brine with improved characteristics in terms of shape and size distribution.

1.6 Potential for practical applications

This project will significantly contribute to a better quality of produced water by enhancing the rejection properties of the membrane desalination system as result of the use of MD unit in the integrated process. In addition, the amount of rejected brine will be decreased which will help in maintaining the sustainability of the desalination plant. The synergic use of MD/MC units on the NF and RO retentate will offer the possibility to obtain additional fresh water with target recoveries >95%, as well as high-quality crystals (NaCl, $MgSO_4*7H_2O$) for successive applications. Keeping water affordable is a consequential purpose of the research project. It is well recognized that driving down the cost of water produced from next-generation desalination technologies will require a dedicated research and development program that focuses on:

- Increasing production efficiency, that involves improving the quantity of water produced per unit of energy consumed.
- Reducing costs.

The innovative concepts and design of integrated desalination schemes are expected to match the PI strategies leading to cheaper, safer and sustainable technique.

REFERENCES

[1] W.T. Cross, C. Ramshaw, Chem. Eng. Res. Des., 64 (1986) 293.
[2] A.I. Stankiewicz, J.A. Moulijn, Process intensification: Transforming chemical engineering, Chemical Engineering Progress, 96 (2000) 22.
[3] http://www.bhrgroup.co.uk/pi/aboutpi.htm.
[4] A.I. Stankiewicz, J.A. Moulijn, Re-engineering the chemical process plant: Process Intensification, Marcel Dekker Inc., New York (2004).
[5] Sustainable Technological Development at DSM: The Future Is Now, DSM Magazine, 83 (1999) 4.
[6] J.C. Charpentier, In the frame of globalization and sustainability, process intensification, a path to the future of chemical and process engineering (molecules into money), Chemical Engineering Journal 134 (2007) 84.
[7] E. Drioli, E. Curcio, Membrane engineering for process intensification: a prospective, Journal of Chemical Technology and Biotechnology 82 (2007) 223.
[8] S. Al-Obaidani, Chemical cleaning of micro-filtration membranes used for pretreatment of oil contaminated seawater, M.Sc. thesis (2004).
[9] IDA Desalination Year book 2007-2008, Water desalination report, (2008).
[10] E. El-Zanati, K.M. El-Khatib, Integrated membrane – based desalination system, Desalination 205 (2007) 15.
[11] A. Brehant et al., Comparison of MF/UF pretreatment with conventional filtration prior to RO membranes for surface seawater desalination, Desalination 144 (2002) 353.
[12] S van Hoop, J.G. Minnery and B. Mack, Dead-end ultrafiltration as alternative pre-treatment to reverse osmosis in seawater desalination: a case study, Desalination, 139 (2001) 161.
[13] M. Wilf and M.K. Schierach, Improved performance and cost reduction of RO sweater systems using UF pretreatment, Desalination, 135 (2001) 61.
[14] G.L. Leslie et al., Proc. AWWA, Water Reuse Conference, Florida (1998).
[15] N. Hilal et al., A comprehensive review of nanofiltration membranes: Treatment, pretreatment, modeling, and atomic force microscopy, Desalination 170 (2004) 281.
[16] M.M. Nederlof, J.C. Kruithof, J.S. Taylor, D. van der Kooij and J.C. Schippers, Comparison of NF/RO membrane performance in integrated membrane systems, Desalination, 131 (2000) 257.
[17] E. Drioli, A. Criscuoli, E. Curcio, Integrated membrane operations for seawater desalination, Desalination 147 (2002) 77.
[18] E. Drioli et al., integrating membrane contactors technology and pressure-driven membrane operations for seawater desalination energy, exergy and costs analysis, Chemical Engineering Research and Design, 84 (A3) (2006) 209.

[19] A. Seigworth, R. Ludlum, E. Reahl, Case study: Integrating membrane processes with evaporation to achieve economical zero liquid discharge at the Doswell combined cycle facility, Desalination 102 (1995) 81.
[20] E. Drioli E, A. Criscuoli A, E. Curcio, Membrane Contactors: Fundamentals, Applications and Potentialities. Elsevier, Amsterdam (2006).
[21] Gabelman, A. and S.T. Hwang, Hollow fiber membrane contactors, Journal of Membrane Science 159 (1999) 61.
[22] K. W. Lawson and D. R. Lloyd, Review: Membrane distillation, Journal of Membrane Science 124 (1997) 1.
[23] E. Curcio, A. Criscuoli, E. Drioli, Membrane crystallizers, Ind. Eng. Chem. Res. 40 (2001) 2679.
[24] E. Drioli, F. Laganà, A. Criscuoli, G. Barbieri, Integrated membrane operations in desalination processes Desalination 122 (1999) 141.
[25] E. Drioli, E. Curcio, A. Criscuoli, and G. Di Profio, Integrated system for recovery of $CaCO_3$, NaCl and $MgSO_4.7H_2O$ from nanofiltration retentate, Journal of Membrane Science, 239 (2004) 27.
[26] E. Drioli, E. Curcio and G. Di Profio, State of the art and recent progresses in membrane contactors, ChERD J, 83 (2005) 223.
[27] K. Huang, S.J. Wang, L. Shan, Q. Zhu, J. Qian, Separation and Purification Technology 57 (2007) 111.

CHAPTER 2
GAS-LIQUID MEMBRANE CONTACTORS

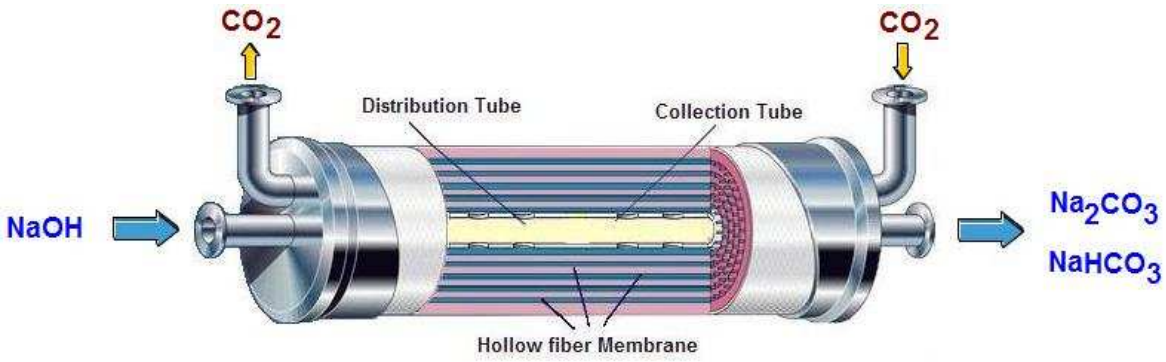

SUMMARY
This chapter is dealing with the optimization of the GLMC. It provides the theoretical background necessary for modeling and simulation. It also covers the experimental parts related to the utilization of the GLMC in the proposed integrated membrane system. Finally, it provides a feasibility study to verify the economics of using such devices in the integrated membrane system.

2.1 Objectives

The preliminary objective of using Gas-Liquid Membrane Contactors (GLMC) in the proposed integrated membrane system is to establish a reactive transfer of carbon dioxide (CO_2) into sodium hydroxide ($NaOH$) solutions to produce sodium carbonate (Na_2CO_3) solution as shown in Figure 2.1. Then Na_2CO_3 is used to limit calcium sulphate ($CaSO_4$) precipitation that causes the reduction of sulphate (SO_4^{2-}) content in the solution and drastically limits the recovery of magnesium sulphate ($MgSO_4$) from the NF retentate stream. Moreover, CO_2 is the largest contributor to greenhouse effect and its efficient recovery might also reduce the environmental impacts due to atmospheric emissions in power plants (CO_2 represents the 10-13% of stack gas) [1].

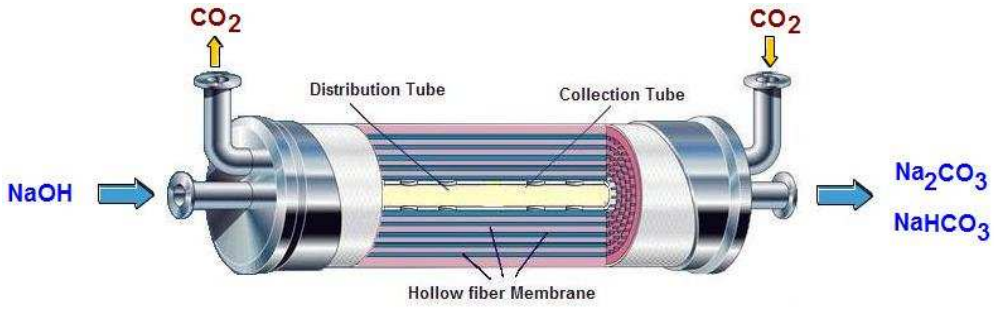

Figure 2.1 Reactive transfer of CO_2 through GLMC

2.2 Introduction

Gas-Liquid Membrane Contactors (GLMC) are devices that achieve gas/liquid mass transfer without dispersion of one phase with the other. They are based on a technology in which porous membranes are used as tools for inter-phase mass transfer. However, the membrane does not act as a selective barrier, but the separation is based on the principles of phase equilibrium. This is established by passing the fluids on opposite sides of the microporous membrane. One of the fluids is immobilized in the pores of the membrane so that the fluid/fluid interface is located at the entrance of each pore due to the hydrophobic nature of the membrane itself that creates a large contact area which activates stripping or absorption processes [2]. In gas-liquid mass transfer, a generic species moves from a phase to the other across a microporous hydrophobic membrane under a partial pressure gradient. For example, dissolved oxygen can be removed from water by stripping with carbon dioxide (CO_2), while CO_2 is absorbed simultaneously in water [3].

The performances of GLMC strongly depend on the properties of the membranes used. In general, high hydrophobicity is required in order to prevent wetting and mixing between contacting phases; elevated porosity leads to high fluxes, but might cause bubble coalescence [4].

The gas/liquid contacting operation is conventionally carried out in direct contact equipment such as packed or bubble columns [5]. GLMC can be used as a substitute for these conventional equipments due to the following advantages:

- *Operational flexibility*. The two phases flow independently on each other since they flow on the opposite sides of the hollow fiber (i.e. shell and lumen) and thus they can be manipulated separately. This is effective for avoiding problems such as flooding, unloading, foaming, channeling and entrainments which are often encountered in packed/tray columns [2].
- *No emulsion formation,* because there is no fluid/fluid dispersion.

- *No density difference is required between the two fluids.* GLMC can deal with fluids of identical densities and can be operated in any orientation.
- *Linear scale-up*. The modularity of the membrane modules makes the design simple and easy to be scaled-up linearly, and it can effectively eliminate the problems associated with the conventional equipments due to the absence of interpenetration of the two phases.
- *Easier performance prediction*, since the interfacial area is known and constant and it does not depend on the operating conditions such as temperature and liquid flow rates.
- *Higher efficiency* due to the compact nature of the GLMC which require less energy consumption and smaller installation space.

On the other hand, GLMC also have some disadvantages such as:

- *Lower mass-transfer coefficients* due to the small diameter of fibers and the small channels around the fibers which normally results on laminar flow of both gas and liquid. However, large interfacial area of GLMC makes them more efficient.
- *Higher mass-transfer resistance* introduced by the membrane itself. However, this resistance is not always important and there are some steps to minimize it.
- *Membrane replacement cost* as additional cost since membrane has a finite life.
- *Membrane may be subjected to fouling*, although this is not a very common problem like in pressure-driven membrane operations.

GLMC can have several membrane configurations including flat sheet and hollow fiber modules. Generally, hollow fiber GLMC's are preferred over flat sheet GLMC due to the higher interfacial area of the former. The hollow fiber GLMC can be used in two different modes of operations (i.e. parallel and cross-flow) based on the flow direction of the gas and the liquid phases [6].

1. *Parallel flow modules* (schematic representation is shown in Figure 2.2 (a)): the flows of both phases are parallel to the axis of the fiber and both fluids flow either in the same direction (co-current) or in the opposite direction (counter-current). Parallel flow modules are characterized by their manufacturing simplicity and they can offer the highest average concentration driving force in the case of counter-current flow and is preferred in situations where membrane or fiber-side mass transfer resistance controls [7]. The main disadvantage of these modules is their lower efficiency in mass transfer compared with the cross-flow modules.
2. *Cross-flow modules* Figure 2.2 (b). The shell-side fluid flows in direction normal to the axis of the fibers. Thus the two fluids flow perpendicularly to each other. The cross-flow modules are preferred when the shell-side mass transfer resistance is significant due to their advantages of relatively high mass transfer coefficients, minimized shell-side channelling and lower shell-side pressure drop compared to the parallel flow modules [8].

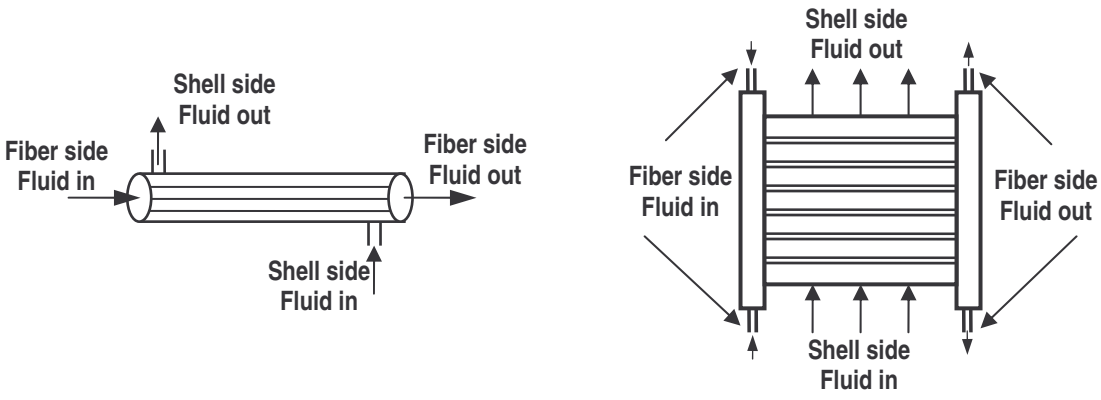

(a) Parallel-flow hollow fiber module (b) Cross-flow hollow fiber module

Figure 2.2 Schematic representations of hollow fiber modules

2.3 Membrane wetting and prevention

The membrane wettability determines of operations efficiency of the contactor. In hydrophobic membrane contactor operation, the pores are filled with non polar fluids while the polar fluids cannot penetrate through the pores. However, because of the pressure exerted on polar fluids due to pumping, they may penetrate into the membrane pores. Therefore, the pressure on the non-wetting side must be kept below a critical value known as the break through pressure which can be estimated by *Laplace* equation [2, 9, 10]:

$$\Delta P = \frac{4\sigma \cos\theta}{d_p} \qquad (1)$$

where σ is the surface tension of the polar fluid, θ is the contact angle between the liquid phase and membrane; and d_p is the membrane pore diameter. As shown from the *Laplace* equation, the breakthrough pressure can be increased by either increasing the surface tension of the wetting fluid or changing the membrane properties i.e. using membrane with smaller pore size or increasing cosine of contact angle by enlarging the polarity difference between the wetting fluid and the membrane material.

Even though the *Laplace* equation is not implicit in operating temperature and process solution composition, these parameters can have significant effects on the liquid-solid contact angle and the liquid surface tension. These effects must not be overlooked when selecting a membrane. In general, the liquid-solid contact angle must he greater than 90° for the system to be used in GLMC. Table 2.1 lists values of the breakthrough pressure for hydrophobic membranes with different pore sizes. The presence of strong surfactants can greatly reduce the value of *cos(θ)*, therefore, care must be taken to prevent contamination of process equipment and process solutions with detergents or other surfacting agents.

Table 2.1 Typical values of breakthrough pressure for membranes with different pore size

Pore size (μm)	Breakthrough pressure (kPa)	Reference
0.03	1200	This work
0.05	1000	[11]
1.00	185	[12]

The following measures are suggested to avoid the wetting problem:

- *Surface modification of membrane* by coating the microporous fibers with a thin, highly permeable polymer or gel [13, 14]
- *Selection of denser hollow fiber membranes* which can offer greater flexibilities in feed pressure. The higher membrane resistance associated with denser membrane can be minimized by applying larger operating pressure in the gas phase [1]
- *Using membrane with smaller pore size* which increases the breakthrough pressure in accordance with *Laplace* equation (equation 1).
- *Optimizing operation conditions*, for example the operating pressure of the liquid phase should generally be higher than that of the gas phase in order to prevent bubble formation, which could result in significant losses of valuable gas components and deteriorate the separation efficiency [12]. In addition, it is advisable to operate at a pressure lower than the breakthrough pressure.

2.4 Mass transfer in membrane contactors

In GLMC, mass can be transferred from the gas phase to the liquid phase (absorption) or from the liquid phase to the gas phase (stripping). For a non-wetted hydrophobic GLMC, mass transfer is determined by three consecutive steps as shown in Figure 2.3 [15]. The first step is the diffusion of gaseous component *A* from the bulk gas phase to the outer surface of the membrane.

Then, diffusion will take place through the totally gas-filled pores of the membrane to the membrane-liquid interface. Finally, the transporting gas will dissolute into the liquid absorbent and liquid-phase diffusion or chemical reaction [4, 16].

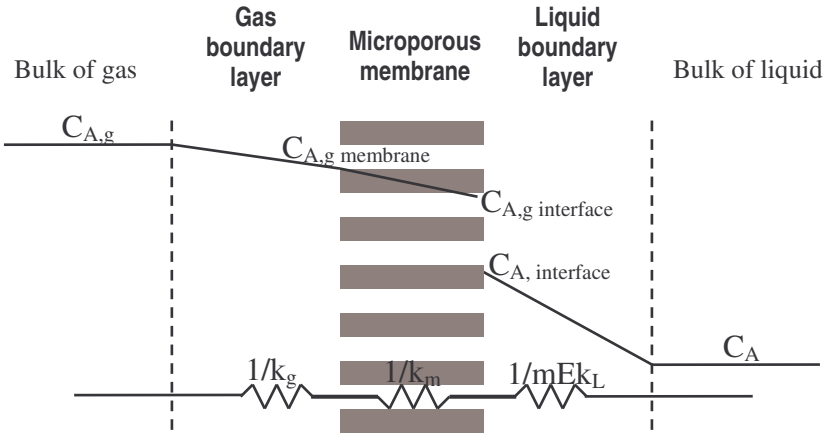

Figure 2.3 Mass transfer regions and resistances in hydrophobic GLMC [15]

The mass transfer of a component A from the gas phase flowing outside the hollow fibers to the liquid can be calculated as shown by equation 2:

$$N_A = K(C_{A,gas} - C_{A,liquid}) \qquad (2)$$

where K is the overall mass transfer coefficient, $C_{A,gas}$ is the concentration of the component A in the gas phase in equilibrium with its concentration in the liquid phase, and $C_{A,liquid}$ is the average concentration of the gas component A in the liquid phase. The Henry's law can be used to link the equilibrium gas concentration in the gas phase $C_{A,gas}$ with its partial pressure as given by equation 3 [4,7].

$$P_A = H_A \,.\, C_A \quad ; P: \text{Partial pressure; } H: \text{Henry's constant} \qquad (3)$$

2.4.1 Mass transfer coefficients

Overall mass transfer coefficient

The overall mass transfer coefficient can be expressed in terms of the individual mass transfer coefficients that characterize the three resistances encountered during gas transfer from gas phase to liquid phase through the membrane. Hence, the overall mass transfer coefficient is expressed using the resistance-in-series model as [17,18]:

$$K = \left[\frac{1}{k_g} + \frac{1}{k_m} + \frac{1}{m E k_L} \right]^{-1} \quad (4)$$

where K is the overall mass transfer coefficient, k_g, k_m and k_L are the mass-transfer coefficients of the gas phase, the membrane and liquid phase, respectively; m is the distribution coefficient between gas and liquid (also called as gas solubility in liquid) and it is equal to the adimensional Henry's constant for physical absorption; and E is the enhancement factor due to chemical reaction [4].

Individual mass-transfer coefficients

Mass transfer coefficients for GLMC's are generally predicted using correlations of the form [2]:

$$Sh \alpha \mathrm{Re}^{\alpha} Sc^{\beta} f(geometry) \quad (5)$$

where *Sh* & *Re* and *Sc* are the Sherwood, the Reynolds and the Schmidt numbers, respectively.

Gas side mass-transfer coefficient

The gas side mass transfer coefficient (k_g) depends on the fluid hydrodynamics in the shell side of the membrane module and is module specific due to the high packing density and non-uniform spacing of the hollow fibers within the membrane module. There is no general expression available to describe the mass transfer in the gas side due to maldistribution of flow, presence of stagnant zones, bypassing or channeling that may occur more frequently than

in the liquid side. A number of correlations from literature to estimate k_g are presented in Table 2.2.

Liquid side mass transfer

The liquid side mass transfer coefficient (k_L), when only physical absorption occurs in the liquid side, can be obtained using Lévesque's solution derived from the heat transfer analogy of *Graetz* heat transfer problem of laminar flow of liquid through a circular duct [19,20]. It is involved with the assumptions of constant gas-liquid interface conditions and fully developed laminar flow of liquid through the fiber. The Lévesque equation is given as [21]:

$$k_L = \frac{Sh.D_A}{d_f}, \quad Sh = 1.62Gz^{1/3} \; ; \quad Gz = \frac{d_f v_L}{D_A} \tag{6}$$

This equation valid only for high *Graetz* numbers. Other correlations for estimation of the liquid side mass transfer coefficient (k_L) valid for the entire range of *Graetz* number are presented in Table 2.2

Table 2.2 Summary of correlation for estimating individual mass transfer coefficients for hydrophobic hollow fiber modules

Correlation		**Conditions**	Ref.
➢ *Shell side parallel flow*			
$Sh = 5.8\left[d_e(1-\phi)/L\right]\mathrm{Re}^{0.6}\, Sc^{0.33}$	(7)	$0<Re<500;\ 0.04<\phi<0.4$	[14]
$Sh = 1.25\left(\mathrm{Re}\, d_e/L\right)^{0.93} Sc^{0.33}$	(8)	$0<Re<500;\ \phi=0.03$	[20]
$Sh = 0.019Gz$	(9)	$Gz<60$; close-packed fibers	[19, 22]
$Sh = 8\left(\mathrm{Re}\ d_e/L\right)Sc^{0.33}$	(10)	Based on diffusion coefficients	[22]
$Sh = \left(0.53-0.58\phi\right)\mathrm{Re}^{0.53}\, Sc^{0.33}$	(11)	$21<Re<324;\ 0.32<\phi<0.76$	[23]
➢ *Tube side parallel flow*			
$Sh = 3.67$	(12)	$Gz<10$	[9]
$Sh = \sqrt[3]{3.67^3 + 1.62^3 Gz}$	(13)	$10<Gz<20$	[17]
$Sh = 1.62\left(d_f v/LD\right)^{1/3}$	(14)	$Gz>20$	[20, 21]

Membrane mass transfer coefficient

The transport through the membrane is assumed to be caused by diffusion only. Hence, Fick's law can be used to describe the mass-transfer k_m as in equation 15:

$$k_m = D_A \frac{\varepsilon}{\sigma\tau} \tag{15}$$

The membrane resistance depends on its thickness and pore structure properties including pore size, porosity and tortuosity. In hydrophobic membranes, the pores are gas-filled and depending on the pore diameter d_p, the diffusion through membrane can be *Knudsen* (d_p<1×10^{-7} m) or bulk (d_p>1×10^{-5} m) or both types of diffusions (1×10^{-7} < d_p< 1×10^{-5} m). The diffusion coefficient D_A for a binary gas mixture is calculated as [9]:

$$D_A = \left[\frac{1}{D_{A,j}} + \frac{1}{D_A^K} \right]^{-1} \tag{16}$$

The bulk diffusion coefficient ($D_{A,j}$) can be calculated based on the kinetic theory of gases and the Knudsen diffusion coefficient (D_A^K) can be estimated using:

$$D_A^K = K_0 \sqrt{\frac{8RT}{\pi M}} \quad ; \quad K_0 = \frac{4\varepsilon d_p}{3\tau} \tag{17}$$

Simplification for the overall mass transfer coefficient

The correlations that express the overall mass transfer coefficient can be simplified for specific situations. For example, the membrane resistance as well as the boundary layer resistance at the gas phase can be neglected compared to the boundary layer at the liquid phase in case of low soluble gas species in the liquid phase or physical absorption. Accordingly, the overall mass transfer coefficient is given as[4]:

$$K = k_L \tag{18}$$

However, when the gas species is highly soluble or reacts rapidly in the liquid phase, both membrane and gas phase boundary resistances become important. In this case, the enhancement factor (E) is introduced to account for the effect of the chemical reaction on the overall mass transfer coefficient and these resistances are called the external resistance as will be discussed in more details in the next sections.

2.4.2 Mass transfer with chemical reaction

The mass transfer is enhanced when chemical reactions are involved between the gaseous solute and components of the liquid. The effect of the chemical reaction on the absorption process is expressed as:

$$E = \frac{N_{A,chem}}{N_{A,phy}} \tag{19}$$

Here, $N_{A,chem}$ is the absorption flux/rate of a gas in a liquid in the presence of chemical reaction and $N_{A,phy}$ is the absorption flux/rate when only physical absorption is present. Equation 19 is based on the assumption that the driving force for the mass transfer for both physical and chemical absorption is identical. The contributions of chemical reaction on mass-transfer rate can be estimated using several approximate solutions based on three mass-transfer models namely; film, penetration and surface renewal theories. All these models assume the presence of a well-mixed bulk liquid and the absence of velocity gradient in the mass transfer zone. However, in case of small fibers diameters, this assumption is not satisfied and the mass transfer zone in the liquid phase may extend up to the axis of fiber depending on the gas-liquid contact time [4]. Therefore, traditional models have limited applications in the approximation of the enhancement factor for such cases. Thus, Differential mass-balance equations are used to describe the absorption process in membrane contactors.

The application of the modified approximate solution is generally limited to relatively high values of *Graetz* number, whereas rigorous numerical solutions

are required to determine the enhancement factor at low *Graetz* numbers and for complex reactions [4, 6, 24]. The differential mass balance for a gas component *A* in a reactive absorption of a gas in a liquid flowing through a microporous hollow fiber is given by:

$$V_z \frac{\partial C_A}{\partial z} = D_A \left[\frac{1}{r} \frac{\partial}{\partial r} \left(r \frac{\partial C_A}{\partial r} \right) \right] + R_A \qquad (20)$$

where V_z is velocity profile in the fibers, C_A is the concentration of the *A* component, *r* is the radial coordinate, and R_A is the source term due to chemical reaction. This equation is based on the assumption of (i) steady state and isothermal conditions; (ii) negligible axial diffusion; (iii) fully developed parabolic velocity profile in the fiber side; (iv) Henry's low is applicable; (v) axis-symmetry of the hollow fiber. As the liquid flow inside the fiber is laminar, the velocity profile in the radial direction is given by[25]:

$$V_z(r) = 2\bar{v} \left[1 - \left(\frac{r}{r_f} \right)^2 \right] \qquad (21)$$

where $\bar{v}$ is the average axial velocity and r_f is the fiber inner radius. The partial differential equation (equation (20)) requires the following initial and boundary conditions in the axial and radial directions, respectively [17,24]:

- at z=0 and $0 \le r \le r_f$, $C_A = C_{A,0}$
- at r=0 , $0 \le z \le L$, $\left(\frac{\partial C_A}{\partial r} \right) = 0$ (axial symmetry)
- at $r=r_f$, $0 \le z \le L$, $\left(\frac{\partial C_i}{\partial r} \right)_{i \ne A} = 0$ (other i components are non-volatile except the gas component *A*)

- at r=r_f , $D_A\left(\frac{\partial C_A}{\partial r}\right) = k_{ext}\left(C_{A,g,b} - C_{A,g,\text{int}}\right)$ (the flux of component *A* in the liquid phase is equal to the flux in the gas phase)

Here, D_A is the diffusion coefficient of the solute *A*, and subscripts *g*, *b* and *int* refer to gas phase, bulk and interface, respectively. The external mass transfer coefficient (k_{ext}) is a lumped parameter consisting of the resistances to mass transport of the species *A* due to the gas phase and microporous membrane and may be expressed as:

$$k_{ext} = \left[\frac{1}{k_g} + \frac{1}{k_m}\right]^{-1} \tag{22}$$

First order irreversible reaction

The local reaction rate is proportional to the concentration of the dissolved gas *A* in case of a first order irreversible reaction. The source term due the reaction (R_A) in equation (20) is substituted by:

$R_A = k_1 C_A$, k_1 is the reaction kinetic constant (23)

Hence, equation (20) can be solved numerically with appropriate initial and boundary conditions. In addition, the asymptotic approximate solution for mass transfer coupled with first order irreversible chemical reaction with infinite bulk based on the renewal theory can be obtained using:

$$E = Ha = \frac{\sqrt{k_1 D_A}}{k_L} \tag{24}$$

Ha is *Hatta* number that compares the maximum rate of reaction in the liquid film to the maximum rate of transport of *A* through the liquid film. This equation give good approximations only in fast reaction regime (*Ha*>2) and high *Graetz* numbers. In case of slow reaction regime (*Ha*<0.3), there is no enhancement due to chemical reaction, and the absorption flux depends on the mass transfer coefficient and hence on the liquid velocity.

Second order irreversible reaction

The rate of reaction in case of a second order irreversible reaction is proportional to the concentration of the dissolved gas *A* as well as the liquid phase reactant *B*. The source term due to a second order irreversible reaction (R_A) in equation (20) is given as:

$$R_A = k_{1,1} C_A C_B \qquad (25)$$

In this case, the saturation of species *A* as well as the depletion of species *B* in the liquid bulk are important. At high *Graetz* numbers and fast reaction regime (*Ha*>2), the penetration depth of reacting species is allocated near the gas-liquid interface and the concentration of the liquid phase reactant *B* at the fiber axis is similar to its concentration at the fiber inlet. Under these conditions, the enhancement factor *E* is equal to the modified *Hatta* number *Ha* [17,25]:

$$E = Ha = \frac{\sqrt{k_{1,1} C_{B,0} D_A}}{k_L} \quad C_{B,0} \text{ is the mixing cup concentration of } B \qquad (26)$$

On the other hand, the penetration depth and hence the reaction zone may extend up to the axis of the fiber at low *Graetz*. Therefore, the absorption regime can continuously change from the liquid entrance to the liquid exit. However, the absorption regime over the entire fiber can be assumed as instantaneous reaction regime of sufficiently low *Graetz* numbers and when: $C_{B,0}/C_{A,l}\, D_A << Ha$. In this case, the absorption rate is limited by the radial diffusion of the reacting species to the reaction plane and the flux is strongly influenced by the mass transfer coefficient. Thus, the enhancement factor is calculated using the modified asymptotic infinite enhancement factor defined as [3,17]:

$$E_\infty = \left(1 + \frac{C_{B,0} D_B}{\nu_B m C_{A,l} D_A}\right)\left(\frac{D_A}{D_B}\right)^q \qquad (27)$$

where ν_B is the stoichiometric coefficient of *B*. The value of q depends on the type of mass transfer model used (film model: *q=0*; penetration model: *q=1/2*; and *Lévesque* model (velocity gradient): *q=1/3*). The explicit approximate solution of

DeCoursey using the definition of modified *Hatta* number and modified infinite enhancement factor is giving as [25]:

$$E_{app} = \frac{-Ha^2}{2(E_\infty - 1)} + \left[\frac{Ha^4}{4(E_\infty - 1)^2} + \frac{E_\infty Ha^2}{(E_\infty - 1)} + 1 \right]^{1/2} \quad (28)$$

This approximation does not offer good predictions for cases of *Graetz* numbers less than 120 [24]. This is due the fact that at very low *Graetz* numbers, the concentration of the solute gas *A* in the liquid bulk is significant and the concentration of the reactive species *B* at the fiber axis is less than its inlet concentration. In such cases, corrections may be necessarily introduced to improve the prediction.

The reactive absorption of CO_2 into NaOH solution

The absorption of *A* species from gas to liquid phase is expressed as a function of concentration gradient and the overall liquid mass transfer coefficient K as described below:

$$N = K \Delta C_A = \left[\frac{1}{Ek_L} + \frac{1}{k_m} \right]^{-1} \left(C_{A,gas} - C_{A,liquid} \right) \quad (29)$$

where the enhancement factor (*E*) is evaluated according to the classical solution of gas absorption with second-order chemical reaction [26]. Depending on the *pH*, two reversible reactions may occur as follows:

$$CO_2 + H_2O \leftrightarrow H^+ + HCO_3^- \quad (k_1, pH < 8) \quad (30)$$

$$CO_2 + OH^- \leftrightarrow H^+ + HCO_3^- \quad (k_2, pH > 8) \quad (31)$$

k_1 and k_2 are the kinetic constant of the reaction. The reaction in the alkaline environment ($pH>8$) is a second-order reaction in the forward direction and limits the CO_2 transfer rate.

2.5 Simulation procedure

The membrane physical properties and the GLMC process operating conditions should be specified. Then, the geometrical configuration parameters (hydraulic diameter, area and velocity for both gas and liquid phases) were calculated. After that, the individual mass transfer coefficients were calculated using equation (6) and equation (9) for the membrane and the liquid side mass transfer coefficients, respectively. The overall mass transfer coefficient was calculated using equation (4). The enhancement factor in equation (4) was calculated based on the type of the transfer as follows:

- For physical absorption with no chemical reaction, equation (18) was used to calculate the overall mass transfer coefficient.
- For mass transfer with first order reaction the enhancement factor was calculated using equation (24).
- For mass transfer with second-order reaction the enhancement factor was calculated using equation (27) and equation (28).

Then, the concentration gradient along the GLMC module was calculated by dividing the GLMC module into a number of differential areas and the calculations were performed in the direction from the liquid phase inlet to the liquid phase outlet. Once the concentration gradient of the whole membrane module is calculated, the gas transfer flux into the liquid phase was calculated using equation (2). A schematic diagram of the modeling procedure is shown in Figure 2.4.

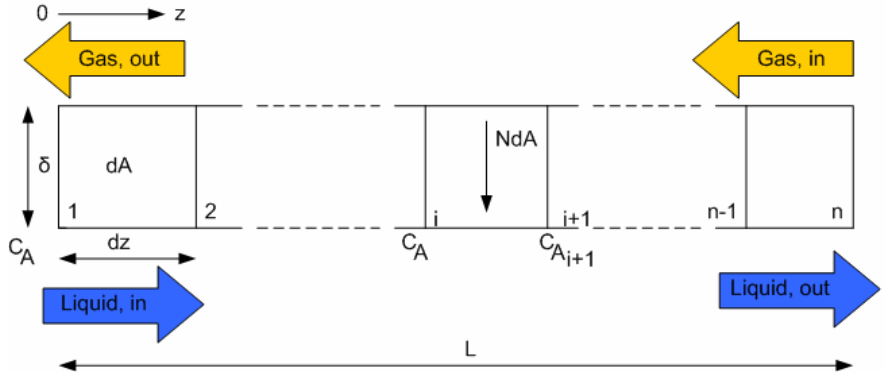

Figure 2.4 Schematic representation of the GLMC modeling

The simulation procedure flow chart is shown in Figure 2.5 and the simulation was executed using Matlab version 7.0.1 (R14). The programming code is shown in Appendix 1.

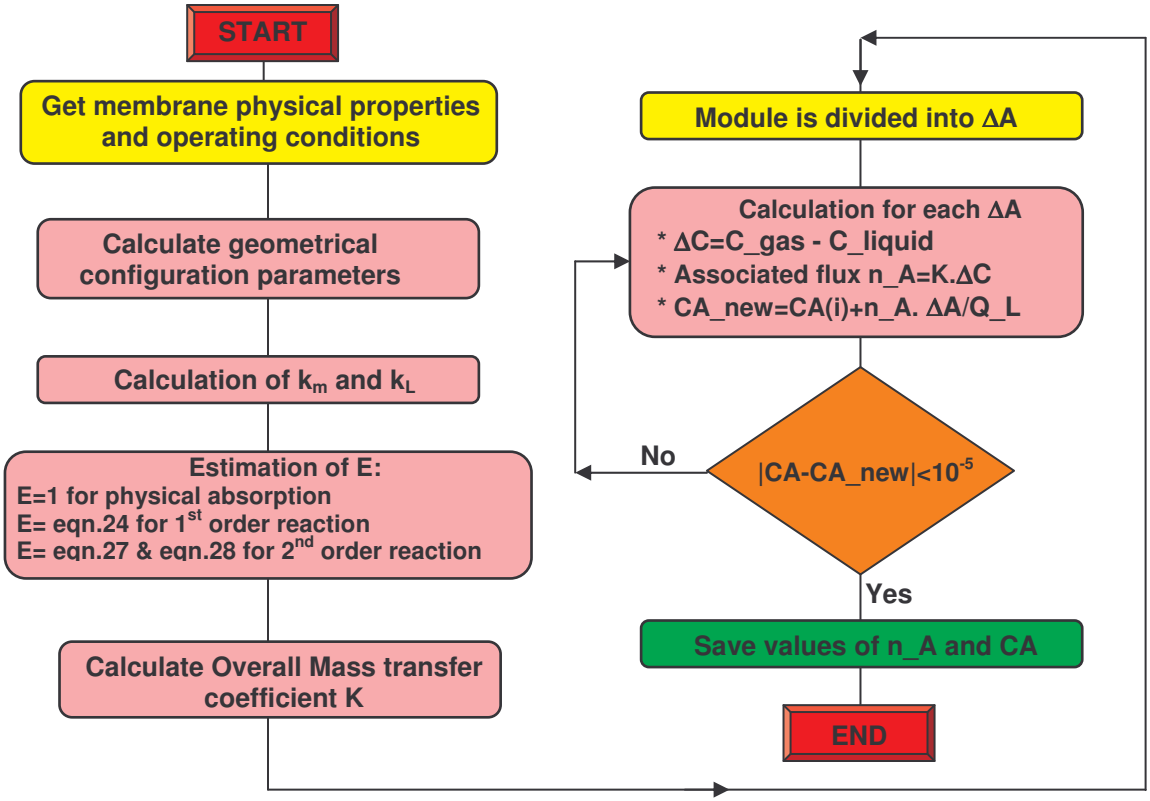

Figure 2.5 Flow chart of the computer simulation procedure of the GLMC

2.6 Experimental tests

Experiments have been carried out using a hollow fiber membrane contactor made by *LiquiCel-Celgard* with contact area of 1.4 m^2 as shown in Figure 2.6. The membrane fibers are made of polypropylene with outer diameter of 300 µm and inner diameter of 240 µm. The fibers length is 16 cm and the nominal pore size is 0.03 µm. The alkaline solution was fed through the fibers in continuous mode countercurrently with respect to the gaseous carbon dioxide stream flowing in the shell side. The transmembrane pressure (P_{liquid} - P_{gas}) was maintained constant at 0.15 bar and the operating temperature was controlled at around 30 ^oC during all tests. The carbon dioxide amount transferred from the

gas phase to the liquid phase was calculated by a mass balance on the gas stream. The pH values of the liquid phase were measured at the module outlet.

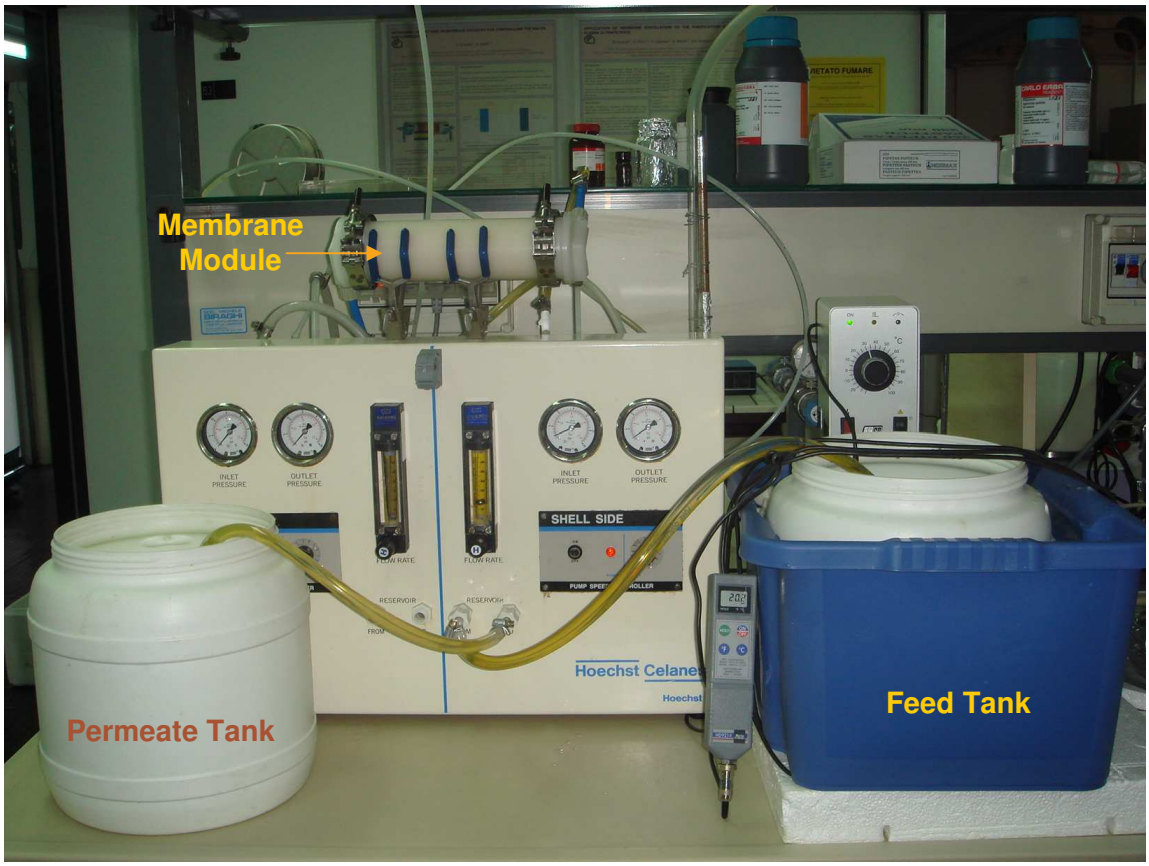

Figure 2.6 The GLMC experimental apparatus

2.7 Results and discussion

Figure 2.7 shows the amount of carbon dioxide transformed from the gaseous phase to the liquid phase by varying the liquid flow rate. Higher transfer rates of carbon dioxide were obtained when the liquid flow rate was increased. As shown in Figure 2.7, the amount of carbon dioxide transferred was increased from 0.16 $mol.m^{-2}.h^{-1}$ up to 0.56 $mol.m^{-2}.h^{-1}$ when the feed flow rate was increased from 10 to 40 L/h in case of using pure water (pH=5.66) as the liquid feed solution. In case of using alkaline solution of sodium hydroxide (*NaOH*) with pH of 12, the amount of carbon dioxide was increased from 0.42 $mol.m^{-2}h^{-1}$ to 0.72

mol.m^{-2}h^{-1} when the feed flow rate was increased from 10 to 40 L/h. This increase in the carbon dioxide transfer was due to the reduction of the liquid resistance when the liquid flow rate was increased since the mass transfer coefficient increases with the *Graetz* number according to equation (9) which is in agreement with the literature results [9, 24].

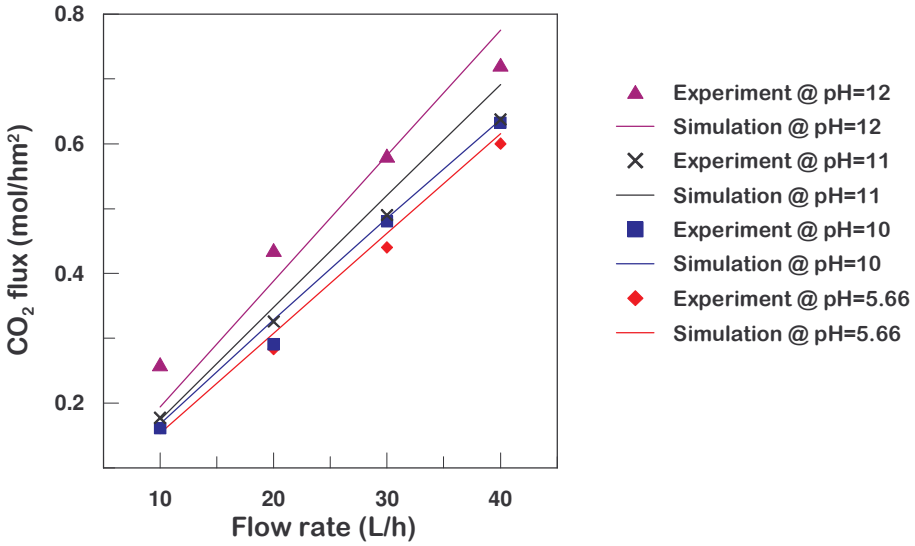

Figure 2.7 Amount of CO_2 transfer in GLMC versus feed flow rate

In addition, higher transfer rates of carbon dioxide were achieved at higher pH values of feed as shown in Figure 2.8. This transfer enhancement was due to the reaction of carbon dioxide with hydroxyl ions to give HCO_3^- *and* CO_3^{--}. On the other hand, the amount of carbon dioxide transfer was not affected by the variations in the gas flow rate since the membranes were hydrophobic and gas-filled and therefore it had negligible resistance in the mass transfer and the main resistance was due to the liquid stream resistance. Both simulation and experimental results showed good agreement with errors not exceeding 10%.

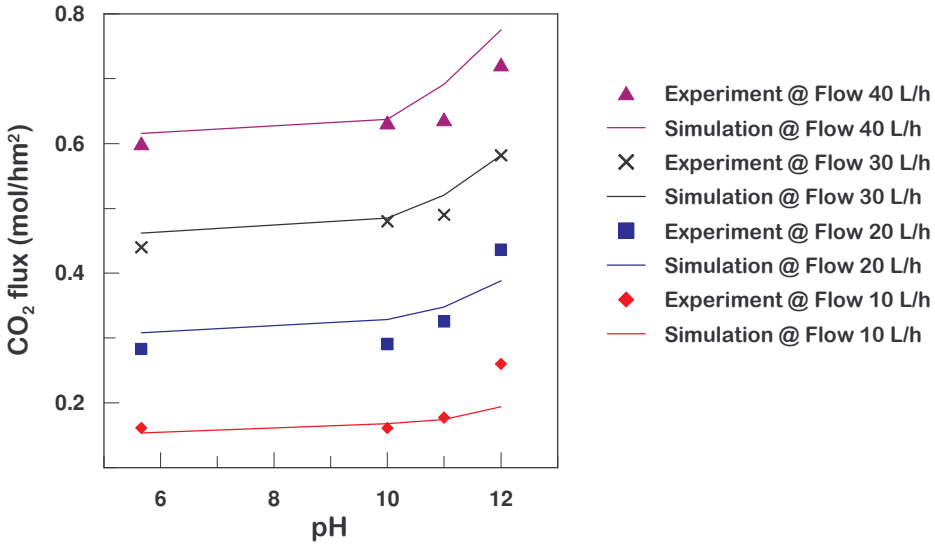

Figure 2.8 Amount of CO_2 transfer in GLMC versus feed pH

The simulation results showed higher values than the ones obtained from the experiments. This might be due to the wetting of some pores of the membrane which caused reduction in the transmembrane flux. On the contrary, there was no such reduction in the modeling results since the membrane pores were assumed gas-filled. The value of the membrane mass transfer coefficient (k_m) for gas-filled pores was $1.5\times10^{-2} m/s$ and the values of the overall mass transfer coefficient ranged between 3.4×10^{-4} and $6.6\times10^{-4} m/s$ depending on the feed flow rate. These results were similar to the ones reported in the literature as in [4, 9, 21, 27].

Case study: The role of GLMC in the integrated membrane system

The role of using GLMC in the proposed integrated system was demonstrated by considering CO_2 transfer in alkaline solution of $NaOH$ with concentration of 10 mol/m^3 and pH of 12. The solution was entering the membrane module at pH 12 and exiting at pH 6 as shown in Figure 2.9. The amount of CO_2 transferred along the module was high at the entrance of the

module and reduced rapidly in the direction of the module exit. This reduction in CO_2 transfer was expected due to the reduction in the driving force of the concentration difference between the gas and the liquid phases since the concentration of the liquid phase approached the concentration of the gas phase as the liquid approached the exit of the module.

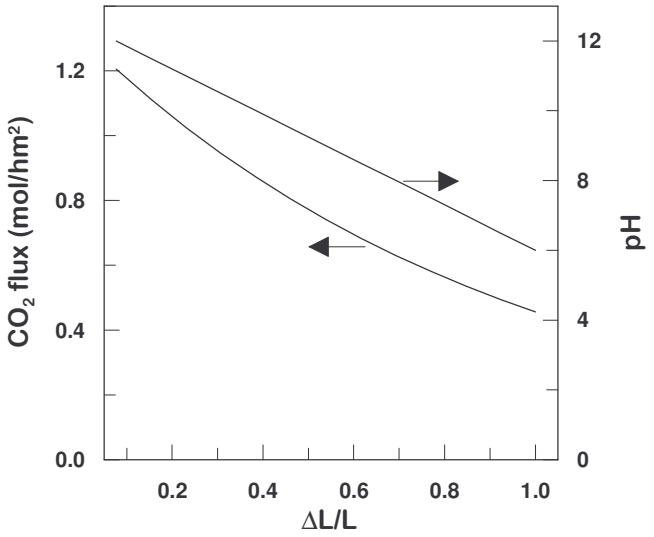

Figure 2.9 The pH and amount of CO_2 transferred along the GLMC module

The amount of CO_2 transferred into the solution will be distributed into four different species according to the pH of the solution as shown in Figure 2.10. Our interest was on the transformation of CO_2 into HCO_3^- *and* CO_3^{--} which will form $NaHCO_3$ and Na_2CO_3, respectively, that will be used to precipitate calcium ions (Ca^{++}) from the retentate of NF or the brine of RO to form limestone ($CaCO_3$) which will be precipitated. This reaction is presented in equations 32 and 33.

$$HCO_3^- + H_2O \leftrightarrow H_3O^+ + CO_3^{--} \quad (32)$$

$$Ca^{++} + CO_3^{--} \rightarrow CaCO_3\downarrow \quad (33)$$

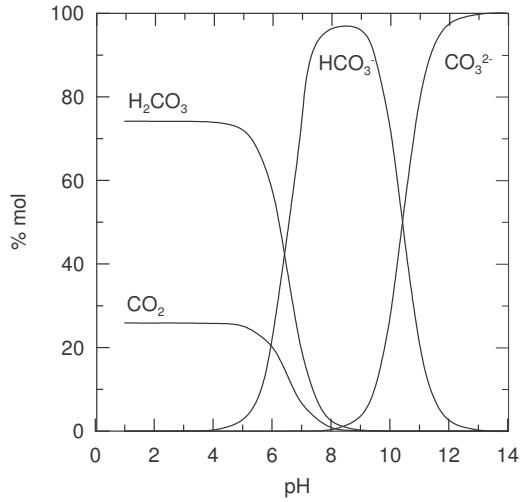

Figure 2.10 The distribution of Carbonate species versus pH [4]

The amount of the HCO_3^- *and* CO_3^{--} species available in the solution were calculated by dividing the membrane module into deferential areas and calculating the amount of CO_2 transferred and pH of the solution in each differential area along the module. The results are shown in Figure 2.10. The total amount of HCO_3^- *and* CO_3^{--} were 15.71 and 11.12 mol/m^3, respectively. They are presented in Figure 2.11 as the area under each graph and calculated by integration of the differential areas.

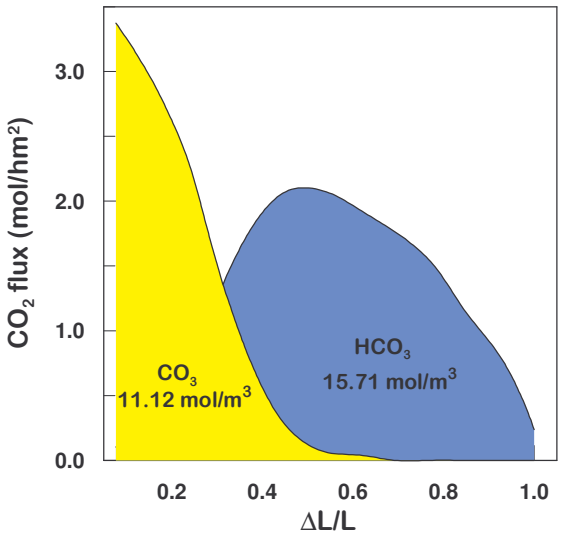

Figure 2.11 The amount of the HCO_3^- *and* CO_3^{--} species after CO_2 transfer

This amount of HCO_3^- *and* CO_3^{--} corresponded to values of 1.32 g/L $NaHCO_3$ and 1.18 g/L Na_2CO_3 which will be mixed with the NF retentane to form $CaCO_3$ that will be precipitated.

For demonstration purposes, a small amount (2 mL) of solution with concentration of 1.32 g/L $NaHCO_3$ and 1.18 g/L Na_2CO_3 was mixed with the same amount of artificial NF retentate solution. Then, the mixed solution was analysed using dynamic light scattering (DLS) as shown in Figure 2.12 to determine the particle sizes by means of a 90 Plus/Bi-Mas Particle Sizing Option (Brookhaven Instruments Corporation) with 15 nW diode laser operating at a wavelength of 678 rim.

Figure 2.12 The DLS device

The results showed that the average particle size was increasing with time especially in the first 15 minutes as shown in Figure 2.13. This was due to the precipitation of the $CaCO_3$. The average particle size was 1.38 µm.

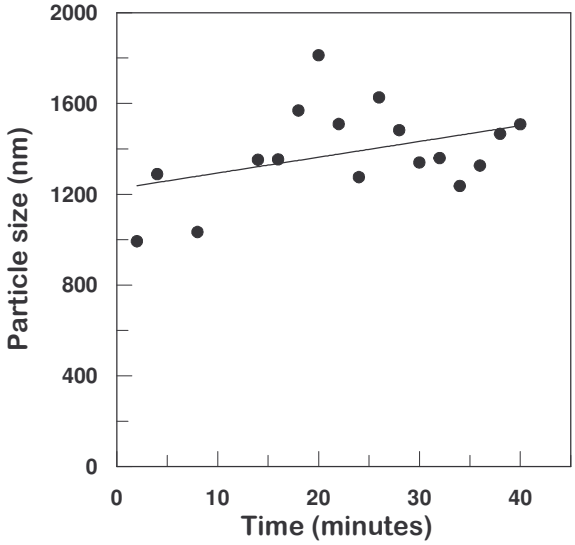

Figure 2.13 The particle size of $CaCO_3$ precipitation versus time

2.8 Feasibility study

As mention earlier, the role of the GLMC is to produce Na_2CO_3 and $NaHCO_3$ from NaOH after reacting with CO_2 transferred through the GLMC. Applying a mass balance for $1m^3$ between the inlet and the outlet of the GLMC for the case studied earlier yields that 0.4 kg NaOH will produce 1.18 kg Na_2CO_3 and 1.32 kg $NaHCO_3$. Considering the cost of commercial grade of NaOH is 2.36 \$/kg, Na_2CO_3 is 1.11 \$/kg and $NaHCO_3$ is 1.57 \$/kg [28]. Hence, the cost of NaOH is 0.94 $/m^3$, Na_2CO_3 is 1.31$/m^3$ and $NaHCO_3$ is 2.07 $/m^3$. This means that using GLMC is more economically feasible. Besides, the GLMC will contribution the reduction of CO_2 emission from desalination plants and reduce their environmental impact.

2.9 Conclusions

Gas liquid membrane contactor (GLMC) is an emerging technology in which the membrane is used as a tool for inter-phase mass transfer. Such extremely compact devices, provided in the form of hollow fibres, are able to immobilize the gas-liquid interface at the membrane pores due to the hydrophobic nature of the membrane itself, and to create a large contact area that activates stripping or absorption processes.

The role of GLMC in the proposed integrated system was to establish a reactive transfer of carbon dioxide (CO_2) into sodium hydroxide ($NaOH$) solutions to produce sodium carbonate (Na_2CO_3) solution which will be used to limit calcium sulphate ($CaSO_4$) precipitation that causes the reduction of sulphate (SO_4^{-2}) content in the solution and drastically limits the recovery of magnesium sulphate ($MgSO_4$) from the NF and RO retentate streams.

The results showed that the GLMC was able to produce a total amount of 15.71 and 11.12 mol/m^3 of HCO_3^- *and* CO_3^{--}, respectively when it was operated using alkaline solution of $NaOH$ with concentration of 10 mol/m^3 and pH of 12. The average particle size of the $CaCO_3$ precipitated was increasing with time and the average particle size was 1.38 µm.

The feasibility study showed that GLMC is more economic for producing Na_2CO_3 and $NaHCO_3$ from NaOH after reacting with CO_2.

REFERENCES

[1] M. Mavroudi, S.P. Kaldis, G.P. Sakellaropoulos, A study of mass transfer resistance in membrane gas-liquid contacting processes, Journal of Membrane Science 272 (2006) 103.

[2] A. Gabelman, S.T. Hwang, Hollow fiber membrane contactors Journal of Membrane Science 159 (1999) 61.

[3] R.S. Kumar et al., New absorption liquids for the removal of CO_2 from dilute gas streams using membrane contactors. Chemical Engineering Science 57(9) (2002) 1639.

[4] E. Drioli E, A. Criscuoli A, E. Curcio, Membrane Contactors: Fundamentals, Applications and Potentialities. Elsevier, Amsterdam (2006).

[5] V.Y. Dindore, G.F. Versteeg, Gas-liquid mass transfer in a cross-flow hollow fiber module: Analytical model and experimental validation, International Journal of Heat and Mass Transfer 48 (2005) 3352.
[6] V.Y Dindore, D.W.F. Brilman, G.F. Versteeg, Modeling of cross-flow membrane contactors: Mass transfer with chemical reactions, Journal of Membrane Science 255 (2005) 275.
[7] H.A. Rangwala, Absorption of carbon dioxide into aqueous solutions using hollow fiber membrane contactor, Journal of Membrane Science 112 (1996) 229.
[8] B.W. Reed, M.J. Semmens, E.L. Cussler, Membrane contactors, Membrane Separations Technology: Principles and Applications, Elsevier, Amsterdam (1995) 474.
[9] R.S. Kumar et al., Approximate solution to predict the enhancement factor for the reactive absorption of a gas in a liquid flowing through a microporous membrane hollow fiber, Journal of Membrane Science 213 (2003) 231.
[10] B. Kim, P. Harriot, Critical entry pressure for liquids in hydrophobic membranes, Journal of Colloid and Interface Science 115 (1) (1987) 1910.
[11]www.liquicel.com:/uploads/documents/Membrane%20Contactors%20%20 An%20Introduction%20To%20The%20Technology.pdf
[12] K. W. Lawson and D. R. Lloyd, Review: Membrane distillation, Journal of Membrane Science 124 (1997) 1.
[13] H.B. Ding, R. Cam, E.L. Cussler, Racemic leucine separation by hollow-fiber extraction, AIChE J 38(10) (1992) 1493.
[14] R. Prasad, K.K. Sirkar, Dispersion-free solvent extraction with microporous hollow-fiber modules, AIChE J, 34(2) (1988) 177.
[15] A. Malek, K. Li, W.Teo, Modeling of microporous hollow fiber membrane modules operated under partially wetted conditions, Ind. Eng. Chem. Res. 36 (1997) 784.
[16] A. Gabelman, S.Y. Hwang, W.B. Krantz, Dense gas extraction using a hollow fiber membrane contactor: experimental results versus model predictions, Journal of Membrane Science 257 (2005) 11.
[17] H. Kreulen et al., Microporous hollow fiber membrane modules as gas liquid contactors. Part 1. Physical mass transfer processes, Journal of Membrane Science 78 (1993) 197.
[18] W. Albrecht et al, Selection of microporous hydrophobic membranes for use in gas/liquid contactors: An experimental approach, Journal of Membrane Science 263 (2005) 66.
[19] S.R. Wickramasinghe, M.J. Semmens, E.L. Cussler, Mass transfer in various hollow fiber geometries, Journal of Membrane Science 69 (1992) 235.
[20] M.C. Yang, E.L. Cussler, Designing hollow-fiber contactors, AIChEJ 32 (1986) 1910.

[21] J. Li, and B.H. Chen, Review of CO_2 absorption using chemical solvents in hollow fiber membrane contactors, Separation and Purification Technology, 41 (2005) 109.
[22] L. Dahuron, E.L. Cussler, Protein extractions with hollow fibers, AIChEJ 34(3) 130.
[23] M.J Costello et al., The effect of shell side hydrodynamics on the performance of axial flow hollow fiber modules, Journal of Membrane Science 80 (1993) 1.
[24] H. Kreulen et al., Microporous hollow fiber membrane modules as gas-liquid contactors. Part 2. Mass transfer with chemical reaction, Journal of Membrane Science 78 (1993) 217.
[25] V.Y. Dindore, D.W.F. Brilman, G.F. Versteeg, Hollow fiber membrane contactor as a gas–liquid model contactor, Chemical Engineering Science 60 (2005) 467.]
[26] R. Danchwerts, Gas-liquid Reactions, New York: McGraw-Hill (1970).
[27] H. Hikita, S. Asai, T. Takatsuka, Absorption of carbon dioxide into aqueous sodium hydroxide and sodium carbonate and bicarbonate solutions, Chemical Engineering Journal 11 (1976) 131.
[28] http://www.chemistrystore.com

CHAPTER 3
MEMBRANE DISTILLATION

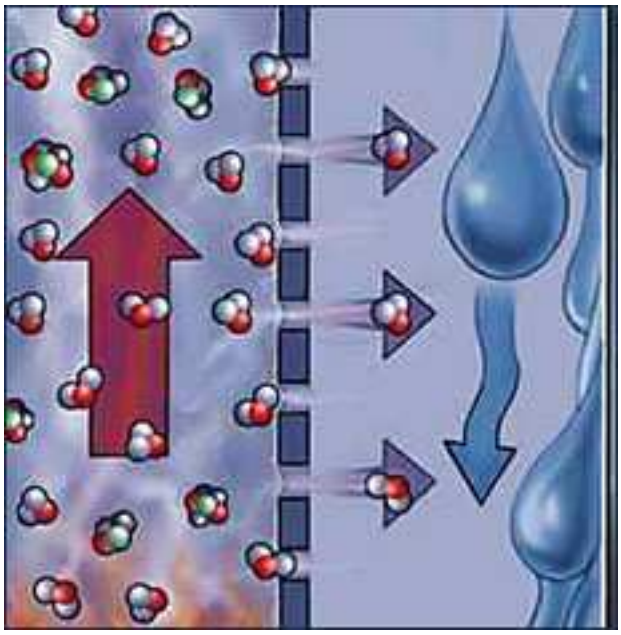

SUMMARY
In this chapter, comprehensive theoretical analysis have been carried out and simulation model was developed to describe the mass flux and heat efficiency in MD processes taking into account temperature polarization phenomenon, membrane physical properties and process dynamics. Some experimental tests were conducted in order to validate the results obtained by the computer simulation. The computer simulation was used to investigate the effects of the membrane properties on the MD performance and to set some criterions to optimize these properties in order to obtain the best performance.

3.1 Introduction

Membrane distillation (MD) is a thermal membrane separation process that involves transport of vapor through microporous hydrophobic membranes and operates on the principle of vapor-liquid equilibrium as a basis for molecular separation. The driving force of the process is supplied by the vapor pressure difference caused by temperature gradient imposed between the liquid-vapor interfaces. MD has potential applications in many areas of scientific and industrial interest, yielding highly purified permeate and separating contaminants from liquid solutions. It has been tested in the treatment of thermally sensitive industrial products such as concentrating aqueous solution in fruit juices [1], in pharmaceutical industry [2], in wastewater treatment [3] and water desalination [4, 5, 6, 7].

In particular, the MD process can be used as a substitute for conventional desalination processes such as multi-stage flash (MSF), reverse osmosis (RO), and multiple effect distillation (MED). The advantages of MD compared to these processes are as follows: (i) lower operating temperatures and vapor space required than MSF and MED, (ii) lower operating pressure than RO, (iii) 100% (theoretical) rejection of non-volatile solute, (iv) performance not limited by high osmotic pressure or concentration polarization.

Recently, the interest of using MD process for desalination is increasing world-wide due to these attractive features, especially when coupled with solar energy or utilizing low-grade heat source [8, 9, 10].

In 2004, researchers at the University of Texas at El Paso (UTEP) in collaboration with the Swedish firm SCARAB DEVELOPMENT AB [11] investigated methods coupling solar pond technology with desalination to create a zero discharge system, and MD was one of the technologies that were investigated as part of the zero discharge concept [12].

In addition, coupling MD with solar energy is the basic concept of the MEDESOL (Seawater Desalination by Innovative Solar-Powered Membrane Distillation System) project, aiming to develop an environmentally friendly desalination technology for fresh water supply in arid and semi-arid regions. The layout involves the concept of multi-step MD, to be implemented in the solar platform of Almeria (Spain), in order to minimize specific energy and membrane area required [13].

The SMAll-scale, stand alone DEsalination System (SMADES system), realized under the namesake EU funded project, and was designed to provide potable water in remote coastal areas with low infrastructure and without connection to a grid. The desalination units were based on membrane distillation (MD) modules with internal heat recovery function; the required energy was supplied by solar thermal collectors in the form of heat on a temperature level of 60-80°C with 72 m^2 of collector area and a solar heat storage water tank of 3 m^3. The electrical auxiliary energy required to drive the pumps and valves was supplied by Photo-Voltage (PV) panels [14].

Memstill® is a newly developed membrane-based distillation concept, claimed to have the potential to improve the economy and ecology of existing desalination technologies for seawater and brackish water to a large extent. This technology combined MSF and MED modes into one air gap membrane distillation module. The process promised to decrease desalination costs to 0.26 $/$m^3$, using low-grade waste steam or heat as driving force [15]. For comparison, the unit cost of water produced by conventional thermal desalination is around

1.00$/m^3 for MED and 1.40$/m^3 for MSF [16], while it is around 0.5 $/m^3 for RO [17].

The integration of direct contact membrane distillation (DCMD) and/or solar-powered vacuum membrane distillation with (VMD) conventional pressure-driven membrane operations (such as MF, UF, NF, MBR and RO) is one of the key issues of the EU-funded MEDINA (MEmbrane Desalination Systems: an INtegrated Approach) project, implemented by a consortium of 14 partners, aimed to limit the brine disposal problem and to drastically enhance the water recovery factor [18].

MD processes have several configurations depending on the way by which the vapor is recovered in the permeate side. In general, MD systems may be classified into four different categories as follows: (i) direct contact membrane distillation (DCMD), (ii) vacuum membrane distillation (VMD), (iii) sweeping gas membrane distillation, and (iv) air gap membrane distillation (AGMD). Among the other MD configurations DCMD is simplest to operate - does not require vacuum pump as in vacuum membrane distillation (VMD), nor condenser as in sweep gas membrane distillation (SGMD) or cooling surface as in air gap membrane distillation (AGMD) - and the distillation process can be carried out in any desired membrane configuration (flat sheet, spiral wound, capillaries or hollow fibers) [19]. Thus, DCMD can be conveniently applied for investigations in which water is the major fluxing component, such as in desalination [20, 21, 22, 23].

The necessity to select carefully the physico-chemical properties of the MD membranes in order to ensure high process efficiency is today accepted [5]; on the other hand, it is recognized that there are no membranes in the market specifically manufactured and optimized to be used for MD desalination processes. Since more than twenty years, the available hardware for MD processes consists of microporous hydrophobic membranes (usually made in polypropylene (PP), polyvinylidenefluoride (PVDF) or polytetrafluoroethylene

(PTFE)) normally designed for pressure-driven filtration processes rather than for concentration/temperature driven mass transfer. Only few specific examples exist for concentration-driven mass transfer, such as: the Liqui-Cel module offered by CELGARD LLC (with fibers in PP for gas/liquid mass transfer or osmotic membrane distillation, but not applicable for MD purposes); the modules with capillary PP membranes provided by Microdyn-Nadir GmbH; the DISSO$_3$LVE™ module with fibers in PTFE commercialized by WL Gore & Associates; the flat sheets PVDF membranes commercialized by GVS [24].

This study is aiming to assign some criteria for the optimization of the membrane properties (such as thickness, porosity, tortuosity and thermal conductivity coefficient) in order to increase the performance of MD unit with respect to both transmembrane flux and thermal efficiency. In addition, exergy analysis, economic evaluation and sensitivity analysis were conducted to assess the feasibility of MD as desalination process.

3.2 Theoretical Background

MD involves mass transfer of water vapor through a microporous membrane, coupled with heat transfer through the membrane and heat transfer to and from the membrane surfaces. The separation process in MD is characterized by both simultaneous heat and mass transfer, since mass (vapor) transport through membrane pores occurs as a result of the difference in temperature and composition between the feed and the permeate [25, 26, 27].

3.2.1 Mass transfer

Mass transfer in MD is achieved by convective and diffusive transport of water vapor across the microporous membrane for which the driving force is the difference in water vapor pressure on either side of membrane. The mass and energy transport phenomena includes two transportation steps. The transportation through boundary layers on both sides of membrane, and the

transportation through the membrane structure [20, 28, 29]. Figure 3.1 illustrates the possible mass transfer resistances in MD using an electrical analogy.

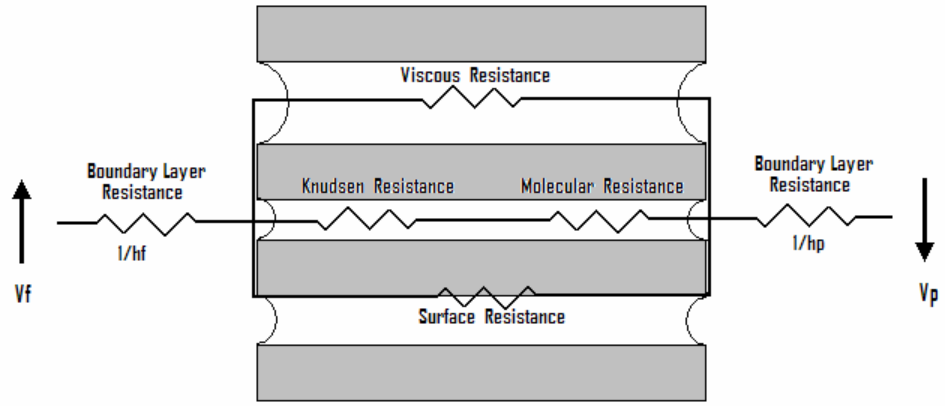

Figure 3.1 Mass transfer resistances in DCMD

Mass transfer in the boundary layers

It is often convenient to operate MD with pure water in order to minimize the boundary layers resistances to mass transfer. However, the presence of concentrated feed layer along the surface of the membrane can scientifically affect the global resistance to mass transfer. This phenomenon is called concentration polarization which results in reduction of the driving force across the membrane [30]. A mass balance across the feed side boundary layer gives the relationship between molar flux N, the mass transfer coefficient k_f, and the solute molar concentrations at the membrane interface c_m and at the bulk location c_b:

$$N = k_f \ln\left(\frac{C_m}{C_b}\right) \tag{1}$$

The boundary layer mass transfer coefficient k_f can be obtained by experiments or be estimated using empirical correlation of dimensions less numbers like Sherwood (Sh), Reynolds (Re) and Schmidt (Sc) numbers. These empirical relationships and usually expressed in the form:

$$Sh = b1\,\mathrm{Re}^{b2}\,Sc^{b3}\left(\frac{\mu_b}{\mu_m}\right)^{b4} \quad with \quad Sh = \frac{k_f d_h}{D},\ \mathrm{Re} = \frac{\rho v d_h}{\mu},\ Sc = \frac{\mu}{\rho D} \tag{2}$$

where d_h is the hydraulic diameter, D the binary diffusion coefficient in the liquid, v the fluid velocity, ρ the fluid density, μ the dynamic viscosity of the fluid. These correlations are still applicable for the case of a non-circular flow channel, by using equivalent diameter of the flow channel d_e defined as in [20]:

$$d_e = 4S / L_p \tag{3}$$

where S is the cross-sectional area and L_p is the length of wetted perimeter of the flow channel.

Mass transfer across the membrane

Resistances to mass transfer within the membrane structure are due to transfer of momentum through the indirect contact with capillary walls via molecule-molecule collision terminating at molecule-wall collision (viscous or momentum resistance), or from collision of a diffusing molecule with other molecules (molecular resistance) or collisions between molecules and membrane walls (Knudsen resistance) [31].

Modeling of mass transfer within the membrane pores was described in many experimental and theoretical studies found in the literature [20, 28, 29, 32]. A major difference among MD models is in the arrangement of the transport resistances in the circuit. In most cases, one or more of the resistances may be omitted. The vapor transport in MD processes is related to the kinetic theory of gases. Accordingly, the vapor transport mechanism depends upon the mean free path length ψ, which can be calculated based on the average process operating conditions (pressure and temperature), and the mean diameter of the membrane pores d_p. The value of ψ, defined as the average distance the molecule of diffusing species travels between two successive collisions, can be calculated from the kinetic theory of gases [33]:

$$\psi = \frac{k_B T}{P\sqrt{2}\pi\sigma_B^2} \tag{4}$$

where k_B is the *Boltzmann* constant (1.381×10^{-23} J/K) and σ_B is the collision diameter of the molecule. For the binary mixture of water vapor and air, the mean free path of water in air $\psi_{w\text{-}a}$ may be evaluated at the average membrane temperature T_m as in [32] using:

$$\psi_{w-a} = \frac{k_B T_m}{\pi\left((\sigma_w + \sigma_a)/2\right)^2 P} \frac{1}{\sqrt{1+\left(M_w / M_a\right)}} \qquad (5)$$

where σ_w and σ_a are the collision diameters for water vapor (2.641×10^{-10} m) and air (3.711×10^{-10} m) [34], and M_w & M_a the molecular weight water and air. The mean free path in the DCMD experiments at a typical operating temperature of 40 ^{o}C calculated using equation (5) is 0.1 µm.

Generally, the mass transport across the membrane occurs in three regions: Knudsen region, transition region, and continuum region as shown in Figure 3.2. The predominance, coexistence or transition between all of these regions can be estimated by comparing the mean free path ψ of the diffusing molecules to the mean pore diameter d_p of the membrane [32].

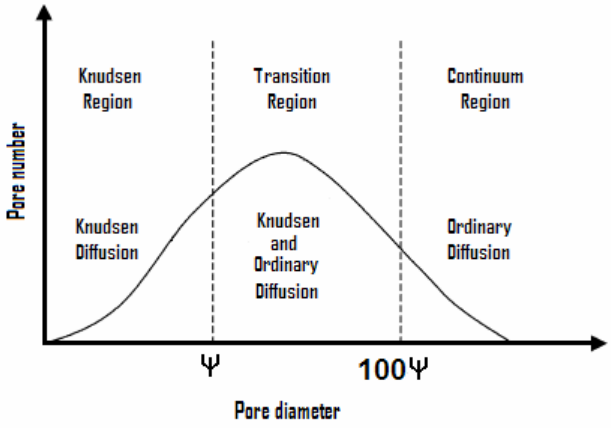

Figure 3.2 Mass transport regions and associated transport mechanisms [32]

In Knudsen region ($d_p < \psi$), the molecule-wall collisions dominate over the molecule-molecule collisions and the mass transport mode is Knudsen diffusion. For the transition region ($\psi < d_p < 100\ \psi$) mass transport takes place within the combination on Knudsen and ordinary molecular diffusion. In the continuum

region ($d_p > 100\psi$), the average membrane diameter is large compared to the free mean path of the vapor and the molecule-molecule collision are dominant. Thus, the transport mechanism is the classical viscous (*Poiseuile*) diffusion. In this region, the membrane pores may contain air. The presence of air in the pores hinders the diffusion of vapor and results in lower flux than the maximum achievable flux for the particular membrane and conditions. Therefore, substantial increase in flux can be achieved by removing the air from the feed (de-aeration) or reducing the pressure of the liquids boundering the membrane (i.e. limiting the total vapor pressure in the pores) [29].

The basic models used to describe water transport in MD system relate the mass flux (N) to the driving force represented by the vapor pressure difference at both liquid-vapor interfaces, via proportionally coefficient (C) as in [20, 27, 29].

$$N = C\,[\,p(T_{fm}) - p(T_{pm})] \qquad (6)$$

where $p(T_{fm})$ and $p(T_{pm})$ are the vapor pressure of transporting fluid at the membrane feed and permeate sides, respectively, and C is the membrane distillation coefficient which is a function of membrane physical properties (pore size, porosity, thickness, and membrane pore tortuosity), transporting fluid physical properties (molecular weight and diffusivity), and operating temperature. There are mainly two different models that describe the vapor flux across the membrane; i.e. the Dusty-Gas Model (DGM) [20] and the model proposed by Schofield et al [29]. The DGM will be used in this study for its simplicity because it is based on the well-developed kinetic theory rather than the arguments required by the momentum transfer method. The complete form of the DGM takes into account surface, Knudsen and viscous diffusions. The DGM applicable to MD is expressed, without the surface diffusion, as:

$$\frac{N_i^D}{D_{ie}^k} + \sum_{j=1\neq i}^{n} \frac{p_j N_i^D - p_i N_j^D}{D_{ije}^0} = \frac{-1}{RT} \nabla p_i \qquad (Diffusive \quad flux) \qquad (7)$$

$$N_i^V = \frac{-p_i B_o}{RT\mu} \nabla P \qquad (Viscous \quad flux) \qquad (8)$$

$$with \qquad D_{ije}^0 = \frac{\varepsilon}{\tau} P D_{ij}, \quad D_{ie}^k = K_o \left(\frac{8RT}{\pi M_i} \right)^{1/2}, \quad K_o = \frac{2\varepsilon r}{3\tau} \quad and \quad B_o = \frac{\varepsilon r^2}{8\tau}$$

where p the partial pressure, M_i the molecular weight, μ the vapor viscosity, r the pore radius, ε the membrane porosity, τ the membrane tortuosity and R is the gas constant. K_o and B_o are constants that can be calculated based on membrane properties or obtained from gas permeation experimental data of non-condensable pure gas such as hydrogen, helium or air [35].

The average pore diameter of the membranes used in this study was 0.2 μm, and thus comparable to the mean free path of water vapor molecules (0.1 μm at 40°C as calculated earlier). Therefore, the reduced Knudsen-molecular diffusion transition form of the Dusty-Gas Model (DGM) was applied for describing the vapor flux of pure water across the membrane [19]:

$$N = -\frac{1}{RT_{avg}} \left(\frac{D_w^k D_{w-a}^0}{D_{w-a}^0 + p_a D_w^k} \right) \frac{\Delta p}{\delta} M \qquad (9.a)$$

with:

$$D_w^k = \frac{2\varepsilon r}{3\tau} \sqrt{\frac{8RT_{avg}}{\pi M}} \qquad (9.b)$$

and

$$D_{w-a}^0 = 4.46 \cdot 10^{-6} \frac{\varepsilon}{\tau} T_{avg}^{2.334} \qquad (9.c)$$

where $D^o_{w\text{-}a}$ is the pressure independent binary diffusion coefficient of water-air [36], T_{avg} is the average membrane surface temperature on the feed and permeate sides, and Δp, the partial pressure gradient of water through both membrane

surfaces generated by a temperature gradient and/or a concentration difference, is the driving force to mass transfer in DCMD.

3.2.2 Heat transfer

Heat transfer in MD processes is always coupled with mass transfer. For heat transfer, heat is first transferred from the heated feed solution across the thermal boundary layer to the membrane surface q_f. Then the heat passes through the membrane in the form of vapor latent heat q_v and heat conduction q_c through the membrane structure. Finally, the heat is removed from the cold permeate side of membrane surface through the boundary layer q_p. The boundary layers next to the membrane surface may contribute significantly to overall heat transfer resistance [20, 28, 32, 37]. Heat transfer in MD is best visualized by drawing the electrical analog, as shown in Figure 3.3.

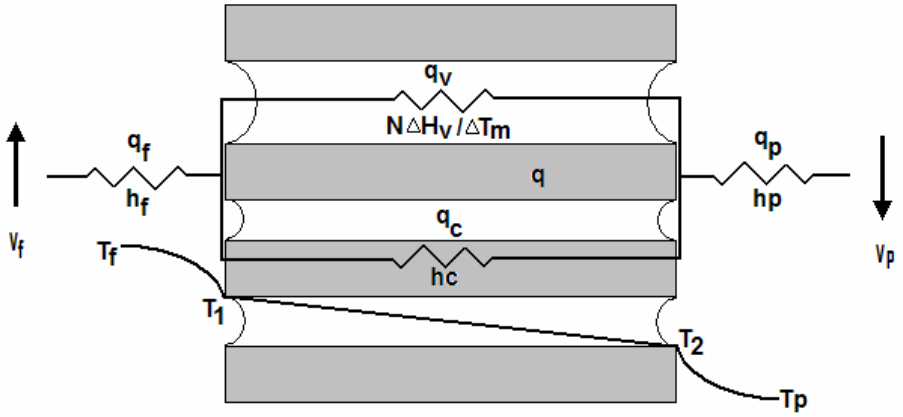

Figure 3.3 Heat transfer resistances in DCMD

The heat transfer equations governing heat flows in and around the membrane are [31]:

- along the module at feed and permeate sides:

$$dQ_f = c_{pf}\left(\dot{m}_f - NdA\right)dT_f \qquad (10.a)$$

$$dQ_p = c_{pp}\left(\dot{m}_p - NdA\right)dT_p \qquad (10.b)$$

- within the boundary layers at feed and permeate sides:

$$dQ_f = h_f\left(T_f - T_1\right)dA \tag{11.a}$$

$$dQ_p = h_p\left(T_2 - T_p\right)dA \tag{11.b}$$

- across the membrane:

$$dQ_m = \left[N\lambda + \frac{k_m}{\delta}\left(T_1 - T_2\right)\right]dA \tag{12}$$

- overall heat balance at the steady state:

$$dQ_f = dQ_m = dQ_p \tag{13}$$

Hence, the overall heat transfer coefficient of the MD process is expressed as [20]:

$$H = \left[\frac{1}{h_f} + \frac{1}{h_c + N\Delta H_v / \Delta T_m} + \frac{1}{h_p}\right]^{-1} \tag{14}$$

where each h represents the corresponding heat transfer coefficient shown in Figure 3.3, N is the molar flux, ΔH_v is the heat of vaporization.

Heat transfer in boundary layers (Temperature polarization)

The liquid heat transfer coefficients depend on the physical properties of the solution as well as on the hydrodynamic conditions acting on the MD system. It is important to minimize the boundary layer resistances by maximizing the boundary layer heat transfer coefficients h_f and h_p. This is to allow the MD system to supply large quantity of heat to the surface of the membrane to vaporize the liquid. In MD processes, the interfacial temperatures (T_1 and T_2) are often differ significantly from the measured temperatures of bulk solutions at the feed and permeate sides (T_f and T_p). This phenomenon is called the temperature polarization [31, 37]. It causes reduction in the driving force of the MD process due the decrease in the vapor pressure difference across the membrane. The interfacial temperatures (T_1 and T_2) cannot be measured directly, and they are significantly affected by applied membrane physical properties and interfacial

film heat transfer coefficient (h_f and h_p). The temperature polarization coefficient (*TPC*) is used to evaluate the efficiency of MD systems by quantifying the magnitudes of the boundary layer resistances relative to the total heat transfer resistance of the MD system. The TPC is defined as [20, 32]:

$$TPC = \frac{T_1 - T_2}{T_f - T_p} \tag{15}$$

The recommended *TPC* range is between 0.4 to 0.7 for satisfactory designed system [20]. The boundary layer heat transfer coefficients may be measured experimentally or they often estimated from empirical correlations based on dimensionless numbers, like *Nusselt* (*Nu*), *Reynolds* (*Re*) and *Prandtl* (*Pr*) numbers. A general expression of these empirical relationships is:

$$Nu = b_1 \mathrm{Re}^{b2} \mathrm{Pr}^{b3} \left(\frac{\mu_b}{\mu_m} \right)^{b4} \qquad and \qquad h_i = \frac{Nu_i \, k_i^T}{d_{h_i}} \tag{16}$$

Some commonly used empirical correlations available from the literature are listed in Table 3.1.

Table 3.1 Commonly used empirical correlations for calculating heat transfer coefficient

Correlation			Reference
$Nu = 3.66 + \frac{0.067 Gz}{1 + 0.04 Gz^{2/3}}$	, $Gz = \frac{\dot{m} C_P}{k^T L}$	(17)	[25]
$Nu = 0.20 (\mathrm{Pr}\, Gz)^{1/4} (l/L)^{1/9}$	, $10^4 < Gz < 10^5$	(18)	[38]
$Nu = 4.36 + \frac{0.036 \mathrm{Re}\, \mathrm{Pr} / (L/d)}{1 + 0.0011 [\mathrm{Re}\, \mathrm{Pr} / (L/d)]^{0.8}}$	, $\mathrm{Re} < 2100$	(19)	[37]
$Nu = 1.62 (\mathrm{Re}\, \mathrm{Pr}\, (d/L))^{0.33}$	, $\mathrm{Re} < 2100$	(20)	[26]
$Nu = 1.25 (\mathrm{Re}\, (d/L))^{0.93} \mathrm{Pr}^{0.33}$	, $0.5 < \mathrm{Re} < 500$	(21)	[39]

Heat transfer across membrane

The heat across the membrane is transferred by both conduction through the membrane material q_c and together with the latent heat of vaporization associated with the vapor flowing through the membrane q_v. Early heat transfer models for calculating membrane interfacial temperatures T_1 and T_2 were developed on the assumptions of linear temperature distribution across the membrane and an associated isenthalpic flow of vapor [19, 28]. In these models, the total heat flux through the membrane q_m is the sum of the heat conduction q_c and the latent heat of vaporization q_v as shown in equation (12). On the other hand, recent MD heat transfer models were based on the assumptions of nonlinear temperature distribution across the membrane and non-isenthalpy of vapor flow [32, 37]. Therefore, the total heat flux through the membrane is given as:

$$q_m = NH_v\{T\} + k_m \frac{dT}{dx} \tag{22}$$

where $H_v\{T\}$ is the transporting vapor enthalpy at a temperature T, and x is the distance to the direction of vapor flux. Since the temperature inside the membrane in MD changes within a range of few degrees and assuming the condensation temperature of vapor T_2 as reference temperature, the enthalpy at temperature T can be written in the form:

$$H_v = h_v\{T_2\} + C_p(T - T_2) \tag{23}$$

where $h_v\{T_2\}$ is the heat of vaporization measured at T_2 and C_p is the specific heat of the vapor. Substituting equation (23) into equation (22) with separation of variables and integration yields:

$$q_m = \frac{NC_p(T_1 - T_2)}{1 - e^{-NC_p \delta / k_m}} + Nh_v \tag{24}$$

Hence, the interfacial temperatures can be driven by combining equation (23) with equation (13) and rearranging :

$$T_1 = \frac{\alpha\left(T_p + \beta T_f\right) + h_f T_f - N\lambda}{\alpha + h_f + \alpha\beta} \tag{25.a}$$

$$T_2 = \frac{\alpha\left(T_f + \beta^{-1} T_p\right) + h_p T_p + N\lambda}{\alpha + h_p + \alpha\beta^{-1}} \tag{25.b}$$

with $\alpha = \frac{k_m}{\delta}$ and $\beta = \frac{h_f}{h_p}$.

As seen from above, latent heat of vaporization is promoting the permeate flux, whereas heat conduction across the membrane is considered as heat loss since there is no corresponding mass transfer. In fact, it was shown that 20-50% of the total heat transferred in MD process is lost by conduction [29]. The conduction heat transfer coefficient k_m is usually estimated from vapor and solid phase thermal conductivities as:

$$k_m = (1-\varepsilon)k_s + \varepsilon k_v \tag{26}$$

where k_s and k_v are the heat transfer coefficients of the solid membrane material and the vapor within the membrane pores, respectively and k_s is generally one order of magnitude greater than k_v [19].Therefore, heat loss by conduction can be reduced by increasing the porosity.

In summary, the mass and heat transport theory discussed above highlights three main forms of transport inefficiency:

i) The mass transfer inefficiency due the air trapped within the membrane pores.

ii) The heat transfer inefficiency due to temperature polarization.

iii) The heat transfer inefficiency caused by conduction heat losses through the membrane structure.

3.2.3 *Correction for shell side flow distribution*

Hollow fiber contactors are compact devices offering high interfacial area for the contact of fluid phases with membrane. Membrane contactors have been demonstrated in a diverse range of gas/liquid and liquid/liquid applications; for DCMD, the diffusive mass transfer across the membrane is typically obtained by flowing the heated feed solution through the lumen side, and the cooled permeate through the shell side of the module.

In most cases, fibers are not arranged in an ordered way inside a module and they are not distributed uniformly on the shell side especially when existing in large number. As a result, hollow fiber modules often exhibit a flow maldistribution that decreases their performance in terms of mass and energy transfer. Voronoi tessellation method was used to evaluate the flow distribution in the shell of a randomly packed hollow fiber module [40]. Voronoi tessellation is a mathematical method able to model the geometric characteristics of random spacing of different objects; according to this approach, the space between randomly packed objects is subdivided by drawing straight boundaries equidistant between neighbouring objects, forming polygonal cells. In details, the cross-section area was subdivided into polygonal cells, each one associated to a single fiber. The probability density distribution function $f(\varphi)$ of polygonal cell area is [41]:

$$f(\varphi) = \frac{s^s}{\overline{\varphi}^s} \frac{\varphi^{s-1}}{(s-1)!} e^{-s\varphi/\overline{\varphi}} \tag{27.a}$$

$$\varphi = a - a_f \tag{27.b}$$

$$\overline{\varphi} = a_0 - \overline{a}_f \tag{1.c}$$

$$a_0 = \frac{\pi R_M^2}{N_f} \tag{27.d}$$

$$\phi = \frac{\overline{a}_f}{a_0} \tag{27.e}$$

s, the number of nearest neighbour fibers, was assumed equal to 4 and 6 at low (<0.6) and high (>0.6) packing density, respectively. The probability Ξ that a polygonal cell has a packing fraction between ϕ_1 and ϕ_2 is [42]:

$$\Xi = \int_{\xi_1}^{\xi_2} s^s \frac{\xi^s}{(s-1)!} e^{-s\xi} d\xi \tag{28.a}$$

$$\xi_i = \frac{(1-\phi_i)\phi}{(1-\phi)\phi_i} \qquad i = 1,2 \tag{28.b}$$

The effective flow distribution in the overall fiber bundles has been evaluated in term of the product of the friction factor (*f*) and the *Reynolds* number (*Re*). Assuming that the pressure drop in all the cells is identical, and that the total mass flow rate is equal to the sum of the individual cell mass flow rate, the effective $(fRe)_e$ is given by:

$$\frac{1}{(f\,\mathrm{Re})_e} = \sum_{i=1}^{m} \frac{1}{(f\,\mathrm{Re})_i} \left[\frac{(1-\phi_i)\phi}{(1-\phi)\phi_i}\right]^3 P_i \tag{29}$$

where $(f\,Re)_i$ and P_i are estimated for the *i-th* category.

3.3 Simulation procedure

The system to be considered in the modeling is the DCMD in which the liquid phases are in direct contact with both sides of the membrane. The configuration is similar to a heat exchanger working in counter-current flow with the feed solution flowing inside the fibers and the permeate solution on the shell side of the membrane module as shown in Figure 3.4. The flow rates, the feed solute concentration, and the temperatures can be varied independently. The physicochemical properties of water and concentrated salt solutions were obtained from [30, 31]. As a first step, morphological parameters (average pore size, porosity, tortuosity, thickness), physical properties of membranes (thermal conductivity), and geometrical parameters of modules (number of fibers, packing factor, hydraulic diameter, flow-channel length) as well as DCMD operating

conditions (temperatures and flow rates of feed and permeate streams) were defined.

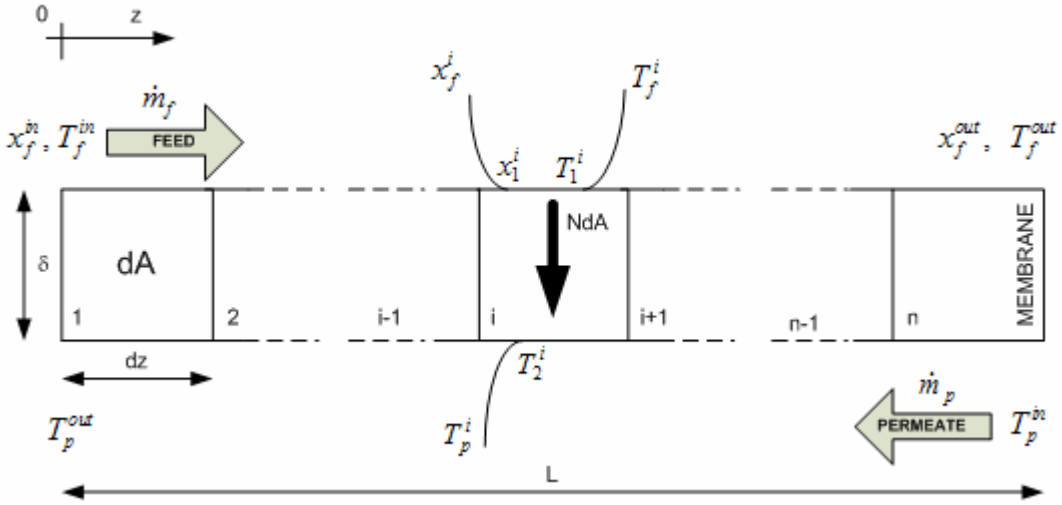

Figure 3.4 Schematic representation of the MD modeling procedure

The temperature and the concentration of the solution vary in the axial direction along the module; variations in the bulk were obtained by solving the heat and mass balance equations for each differential element in which a membrane module is supposed to be divided (as schematised in Figure 3.4). The heat and mass balance equations are:

$$\frac{dT_f}{dz} = \frac{[N\lambda + \alpha(T_1 - T_2)]N_f \pi d_{m,\ln}}{\dot{m}_f c_{pf}} \tag{30.a}$$

$$\frac{dT_p}{dz} = \frac{[N\lambda + \alpha(T_1 - T_2)]N_f \pi d_{m,\ln}}{\dot{m}_p c_{pp}} \tag{30.b}$$

Differential equation (30.a) and (30.b) were solved with the following boundary conditions:

$$T_f = T_f^{in} \quad \text{at} \quad z=0 \tag{31.a}$$

$$T_p = T_p^{out} \quad \text{at } z=L \tag{31.b}$$

The increase of feed concentration alongside the module was calculated as:

$$dx_f = \frac{N\,dA(1-x_f)}{\dot{m}_f - NdA} \tag{32}$$

assuming the boundary condition:

$$x_f = x_f^{in} \quad \text{at} \quad z=L \tag{33}$$

The heat lost to the surroundings was assumed negligible for two main reasons: i) the housings of the membrane modules used in this research were made of PVC, a thermal-insulator material with low thermal conductivity (~0.2 W/mK); ii) the cold permeate stream was recirculated in the shell side.

The overall heat flux in the MD process, expressed in terms of the global heat transfer coefficient *H*, was calculated as [43]:

$$Q_{tot} = H(T_f - T_p) = \left(\frac{1}{h_f} + \frac{1}{\frac{k_m}{\delta} + \frac{N\lambda}{T_1 - T_2}} + \frac{1}{h_p} \right)^{-1} (T_f - T_p) \tag{34}$$

The thermal efficiency of the MD process, defined as the ratio of the vaporization heat associated with the transmembrane water flux over the total heat flux, was expressed as:

$$\eta(\%) = \frac{N\lambda}{\left(\frac{1}{h_f} + \frac{1}{\frac{k_m}{\delta} + \frac{N\lambda}{T_1 - T_2}} + \frac{1}{h_p} \right)^{-1} (T_f - T_p)} \times 100 \tag{35}$$

Equations (9), (25) and (30) show the complex relationships between heat and mass transfer existing in MD; calculating mass and energy fluxes follows an iterative scheme to be solved by computational procedures. Therefore, the MD module was subdivided into *n* differential elements as shown in Figure 3.4. The differential mass and heat balance equations were written for each differential element and they were solved by numerical fourth order Runge-Kutta method.

In order to solve the system of ordinary differential equations (30.a), (30.b) and (32) with splitting boundary values, a shooting method has been employed. The boundary condition equations (31.a) and (33) were applied and the permeate temperature at $z = 0$ was assumed equal to (T_p^{out}). For each *i-th* differential element, the interfacial temperatures T_1^i and T_2^i were assumed - as an initial guess - equal to feed and permeate bulk temperatures T_f^i and T_p^i, respectively. Analogously, the interfacial concentration x_f^i was assumed – as an initial guess - equal to feed bulk concentration x_f. Effective values of *Reynolds* number, evaluated for non uniform module packing fractions, were used in the calculation of mass and heat transfer coefficients. The vapor flux and the corresponding temperature and concentration distributions for each *i-th* differential element were computed iteratively using the method of successive substitution until the difference between two consecutive iterations was less than 0.1%. Then, the solution was marched forward until $z = L$, and then the guessed value of T_p^{out} was adjusted by secant method; this procedure was repeated until the boundary condition in equation (31.b) was met within an error of 0.1%.

The algorithm is summarized in Figure 3.5 and it was implemented in Matlab version 7.0.1 (R14). The programming code is shown in Appendix 2.

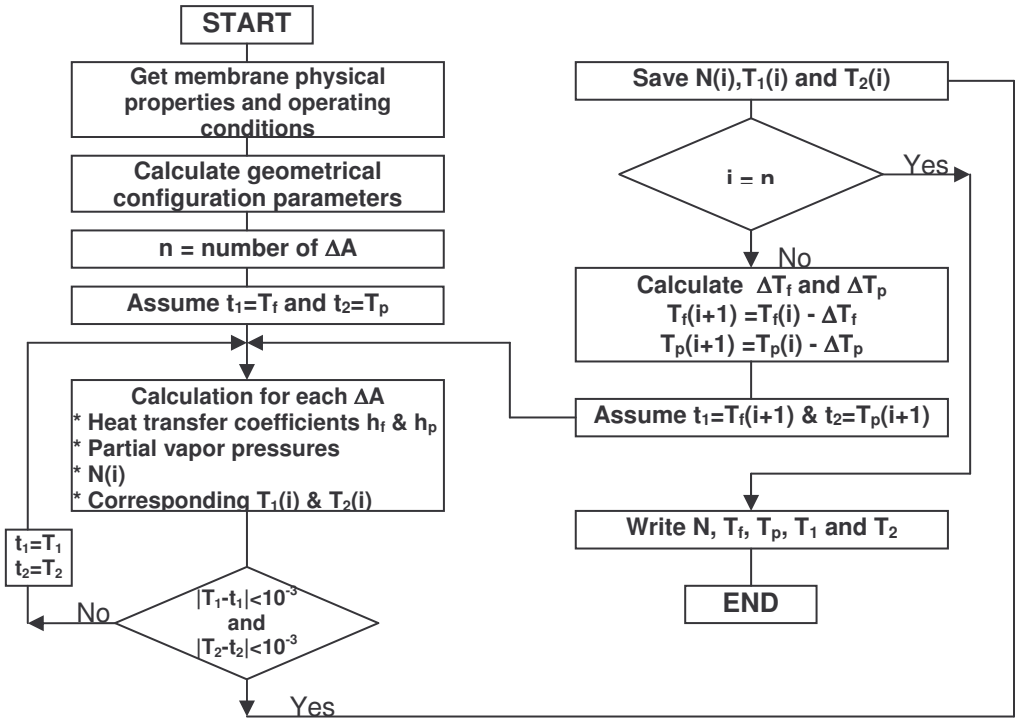

Figure 3.5 The algorithm of the computer simulation for MD

For a single differential element, the mass and heat transfer coefficients on both feed and permeate sides were evaluated using suitable empirical correlations provided by literature [19]. The vapor pressure was calculated using Antoine equation [44]:

$$\ln p^0 = 23.238 - \frac{3841}{T - 45} \tag{36}$$

where p^0 is measured in *Pa* and *T* in *K*.

The values of the activity a_w for NaCl-H_2O system, defined according to equation (37), were extrapolated from data of water activity a_w reported in Table 3.2 [45]:

$$a_w = \frac{p^{sol}}{p^0} \tag{37}$$

p^{sol} and p^0 are the vapor pressure of the NaCl-H_2O solution and pure water, respectively.

Table 3.2 Values of water activity in NaCl-H_2O solutions at different molality (data at 294K) [45]

Molality (mol/kg)	a_w
1.245	0.9584
1.671	0.9438
2.200	0.9250
2.617	0.9076
3.141	0.8855
3.655	0.8635
4.086	0.8456
4.608	0.8221
5.423	0.7848

3.4 Experimental section

The experimental apparatus used for MD tests is illustrated in Figure 3.6. Feed and distillate streams were driven by CASTER MT7002PP pumps (A), and flow rates measured by BROOKS INSTRUMENTS flow-meters (B). A thermostatic bath Digital Plus NESLAB RTE17 (C) and an ISCO GTR 2000 heater (D) provided, at the inlet of the module, the maintenance of distillate and feed temperatures, respectively. A REFLEX HP 8200 balance (E) connected to the distillate tank has been used to estimate the transmembrane solvent flux by measuring the weight variations (±0.1g) over time. Temperatures were monitored by SPER SCIENTIFIC 800012 Pt thermocouples (T) with sensitivity ±0.1°C.

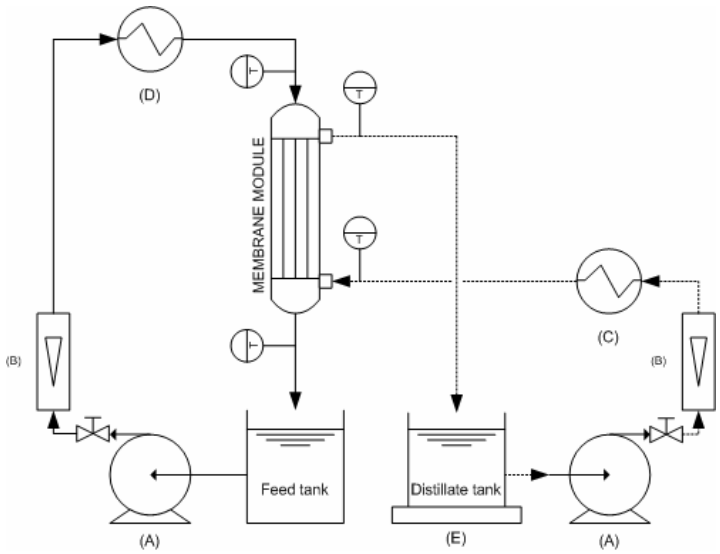

Figure 3.6 A scheme of the experimental apparatus

The system was operated in a counter-current flow configuration with the feed solution flowing inside the fibers and the permeate solution on the shell side of the membrane module.

Validation experiments were performed using four different modules (specifications listed in Table 3.3) in order to confirm the general validity of the simulation model. Feed solutions for MD tests were aqueous NaCl solutions at concentration of 35 g/L (TDS of standard seawater).

Table 3.3 MD modules characteristics and membrane properties

	MD020CP2N	**MD080CO2N**	**Home-made**	**MD020TP2N**
Manufacturer	Microdyn	Enka-Microdyn	-	Enka-Microdyn
Membrane material	Polypropylene	Polypropylene	Polypropylene	Polypropylene
Pore size (μm)	0.2	0.2	0.2	0.2
Fiber outer diameter (mm)	2.8	2.8	0.3	8.6
Fiber inner diameter (mm)	1.5	1.5	0.2	5.5
Membrane thickness (mm)	0.65	0.65	0.05	1.55
Number of fibers	40	467	1500	3
Shell inner diameter (m)	0.021	0.085	0.03	0.021
Packing factor	0.7	0.5	0.15	0.5
Length (m)	0.45	1.0	0.24	0.75
Surface area (m^2)	0.1	2	0.35	0.036
Porosity	0.7	0.7	0.45	0.7
Tortuosity*	1.4	1.4	2.2	1.4

(*) assumed as $1/\varepsilon$ [46]

3.5 Results and discussion

3.5.1 Correction for randomly packed hollow fiber bundles

The fluid maldistribution in the shell side due to a non-uniform packing of the fibers is mathematically quantified by the cumulative probability distribution reported in Figure 3.7, generated by equations (28.a-b). It was shown that, for a global packing fraction of 0.7 (i.e.: MD020CP2N module), the cross-section area at the shell side with local packing fractions comprised within the range 0.7±10% represents the 56% of the total cross-section area of the module. On the other hand, at lower global packing fraction (i.e.: MD080CO2N module), the cross-section area at the shell side with local packing fractions comprised between 0.5±10% decreased to 27% of the total cross-section area of the module, so exacerbating the negative effects of the flow maldistribution.

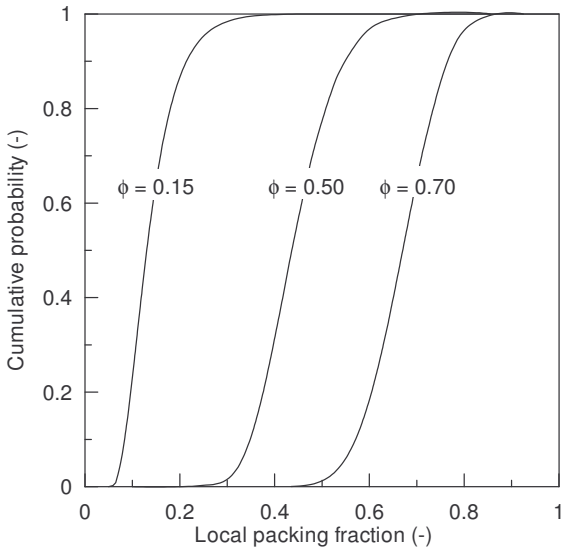

Figure 3.7 Cumulative probability distribution versus local packing fraction for different packing densities.

As shown in Figure 3.8, the non-uniform distribution of the hollow fiber bundles has a detrimental effect on the fluid-dynamics of the contactor, whose performance (described in terms of $f \cdot Re$, as from equation (29)) approaches ideality at increasing packing fraction. Mass and heat transfer coefficients at the

shell side are therefore improved at higher packing fractions, in agreement the well-known behavior of tube-and-shell heat exchangers [36]. In particular, the ratio $(f \cdot Re)_e/(f \cdot Re)_{id}$ increased from 0.26 to 0.69 when the global packing fraction of the module increased from 0.15 to 0.7.

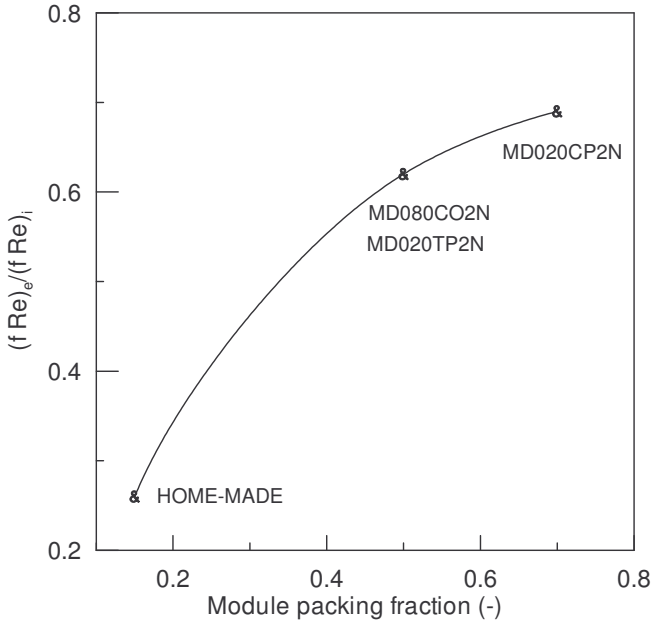

Figure 3.8 Effect of the non-uniform packing of fibers on the fluid-dynamics of different MD modules.

The consequent benefits in terms of transmembrane flux can be deduced from simulation data reported in Table 3.4, showing that the MD080CO2N module exhibits a flux 28% lower with respect to MD020CP2N module, although both of them are manufactured using the same kind of fibers but with different lengths, which might slightly contribute to a reduction in flux for the longer module (t_f^{in}= 55°C, t_p^{in} = 25°C). Zhongwei et al. [42] have found that fluxes differ by 25% between modules with packing fractions of 0.5 and 0.7 (t_f^{in}-t_p^{in} = 45°C).

Table 3.4 Flux and temperature profiles alongside MD020CP2N and MD080CO2N modules (t_f^{in}= 55°C, t_p^{in}=25°C, *Re*=900 at feed side, ideal *Re* = 500 at permeate side)

MD020CP2N				MD080CO2N			
Cumulative length (cm)	***N*** **(kg/m²h)**	T_f **(°C)**	T_p **(°C)**	**Δ*L* (cm)**	***N*** **(kg/m²h)**	T_f **(°C)**	T_p **(°C)**
0		**55.00**	30.00	0		**55.00**	32.00
2.25	5.55	55.00	30.00	5.00	4.11	55.00	32.00
4.50	5.48	54.72	29.72	10.00	4.05	54.61	31.60
6.75	5.42	54.44	29.44	15.00	3.98	54.22	31.21
9.00	5.35	54.16	29.16	20.00	3.92	53.83	30.82
11.25	5.29	53.89	28.89	25.00	3.86	53.45	30.44
13.50	5.23	53.61	28.61	30.0	3.80	53.07	30.07
15.75	5.17	53.34	28.34	35.00	3.74	52.70	29.69
18.00	5.11	53.07	28.07	40.00	3.68	52.34	29.32
20.25	5.05	52.80	27.80	45.00	3.63	51.97	28.96
22.50	4.99	52.53	27.53	50.00	3.57	51.61	28.60
24.75	4.93	52.27	27.27	55.00	3.52	51.26	28.24
27.00	4.88	52.01	27.01	60.00	3.47	50.91	27.89
29.25	4.82	51.74	26.74	65.00	3.42	50.56	27.54
31.50	4.77	51.48	26.48	70.00	3.37	50.22	27.20
33.75	4.71	51.22	26.22	75.00	3.32	49.88	26.86
36.00	4.66	50.97	25.97	80.00	3.27	49.54	26.52
38.25	4.60	50.71	25.71	85.00	3.22	49.21	26.18
40.,50	4.55	50.46	25.46	90.00	3.18	48.88	25.85
42.75	4.50	50.21	25.21	95.00	3.13	48.56	25.53
45.00	4.5	50.00	**25.00**	100.00	3.09	48.23	**25.00**
Average flux	**4.98**			Average flux	**3.57**		

3.5.2 *Effects of the operating conditions*

In order to prove the validity of the MD model, the predicted values of transmembrane flux were compared with experimental results obtained using four different modules. Flux measurements were carried out by keeping the temperature at the permeate side constant at 15°C and the mass flow rate was kept at 0.055 kg/s at feed side and 0.028 kg/s at permeate side for all modules. As shown in Figure 3.9, when the feed side temperature was increased from 25 to 70 °C, the flux was increasing exponentially as a consequence of the increase in the thermal driving force, as predicted by the Clausius-Clapeyron equation which describes the dependence of water vapor pressure on temperature.

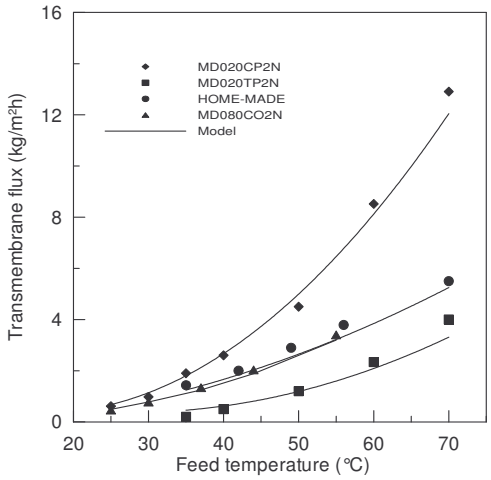

Figure 3.9 Experimental and simulation results showing the effects of the feed temperature on the MD flux for different membrane modules ($\dot{m}_f$ = 0.055 kg/s, $\dot{m}_p$ = 0.027 kg/s, T_p^{in} = 15°C, feed concentration = 35g/L)

The simulation results reported in Figure 3.10 confirmed that the thermal efficiency significantly enhanced at higher feed temperatures: for instance, it improved by 35%, 32%, 6% for MD020CP2N, MD020TP2N and home-made modules, respectively, when feed temperature increased from 25 to 70°C. The thermal efficiency of MD080CO2N module improved by 14% when feed temperatures increased from 25 to 55°C.

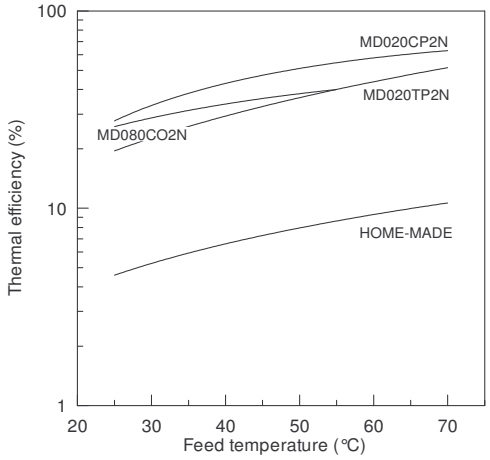

Figure 3.10 Simulation results showing the effects of the feed temperature on the thermal efficiency of MD for different membrane modules ($\dot{m}_f$ = 0.055 kg/s, $\dot{m}_p$ = 0.027 kg/s, T_p^{in} = 15°C, feed concentration = 35g/L)

Additionally, the transmembrane flux and thermal efficiency can be enhanced by increasing the feed flow rate, i.e. improving the hydrodynamic conditions in terms of Reynolds number, mass and heat transfer coefficients. Figure 3.11 shows the results of two sets of experiments conducted on the MD020CP2N module at feed temperatures of 40 and 60°C; the feed flow velocity was increased from 0.2 to 1.0 m/s, while the permeate flow velocity and temperature were kept constant at 0.28 m/s and 15 °C, respectively.

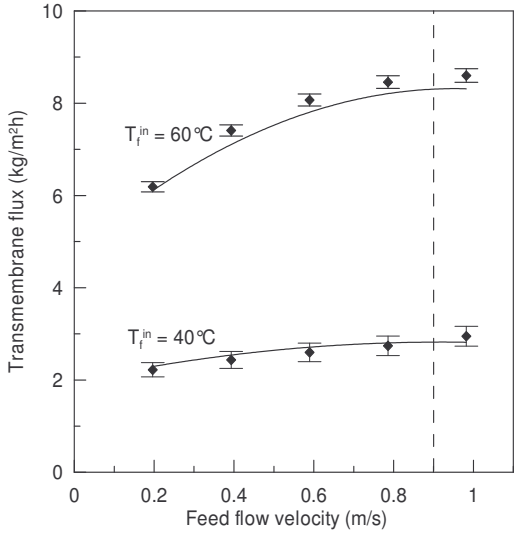

Figure 3.11 Experimental and simulation results showing the effects of the feed flow velocity on the MD flux ((MD020CP2N module, v_p = 0.28 m/s, T_p^{in} = 15°C, feed concentration = 35g/L)

The results showed that the flux was increased by 24 and 38% at feed temperatures of 40 and 60°C, respectively. Curves of Figure 3.11 tend to reach a plateau; at this point, an increase in feed velocity does not lead to significant benefits in terms of transmembrane flux. Therefore, it is possible to set a recommended fluid velocity through hollow fibers - in laminar regime - that ranges within 0.9-1.0 m/s, corresponding for MD020CP2N module (the most efficient among the four modules tested) to Reynolds number around 1900.

There was slight enhancement in the thermal efficiency since it increased by only 2% and 5% at feed temperature of 40 and 60°C, respectively, as reported in Figure 3.12.

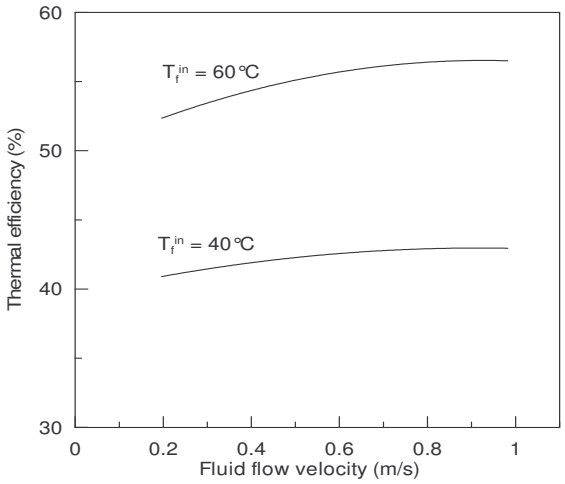

Figure 3.12 Experimental and simulation results showing the effects of the feed flow velocity on the MD thermal efficiency ((MD020CP2N module, v_p = 0.28 m/s, T_p=15°C, feed concentration = 35g/L)

The MD performance with solution concentration ranging from 35 g/L to 350 g/L (saturated NaCl solution) is reported in Figure 3.13 (MD020CP2N module, T_f^{in}= 55°C; T_p^{in}= 25°C; feed and permeate flow velocities set to 0.39 and 0.28 m/s, respectively).

The results showed that the MD transmembrane flux was decreasing slightly (by 5%) when the concentration increased from 35 to 75 g/L (a value close to typical RO brine composition). Since the driving force in MD process is a partial pressure difference, the transmembrane flux was not limited by the osmotic pressure; this fact allowed operation at high solution concentration ranges where RO normally fails. Therefore, MD seems an attractive technique for seawater desalination when integrated with RO in the logic of the Zero Liquid Discharge (ZLD) concept. The total flux decay was about 50% when the feed concentration was increased from 35 to 350 g/L, mainly because of the reduction

in the activity of the solution that decreased from an initial value of about 0.99 down to 0.73 in proximity of the saturation level, as shown in Figure 3.13.

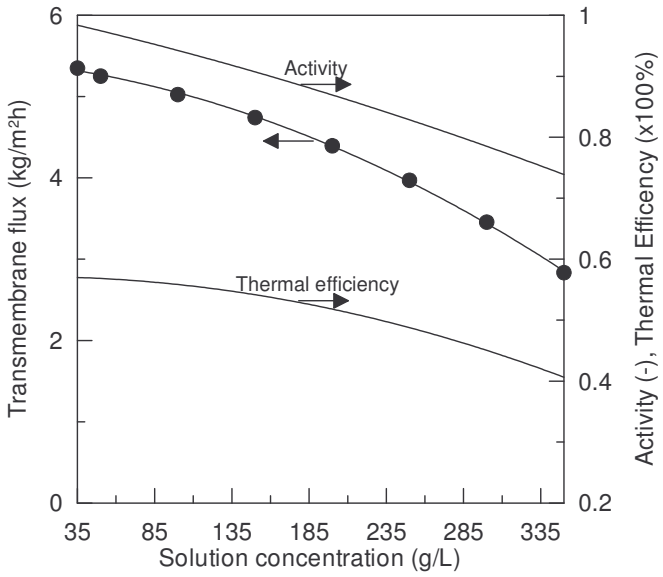

Figure 3.13 Effect of the solution concentration on the MD performance (MD020CP2N module, feed flow velocity = 0.39 m/s, permeate flow velocity = 0.28 m/s, T_f^{in}= 55°C; T_p^{in}= 25°C). Points from experiments and lines from simulation

The thermal efficiency was decreasing from 58% to 40% as the feed concentration was increased from 35 g/L to 350 g/L due to the reduction in the vaporization heat associated with the transmembrane flux (Figure 3.13).

Investigations were also conducted to compare both RO and MD transmembrane fluxes when increasing the feed concentration for seawater applications. Sodium chloride solutions of concentrations ranged from 55 g/L to 100 g/L were used in the investigations. The main observation from these results is that RO flux drastically dropped off due to the increase of osmotic pressure with increasing the concentration as shown in Figure 3.14. RO flux dropped by 60 % when the feed concentration was increased from 55 g/L to 70 g/L and the flux reached zero at feed concentration 85 g/L when the feed pressure was equal

to the osmotic pressure. On the other hand, MD flux was not greatly affected by increasing the solute concentration. This is due to the fact that the driving force in MD process is the partial pressure difference generated by the temperature difference and therefore MD flux is independent on the osmotic pressure which allows to operate it at very high feed concentration ranges where RO normally fails to operate at these ranges. Therefore, MD is a very promising technique for seawater desalination application especially if integrated with RO to be operating on the brine to increase the overall process recovery.

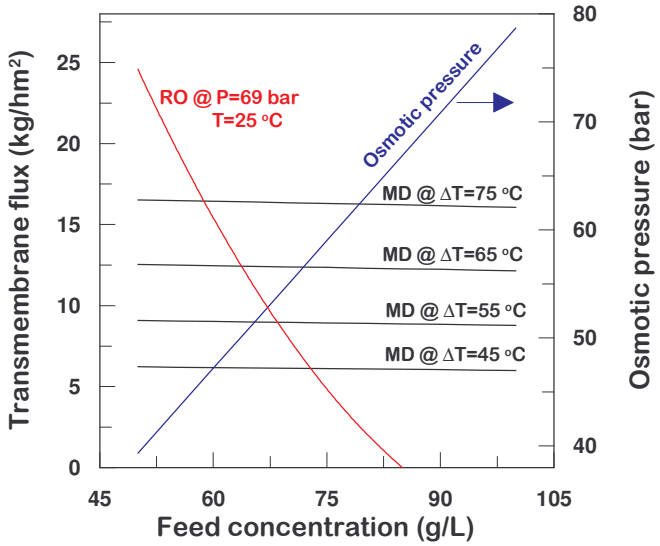

Figure 3.14 Comparison of the MD and RO flux at different concentration

As shown from above, the simulation model was capable to estimate the transmembrane flux with average errors not exceeding 5%; therefore, it was used as a reliable tool for describing the MD process performance at different operating conditions and different membrane physical properties.

3.5.3 Effects of the membrane physical properties

Basic membrane physical properties, namely thickness, thermal conductivity and porosity were considered in this study. The operating conditions were always kept constant at feed inlet temperature of 55°C,

temperature difference of 30°C, feed flow velocity of 0.90 m/s, permeate flow velocity of 0.28 m/s and feed concentration of 35 g/L. The results are presented in Figures 3.15-3.17.

At present, available polymeric materials for manufacturing hydrophobic membranes suitable for MD are, typically, polypropylene (PP), polyvinylidenefluoride (PVDF) and polytetrafluoroethylene (PTFE). As shown in Figure 3.15, membrane materials with high thermal conductivity result in the reduction of both transmembrane flux and thermal efficiency (by 26% and 55%, respectively, when the thermal conductivity of the membrane increased from 0.05 to 0.5 W/m K). Polymeric membrane materials with higher thermal conductivity offer a lower thermal resistance; therefore, the conduction heat transferred through the membrane increases (according to equation (26)), which in turn reduces the amount of vaporization heat and, ultimately, both flux and thermal efficiency.

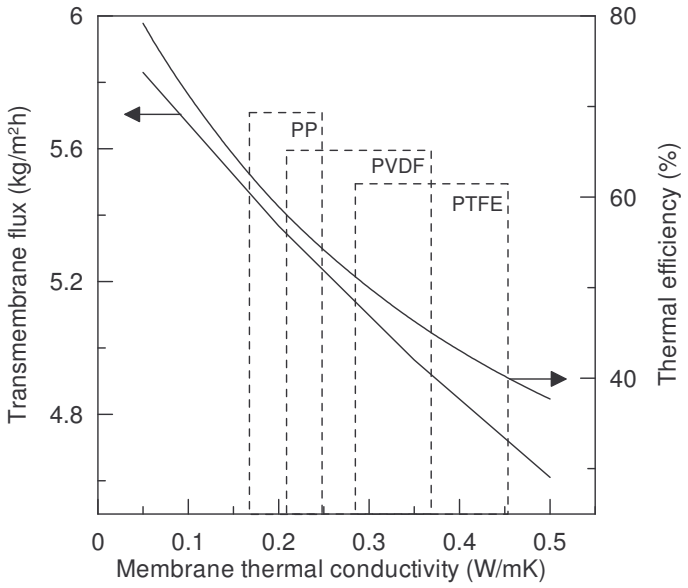

Figure 3.15 Simulation results of the effects of the membrane thermal conductivity on the MD performance (v_f = 0.90 m/s, v_p = 0.28 m/s, T_f^{in} = 55°C, ΔT = 25°C, feed concentration = 35 g/L, based on MD020CP2N module as a reference for membrane properties with changing k for simulation)

In principle, the membrane surface should be made of material with small thermal conductivity; however, as shown in Figure 3.15, for common hydrophobic polymers used in MD it is above 0.2 W/mK. Some materials exhibit thermal conductivities in the range of 0.13-0.18 W/mK (cellulose acetate and polyvinylchloride, polystyrene) and even less (polyurethane) [47]. In order to improve the performance of MD membranes, recent approaches consider the use of microporous hydrophobic/hydrophilic composite membrane, with a top hydrophobic thin layer responsible for the mass transport, and a hydrophilic sub-layer able to reduce the conductive heat loss through the whole membrane matrix. Specifically, they include: cellulose acetate or cellulose nitrate membranes modified via radiation graft polymerization of vinyltrimethylsilicon/carbon tetrafluoride and octafluoro-cyclobutane [48], or surface modification of hydrophilic membranes by adding fluorinated surface-modifying macromolecules [49].

As shown in Figure 3.16, the transmembrane flux declined rapidly when the membrane thickness was increased, as expected from the inverse proportional relationship between N and δ in equation (9.a). As a matter of fact, the flux dropped by about 70% when the membrane thickness increased from 0.25 to 1.55 mm. However, a conflict exists between the requirements of high mass transfer associated with thinner membranes and low conductive heat losses achieved by using thicker membranes. In fact, the thermal efficiency increased gradually as the membrane thickness was increased when operating at temperature gradient higher than 10 ^{o}C. Therefore, the efficiency improved since the reduction in the heat conduction through the membrane (term k_m/δ in equation (35)) was always more significant than the decrease in the vaporization heat (term $N\lambda$ in equation (35)) due to flux decline occurring at higher membrane thickness. At low temperature difference (< 5°C), the thermal efficiency exhibited a maximum around 0.7 mm membrane thickness, as shown in the magnified

scale in Figure 3.16. In this case, the positive effect on the efficiency due to the reduction of k_m/δ was counterbalanced by the reduction of $N\lambda$, hence creating a plateau in the thermal efficiency profile.

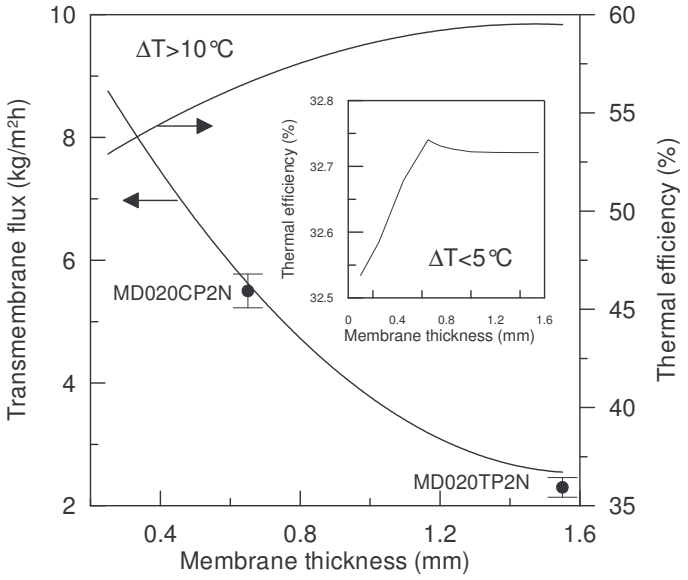

Figure 3.16 Simulation and experimental results of the effects of the membrane thickness on the MD performance (v_f = 0.90 m/s, v_p = 0.28 m/s, T_f^{in} = 55°C, ΔT = 25°C, feed concentration = 35 g/L, based on MD020CP2N module as a reference for membrane properties with changing δ for simulation)

Figure 3.17 illustrates the effect of increasing membrane porosity on the MD performance. According to equations (9.b) and (9.c), membranes with higher porosity have higher effective molecular diffusions, leading to a flux enhancement. In addition, a high void fraction of the polymeric matrix reduces the thermal conductivity of the membrane, as in equation (26) and, ultimately, decreases the efficiency loss associated with the conductive heat flux. The calculations showed that as the membrane porosity was increased by 15%, the vapor flux and the thermal efficiency for the MD020CP2N module (ε=0.70) increased by 26% and 13%, respectively. A similar trend was found for the Home-Made module (ε=0.45), whose vapor flux and thermal efficiency increased by 37% and 3%, respectively.

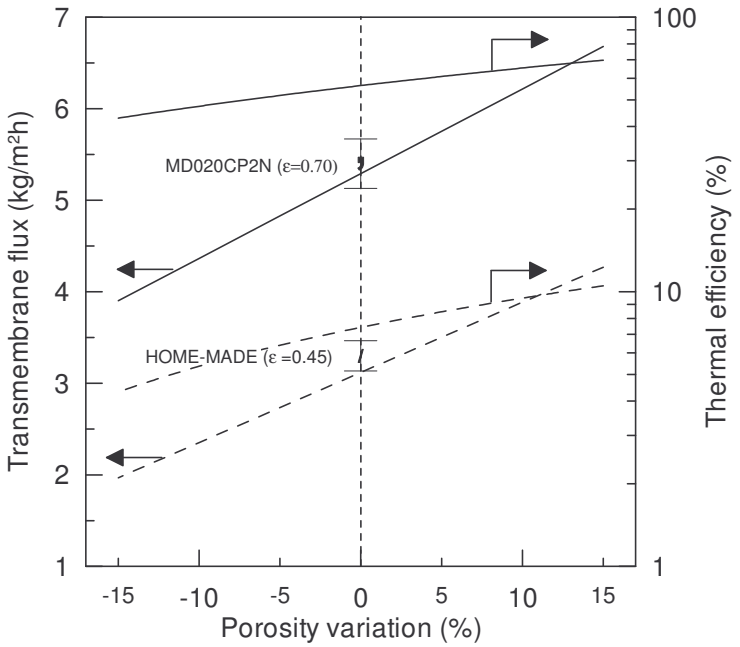

Figure 3.17 Simulation and experimental results of the effects of the membrane porosity on the MD performance (v_f = 0.90 m/s, v_p = 0.28 m/s, T_f^{in} = 55°C, ΔT = 25°C, feed concentration = 35 g/L, based on MD020CP2N module as a reference for membrane properties with changing ε for simulation)

At present, typical porosity of commercial membranes used in MD operations are 0.7 for Accurel PP membranes (Mycrodyn), 0.75 for PVDF-made GVHP/HVHP membranes (Millipore) and 0.6 for TF series PTFE/PP supported membranes [20].

3.6 Conclusions

Mass and heat transport mechanisms in MD process are always coupled and it is necessary to solve heat and mass balance equations together. Therefore, calculating heat and mass flux for a real MD system is an iterative process that is normally solved by computer.

There was a good agreement between the results obtained by the simulation model and the experimental results with average errors not exceeding

5% and therefore, it was used as a reliable tool for describing the MD process performance at different operating conditions and different membrane physical properties.

The results showed that an increase of the temperature gradient resulted in the enhancement of both transmembrane flux and thermal efficiency. On the other hand, feed concentration had low effect in flux reduction even at high values close to saturation which contribute to only 30-50% flux reduction. This makes the MD process attractive technique for seawater desalination especially when integrated with RO in the logic of the Zero Liquid Discharge (ZLD) concept. Furthermore, the results revealed that better performance of MD process in terms of thermal efficiency can be achieved by increasing the flow rates and the operating temperatures. However, care must be taken when increasing flow rates and operating temperatures in order to avoid membrane wetting. In addition, operations at high flow rates and temperatures will require higher energy which in turn increases the cost of operation.

The investigation of the effects of membrane properties confirmed that better MD performance was achieved when using polymeric membranes characterized by low thermal conductivity (flux and thermal efficiency declined by 26% and 50%, respectively, when increasing thermal conductivity from 0.1 to 0.5 W/m K), and high porosity. The investigation of the complex correlations between physico-chemical properties of the membrane and MD performance confirms the need for a customized hardware, i.e. high porosity hydrophobic membranes with appropriate thickness and made by low-heat conductive polymers in order to reduce the amount of wasted energy.

REFERENCES

[1] V. Calabrò, B.L. Jiao and E. Drioli, Theoretical and experimental study on membrane distillation in the concentration of orange juice, Ind. Eng. Chem. Res. 33 (1994) 1803.

[2] M.S. El-Bourawi, Z. Ding and M. Khayet, A framework for better understanding membrane distillation separation process, Journal of Membrane Science 285 (2006) 4.

[3] V. Calabrò, E. Drioli and F. Matera, Membrane distillation in textile wastewater treatment, Desalination 83 (1991) 209.

[4] A.M. Alklaibi and N. Lior, Membrane-distillation desalination: Status and potential, Desalination 171 (2005) 111.

[5] C. Cabassud and D. Wirth, Membrane Distillation for water desalination: How to choose an appropriate membrane?, Desalination 157 (2003) 307.

[6] R. Chouikh, S. Bouguecha and M. Dhahbi, Modeling of a modified air gap distillation membrane for the desalination of seawater, Desalination 181 (2005) 257.

[7] T. Y. Cath, V. Dean Adams and A. E. Childress, Experimental study of desalination using direct contact membrane distillation: a new approach to flux enhancement. Journal of Membrane Science 228 (2004) 5.

[8] F. Banat, R. Jumah and M. Garaibeh, Exploitation of solar energy collected by solar stills for desalination by membrane distillation, Renewable Energy 25 (2002) 293.

[9] Z. Ding, L. Liu, M.S. El-Bourawi and R. Ma, Analysis of a solar-powered membrane distillation system, Desalination 172 (2005) 27.

[10] J. Koschikowski, M. Wieghaus and M. Rommel, Solar thermal-driven desalination plants based on membrane distillation, Desalination 156 (2003) 295.

[11] www.scarab.se

[12] J. Walton, H. Lu, C. Turner, S. Solis and H. Hein, Solar and Waste Heat Desalination by Membrane Distillation, 98-FC-81-0048, DWPR n. 81, El Paso TX, April 2004.

[13] http://www.psa.es/webeng/projects/medesol/index.html

[14] F. Banat, N. Jwaied, M. Rommel, J. Koschikowski and M. Wieghaus, Performance evaluation of the "large SMADES" autonomous desalination solar-driven membrane distillation plant in Aqaba, Jordan, Desalination 217 (2007) 17.

[15] J.H. Hanemaaijer, J. van Medevoort, A.E. Jansen, C. Dotremont and E. van Sonsbeek, Memstill membrane distillation - a future desalination, Desalination 199 (2006) 175.

[16] B. Van der Bruggen, Desalination by distillation and by reverse osmosis – trends towards the future, Membrane Technology, February/2 (2003) 6

[17] C. Fritzmann, J. Löwenberg, T. Wintgens and T. Melin, State-of-the-art of reverse osmosis desalination, Desalination 216 (2007) 1.
[18] http://medina.unical.it
[19] E. Curcio and E. Drioli, Membrane Distillation and Related Operations - A Review, Separation & Purification Reviews 34 (2005) 35.
[20] K.W. Lawson and D.R. Lloyd, Membrane distillation. II. Direct contact membrane distillation, Journal of Membrane Science 120 (1996) 123.
[21] B. Li and K.K. Sirkar, Novel membrane and device for direct contact membrane distillation-based desalination processes, Ind. Eng. Chem. Res. 43 (2004) 5300.
[22] L. Martínez-Díez, M. I. Vázquez-González and F. J. Florido-Díaz, Study of membrane distillation using channel spacers, Journal of Membrane Science 144 (1998) 45.
[23] E. Drioli, E. Curcio, A. Criscuoli and G. Di Profio, Integrated system for recovery of $CaCO_3$, NaCl and $MgSO_4 \cdot 7H_2O$ from nanofiltration retentate, Journal of Membrane Science 239 (2004) 27.
[24] A. Gabelman and S.-T. Hwang, Hollow fiber membrane contactors, Journal of Membrane Science 159 (1999) 61.
[25] S. Bandini and G.C. Sarti, Heat and mass transport resistances in vacuum membrane distillation, AIChEJ 45(7) (1999) 1422.
[26] S. Kimura and T.p.i.m.d. S. Nakao, J. Membr. Sci. 33 (1987) 285–298., Transport phenomena in membrane distillation, Journal of Membrane Science 33 (1987) 285.
[27] L. Martínez-Díez, F. J. Florido-Díaz, Theoretical and experimental studies on desalination using membrane distillation, Desalination 139 (2001) 373.
[28] Z. Ding, R. Ma, A.G. Fane, A new model for mass transfer in direct contact membrane distillation, Desalination 151 (2002) 217.
[29] R.W. Schofield, A.G. Fane and C.J.D. Fell, Gas and vapour transport through microporous membrane. II. Membrane distillation, Journal of Membrane Science 53 (1990) 173.
[30] M. Courel, M. Dornier, G.M. Rios, M. Reynes, Modeling of water transport in osmotic distillation using asymmetric membrane, Journal of Membrane Science, 173 (2000) 107.
[31] A.O. Imdakm, T. Matsuura, Simulation of heat and mass transfer in direct contact membrane distillation (MD): The effect of membrane physical properties, Journal of Membrane Science 262 (2005) 117.
[32] J. Phattaranawik, R. Jiraratananon and A.G. Fane, Heat transport and membrane distillation coefficients in direct contact membrane distillation, Journal of Membrane Science 212 (2003) 177.
[33] R.D. Present, Kinetic Theory of Gases. McGraw-Hill, New York. (1958).
[34] R.A. Albert and R.J. Silbey, Physical Chemistry, 2nd ed. Wiley, New York. (1997).

[35] C.M. Guijt, I.G. Racz, J.W.v. Heuven, T. Reith, A.B.d. Haan, Modeling of a transmembrane evaporation module for desalination of seawater, Desalination 126 (1999) 119.
[36] R.H. Perry and D. Green, Perry's Chemical Engineers' Handbook, 6th Edition, McGraw Hill, New York, (1984).
[37] M. Gryta, M. Tomaszewska, Heat transport in the membrane distillation process, Journal of Membrane Science 144 (1998) 211.
[38] H. Kurokawa, K. Ebara, O. Kuroda, S. Takahashi, Vapor permeate characteristics of membrane distillation, Separation Science Technology 25 (1990) 1349.
[39] E. Curcio, Membrane Crystallizers. Ph.D. Thesis in Chemical Engineering and Materials Department, University of Calabria, Italy (2004).
[40] J.D. Rogers and R. Long, Modeling hollow fiber membrane contactors using film theory. Voronoi tessellation and facilitation factors for systems with interface reactions, Journal of Membrane Science 134 (1997) 1.
[41] J. Wu and V. Chen, Shell-side mass transfer performance of randomly packed hollow fiber modules, Journal of Membrane Science 172 (2000) 59.
[42] D. Zhongwei, L. Liying and R. Ma, Study on the effect of flow maldistribution on the performance of the hollow fiber modules used in membrane distillation, Journal of Membrane Science 215 (2003) 11.
[43] M. Qtaishat, T. Matsuura, B. Kruczek and M. Khayet, Heat and mass transfer analysis in direct contact membrane distillation, Desalination 219 (2008) 272.
[44] R.C. Reid, J.M. Prausnitz and T.K. Sherwood, The Properties of Gases and Liquids, 3rd edition., McGraw-Hill, New York, 1977.
[45] N. Hubert, Y. Gabes, J.-B. Bourdet and L. Schuffenecker, Vapor Pressure Measurements with a Nonisothermal Static Method between 293.15 and 363.15 K for Electrolyte Solutions. Application to the H_20 + NaCl System, J. Chem. Eng. Data 40 (1995) 891.
[46] N. Wakao and J.M. Smith, Diffusion in catalyst pellets, Chem. Eng. Sci. 17 (1962) 825.
[47] N.P. Cheremisinoff, Handbook of Engineering Polymeric Materials, Dekker, New York (1997).
[48] Y. Wu, Y. Kong, X. Lin, W. Liu and J. Xu, Surface-modified hydrophilic membranes in membrane distillation, Journal of Membrane Science 72 (1992) 189.
[49] M. Khayet, J.I. Mengual and T. Matsuura, Porous hydrophobic/hydrophilic composite membranes Application in desalination using direct contact membrane distillation, Journal of Membrane Science 252 (2005) 101.

CHAPTER 4
MEMBRANE DCRYSTALLIZATION

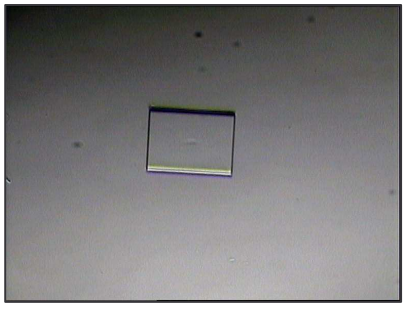

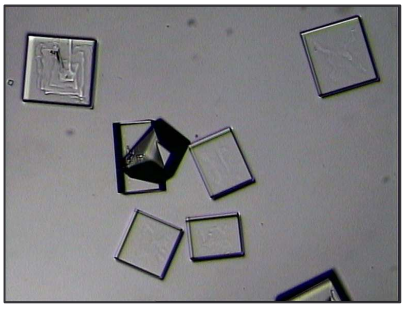

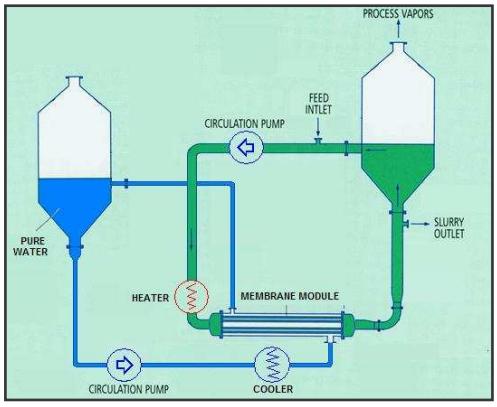

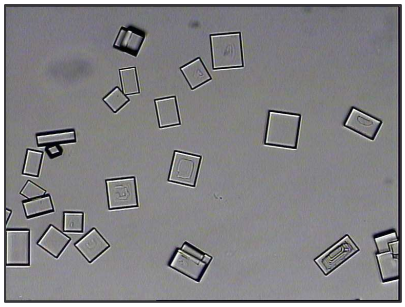

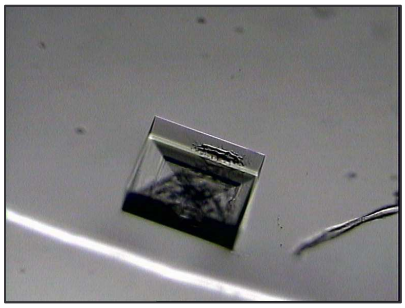

SUMMARY
This chapter offers a theoretical insight to the basic mechanisms of crystallization especially the ones necessary for modeling and simulation of the membrane crystallizers. It also encloses some experimental tests aiming to improve the design and performance of the crystallizers.

4.1 Introduction

Crystallization from solution or from melt is one of the oldest and economically most important industrial separation and purification processes. It is an excellent purification technique by solidification from a liquid mixture to obtain solid products of high purity at low costs [1]. It is applied as a large scale continuous process for the production of variety of materials like inorganic (e.g. potassium chloride, ammonium sulphate) and organic (e.g. adipic acid) materials. On a small scale it is often applied as a batch operation to produce high purity pharmaceuticals or fine chemicals for electronic industries like semiconductors [2, 3]. Two types of crystallization are distinguished: crystallization from melt and crystallization from solution. In melt crystallization, the separation of the mixture components takes place without any addition of diluent solvent and the solid phase is formed by only cooling the melt. On the other hand, in crystallization from solution, the solvent is evaporated from the solution and/or the solution can be indirectly cooled. The crystals obtained by evaporation are formed because the less solvent available for the dissolved solutes which leads to a metastable or supersaturation state which in turn activates nucleation and crystal growth.

4.1.1 Conventional Crystallizers

The design and operation of the industrial crystallizers is still not well optimized even that industrial crystallizers are in operation since many decades. A critical issue in the design of an industrial crystallization process is the strong interaction between kinetic aspects and hydrodynamics. Parameters such as temperature, supersaturation and turbulence are typically not uniformly

distributed in the crystallizer body, and the slurry is not well-mixed and suspended. These types of unhomogeneity have a major impact on the final product quality of the crystallization process [4]. Conventional crystallization equipments can have several varieties and configuration. However, they can be categorized into two types: the Forced Circulation (FC) and the Draft-Tube-Baffed (DTB) as shown in Figure 4.1. The main design problem in FC crystallizers is the thermal short-circuiting caused by vortexing in the crystallizer body which leads to higher levels of supersaturation thought the body, variable nucleation rates and consequently cycling of the crystal size distribution (CSD) between fine and coarse particles [5, 6]. In DTB crystallizers, an impeller is used to direct the slurry to the liquid surface to avoid thermal short-circuiting. However, the final shape of the crystals is often unsatisfactory due to the fact that large crystals are rounded off by the abrasion and attrition with the moving parts in the system. These problems in both types of the crystallizers occur mainly due to the fact that the solvent evaporation and the solute crystallization take place at the same location (the crystallizer body).

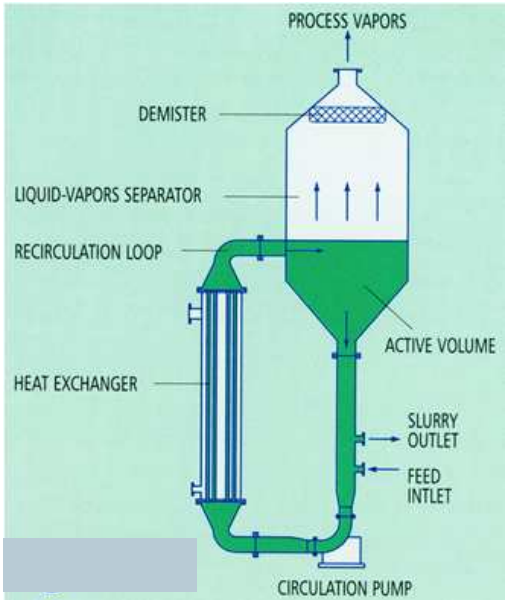

(a) FC crystallizer

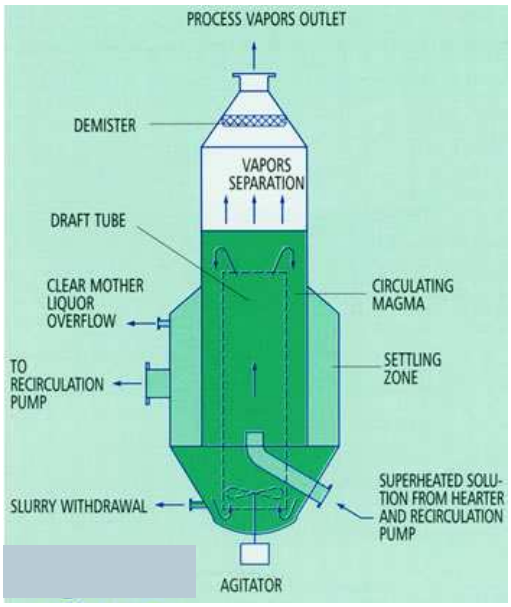

(b) DTB crystallizer

Figure 4.1 Conventional industrial crystallizers

4.1.2 Membrane Distillation Crystallization

Membrane Distillation/Crystallization (MDC) is an interesting and promising extension of the Membrane Distillation (MD) concept. This technology involves vapor mass transfer of volatile solvents through microporous hydrophobic membranes in order to concentrate solution above the saturation limit and achieving a metastable state (supersaturation) in which crystals may nucleate and grow. In membrane crystallizers, the solvent evaporation is occurring inside the membrane module (where the flowing solution is below the supersaturation conditions) and the crystallization stage is performed in a separate tank on the retentate line which is operating in the metastable regime of supersaturation as shown in Figure 4.2. Therefore, the product crystals are expected to have good structural properties and global quality. Another feature of membrane crystallizers is that the membrane induces heterogeneous nucleation starting at low supersaturation rates depending on the surface characteristics of the membrane. Optimization of the design items like circulation rates, size of the crystallizer body and temperatures is essential in order to prevent the membrane blocking due to crystals deposition.

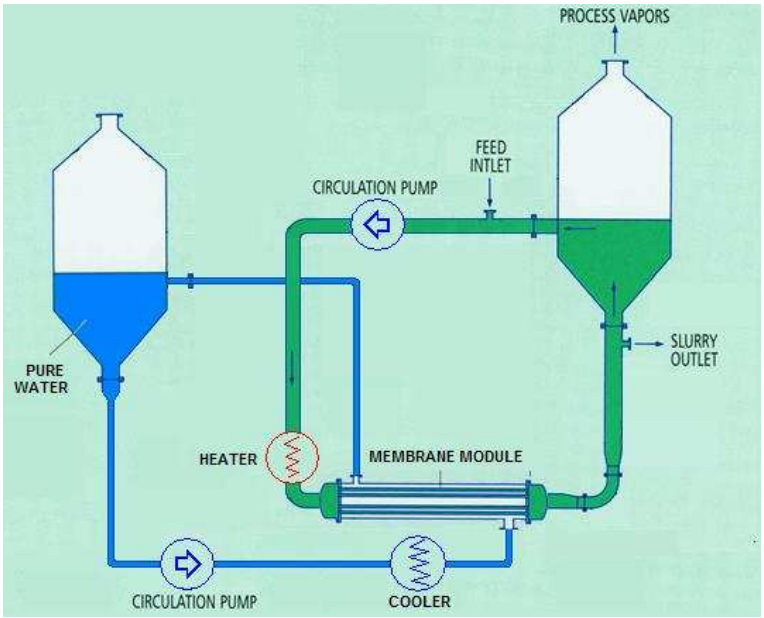

Figure 4.2 Membrane crystallizer

4.2 Thermodynamic approach

The fundamental force for crystallization is the difference in the chemical potential of a molecule in the supersaturated and saturated solution [7]. The molar Gibbs free energy (ΔG) of a substance transformed from phase *1* to phase *2* can be expressed as the difference in the chemical potentials of the phase considered. The molar Gibbs free energy can also be expressed in terms of activity as:

$$\Delta G = \left(\mu_2 - \mu_1\right) = -RT \ln\left(\frac{a}{a^*}\right) \tag{1}$$

In practice, the concentration ratio is used in place of the activity coefficients, with assumption that the solution activity coefficient of a supersaturated solution is equal to the saturated solution. Therefore, the driving force is expressed as:

$$\Delta G = -RT \ln\left(\frac{C}{C^*}\right) \tag{2}$$

where C is the solute concentration and C^* the equilibrium solubility at the temperature and pressure [8]. The supersaturation (S) is generally expressed in terms of concentration driving force given as:

$$S = \frac{C}{C^*} \tag{3}$$

Solubility data and their dependence on temperature are mandatory. Some complications arise if specie can crystallize in different forms depending on temperature [9].

Crystallization from solution involves two steps namely: nucleation which is a diffusion and phase separation process, whereby solute molecules are transported from the bulk of the solution to the crystal surface; and subsequent growth of nuclei to crystals by an interface kinetics reaction process in which the solute molecules arrange themselves into the crystal lattice [10]. The driving force for crystallization to occur is a supersaturated solution, however,

supersaturated solutions are not at equilibrium. Since every system strives to reach equilibrium, supersaturated solutions finally crystallize. The solutions move towards equilibrium by crystallizing and thus relieving supersaturation by a combination of nucleation and crystal growth [11, 12].

4.2.1 Nucleation rate

There are three main categories of nucleation; primary homogeneous, primary heterogeneous, and secondary nucleation as shown in Figure 4.3 [12].

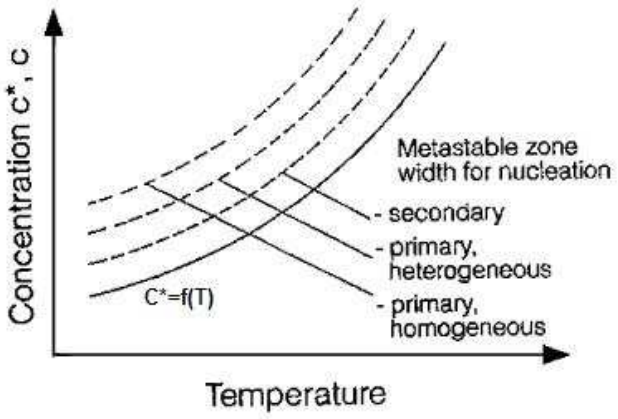

Figure 4.3 Categories of nucleation [12]

The mechanisms governing the various types of primary and secondary nucleation are different and result in different rate expressions. The relative importance of each type of nucleation varies with the crystallization conditions. The primary homogeneous nucleation is taking place in supersaturated solution when solute molecules combine to produce clusters, or embryos. The overall free energy per embryo of the aggregate is a result of two terms, the free energy due to the new surface and the free energy due to the formation of new solid. The heterogeneous nucleation takes place at a lower critical supersaturation on a foreign surface, which has a lower surface energy than that of a new solute particle [2]. Most primary nucleation is likely to be heterogeneous nucleation induced by other surfaces. The heterogeneous nucleation rate is similar to the

homogeneous nucleation rate except that the interfacial energy is altered by the cosine of the contact angle, θ, between the crystal, solution, and foreign particle. The secondary nucleation is originating either from the seed crystals or from the boundary layer of the growing crystals. The secondary nucleation is induced only because of the presence of crystals of the material being crystallized and it generally occurs at much lower supersaturation than primary homogeneous or even heterogeneous nucleation [13].

Nuclei can be born in a clear supersaturated solution as homogeneous nucleation, on foreign particles as heterogeneous nucleation or by interacting between crystals as secondary nucleation. Supersaturated solutions exhibit a metastable zone, which constitutes the allowable supersaturation level during every crystallization process. Nucleation is not likely to occur within this metastable zone. However, by further increase of supersaturation, a certain degree of supersaturation will be reached at which spontaneous nucleation will take place. It can be shown that a maximum in Gibbs free energy, which is the sum of the contributions from the bulk and the surface free energies, occurs at a critical cluster size. This critical cluster size, also called critical nucleus (r^*), corresponds to the size at which further growth of the cluster leads to a decrease in free energy. All those clusters with sizes larger than the size of critical nucleus (r^*) will be likely to grow spontaneously. Therefore, there is an energetic barrier ΔG^*, called as nucleation barrier, that must be crossed in order to induce the formation of stable nuclei [2]. The values of r^* and ΔG^* vary inversely with supersaturation as shown in equation (4):

$$\Delta G^* = \frac{16\pi v^2 \gamma^2}{3\left[k_B T \ln S\right]^2} \qquad (4)$$

where v is the molar volume occupied by a growth unit, γ is the surface energy, k_B is the Boltzman constant, T is the absolute temperature and S is the supersaturation. The height of the energy barrier is decreasing as the supersaturation increases and eventually this leads to induce spontaneous

nucleation as shown in Figure 4.4. The existence of this energy barrier justifies the fact that a solution will experience a homogenous nucleation under thermodynamic conditions only if a certain value of supersaturation is exceeded.

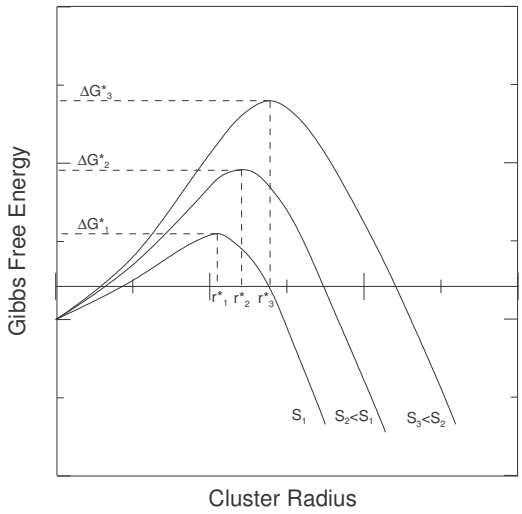

Figure 4.4 The Gibbs free energy versus the critical cluster size [2]

The presence of a foreign interface in the crystallizing system decreases the energy required to create critical nuclei and therefore increases the probability of nucleation with respect to other locations in the system. The interfacial energy is altered by the cosine of the contact angle θ between the crystallizing solution and the interface as given by equation (5):

$$\Delta G^{het} = \Delta G^{\hom}\left[\frac{1}{2} - \frac{3}{4}\cos\theta + \frac{1}{4}\cos^3\theta\right] \qquad (5)$$

If the surface is perfectly hydrophobic (θ=180°), the energy barrier of the heterogeneous nucleation is equal to the homogenous nucleation i.e. $\Delta G^{het} = \Delta G^{hom}$; and when contact angle is 90°, where the situation is limited between hydrophobic and hydrophilic behavior, $\Delta G^{het} = ½\ \Delta G^{hom}$. For practical purposes, the nucleation rate (B) per unit mass of solvent can be estimated using a semi-empirical expression as [2]:

$$B = k_n M_D{}^j \left(C - C^*\right)^n \qquad (6)$$

The nucleation rate constant k_n depends on temperature, hydrodynamics, presence of impurities and crystal properties. The effects of the secondary nucleation are taken into account by the magma density term M_D in the kinetic expression.

4.2.2 Growth rate

Crystal growth is generally considered into two main categories. The first one is the growth of ''rough'' crystal surfaces in which the growth units are deposited on and removed from the crystal surface in a more or less random way. This type of growth rate is high and is characterized by crystal surfaces with weak dimensionless bond energies (thermal roughening), for high super-saturations (kinetic roughening) and for surfaces that are highly misoriented from a flat face [10]. The second category is the growth of flat, stepped crystal faces. Here growth is relatively slow and a nucleation barrier exists for the generation of a new growth layers on the atomically smooth surface. Overcoming of this barrier is realized by a ''spontaneous'' creation of closed loop steps via homogeneous or heterogeneous *2D* nucleation [14], or by the generation of steps from crystal defects [15].

Growth rate in solution is generally occurring in two steps which involve diffusion of the solute from the bulk solution to the surrounding of the crystal interface followed by integration into the crystal lattice. The Burton-Cabrera-Frank (BCF) surface diffusion theory introduced the concept of the roughening transition [15]. It implies that below a certain temperature, the crystal surfaces are flat and above this temperature they are rough. The BCF surface diffusion theory can be simplified and employed for the crystallization kinetic estimation. A simple power-low relationship can be used for estimating the overall rate of crystal growth. For practical purposes, this relationship is expressed as [2, 16]:

$$G_r = k_g \left(C - C^*\right)^g \tag{7}$$

The overall growth rate coefficient k_g is depending on several variables such as crystal size, temperature, hydrodynamics and presence of impurities in the crystallization system. The kinetic parameters k_g and g can be obtained from growth rate experiments as the abscissa and the slope of the plot of $ln(G_r)$ versus $ln(C-C^*)$, respectively [2, 16].

Combination of equations equation (6) & (7) allows eliminating the concentration gradient $(C-C^*)$ and the relationship between the nucleation rate B and the growth rate G_r is given as:

$$B = kM_D{}^j G_r{}^i \tag{8}$$

The values of the relative kinetic order i is ranged between 1 and 2. High rates of i are expected when primary nucleation is the dominant mechanism, due to its non linear dependence on supersaturation [17].

4.2.3 Crystal Size Distribution (CSD)

One important quality aspect of crystalline product is the crystal size distribution (CSD). The CSD is a function of the process performance in terms of crystal nucleation and growth rates. The CSD is also essential for the storage and handling of the final product. For example, relatively large crystals limit the adhesion of the mother liquor after filtration and, therefore, show a low tendency towards caking [2, 10]. On the other hand, small crystals are preferred whenever reduced dissolution times are required. Therefore, a narrow distribution around the mean crystal size is required. The size distribution $f(L_n)$ is generally expressed as the number fraction of crystals having a certain size group (n) divided by the length of the crystals of the same group:

$$f\left(L_n\right) = \frac{\Delta N_n}{\Delta L_n} \tag{9}$$

where ΔN the number of crystals in a unit volume of slurry having a size between L and $L+\Delta L$.

In addition, the width of a distribution around the mean size is often characterized by the coefficient of variation (*CV*), equal to the standard deviation divided by the mean size.

$$CV = \frac{\text{standard deviation}}{\text{length based mean size}} = \frac{L_{80\%} - L_{20\%}}{2L_{50\%}} \tag{10}$$

CV is expressed as percentage and *L* is the crystal length at the percentage indicated.

4.2.4 Membrane Distillation/Crystallization Kinetics

The transmembrane flux of water vapor can be approximated using the equation [18, 19]:

$$N = C\,\Delta p \tag{11}$$

where *C* is the membrane permeability and Δp is vapor pressure difference across the membrane walls. A simplified equation for calculating the transmembrane flux in Direct Contact Membrane Distillation (DCMD) when used for desalination is proposed by Lawson and Lloyd [18] given as:

$$N = \frac{-1}{RT_{avg}}\left(\frac{D_w^k\, D_{w-a}^o}{D_{w-a}^o + p_a\, D_w^k}\right)\left(\frac{p_p - p_f}{\delta}\right) \tag{12}$$

$$with \quad D_w^k = K_o\left(\frac{8RT_{avg}}{\pi M}\right)^{1/2} \qquad and \qquad D_{w-a}^o = \frac{\varepsilon}{\tau}\times 4.46\times 10^{-6}\, T_{avg}^{2.334}$$

The concentration polarization coefficient (*CPC*) is described by the film model:

$$CPC = \frac{C_m}{C_f} = \exp\left(\frac{N}{\rho\, k_f}\right) \tag{13}$$

where C_m and C_f are the concentration at the membrane wall and in the bulk, respectively. The value of the mass transfer coefficient (k_f) is required to estimate the *CPC*. It can be obtained using the Levegue equation [19]:

$$k_f = 1.62\left[\frac{d_f v}{l}\right]^{1/3} D^{2/3} \quad (14)$$

where d_f is the fiber inner diameter, v is the solution velocity, l is the fiber length and D is the diffusion coefficient of solvent in the solution. The *CPC* will be used to estimate the feed concentration at the membrane surface C_m which measures the level of supersaturation along the membrane surface in order to determine the nucleation rate.

The temperature polarization coefficient is defined as [18, 20]:

$$TPC = \frac{T_1 - T_2}{T_f - T_p} \quad (15)$$

where T_1 and T_2 are the interfacial temperatures at the feed and the permeate sides, respectively; and T_f and T_p are the bulk temperatures at the feed and permeate sides.

The interfacial temperatures T_1 and T_2 can not be measured directly but they can be estimated from the mass and energy balances across the membrane as discussed in details in chapter 3. They are calculated as:

$$T_1 = \frac{\alpha\left(T_p + \beta T_f\right) + h_f T_f - N\lambda}{\alpha + h_f + \alpha\beta} \quad (16.a)$$

$$T_2 = \frac{\alpha\left(T_f + \beta^{-1} T_p\right) + h_p T_p + N\lambda}{\alpha + h_p + \alpha\beta^{-1}} \quad (16.b)$$

with $\alpha = \frac{k_m}{\delta}$ and $\beta = \frac{h_f}{h_p}$.

where h is the heat transfer coefficient and can be estimated using an empirical correlation as [21]:

$$h = \frac{Nu\, k^T}{d_h}, \quad Nu = 4.36 + \frac{0.036\,\mathrm{Re}\,\mathrm{Pr}/(L/d)}{1 + 0.0011\left[\mathrm{Re}\,\mathrm{Pr}/(L/d)\right]^{0.8}} \quad , \mathrm{Re} < 2100 \quad (17)$$

A computer simulation was applied in a similar manner as done to the MD process in chapter 3 in order to solve the set of equations (equations (12), (16) and

(18)) by iteration to estimate the transmembrane flux, temperatures and concentrations of the membrane distillation crystallization process.

4.3 Computer simulation procedure

The computer simulation of the MDC was similar to the one of the MD presented in chapter 3 with addition of crystallization kinetics calculation. The programming code is shown in Appendix 3. For the batch mode, the time interval as the total elapsed time must be involved. Figure 4.5 shows the flow chart of the simulation procedure.

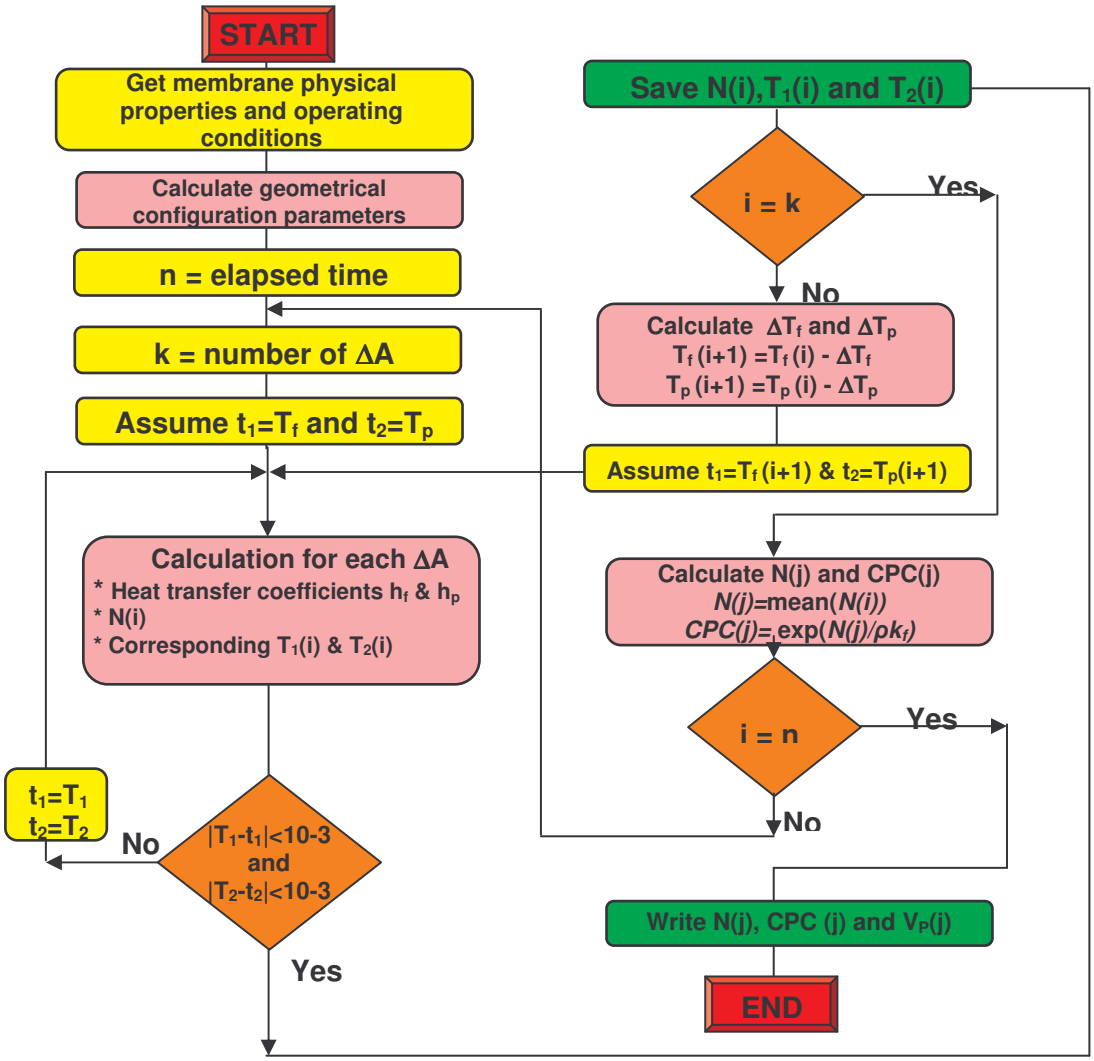

Figure 4.5 Flow chart of the computer simulation procedure of the batch crystallizer

4.4 Experimental Apparatus

A bench-scale membrane crystallizer apparatus was used in the study. A schematic representation of the experimental apparatus is shown in Figure 4.6. The membrane modules were supplied by MICRODYN and each one contains 40 hydrophobic polypropylene hollow fibers of 0.1m^2 total interfacial area. The main specifications of the membrane module are represented in Table 4.1.

Table 4.1 The main specifications of the membrane modules

Membrane material	Polypropylene
Fiber outer diameter	2.8 mm
Fiber inner diameter	1.5 mm
Nominal pore size	0.2 μm
Length of fibers	0.45 m
Packing density	70 %
Shell diameter	21 mm

The retentate and distillate streams were held at different temperatures and circulated in countercurrent arrangements towards the membrane module where the retentate solution was concentrated by solvent evaporation. Crystallization was occurring inside the retentate recirculation tank (Crystallization Tank) where a centrifugal pump was used to circulate the mother liquor to the membrane module on the retentate side. On the distillate line, the cold stream, which was used to recover water vapor passing across the membrane pores form saline solution, was circulated using a centrifugal pump. The water transmembrane flux was estimated by measuring the weight variations with time in the distillate tank.

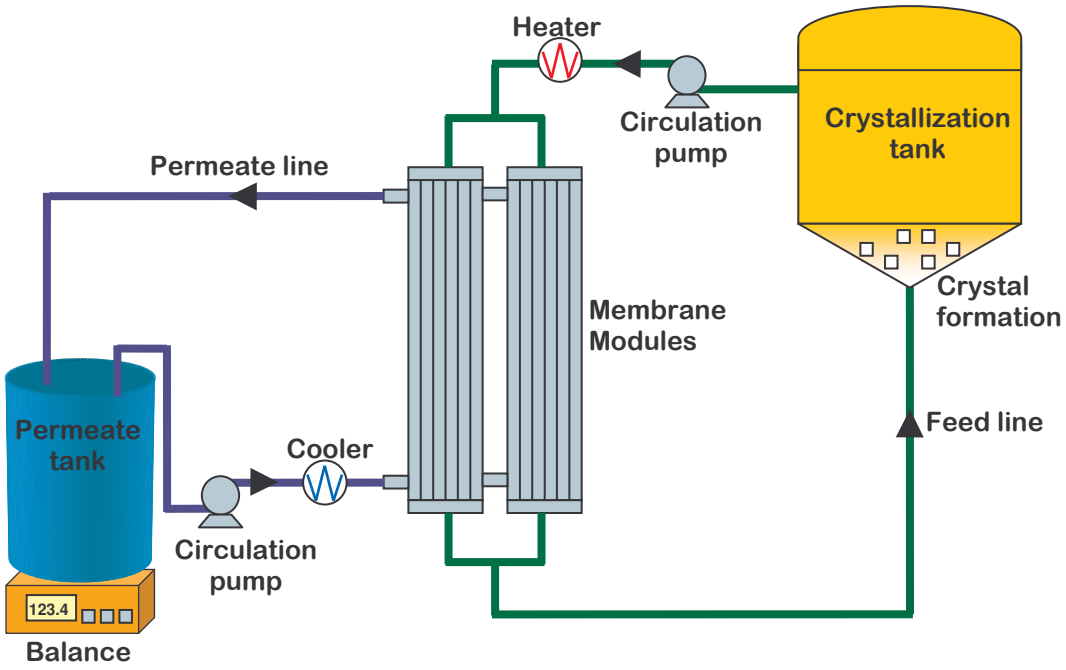

Figure 4.6 Schematic representation of the bench-scale membrane crystallizer experimental apparatus

A crucial requirement for a membrane crystallizer is to prevent crystal deposition inside the membrane. Therefore, a suitable heating must be established so that the temperature of the retentate solution flowing along the membrane is fairly high to insure under saturation conditions for solutions which increase their solubility of solids with the increase in temperature. Besides, a filter may be introduced in the suction line of the feed stream in order to stop crystals before going to the membrane module to avoid the blockage of the membrane pores which would disserve the system performance.

4.5 Experimental procedure

The bench-scale membrane crystallizer was operated in a batch mode. Artificial NF retentate solutions of elevated concentration (8 to 9 times) where used as the feed for the membrane crystallizer. These solution were prepared by dissolving analytical grade of NaCl, $MgSO_4*7H_2O$ and $MgCl_2*6H_2O$ regents in

demineralised water. Table 4.2 shows the original NF retentate composition of these salts at 70% recovery ratio, their saturation limit and the concentrations used in the experiments.

Table 4.2 Composition of NF retentate and MDC feeds

Salt	NF retentate (@ 70% recovery) g/L	Saturation limit g/L	MDC feed (8 times of NF) g/L	MDC feed (9 times of NF) g/L
NaCl	33.51	362	268.1	301.6
$MgSO_4*7H_2O$	25.95	355	207.6	233.6
$MgCl_2*6H_2O$	18.82	545	151.1	170.0

4.6 Results and discussion

4.6.1 Test run using an initial feed concentration of original NF retentate

This test run was executed using the computer simulation. The operation was assumed on a batch mode and the operating conditions are presented in Table 4.3.

Table 4.3 Operating conditions (simulation only)

Operating condition	Value
Feed flow rate (L/h)	100
Permeate flow rate (L/h)	100
Feed Inlet temperature (T_f) ^oC	40
Permeate outlet temperature (T_p) ^oC	20
Initial feed volume (L)	5
Initial feed concentration of NaCl (g/L)	33.1
Total run time (hours)	16

The results showed that the required run time in order to reach the saturation limit of NaCl (362 g/L) in the crystallization feed solution was 16 hours. At the first ten hours the transmembrane flux was steady with slight decrease from 1.5 to 1.4 (kg/m^2h). After that, the flux decreases rapidly due to

the rapid increase in the feed concentration which caused a reduction in the driving force of partial pressure difference due to the reduction in the activity coefficients as shown in Figure 4.7. As a result of the concentration polarization effects, the feed concentration at the membrane surface (C_m) was 2.7% higher than the feed concentration at the bulk side (C_f) during the first stages of the run. However, the effects of the concentration polarization were lower during the last period of the test due to the reduction in the transmembrane flux.

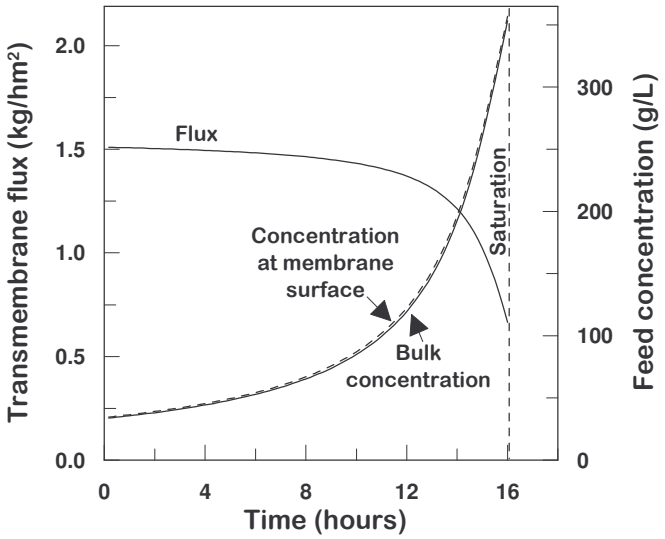

Figure 4.7 Transmembrane flux and feed concentration versus time

4.6.2 Test run using an initial feed concentration of 8 times of NF retentate

This experimental test was performed on a batch mode. The operating conditions are presented in Table 4.4.

Table 4.4 Operating conditions using 8 times of NF retentate

Operating condition	Value
Feed flow rate (L/h)	100
Permeate flow rate (L/h)	100
Feed Inlet temperature (T_f) ^oC	40
Permeate outlet temperature (T_p) ^oC	22
Initial feed volume (L)	3
Initial feed concentration (g/L)	268.1
Total run time (min)	330

At the beginning of the test, the transmembrane flux of the MDC declined gradually with time due to the increase of the solution concentration and the consequent decrease of the solution activity coefficient as shown in Figure 4.8. However, the transmembrane flux decreased sharply when the crystals started to appear in the solution after three hours operation. This flux decline was due to the rapid growth of crystal deposits on the membrane surface which caused blockage of some of the membrane pores. The transmembrane flux values obtained from the simulation results did not show such decrease after the appearance of the crystals since no pore blockage by crystals was assumed in the modeling Figure 4.8.

The concentration polarization coefficient (*CPC*) was calculated using equation (13). It was found that the *CPC* was decreasing gradually during the batch run due to the decrease in the transmembrane flux Figure 4.8.

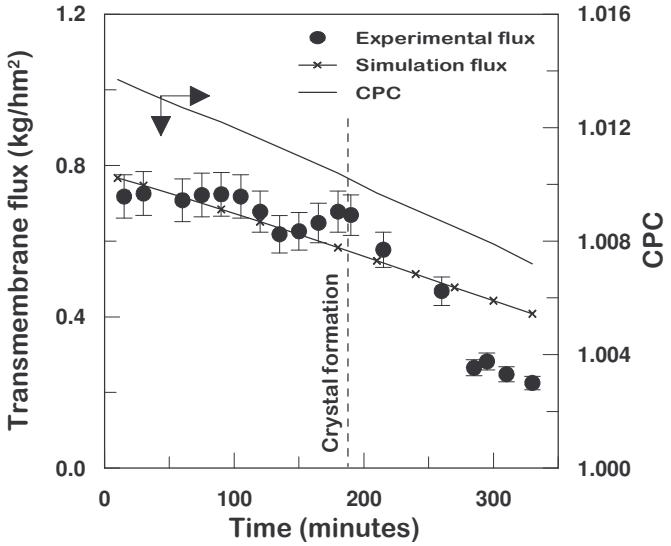

Figure 4.8 MDC transmembrane flux and *CPC* versus time

The crystallization of NaCl was started after run time of around 185 minutes when the saturation limit of the solution was exceeded. The saturation limit was estimated to be 305.2 g/L when a total permeate volume of 430 mL was

extracted from the feed solution as shown in Figure 4.9. The total permeate volume at the end of the experiment was 625 mL.

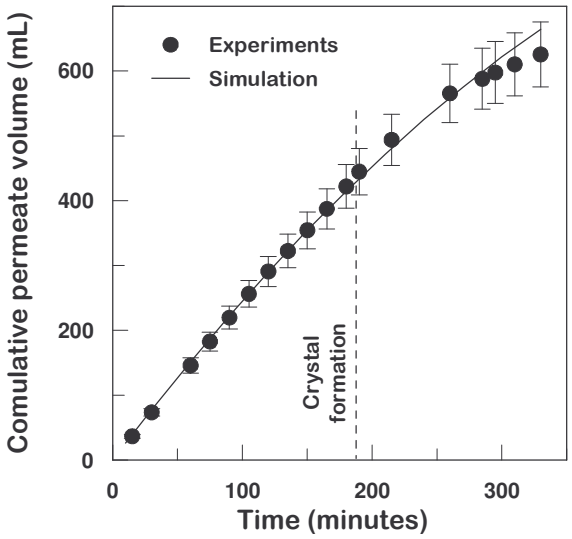

Figure 4.9 Permeate volume versus time

4.6.3 Test run using an initial feed concentration of 9 times of NF retentate

A higher feed flow rate was used in this experimental test and it was conducted in a batch mode as well. The objective of this run was to improve the removal of crystals from the membrane surface by increasing the feed flow rate. The operating conditions are summarized in Table 4.5.

Table 4.5 Operating conditions using 9 times of NF retentate

Operating condition	Value
Feed flow rate (L)	250
Permeate flow rate (L)	100
Feed Inlet temperature (T_f) ^oC	40
Permeate outlet temperature (T_p) ^oC	21
Initial feed volume (L)	3
Initial feed concentration (g/L)	301.6
Total run time (min)	300

Again, the transmembrane flux of the MDC declined gradually with time due to the decrease in the vapor pressure difference as a consequent of the

increase in the solution concentration as shown in Figure 4.10. In this run, however, the flux decline after crystallization was lower than the previous runs because the crystal deposition on the membrane surface was lower due to the higher feed flow rate used. Nevertheless, the introduction of the crystals into the recirculating feed was not possible to be stopped completely.

The concentration polarization coefficient (*CPC*) was calculated and found to be decreasing gradually during the batch run due to the decrease in the transmembrane flux Figure 4.10.

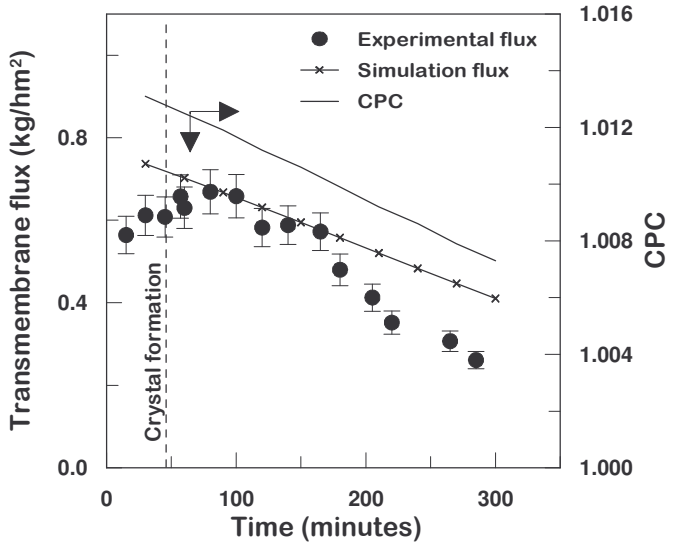

Figure 4.10 MDC transmembrane flux and CPC versus time

The crystallization of NaCl was started after run time of around 45 minutes when the saturation limit (305.2 g/L) of the solution was exceeded. The total permeate volume extracted from the feed at the saturation limit was 91 mL and the total permeate volume at the end of the test was 505 mL as shown in Figure 4.11.

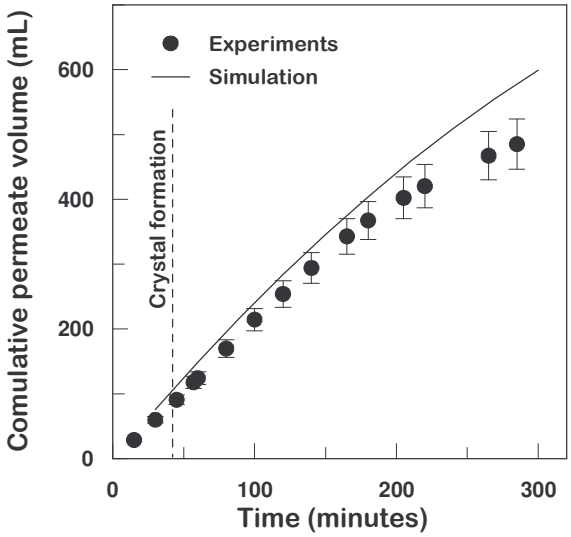

Figure 4.11 Permeate volume versus time

4.6.4 Crystal size distribution (CSD)

Samples were taken from the crystallization tank solution at times of 60, 120, 180 and 240 minutes in order to calculate the crystal size distribution *CSD*. The results are presented in Figure 4.12 (a-d).

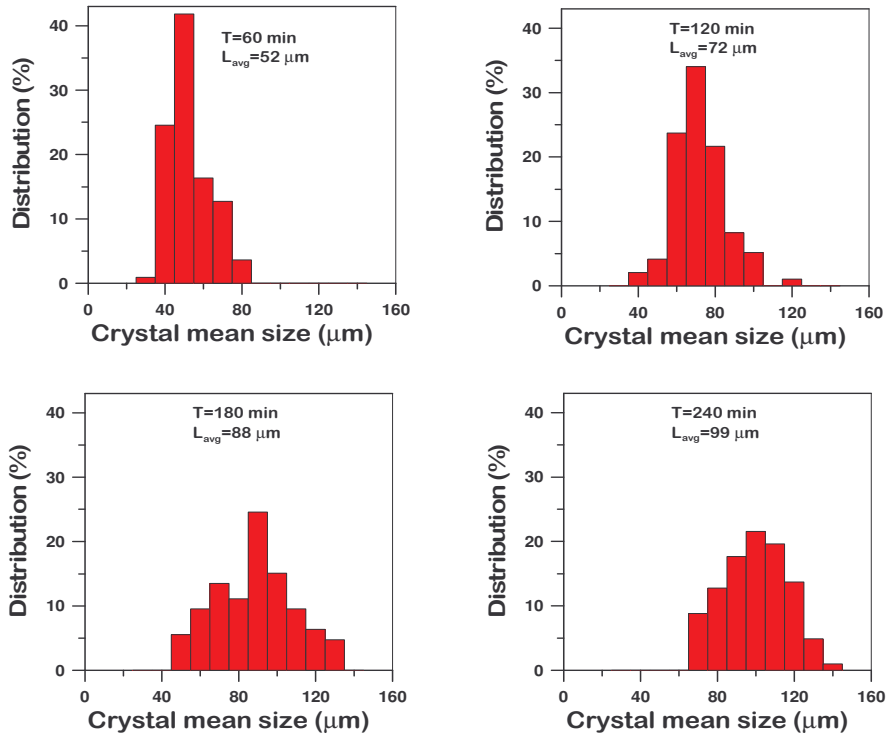

Figure 4.12 Crystal size distribution at different time

The CSD results showed that, after the detection of the first solid crystals, the mean crystal size was increasing with elapsed time due to crystal growth process. The mean crystal length was 52.3, 72.4, 87.7 and 99.0 μm at elapsed time of 60, 120, 180 and 240 minutes, respectively. The values of the coefficient of variation (*CV*) varied from 16.8 to 22.8%.

The images obtained using the optical microscope showed that the crystals have cubic block-like geometry which corresponded with the characteristics of the NaCl crystals as shown in Figure 4.13.

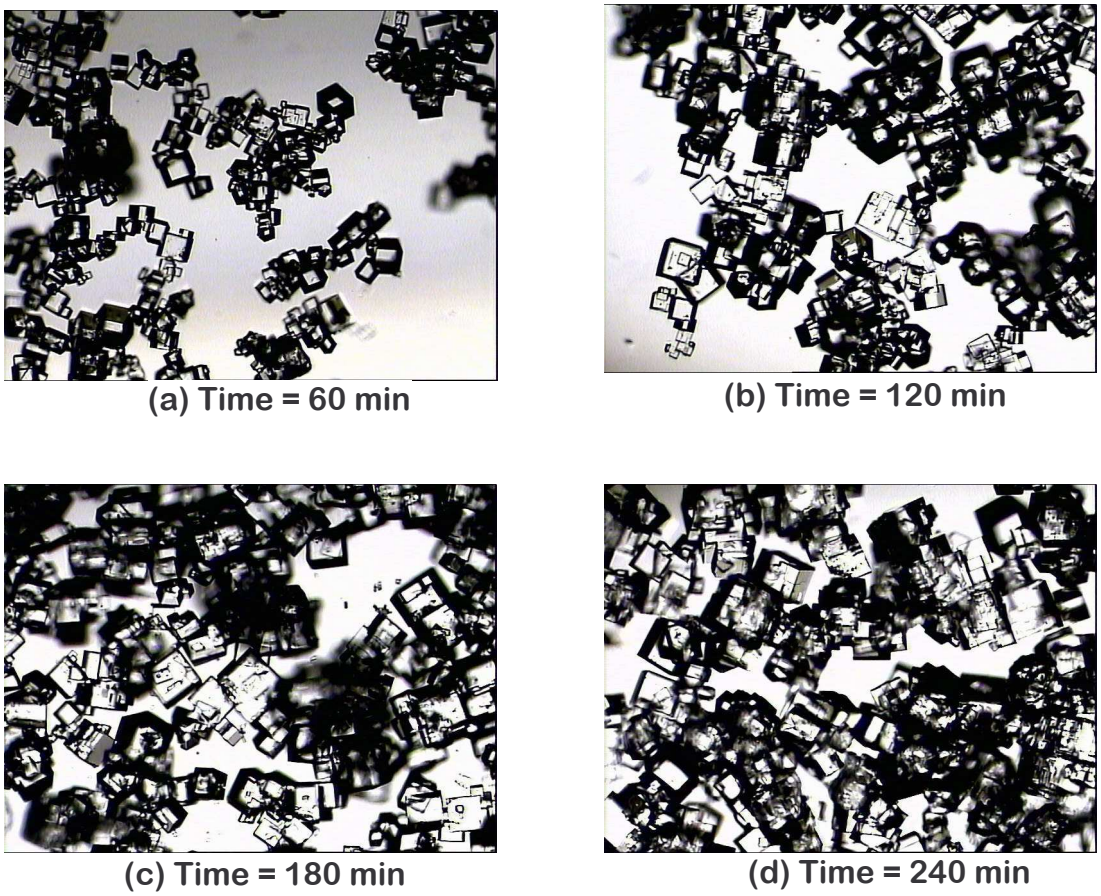

Figure 4.13 Morphology of NaCl crystals (magnification X10)

4.7 Conclusions

Crystallization is an important separation process in the production of commodity and specialty chemicals. Membrane crystallizers are able to produce crystals with good structural properties and global quality. This is due the fact that in membrane crystallizers, the solvent evaporation is occurring inside the membrane module below the supersaturation conditions and the crystallization stage is performed in a separate tank on the retentate line which is operating in the metastable regime of supersaturation.

The experimental tests showed that it was possible to obtain NaCl crystals from the NF retentate at a good quality and narrow CSD.

The effects of the concentration polarization in the transmembrane flux were very limited, however, there was an expected flux decline after the formation of the crystals in the system. This was due to the deposition of the salts crystals on the membrane surface which caused pore blockage and hence flux drop. Therefore, this problem must be avoided in designing for the semi-pilot MD/MDC plant.

4.8 The crystallizer design improvements

The problem of membrane pore blockage was due to the fact that during operation some crystals were sucked from the crystallization tank and circulated with the feed solution. This caused the accumulation and deposition of crystals along the membrane surface. So, in order to reduce this problem, some improvements in the design of the crystallizer as well as in the fluid dynamics of the system must be established. The crystallizer was redesigned and another opening was introduced near its bottom so that this opening can be used for removing the crystals from the crystallization tank. In addition, a filter will be installed in the suction side of the feed solution in order to stop crystals before going into the membrane module. In terms of fluid dynamics, higher flow rates

as well as higher operating temperatures will be applied in order to avoid any disposition of crystals on the membrane surface.

REFERENCES

[1] S. Chimie, G. Fevotte, C. Hoff, J.P. Klein, Model identification of batch cooling crystallizations through calorimetry and image analysis Chemical Engineering Science 52(7) (1997) 1125.
[2] E. Drioli E, A. Criscuoli A, E. Curcio, Membrane Contactors: Fundamentals, Applications and Potentialities. Elsevier, Amsterdam (2006).
[3] A. Gerstauer, S. Motz, A. Mitrovic, E.D. Gilles, Development, analysis and validation of population models for continuous and batch crystallizers Chemical Engineering Science 57 (2002) 4311.
[4] E.D. Hollander, J.J. Derksen, O.S.L. Bruinsma, V. Akker, and G.M.v. Rosmalen, A numerical study on the coupling of hydrodynamics and orthokinetic agglomeration Chemical Engineering Science 56 (2001) 3531.
[5] W.I. Genck, Guidelines for crystallizer selection and operation. Chemical Engineering and Processing 40(10) (2004) 2679.
[6] H.J.M Kramer, P.J. Jansen, Tools for design and control of industrial crystallizers. Proceeding of the 15th Symposium on Industrial Crystallization, Sorrento Italy (2002).
[7] R. Mohan, A.S. Myerson, Growth kinetics: a thermodynamic approach, Chemical Engineering Science 57 (2002) 4277.
[8] J. Dirksen, T.A. Ring, Fundamentals of crystallization kinetic on particle size distribution and morphology. Chemical Engineering Science 46 (1991) 2379.
[9] J. Garside, A. Mersmann, J. Nyvlt, Measurements of crystal growth and nucleation rates (2002).
[10] K.D. Samant, L. O'Young, Understanding crystallization and crystallizers, Chemical Engineering Progress 102(10) (2006) 28.
[11] A.S. Myerson, R. Ginde, Handbook of Industrial Crystallization, Boston: Butterworth-Heinemann 2nd edition (1993).
[12] J. Ulrich, C. Strege, Some aspects of the importance of metastable zone width and nucleation in industrial crystallizers Journal of Crystal Growth 237 (2002) 2130.
[13] B.S Choi, T.A. Ring, Evolution of crystal size distributions in a CMSMPR—the effect of temperature, flow rate, and mixing speed with time, Fluid Phase Equilibria 228 (2005) 99.
[14] W.J.P. Enckevort, Contact nucleation of steps: theory and Monte Carlo simulation. Journal of Crystal Growth 259 (2003) 190.
[15] W.K. Burton, N. Cabrera, F.C. Frank, The Growth of Crystals and the Equilibrium Structure of their Surfaces. Philosophical Transactions of the Royal Society of London. Series A, Mathematical and Physical Sciences 243(866) London (1951).

[16] E. Curcio, G. Di Profio, E. Drioli, Recovery of fumaric acid by membrane crystallization in the production of L-malic acid, Separation and Purification Technology 33 (2003) 63.
[17] E. Curcio, Membrane Crystallizers. University of Calabria: Ph.D. Thesis in Chemical Engineering and Materials Department. Italy (2004).
[18] K.W. Lawson, D.R. Lloyd, Membrane distillation, Journal of Membrane Science124 (1997) 1.
[19] C.M. Tun, A.G. Fane, J.T. Matheickal, and R. Sheikholeslami, Membrane distillation crystallization of concentrated salts - flux and crystal formation, Journal of Membrane Science 257 (2005) 144.
[20] J. Phattaranawik, R. Jiraratananon and A.G. Fane, Heat transport and membrane distillation coefficients in direct contact membrane distillation, Journal of Membrane Science 212 (2003) 177.
[21] M. Gryta, M. Tomaszewska, Heat transport in the membrane distillation process. Journal of Membrane Science144 (1998) 211.

CHAPTER 5
ECONOMIC ASPECTS, EXERGY ANALYSIS AND SENSITIVITY STUDY

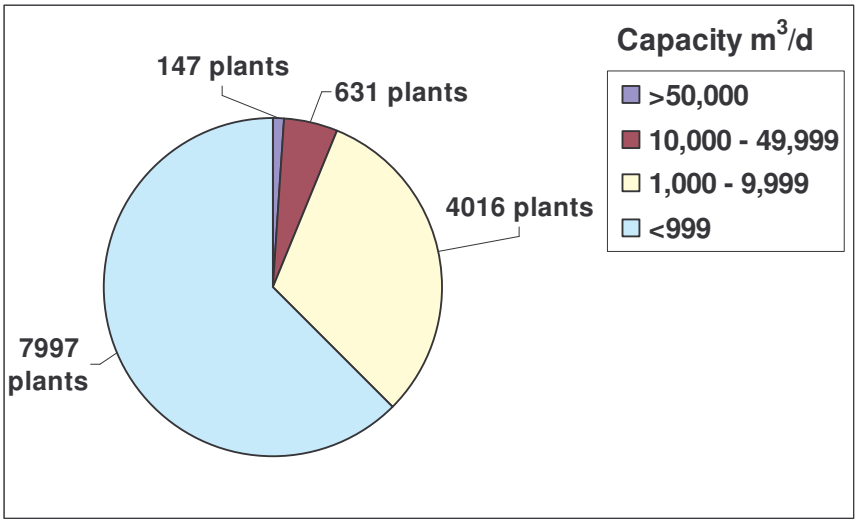

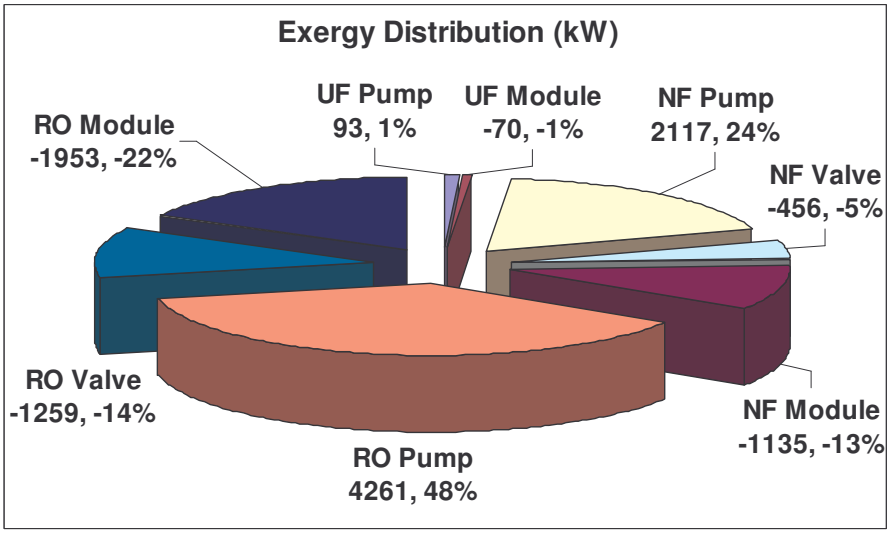

SUMMARY
This chapter contains the exergy analysis to evaluate the performance of several configurations of the integrated membrane system. In addition, economical aspects have been considered in order to estimate the total water cost for each configuration. Finally, a sensitivity study was performed in order to identify the most sensitive parameters in the total water cost of desalination.

5.1 Introduction

Water shortage is now becoming a serious problem due to the rapid increase in population and industrial growth with limited water. This problem is more obvoius in arid and semi-arid countries like the Middle East countries. However, in the last years water shortage is becoming a growing issue even in countries that are not typically considered to have problems with water scarcity but in which the continuous growth in population, in the standard of life, in tourist infrastructure and industrial development have increased water consumption and hence increased the stress on water supplies as shown in Figure 5.1 [1].

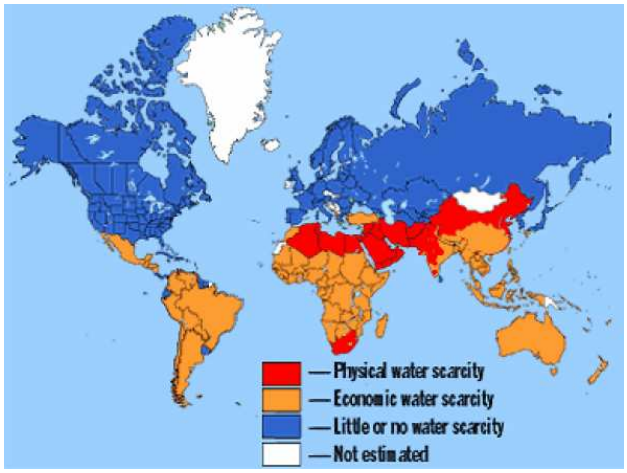

Figure 5.1 Water situations around the world [1]

Considering that 97.5% of the overall water in Earth is seawater, it appears that seawater desalination is the inevitable rout to follow especially in these countries where the water problem is already dramatic. Desalination is no longer a marginal water resource for municipal and industrial use as in some countries

like as Qatar, Saudi Arabia and Kuwait. Two-third of the world's desalination plants are located in Gulf Cooperation Council (GCC) countries: Saudi Arabia, Kuwait, Qatar, Bahrain, UAE, and Oman [2, 3]. Seawater desalination processes have been developed to commercial capacity since more than thirty years ago [4]. Among different technologies available, multi-stage flash (MSF) distillation and reverse osmosis (RO) dominate the existing plants as shown in Figure 5.2. Other technologies include multi-effect distillation (MED), vapor compression (VC), and electrodialysis (ED). The two most widely applied processes are MSF and RO producing 33% and 50% of the total global output, respectively [5].

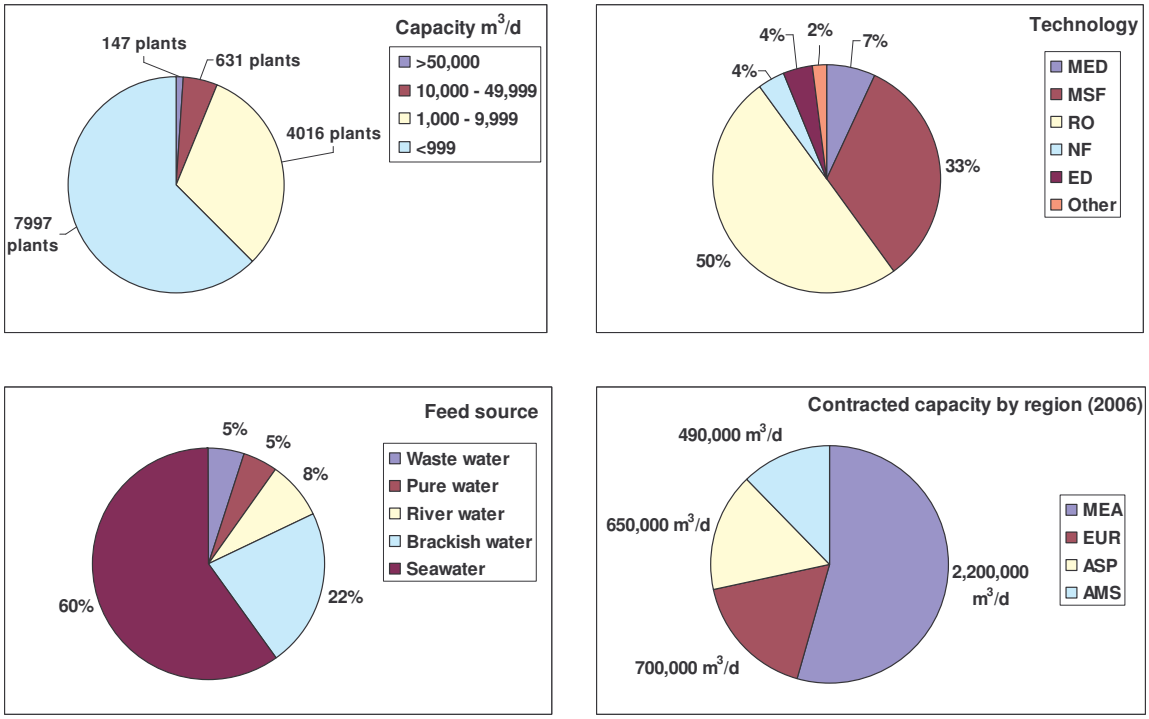

Figure 5.2 Desalination plants sorted by capacity, technology, feed source and regions [5]

The GCC plants are dominated by thermal processes (Multi Stage Flash, MSF) and the rest of the world by membrane processes (Reverses Osmosis, RO). The main reasons for the domination of the MSF process are due to low fuel cost and difficulties of proper treatment of high salinity seawater using RO technologies [6]. Recently, however, membrane-based desalination techniques

(especially RO) have grew to be the dominant technology for water treatment; and both brackish and seawater desalination. This was as a result of the rapid improvements in membrane-based processes performance in terms of efficiency, chemical stability, high rejection and utilization of energy recovery devices. Today, more than 15,000 desalination facilities (thermal and membrane based) operating in more than 120 countries around the world with a global capacity around 40 million cubic meter per day [5].

Membrane processes, mainly RO, are the fastest-growing technology among the current processes [7]. The RO membrane technique is considered the most promising for brackish and seawater desalination. Advantages of the membrane processes are: (i) low energy consumption, (ii) moderate capital and operation costs, (iii) easier operation and control, (iv) compact and modular, (v) faster delivery time of plant, (vi) possibilities of combining different membrane operations in one integrated system. In addition, the pressure-driven membrane operations (UF, NF and RO) can be integrated with the innovative units of membrane contactors such as Gas/Liquid Membrane contactors and Membrane Distillation/Crystallization technologies.

5.2 Technology choice and cost influencing factors

The cost of desalination, particularly for membrane technology, has fallen considerably over the last few decades. Meanwhile, the cost of obtaining and treating water from conventional sources has tended to increase because of the increased levels of treatment being required in various countries to meet more stringent water quality standards. This rise in cost for conventionally treated water also is the result of an increased demand for water, leading to the need to develop more expensive conventional supplies, since the readily obtainable water sources have already been used. In any country or region, the economics of using desalination is not just the number of dollars per cubic meter, but the cost

of desalted water versus the other alternatives. In many water-short areas, the cost of alternative sources of water is already very high and often above the cost of desalination [8].

In general, the costs for membrane plants tend to be lower than for thermal plants of a similar capacity. Thermal processes are practical for higher capacities, and particularly where a low energy cost and/or high quality waste heat source (i.e. latent heat from an industrial process, such as an electricity or manufacturing plant) is readily available [9]. The technical operational boundaries for several desalination technologies are summarised in Table 5.1.

Table 5.1 The technical operational boundaries of different desalination processes [9]

Process		Feed TDS (mg/L)	Product TDS (mg/L)	Recovery or performance ratio	Energy consumption	Minimum production m^3/day	Required space
Thermal process	MSF	30,000 – 500,000	<10	PR 10 – 20	Thermal 258 MJ/m^3 + Electricity 3.6 kWh/m^3	120	Very large
	MED	30,000 – 500,000	<10	PR 40 – 65	Thermal 145 MJ/m^3 + Electricity 2.3 kWh/m^3	120	Large
Membrane based	EDR	3,000 – 12,000	<10	Recovery >90	0.6 – 4.2 kWh/m^3	90	Small
	RO	5,000 – 50,000	<500	Recovery 30 – 60	1.0 – 6.5 kWh/m^3	0.5	Small

The choice of technology as well as the capital and operating costs for desalination plants may be influenced by many variables such as [3, 4, 5, 9]:

- *The location of the plant*. If the plant is to be remotely located, the technology should be tough and as maintenance free as possible. The costs of transporting water to and from the plant, the costs of power transmission and infrastructure will be added to the overall capital costs.

The further away the feed water is from the desalination plant, the higher the construction and operating costs associated with the plant.

- *The availability and cost of energy*. The form of energy available, the associated cost and the environmental constraints related to the energy source, are playing a major role in the desalination technology selection. There are mainly two types of energy sources, namely, electrical and thermal. In membrane-based desalination the primary energy input is the electrical energy whereas the thermal energy is the primary energy input in thermal desalination and the electrical energy is used to drive recirculation and transfer pumps only. Desalination water costs are sensitive to changes in energy prices; therefore cheaper energy sources are very important.
- *The quality and quantity of the feed* will heavily state the desalination technology to be used. They depend on the type of the feed source i.e. seawater or brackish water; and they ordain the type of the pretreatment to be installed. The key water quality parameters involved in the design of the pretreatment can include salinity (TDS), turbidity, organic content, pH and concentration of scale forming salts and fouling species.
- *The capacity of the plant*. In general, the unit cost of desalted water is inversely proportional to the plant size (economy of scale) i.e. if all other factors remain the same, the cost of product water would be lower for bigger plants.
- *Pretreatment requirements*. They may be more or less complex and, therefore, more or less costly, depending on feed water quality and the type of technology which is going to be used. The best possible feed water quality must be insured by choosing the best possible abstraction methods and location for installing the desalination plant. However, there are some cases in which this situation is not possible, requiring more systems that are more sophisticated, which, logically, results in an increase of the cost

of the mentioned pretreatment. In general, membrane-based technologies need more sophisticated pretreatment than the thermal ones.

- *Post treatment requirements* including chlorination, UV disinfection and pH stabilization processes. In some cases of membrane-based process, additional stage of post treatment membrane unit might also need to be considered, depending on the final product water end use requirements and drinking water standards.
- *The costs for environmental protection*. Brine (concentrate) disposal from a desalination plant represents its most relevant environmental drawback and adds to the freshwater cost, as it must be treated in many cases to avoid all potential environmental risks. The brine is commonly discharged into the sea for coastal plants and for inland brine, disposal may be in the form of a stream, salt ponds or injected underground. However, the new developments in desalination industry for higher recovery rates as well as the combination of different processes in a single integrated system have a great potential in reducing the brine disposal problem as they approach the zero-liquid-discharge concept.
- *Storage and distribution costs*. These costs are add to the capital costs, as pumping is required for delivering the freshwater to storage or consumers through the distribution networks. Seawater desalination plants are best to be build as close as possible to the point where the product water is going to be consumed in order to minimize the transfer infrastructure and, therefore, reduce the required investment costs. However, this option is not always possible.
- *Plant life and amortization* affect the capital costs

The essential elements for the economic evaluation of the desalination plants may be categorized as direct capital costs, indirect capital costs and annual operating costs [10, 11].

The direct capital costs are the costs associated for purchasing the major items for plant construction and they include:

- Land
- Building and construction
- Process Equipment
- Auxiliary equipment

The indirect capital costs are normally expressed as a percentage of the total direct capital costs and they include:

- Insurance
- Freight
- Construction overhead
- Owner's costs
- Contingency costs

The annual operating costs are the costs incurred after plant commissioning and during actual operation and they include:

- Energy cost
- Labor
- Membrane replacement costs (for membrane-based process)
- Maintenance and spares
- Chemicals
- Amortization

5.3 Energy and Exergy analysis

Exergy is defined, from thermodynamic point of view, as the maximum amount of work which can be produced by a system or a flow of matter or energy as it comes to equilibrium with a reference environment. Unlike energy, exergy is not subject to a conservation law (except for ideal, or reversible, processes). Instead, exergy is consumed or destroyed, due to irreversibilities in any real process. The exergy consumption during a process is proportional to the entropy created due to irreversibilities associated with the process [12].

Practically, exergy is defined as the availability to perform useful work from a given energy source, and can also be expressed in mathematical terms as the product of energy (or enthalpy) of the primary energy source and the ideal thermal (or power) conversion process. Exergy is that part of energy that is convertible into all other forms of energy. Exergy represents the useful part of energy for a system in its environment, i.e., the maximum quantity of work that the system can execute in its environment [13, 14].

Exergy analysis is a method that uses the conservation of mass and conservation of energy principles together with the second law of thermodynamics for the analysis, design and improvement of energy and other systems. The exergy method is a useful tool for furthering the goal of more efficient energy-resource use, for it enables the locations, types, and true magnitudes of wastes and losses to be determined. In general, more meaningful efficiencies are evaluated with exergy analysis rather than energy analysis, since exergy efficiencies are always a measure of the approach to the ideal. Therefore, exergy analysis can reveal whether or not and by how much it is possible to design more efficient energy systems by reducing the inefficiencies in existing systems. In addition, the exergy analysis provides valuable of information about the influence of the individual efficiency of equipment on the efficiency of the global plant and the exergy cost of the product (exergy used to generate it).

Accordingly, Exergy analysis is considered as a key component in obtaining sustainable development for a process [13].

The use of exergy analysis in actual desalination processes from a thermodynamic point of view is of growing importance to identify the sites of greatest losses and to improve the performance of the processes. In many engineering decisions, other facts such as the impact on the environment and society must be considered when analyzing the processes. This involves a comparison of exergy input and exergy destruction along various desalination processes [15].

5.3.1 Exergy calculations

The exergy of a flow stream for a system in which the governing parameters are the temperature, the pressure and the composition, can be written as [16, 17]:

$$Ex = Ex^T + Ex^P + Ex^C \quad (1)$$

with

$$Ex^T = \dot{m} c_p \left[(T - T_o) - T_o \ln\left(\frac{T}{T_o}\right) \right] \Rightarrow \text{Temperature Exergy} \quad (2)$$

$$Ex^P = \dot{m}\left(\frac{P - P_o}{\rho}\right) \Rightarrow \text{Pressure Exergy} \quad (3)$$

$$Ex^C = -\dot{m}\left(N_{solv} R T_o \ln x_{solv}\right) \Rightarrow \text{Concentration Exergy} \quad (4)$$

and

$$N_{solv} = \frac{1000 - \sum_i \frac{C_i}{\rho}}{MW_{solv}} \Rightarrow \text{moles of solvent in unit weight of soultion} \quad (5)$$

$$x_{solv} = \frac{N_{solv}}{\left[N_{solv} + \sum_i \left(\frac{\beta_i C_i}{\rho MW_i} \right) \right]} \Rightarrow \text{molar fraction of solvent} \quad (6)$$

The total irreversible entropy production (R_sT_o) is obtained by applying the energy balance according to the second low of thermodynamics as follows [18]:

$$R_sT_o = Ex_{electrical} + Ex_{thermal} - \Delta Ex \quad (7)$$

with

$$\Delta Ex = \sum Ex_{in} - \sum Ex_{out} \quad (8)$$

where $Ex_{electrical}$ is the electrical exergy supplied to the plant and $Ex_{thermal}$ is the thermal exergy supplied to the plant and defined as:

$$Ex_{electrical} = W_{electrical} = \dot{m}\frac{1000\,\Delta P}{\eta},\ P\ is\ pressure\ in\ MPa\ and\ \eta\ is\ pump\ efficiency \quad (9)$$

$$E_{thermal} = q\left(1 - \frac{T_o}{T}\right)\ ,\ q\ is\ the\ heat\ energy \quad (10)$$

The exergy efficiency ψ is used as a criterion of performance to evaluate the exergy efficiency of a process and to compare with conventional ones. It is defined as the ratio of the exergy output over the exergy input:

$$\psi = \frac{\sum Ex_{out}}{\sum Ex_{in}} \quad (11)$$

5.4 Results and discussion

The energy and exergy calculations as well as economical investigations were performed for evaluating desalination plants. This study covered the pressure-driven membrane operations, the membrane contactors technology as well as the combination of the two technologies.

5.4.1 Energy and exergy evaluation

The plant capacity was assumed always as 1000 m^3/h in all cases. The feed seawater was considered as open surface seawater of the Omani Gulf with

total dissolved salts (TDS) of 42,052 mg/L. The seawater composition is shown in Table 5.2 [2].

Table 5.2 The Omani Gulf seawater compositions [2]

Ion	Concentration (mg/L)
Ca^{++}	499
Mg^{++}	1,554
Na^{+}	12,902
K^{+}	468
CO_3^{--}	0.0
HCO_3^{-}	174
$SO4^{--}$	3,241
Cl^{-}	23,214
TDS	42,052

The energy and exergy calculations were carried out using the equations reported earlier (equations 1-11). The reference state was considered as pure water at temperature of 30°C and atmospheric pressure 1 bar.

I) Pressure-driven membrane operations

a) UF-RO

The ultrafiltartion (UF) membranes are used as a pretreatment for the reverses osmosis (RO) desalination plant instead of the conventional pretreatment methods like sand and multi-media filtration. A schematic diagram of such plant is presented in Figure 5.3.

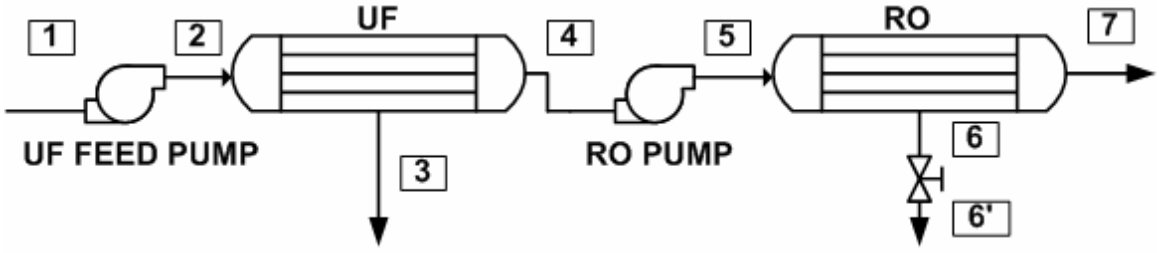

Figure 5.3 Pressure-driven membrane operations (UF-RO)

The overall water recovery of the plant in the case was 47.5% assuming 95% and 50% water recovery rates of the UF and the RO, respectively. The

composition and the exergy variations were calculated for each stream and the results were presented in Table 5.3 and Figure 5.4.

Table 5.3 The composition and the exergy variations calculated for each stream in the pressure-driven membrane operations (UF-RO) *

Stream No.	1	2	3	4	5	6	6'	7
Ca (g/L)	0.499	0.499	0.499	0.499	0.499	0.997	0.997	0.002
Mg (g/L)	1.554	1.554	1.554	1.554	1.554	3.102	3.102	0.006
Na (g/L)	12.902	12.902	12.902	12.902	12.902	25.662	25.662	0.142
K (g/L)	0.468	0.468	0.468	0.468	0.468	0.927	0.927	0.009
CO_3 (g/L)	0.000	0.000	0.000	0.000	0.000	0.000	0.000	0.000
HCO_3 (g/L)	0.174	0.174	0.174	0.174	0.174	0.345	0.345	0.003
SO_4 (g/L)	3.241	3.241	3.241	3.241	3.241	6.469	6.469	0.013
Cl (g/L)	23.214	23.214	23.214	23.214	23.214	46.184	46.184	0.244
Total concentration (g/l)	42.052	42.052	42.052	42.052	42.052	83.686	83.686	0.418
Flow rate (m^3/h)	2,105	2,105	105	2,000	2,000	1,000	1,000	1,000
Pressure (MPa)	0.10	0.20	0.10	0.10	7.0	6.9	0.1	0.1
Temperature (K)	303.0	303.0	303.0	303.0	303.0	303.0	303.0	303.0
Ex^C (kW)	1,949	1,949	97	1,851	1,851	1,818	1,818	10
Ex^P (kW)	0	58	0	0	3,833	1,889	0	0
Ex^T (kW)	0	0	0	0	0	0	0	0
Ex Total (kW)	1,949	2,007	97	1,851	5,685	3,707	1,818	10

* UF recovery 95% and RO recovery 50%

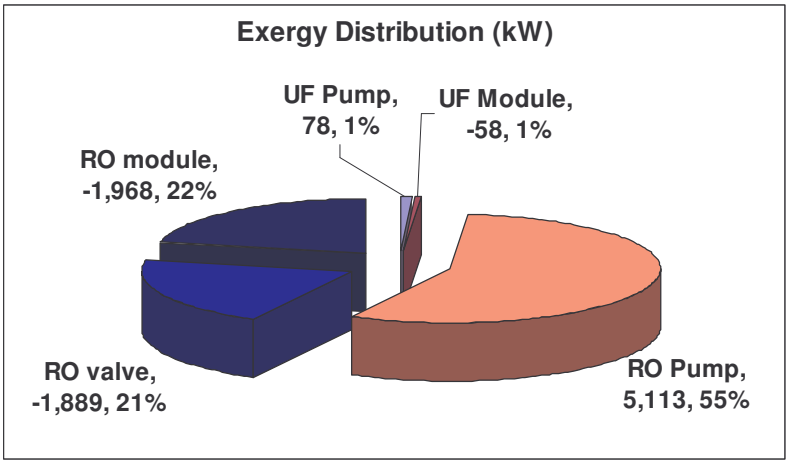

Figure 5.4 The exergy distribution in UF-RO plant without energy recovery system

The results showed that the variations in exergy were due to the changes of pressure and concentration among the streams. The process was carried out at reference temperature and therefore the exergy associated with temperature change was always zero. The main exergy input was related to the electrical power supply input to the RO high pressure pump which contributed for 55% the total exergy in the system. The main exergy destruction was through the RO modules due to the separation process. There was also significant exergy destruction of 1,889 kW (21% of the total exergy) through the RO valve. It was not possible to recover the exergy destructions associated with RO modules since they were used for the separation process. However, some exergy can be recovered by replacing the RO valve with an energy recovery device. In other words, it was possible to use the high pressure of the rejected brine stream to pressurize the feed water by using energy recovery devices such as Pelton turbines and pressure exchanger devices. This study will focus on the utilization of pressure exchanger devices as energy recovery system. The efficiency of the energy recovery system was assumed as 95%. The scheme of the energy recovery system is shown in Figure 5.5.

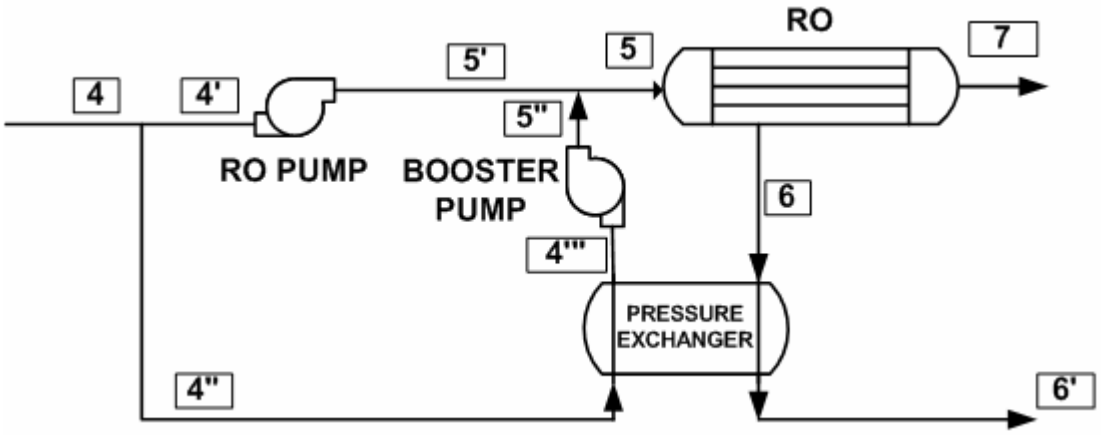

Figure 5.5 The energy recovery device in UF-RO plant

The exeryg distribution after installing the recovery system in the desalination process using the pressure-driven membrane operation (UF-NF-RO) is shown in Table 5.4 and Figure 5.6.

The results showed that it was possible to recover 31% of the total exergy input used in the plant by replacing the RO valve with the energy recovery system. Therefore, it is recommended to use energy recovery systems to improve the efficiency of the pressure-driven membrane operations.

Table 5.4 The composition and the exergy variations calculated for each stream in pressure-driven membrane operations (UF-RO) with energy recovery*

Stream No.	4	4'	4''	4'''	5''	5'	5	6	6'	7
Ca (g/L)	0.499	0.499	0.499	0.499	0.499	0.499	0.499	0.997	0.997	0.002
Mg (g/L)	1.554	1.554	1.554	1.554	1.554	1.554	1.554	3.102	3.102	0.006
Na (g/L)	12.902	12.902	12.902	12.902	12.902	12.902	12.902	25.662	25.662	0.142
K (g/L)	0.468	0.468	0.468	0.468	0.468	0.468	0.468	0.927	0.927	0.009
CO_3 (g/L)	0.000	0.000	0.000	0.000	0.000	0.000	0.000	0.000	0.000	0.000
HCO_3 (g/L)	0.174	0.174	0.174	0.174	0.174	0.174	0.174	0.345	0.345	0.003
SO_4 (g/L)	3.241	3.241	3.241	3.241	3.241	3.241	3.241	6.469	6.469	0.013
Cl (g/L)	23.214	23.214	23.214	23.214	23.214	23.214	23.214	46.184	46.184	0.244
Total concentration (g/l)	42.052	42.052	42.052	42.052	42.052	42.052	42.052	83.686	83.686	0.418
Flow rate (m^3/h)	2,000	1,000	1,000	1,000	1,000	1,000	2,000	1,000	1,000	1,000
Pressure (MPa)	0.10	0.10	0.10	6.2	7.0	7.0	7.0	6.9	0.1	0.1
Temperature (K)	303.0	303.0	303.0	303.0	303.0	303.0	303.0	303.0	303.0	303.0
Ex^C (kW)	1,851	926	926	926	926	926	1,851	1,818	1,818	10
Ex^P (kW)	0	0	0	1,697	1,917	1,917	3,833	1,889	0	0
Ex^T (kW)	0	0	0	0	0	0	0	0	0	0
Ex Total (kW)	1,851	926	926	2,623	2,842	2,842	5,685	3,707	1,818	10

* UF recovery 95% and RO recovery 50%

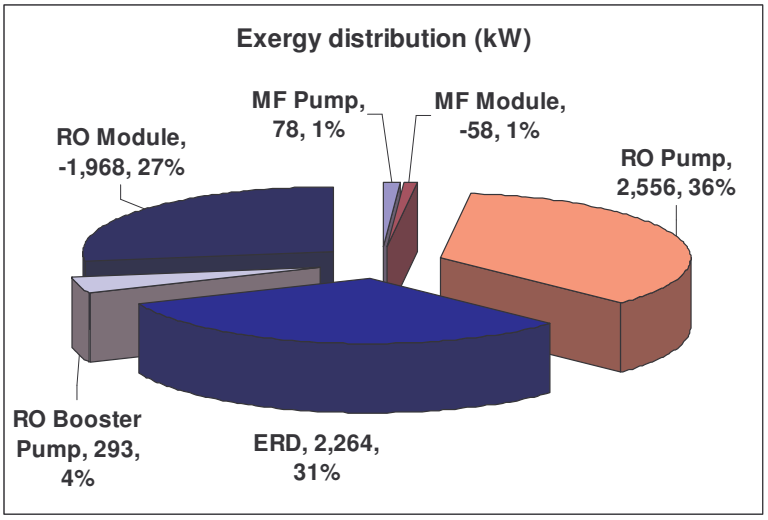

Figure 5.6 The exergy distribution in UF-RO plant with energy recovery system

b) UF-NF-RO

In this case a nanofiltration (NF) unit was installed between the UF and the RO as shown in Figure 5.7.

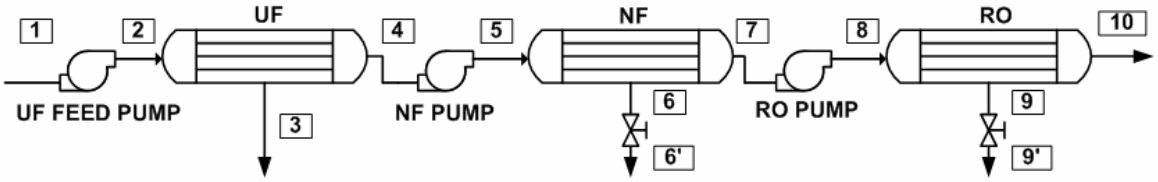

Figure 5.7 Pressure-driven membrane operations (UF-NF-RO)

The water recoveries were 95%, 70% and 60% for the UF, NF and RO, respectively. The overall plant recovery was 39.9%. The three terms contributing to the total exergy ($Ex^C + Ex^P + Ex^T$) were calculated for each stream in the plant and the results are presented in Table 5.6 and Figure 5.7.

Table 5.5 The composition and the exergy variations calculated for each stream in the pressure-driven membrane operations (UF-NF-RO) *

Stream No.	1	2	3	4	5	6	6'	7	8	9	9'	10
Ca (g/L)	0.499	0.499	0.499	0.499	0.499	1.528	1.528	0.058	0.058	0.144	0.144	0.000
Mg (g/L)	1.554	1.554	1.554	1.554	1.554	4.780	4.780	0.171	0.171	0.427	0.427	0.001
Na (g/L)	12.902	12.902	12.902	12.902	12.902	19.525	19.525	10.064	10.064	24.993	24.993	0.111
K (g/L)	0.468	0.468	0.468	0.468	0.468	0.697	0.697	0.370	0.370	0.913	0.913	0.007
CO_3 (g/L)	0.000	0.000	0.000	0.000	0.000	0.000	0.000	0.000	0.000	0.000	0.000	0.000
HCO_3 (g/L)	0.174	0.174	0.174	0.174	0.174	0.426	0.426	0.066	0.066	0.164	0.164	0.001
SO_4 (g/L)	3.241	3.241	3.241	3.241	3.241	10.047	10.047	0.324	0.324	0.808	0.808	0.001
Cl (g/L)	23.214	23.214	23.214	23.214	23.214	30.147	30.147	20.243	20.243	50.288	50.288	0.213
Total concentration (g/l)	42.052	42.052	42.052	42.052	42.052	67.151	67.151	31.295	31.295	77.737	77.737	0.334
Flow rate (m^3/h)	2,506	2,506	125	2,380	2,380	714	714	1,667	1,667	667	667	1,000
Pressure (MPa)	0.10	0.20	0.10	0.10	2.50	2.40	0.10	0.10	7.00	6.90	0.10	0.10
Temperature (K)	303.0	303.0	303.0	303.0	303.0	303.0	303.0	303.0	303.0	303.0	303.0	303.0
Ex^C (kW)	2,320	2,320	116	2,204	2,204	1,010	1,010	1,190	1,190	1,165	1,165	8
Ex^P (kW)	0	70	0	0	1,587	456	0	0	3,194	1,259	0	0
Ex^T (kW)	0	0	0	0	0	0	0	0	0	0	0	0
Ex Total (kW)	2,320	2,390	116	2,204	3,791	1,467	1,010	1,190	4,385	2,424	1,165	8

* UF recovery 95%, NF recovery 70% and RO recovery 60%

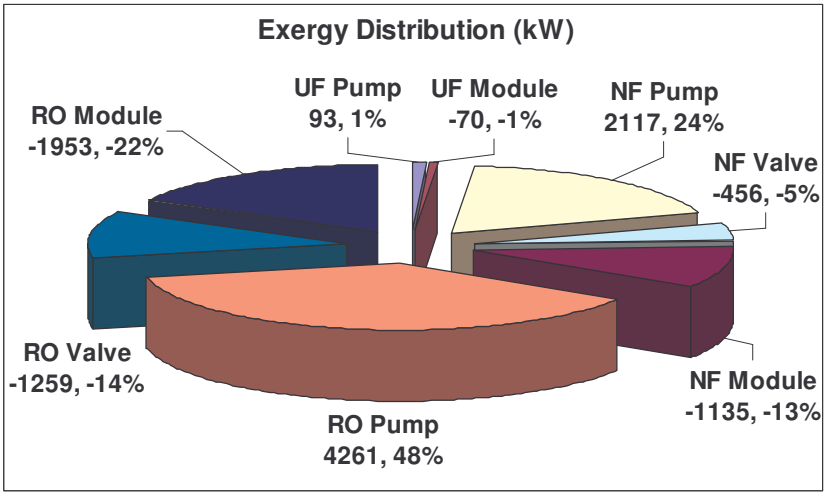

Figure 5.8 The exergy distribution in UF-NF-RO plant without energy recovery system

The main exergy inputs were associated with the electrical power supply input to the RO and the NF pumps which contributed for 48% and 24% of the total exergy of the system, respectively. The main exergy destruction was through the NF and RO modules due to the separation process. The exergy destruction through the RO valve was 1,259 kW (14% of the total exergy). Therefore, when replacing this valve with an energy recovery system using pressure exchanger (Figure 5.9), it would be possible to recover exergy of 1,886 kW (27% of the total exergy) as shown in Table 5.6 and Figure 5.10.

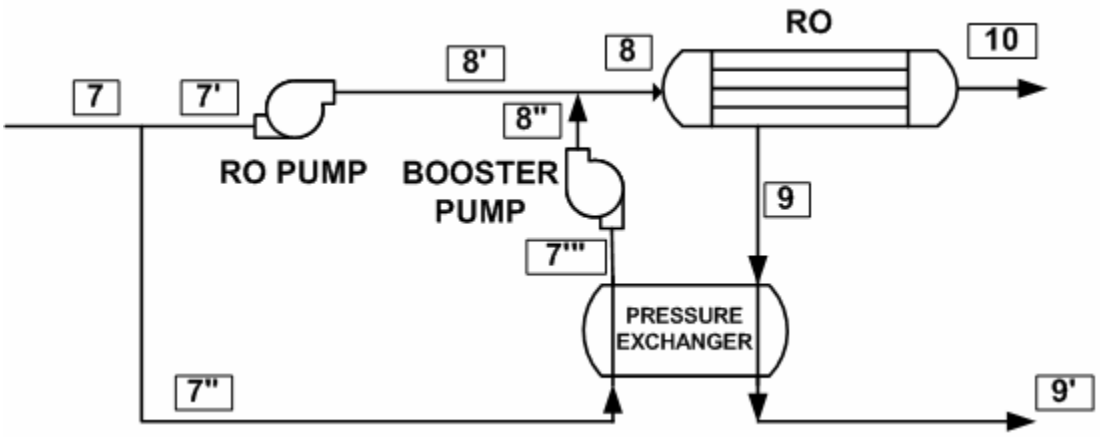

Figure 5.9 The energy recovery device in UF-NF-RO plant

Table 5.6 The composition and the exergy variations calculated for each stream in pressure-driven membrane operations (UF-NF-RO) with energy recovery *

Stream No.	7	7'	7''	7'''	8''	8'	8	9	9'	10
Ca (g/L)	0.058	0.058	0.058	0.058	0.058	0.058	0.058	0.144	0.144	0.000
Mg (g/L)	0.171	0.171	0.171	0.171	0.171	0.171	0.171	0.427	0.427	0.001
Na (g/L)	10.064	10.064	10.064	10.064	10.064	10.064	10.064	24.993	24.993	0.111
K (g/L)	0.370	0.370	0.370	0.370	0.370	0.370	0.370	0.913	0.913	0.007
CO_3 (g/L)	0.000	0.000	0.000	0.000	0.000	0.000	0.000	0.000	0.000	0.000
HCO_3 (g/L)	0.066	0.066	0.066	0.066	0.066	0.066	0.066	0.164	0.164	0.001
SO_4 (g/L)	0.324	0.324	0.324	0.324	0.324	0.324	0.324	0.808	0.808	0.001
Cl (g/L)	20.243	20.243	20.243	20.243	20.243	20.243	20.243	50.288	50.288	0.213
Total concentration (g/l)	31.295	31.295	31.295	31.295	31.295	31.295	31.295	77.737	77.737	0.334
Flow rate (m^3/h)	1,667	833	833	833	833	833	1,667	667	667	1,000
Pressure (MPa)	0.10	0.10	0.10	6.20	7.00	7.00	7.00	6.90	0.10	0.10
Temperature (K)	303.0	303.0	303.0	303.0	303.0	303.0	303.0	303.0	303.0	303.0
Ex^C (kW)	1,190	595	595	595	595	595	1,190	1,165	1,165	8
Ex^P (kW)	0	0	0	1,414	1,597	1,597	3,194	1,259	0	0
Ex^T (kW)	0	0	0	0	0	0	0	0	0	0
Ex Total (kW)	1,190	595	595	2,009	2,192	2,192	4,385	2,424	1,165	8

* UF recovery 95%, NF recovery 70% and RO recovery 60%

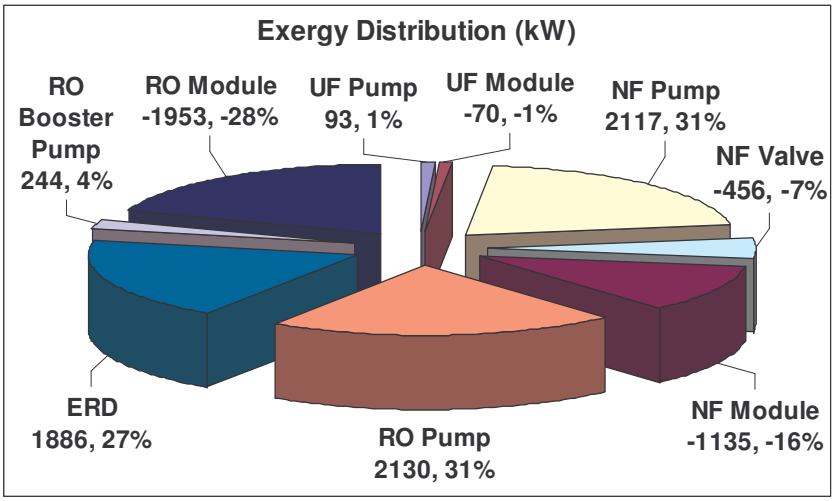

Figure 5.10 The exergy distribution in UF-NF-RO plant with energy recovery system

A summary of the exergy analysis for the desalination process using pressure-driven membrane operations with and without the energy recovery system is presented in Table 5.7. The net exergy change between the in and out streams was -24 kW and -21 kW in case of UF-RO and UF-NF-RO, respectively. The total exergy input ($Ex_{in} + Ex_{electrical} + Ex_{thermal}$) of the plant without energy recovery was higher than the one of the plant with heat recovery by 2,264 kW in case of the UF-RO plant and 1,887 kW in case of UF-NF-RO plant. The thermal exergy input ($Ex_{thermal}$) was zero in all cases since they were not involved with temperature changes.

Generally, the exergy efficiency of the plant without energy recovery was lower than the efficiency of the plant with energy recovery. It was 12.5% less in case of UF-RO plant and 7.2% in case of UF-NF-RO plant. Therefore, from an exergy point of view, it was shown that the introduction of the energy recovery system to the pressure-driven plants will improve the plant performance and will increase its efficiency.

Table 5.7 Summary of exergy analysis for the desalination process using pressure-driven membrane operations

	UF-RO		UF-NF-RO	
	Without ER	With ER	Without ER	With ER
Ex out (kW)	1,925	1,925	2,299	2,299
Ex in (kW)	1,949	1,949	2,320	2,320
delta Ex (kW)	-24	-24	-21	-21
Work input (kW)	5,191	2,927	6,471	4,584
Recovered work (kW)	0	2,264	0	1,886
Heat input (kW)	0	0	0	0
Exergy of work input (kW)	5,191	2,927	6,471	4,584
Exergy of heat input (kW)	0	0	0	0
Exergy of input streams (kW)	1,949	1,949	2,320	2,320
Total exergy input (Ex_inlet) (kW)	7,140	4,876	8,791	6,904
Exergy output (Ex_outlet) (kW)	1,925	1,925	2,299	2,299
Entropy production RsTo (kW)	5,215	2,951	6,492	4,605
Exergy efficiency (%)	26.96	39.48	26.15	33.30

II) Membrane Distillation/Crystallization (MDC) processes

Two case studies of membrane distillation (MD) plants were considered in order to obtain the optimal performance of these plants. In the first case, MD was operated without heat recovery as shown in Figure 5.11. In the second case, a heat recovery system with heat exchange efficiency of 0.8 was installed in order to use the heat from the brine to preheat the feed seawater using heat exchangers as illustrated in Figure 5.12. The water recovery in both cases was 80%.

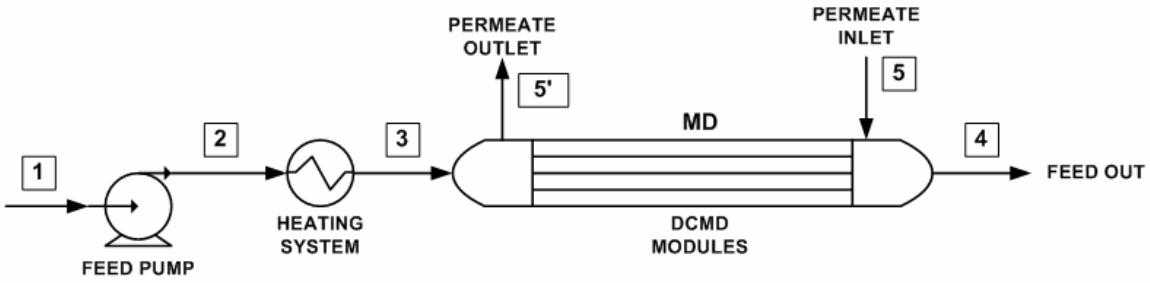

Figure 5.11 MD without heat recovery

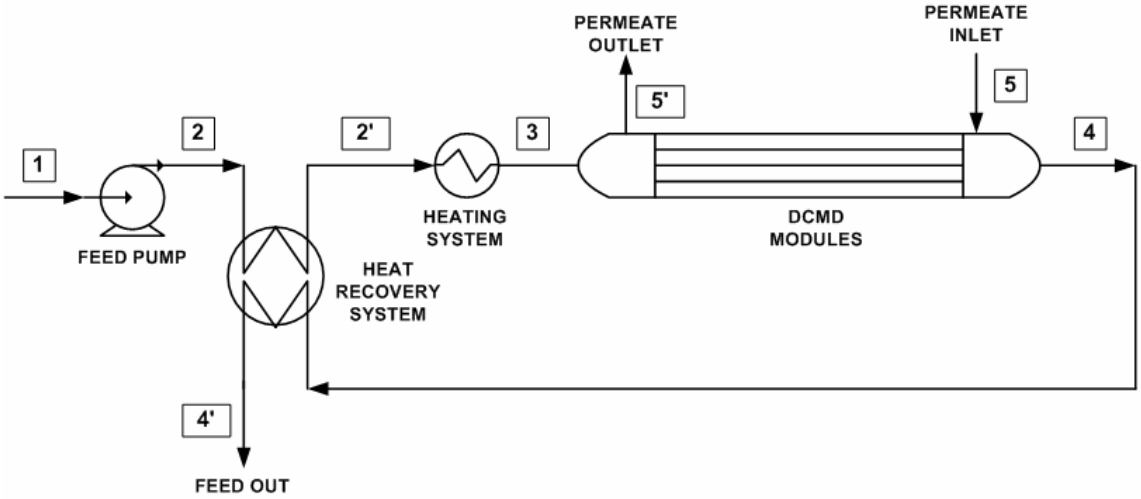

Figure 5.12 MD with heat recovery

The composition and the exergy variations were calculated for each stream and the results were presented Table 5.8 for MD without heat recovery system and Table 5.9 for MD with heat recovery system.

Table 5.8 The composition and the exergy variations calculated for each stream in MD without heat recovery *

Stream No.	1	2	3	4	5	5’
Ca (g/L)	0.499	0.499	0.499	2.491	0.001	0.001
Mg (g/L)	1.554	1.554	1.554	7.758	0.003	0.003
Na (g/L)	12.902	12.902	12.902	64.407	0.026	0.026
K (g/L)	0.468	0.468	0.468	2.336	0.001	0.001
CO_3 (g/L)	0.000	0.000	0.000	0.000	0.000	0.000
HCO_3 (g/L)	0.174	0.174	0.174	0.869	0.000	0.000
SO_4 (g/L)	3.241	3.241	3.241	16.179	0.006	0.006
Cl (g/L)	23.214	23.214	23.214	115.884	0.046	0.046
Total concentration (g/l)	42.052	42.052	42.052	209.924	0.084	0.084
Flow rate (m^3/h)	1,250	1,250	1,250	250	250	1,250
Pressure (MPa)	0.10	0.12	0.12	0.10	0.11	0.10
Temperature (K)	303.0	303.0	340.0	333.0	303.0	310.0
Ex^C (kW)	1,157	1,157	1,157	1,089	0	2
Ex^P (kW)	0	7	7	0	1	0
Ex^T (kW)	0	0	3,037	405	0	116
Ex Total (kW)	1,157	1,164	4,201	1,494	1	118

* MD recovery = 80%

Table 5.9 The composition and the exergy variations calculated for each stream in MD with heat recovery *

Stream No.	1	2	2'	3	4	4'	5	5'
Ca (g/L)	0.499	0.499	0.499	0.499	2.491	2.491	0.001	0.001
Mg (g/L)	1.554	1.554	1.554	1.554	7.758	7.758	0.003	0.003
Na (g/L)	12.902	12.902	12.902	12.902	64.407	64.407	0.026	0.026
K (g/L)	0.468	0.468	0.468	0.468	2.336	2.336	0.001	0.001
CO_3 (g/L)	0.000	0.000	0.000	0.000	0.000	0.000	0.000	0.000
HCO_3 (g/L)	0.174	0.174	0.174	0.174	0.869	0.869	0.000	0.000
SO_4 (g/L)	3.241	3.241	3.241	3.241	16.179	16.179	0.006	0.006
Cl (g/L)	23.214	23.214	23.214	23.214	115.884	115.884	0.046	0.046
Total concentration (g/l)	42.052	42.052	42.052	42.052	209.924	209.924	0.084	0.084
Flow rate (m^3/h)	1,250	1,250	1,250	1,250	250	250	250	1,250
Pressure (MPa)	0.10	0.12	0.12	0.12	0.10	0.10	0.11	0.10
Temperature (K)	303.0	303.0	307.5	340.0	333.0	305.0	303.0	310.0
Ex^C (kW)	1,157	1,157	1,157	1,157	1,089	1,089	0	2
Ex^P (kW)	0	7	7	7	0	0	1	0
Ex^T (kW)	0	0	48	3,037	405	2	0	116
Ex Total (kW)	1,157	1,164	1,212	4,201	1,494	1,091	1	118

* MD recovery = 80%

In case of MD without heat recovery system, the brine was exiting with relatively high temperature 333 K (60 ^{o}C) as shown in Table 5.8 and this heat will be lost with the brine. However, this heat was utilized to preheat the coming feed before going to the heater using the heat exchanger and therefore reduce the load on the heater as shown in Table 5.9. In addition, the brine was rejected at temperature of 305 K (32 ^{o}C) which was close to the feed seawater temperature. This will minimize the environmental impact of the temperature difference on the marine life near the desalination plants. The exergy supply or destruction of each component in both cases was studied and the results are presented in Figure 5.13 for MD without heat recovery and in Figure 5.14 for MD with heat recovery system.

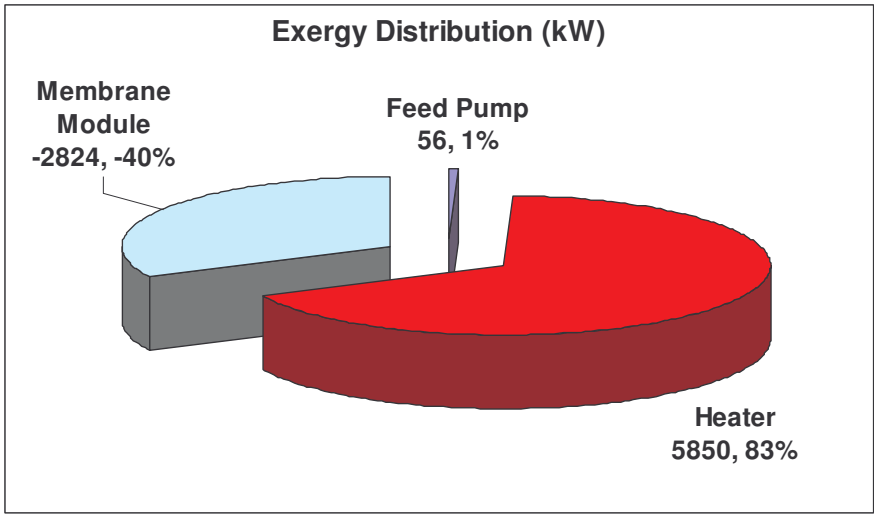

Figure 5.13 The exergy distribution in MD plant without heat recovery system

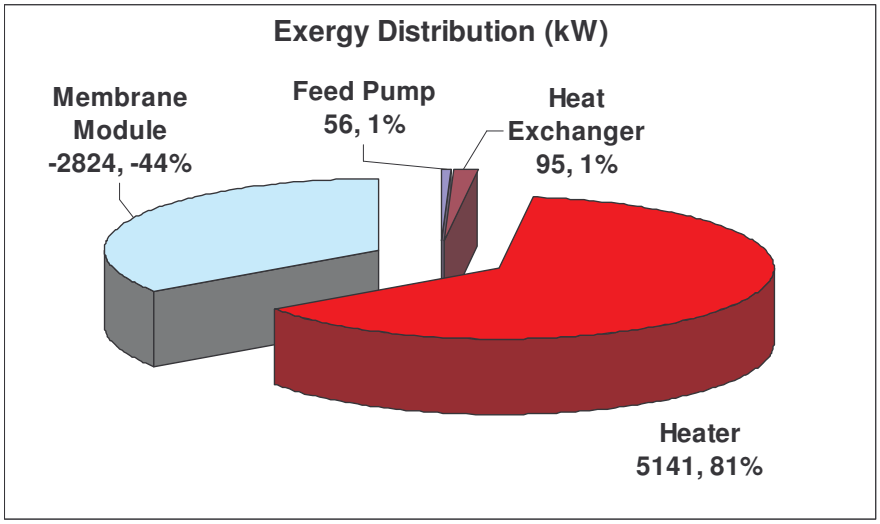

Figure 5.14 The exergy distribution in MD plant with heat recovery system

Considering Figure 5.13 and Figure 5.14, it is obvious that the main exergy input to the MD plant was as heat exergy supplied by the heaters. The heat exchanger was able to save more than 6,000 kW of the total heat input to the system in case of MD with heat recovery system.

A summary of the exergy analysis for MD plants with and without the heat recovery system is presented in Table 5.10. The net exergy change between the in and out streams was 50 kW in case of MD with heat recovery and 453 kW in case of MD without heat recovery. The total exergy input (Ex_{in} + $Ex_{electrical}$ + $Ex_{thermal}$) of the MD plant without heat recovery was higher than the one of the MD plant with heat recovery by a value of 708 kW. Therefore, the exergy efficiency of the MD plant without heat recovery was less than the efficiency of the MD plant with heat recovery. The total irreversible entropy production (R_sT_o) was 5,452 kW and 5,146 kW for MD without and with heat recovery system, respectively.

Table 5.10 Summary of exergy analysis for MD plants with and without heat recovery system

	MD Without HR	MD With HR
Ex out (kW)	1,612	1,209
Ex in (kW)	1,158	1,158
delta Ex	453	50
Work input (kW)	56	56
Recovered Heat (kW)	0	95
Heat input (kW)	53,753	47,244
Exergy of work input (kW)	56	56
Exergy of heat input (kW)	5,850	5,141
Exergy of input streams (kW)	1,158	1,158
Total exergy input (Ex_inlet) (kW)	7,063	6,355
Exergy output (Ex_outlet) (kW)	1,612	1,612
Entropy production RsTo (kW)	5,452	5,146
Exergy efficiency (%)	22.82	25.36

III) Integration of pressure-driven membranes with membrane distillation/crystallization processes

In this case, the desalination plant was consisting of the pressure-driven membranes (UF-NF-RO) in combination with MDC units which were operated on the concentrate stream of NF and on the brine stream of RO. This means that the normally rejected streams of NF concentrate and RO brine will be used as the mother liquid feed for the MDC units which can be operated at high feed concentrations since they are thermal processes and hence not limited by the osmotic pressure and concentration polarization phenomena. Several configuration strategies can be achieved in this integrated system since the MDC units can be operated as membrane distillation (MD) or membrane crystallization (MC) by increasing the water recovery factor. In all cases, the water recoveries of the UF, NF and RO units were assumed always as 95%, 70% and 60%, respectively.

a) UF-NF-RO with MC_NF+MD_RO

This system consisted of the pressure-driven membrane operation (UF-NF-RO) integrated with MC unit operating on the NF concentrated stream and MD unit operating on RO brine stream as shown in Figure 5.15.

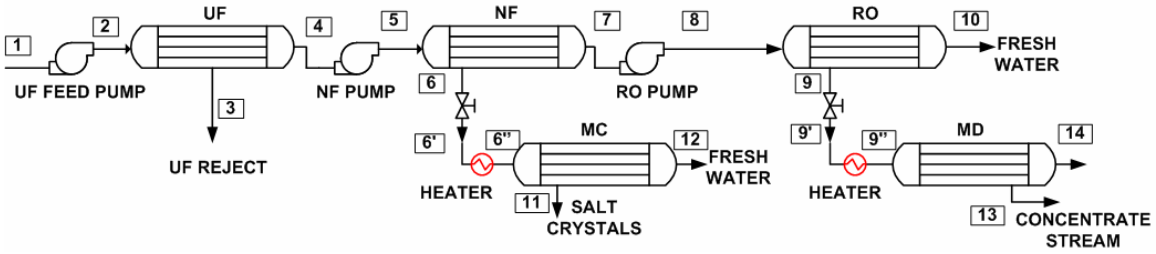

Figure 5.15 UF-NF-RO with MC_NF+MD_RO

The NF concentrated stream was passed through a bath of sodium carbonates (Na_2CO_3) for precipitating calcium ions (Ca^{+2}) as $CaCO_3$ before it was introduced to the MC to avoid scaling problems and increase the amount of $MgSO_4$ precipitation. The Na_2CO_3 was assumed to be obtained from the reactive transfer of carbon dioxide (CO_2) into sodium hydroxide (NaOH) through gas liquid membrane contactors mentioned earlier. The composition and the exergy variations through the MC streams are listed in Table 5.11.

Table 5.11 The composition and the exergy variations of each stream in MC unit operating on the NF concentrate within the integrated system *

Stream No.	6'	6''	11	12
Ca (g/L)	0.0764	0.0764	3.1189	0.0002
Mg (g/L)	4.7804	4.7804	112.6808	0.0096
Na (g/L)	21.1949	21.1949	207.6987	0.0424
K (g/L)	0.6973	0.6973	28.4620	0.0014
CO_3 (g/L)	2.1778	2.1778	88.8892	0.0044
HCO_3 (g/L)	0.4257	0.4257	17.3763	0.0009
SO_4 (g/L)	10.0471	10.0471	283.2900	0.0201
Cl (g/L)	30.1472	30.1472	219.3720	0.0603
Concentration (g/l)	69.547	69.547	960.888	0.139
Flow rate (m^3/h)	320	320	8	8
Pressure (MPa)	0.12	0.12	0.10	0.11
Temperature (K)	303.0	340.0	333.0	303.0
Ex^C (kW)	469	469	30	0
Ex^P (kW)	2	2	0	0
Ex^T (kW)	0	778	13	0
Ex Total (kW)	470	1,249	43	0

* MC recovery = 97.55%

Furthermore, when operating the MC on the NF concentrated stream, it was possible to crystallize amount of 1,642 kg/h of $MgSO_4$ and 13,093 kg/h of NaCl as shown in Table 5.12.

Table 5.12 The amount of chemicals used and crystallized salts from the NF concentrated stream

Item	Amount (kg/h)
NaCl	13,093
$MgSO_4$	1,642
$CaCO_3$	1,163
Na_2CO_3 (produced from GLMC)	1,232
NaOH (used in GLMC)	418

The MD unit operating on the RO brine stream was assumed with heat recovery system and water recovery of 80%. Table 5.13 lists the composition and the exergy variations in the MD plant.

Table 5.13 The composition and the exergy calculated for each stream in MD unit with heat recovery operating on the RO brine within the integrated system *

Stream No.	9'	9''	13	14
Ca (g/L)	0.144	0.144	0.721	0.000
Mg (g/L)	0.427	0.427	2.132	0.001
Na (g/L)	24.993	24.993	124.764	0.050
K (g/L)	0.913	0.913	4.559	0.002
CO_3 (g/L)	0.000	0.000	0.000	0.000
HCO_3 (g/L)	0.164	0.164	0.817	0.000
SO_4 (g/L)	0.808	0.808	4.035	0.002
Cl (g/L)	50.288	50.288	43.874	0.101
Total concentration (g/l)	77.737	77.737	180.903	0.155
Flow rate (m^3/h)	299	299	60	60
Pressure (MPa)	0.12	0.12	0.10	0.11
Temperature (K)	307.5	340.0	305.0	303.0
Ex^C (kW)	522	522	270	0
Ex^P (kW)	2	2	0	0
Ex^T (kW)	11	726	0	0
Ex Total (kW)	535	1,250	271	0

* MD recovery = 80%

The overall fresh water recovery of the whole integrated system in this configuration was 89%.

b) UF-NF-RO with MC_NF+MC_RO

This system consisted of the pressure-driven membrane operations (UF-NF-RO) integrated with two MC units one operating on the NF concentrated stream and other on the RO brine stream as shown in Figure 5.16.

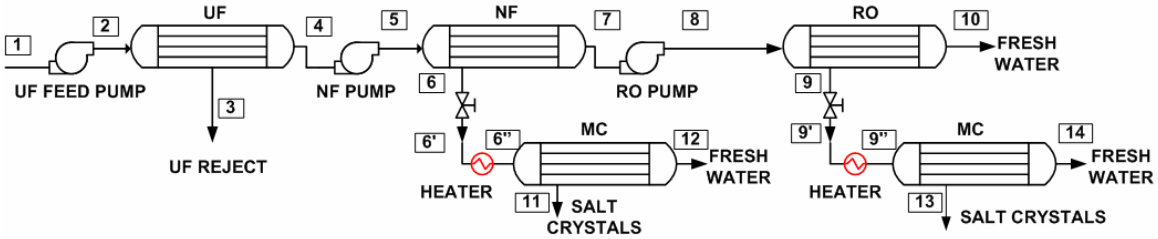

Figure 5.16 UF-NF-RO with MC_NF+MC_RO

In this case, the composition and the exergy variations of the MC operating on the NF concentrated stream were exactly like the ones showed in the previous case as in Table 5.11. For the MC operating on the RO brine stream, the variations of composition and exergy are presented in Table 5.14.

Table 5.14 The composition and the exergy variations of each stream in MC unit operating on the RO brine within the integrated system *

Stream No.	9'	9''	13	14
Ca (g/L)	0.1444	0.1444	5.8844	0.0003
Mg (g/L)	0.4271	0.4271	17.3986	0.0009
Na (g/L)	24.9929	24.9929	142.6280	0.0500
K (g/L)	0.9132	0.9132	37.2011	0.0018
CO_3 (g/L)	0.0000	0.0000	0.0000	0.0000
HCO_3 (g/L)	0.1637	0.1637	6.6691	0.0003
SO_4 (g/L)	0.8083	0.8083	32.9277	0.0016
Cl (g/L)	50.2877	50.2877	702.9197	0.1006
Total concentration (g/l)	77.737	77.737	945.629	0.155
Flow rate (m^3/h)	284	284	7	7
Pressure (MPa)	0.12	0.12	0.10	0.11
Temperature (K)	303.0	340.0	333.0	303.0
Ex^C (kW)	496	496	34	0
Ex^P (kW)	2	2	0	0
Ex^T (kW)	0	690	11	0
Ex Total (kW)	498	1,188	46	0

* MC recovery = 97.55%

In this case, it was possible to crystallize a total amount of 27,939 kg/h (12,441 kg/h from NF stream and 15,498 kg/h from RO stream) of NaCl and 1,560 kg/h of $MgSO_4$ from NF stream only as shown in Table 5.15. The overall fresh water recovery of the whole integrated system in this configuration was 94.7%.

Table 5.15 The amount of chemicals used and crystallized salts from the NF concentrated and RO brine streams

Item	Amount (kg/h)
NaCl	27,939
$MgSO_4$	1,560
$CaCO_3$	1,105
Na_2CO_3 (produced from GLMC)	1,171
NaOH (used in GLMC)	397

c) UF-NF-RO with MD_NF+MD_RO

This system consisted of the pressure-driven membrane operation (UF-NF-RO) integrated with two MD units one operating on the NF concentrated stream and the other on the RO brine stream as shown in Figure 5.17.

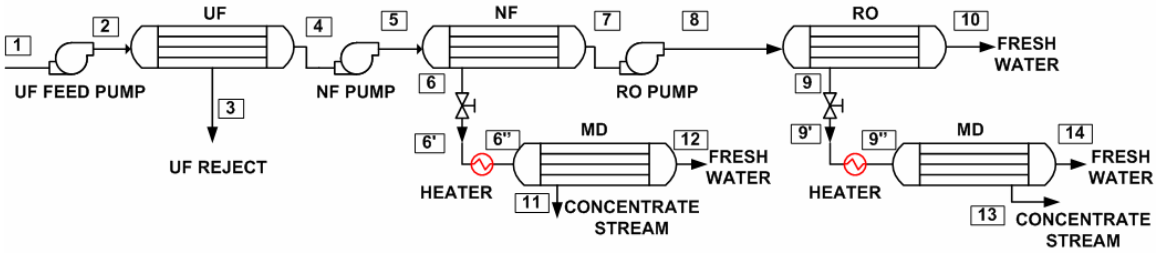

Figure 5.17 UF-NF-RO with MD_NF+MD_RO

The composition and the exergy variations of the MD operating on the RO brine stream were similar to the ones showed in Table 5.13. On the other hand, the compositions and the exergy variations of the MD operating on the NF concentrated stream are shown in Table 5.16. The overall fresh water recovery of the whole integrated system in this configuration was 84%.

Table 5.16 The composition and the exergy variations of each stream in MD unit with heat recovery operating on the NF concentrate within the integrated system*

Stream No.	6'	6''	11	12
Ca (g/L)	0.076	0.076	0.382	0.000
Mg (g/L)	4.780	4.780	71.710	0.010
Na (g/L)	21.195	21.195	142.628	0.042
K (g/L)	0.697	0.697	3.487	0.001
CO_3 (g/L)	2.178	2.178	10.889	0.004
HCO_3 (g/L)	0.426	0.426	2.129	0.001
SO_4 (g/L)	10.047	10.047	283.290	0.020
Cl (g/L)	30.147	30.147	219.372	0.060
Total concentration (g/l)	69.547	69.547	733.886	0.139
Flow rate (m^3/h)	339	339	68	68
Pressure (MPa)	0.12	0.12	0.10	0.11
Temperature (K)	303.5	340.0	305.0	303.0
Ex^C (kW)	497	497	571	0
Ex^P (kW)	2	2	0	0
Ex^T (kW)	0	825	1	0
Ex Total (kW)	499	1,323	572	0

* MD recovery = 80%

Calculations of the process exergy variations and flow rates of all the suggested configurations of the integrated membrane system are summarized in Table 5.17. The highest work input was for the plant which involved the pressure-driven membranes UF-NF-RO due to the high pumping and pressurizing energy requirement especially in NF and RO pumps. On the other hand, the highest heat energy input was associated with the membrane distillation plant as a stand alone process. In this case, the heat energy input was more than double of the integrated plant which involves two MC units combined with the pressure-driven operations (UF-NF-RO). The exergy efficiency was generally higher in case of pressure-driven operations than thermal processes. In addition, the performance of plants with energy and heat recovery systems was always better than the ones without energy and heat recovery systems.

Table 5.17 Summary of the exergy analysis calculation for the integrated membrane system (Seawater)

	UF-RO		UF-NF-RO		MD only		UF-NF-RO-MC_NF-MD_RO		UF-NF-RO-MC_NF-MC_RO		UF-NF-RO-MD_NF-MD_RO	
Exergy (kW)	Without ER	With ER	Without ER	With ER	Without HR	With HR	Without ER+HR +GLMC	With ER+HR +GLMC	Without ER+HR +GLMC	With ER+HR +GLMC	Without ER+HR +GLMC	With ER+HR +GLMC
delta Ex	-24	-24	-21	-21	453	50	-409	-664	-842	-874	202	-69
Work input	5,191	2,927	6,471	4,584	56	56	2,906	2,060	2,761	1,957	3,079	2,183
Heat input	0	0	0	0	53,753	47,244	26,628	25,072	25,301	25,120	28,214	26,565
Exergy of work input	5,191	2,927	6,471	4,584	56	56	2,906	2,060	2,761	1,957	3,079	2,183
Exergy of heat input	0	0	0	0	5,850	5,141	2,898	2,728	2,753	2,734	3,070	2,891
Exergy of input streams	1,949	1,949	2,320	2,320	1,158	1,158	1,041	1,041	989	989	1,103	1,103
Total exergy input	7,140	4,876	8,791	6,904	7,063	6,355	6,845	5,829	6,503	5,680	7,253	6,177
Exergy output	1,925	1,925	2,299	2,299	1,612	1,612	632	376	146	114	1,305	1,034
Entropy production RsTo	5,215	2,951	6,492	4,605	5,452	5,146	6,213	5,453	6,357	5,565	5,947	5,142
Exergy efficiency (%)	27.0	39.5	26.2	33.3	22.8	25.4	9.2	7.9	2.3	2.4	18.0	20.4
Flow rate												
Feed (m^3/h)	2,105	2,105	2,506	2,506	1,250	1,250	1,124	1,124	1,068	1,068	1,191	1,191
Concentrate (m^3/h)	1,000	1,000	1,506	1,506	250	250	68	68	14	14	131	131
UF Recovery (%)	95.0	95.0	95.0	95.0	-	-	95.0	95.0	95.0	95.0	95.0	95.0
NF Recovery (%)	-	-	70.0	70.0	-	-	70.0	70.0	70.0	70.0	70.0	70.0
RO Recovery (%)	50.0	50.0	60.0	60.0	-	-	60.0	60.0	60.0	60.0	60.0	60.0
MDC_NF Recovery (%)	-	-	-	-	80.0	80.0	97.6	97.6	97.6	97.6	80.0	80.0
MDC_RO Recovery (%)	-	-	-	-	0	0	80.0	80.0	97.6	97.6	80.0	80.0
Total Water recovery (%)	47.5	47.5	39.9	39.9	80.0	80.0	89.0	89.0	93.7	93.7	84.0	84.0
NaCl (kg/h)	0	0	0	0	0	0	13,093	13,093	27,939	27,939	0	0
$MgSO_4$ (kg/h)	0	0	0	0	0	0	1,642	1,642	1,560	1,560	0	0
$CaCO_3$ (kg/h)	0	0	0	0	0	0	1,265	1,265	1,202	1,202	1,340	1,340
Na_2CO_3 (kg/h)	0	0	0	0	0	0	1,341	1,341	1,274	1,274	1,421	1,421

The same analyses were repeated for the integrated membrane system for brackish water desalination. One of the underground wells in the A'Dakhelya Region (Oman) was taken as an example for the brackish feed water source. The total dissolved salts (TDS) in this well was 11,903 mg/L. The RO water recovery rate was assumed as 80% in case of UF-RO system and the water recovery rates of UF-NF-RO were assumed as 95%, 80% and 75%, respectively, in the integrated membrane system. The same procedure used for seawater desalination was applied for the brackish water desalination and the results are summarized in Table 5.18.

As shown in Table 5.18, the highest exergy efficiency was associated with the pressure-driven membrane operations (UF-RO was 30.2% and UF-NF-RO was 23.1%). The lowest total water recovery was 57% for the UF-NF-RO plant and the highest plant total water recovery was 94.1% for the combination of the pressure-driven membranes (UF-NF-RO) with two MC units operating on the concentrate stream of NF and RO brine. The problems related to brine disposal can be minimized since the rejected concentrate streams of the integrated membrane system may reach values less than 1% of the total feed. Minimizing the amount of rejected streams is essential especially in case of inland brackish desalination plants since brine management represent a major obstacle of such plants.

Table 5.18 Summary of the exergy analysis calculation for the integrated membrane system (Brackish water)

	UF-RO		UF-NF-RO		MD only		UF-NF-RO-MC_NF-MD_RO		UF-NF-RO-MC_NF-MC_RO		UF-NF-RO-MD_NF-MD_RO	
Exergy (kW)	Without ER	With ER	Without ER	With ER	Without HR	With HR	Without ER+HR +GLMC	With ER+HR +GLMC	Without ER+HR +GLMC	With ER+HR +GLMC	Without ER+HR +GLMC	With ER+HR +GLMC
delta Ex	-4	-4	-2	-2	516	113	3	-64	-150	-200	445	375
Work input	1,299	760	1,868	1,470	56	56	1,177	927	1,135	894	1,222	962
Heat input	0	0	0	0	53,753	47,244	18,010	16,919	17,371	17,242	18,697	17,565
Exergy of work input	1,299	760	1,868	1,470	56	56	1,177	927	1,135	894	1,222	962
Exergy of heat input	0	0	0	0	5,850	5,141	1,960	1,841	1,890	1,876	2,035	1,911
Exergy of input streams	334	334	445	445	318	318	280	280	270	270	291	291
Total exergy input	1,633	1,094	2,313	1,916	6,223	5,515	3,417	3,048	3,295	3,040	3,547	3,165
Exergy output	330	330	443	443	834	834	283	216	120	70	736	666
Entropy production RsTo	1,303	764	1,870	1,473	5,390	5,084	3,133	2,832	3,176	2,970	2,811	2,499
Exergy efficiency (%)	20.2	30.2	19.2	23.1	13.4	15.1	8.3	7.8	3.6	2.5	20.8	23.2
Flow rate												
Feed (m^3/h)	1,316	1,316	1,754	1,754	1,250	1,250	1,102	1,102	1,063	1,063	1,144	1,144
Concentrate (m^3/h)	250	250	666	666	250	250	47	47	10	10	87	87
UF Recovery (%)	95.0	95.0	95.0	95.0	-	-	95.0	95.0	95.0	95.0	95.0	95.0
NF Recovery (%)	-	-	80.0	80.0	-	-	80.0	80.0	80.0	80.0	80.0	80.0
RO Recovery (%)	80.0	80.0	75.0	75.0	-	-	75.0	75.0	75.0	75.0	75.0	75.0
MDC_NF Recovery (%)	-	-	-	-	-	-	97.6	97.6	97.6	97.6	97.6	97.6
MDC_RO Recovery (%)	-	-	-	-	80.0	80.0	80.0	80.0	97.6	97.6	80.0	80.0
Total Water recovery (%)	76.0	76.0	57.0	57.0	80.0	80.0	90.7	90.7	94.1	94.1	87.4	87.4
NaCl (kg/h)	0	0	0	0	0	0	1,400	1,400	4,762	4,762	0	0
$MgSO_4$ (kg/h)	0	0	0	0	0	0	0	0	0	0	0	0
$CaCO_3$ (kg/h)	0	0	0	0	0	0	1,860	1,860	1,794	1,794	1,931	1,931
Na_2CO_3 (kg/h)	0	0	0	0	0	0	1,971	1,971	1,901	1,901	2,047	2,047

5.4.2 Economical aspects and cost evaluation

An economic cost evaluation has been made in order to determine the unit cost of the potable water produced. All calculations were based on recent economic data presented in Table 5.19 which were obtained from field data and literature.

Table 5.19 Data and assumptions used in the economical study

Plant availability, f	90 %
Plant capacity, Q_P	1,000 m^3/h
Plant Annual Capacity	8760000
Plant life, n	20 years
Interest rate, i	5 %

Amortization factor: $a = \frac{i(1+i)^n}{(1+i)^n - 1}$

Fluxes

UF flux = 90 L/m^2 h
NF flux = 28 L/m^2 h
RO flux = 15 L/m^2 h
MD flux = 8.2 L/m^2 h
MC flux = 6.8 L/m^2 h

Efficiencies

Pumps-motor combined efficiency = 0.75
Pressure exchanger efficiency = 0.95
Heat exchanger efficiency = 0.8

Direct Capital Cost, DCC

Intake =658 $(Q_p/\eta)^{0.8}$	[19]
Civil work = 1945$(Q_p/\eta)^{0.8}$	[20]
UF membrane cost =90 $/m^2	[11]
Steam Heat exchanger cost = 2000 $/m^2	[21]
Heat recovery exchanger cost = 1540 $/m^2	[21]

Indirect Capital Cost = 10% DDC

Annual fixed charges = a×DCC/f×Q

O&M specific costs

Electricity cost	0.03 $/kWh	[11]
Membrane replacement	15% /y	[11]
Steam cost	7 $/ton	[20]
Spares cost	0.033 $/$m^3$	[19]
Labor cost	0.03-0.05 $/$m^3$	[20]
Chemical cost	0.018 $/$m^3$	[11]
Brine disposal	0.0015 $/$m^3$	[17]

Cost of salt crystals

NaCl ($/kg)	0.030	[22]
$MgSO_4$ ($/kg)	0.570	[23]
$CaCO_3$ ($/kg)	0.032	[24]
Na_2CO_3 ($/kg)	0.336	[25]

In order to emphasize the importance of combining several membrane operations in a single integrated system for water desalination, all cases discussed earlier were considered in the study. The plant capacity was assumed

to be the same (1000 m^3/h). The MDC units were operated under the same conditions of 30 degrees temperature difference and producing a flux of 8.2 kg/m^2h in case of MD and a flux of 6.8 kg/m^2h in case of MC as obtained from the MDC simulation program using MATLAB discussed earlier in chapter 3. The economic data presented in Table 5.19 were used as inputs for all cases. The results were summarized and tabulated in Table 5.20 for seawater plants and in Table 5.21 for brackish water plants. The results showed that the plant average capital cost was 27 millions US dollars. It was comparable with difference of ±13% among all cases. This was due to the fact that the additional costs of the equipments (membrane modules, pumps, heat exchangers, etc.) in the integrated system were compensated by the reduction in the costs of the civil work and the intake/discharge facilities due to the increase in the plant overall water recovery. On the other hand, the total capital cost in case of brackish water desalination plants was within the range 13.8-24.2 millions US dollars. The capital investment costs of the MD plant as a stand-alone plant was 75% higher than the costs of the pressure-driven (UF-RO) plant. This was due to the fact that the pressure-driven membranes can be operated at high recovery rates in case of brackish water due to lower osmotic pressures than of seawater. Hence, operating the NF and RO units at higher recovery rates will lead to decrease the capital costs (intake systems, number of membrane modules and pump sizes) as well as reduction in the operating costs (power consumption).

Generally, the lowest membrane replacement cost was in case of using pressure-driven membrane operations, and it increased in the integrated system since more membranes (MC and MD) were installed. The annual electricity cost was the same for all plants (excluding UF-RO and MD alone plants) since the recoveries of UF, NF and RO were assumed always the same.

The MD plant when it was operated as a stand alone operation had the highest annual cost of steam (5.47 millions US dollars for both seawater and

brackish water plants), and the cost of steam was decreasing as the overall plant recovery was increased in the integrated membrane system.

The lowest total water costs were 0.51 and 0.29 $/m^3 when using UF-RO plant with energy recovery system for seawater and brackish water desalination, respectively. However, considering the combination of different operations in the integrated system, the best performance was obtained when using the UF-NF-RO with an MC unit operating on the NF concentrated stream and an MD unit operating on the RO brine stream. The total water cost in this case was 1.27 $/m^3 for seawater plants and 1.10 $/m^3 for brackish water plants. In addition, this combination had the highest performance ratio (21.6 and 32.1 for seawater and brackish water plants, respectively); and the lowest primary energy, defined as the energy supplied by fuel combustion to produce thermal energy, was 43 and 29 MW for seawater and brackish water plants, respectively.

There was no considerable difference between the cost of water produced by plants with and without energy recovery devices in case of brackish water desalination. This was due to the lower applied pressure compared with the case of seawater desalination.

Considering the possibility of obtaining salts crystals at commercial grade from the crystallization units, the final water cost obtained by the integrated membrane system can be reduced significantly especially in case of seawater desalination. In this case, a profit of 0.10 $/m^3 can be gained when using integrated system with MC units operating on the NF concentrated stream and MD units operating on the RO brine stream. This profit can as high as 0.48 $/m^3 when using two MC units operated on the NF concentrated and the RO brine streams. Additionally, the environmental problems related to brine disposal were eliminated completely in the integrated membrane system due to the low amount of brine which will be rejected.

Table 5.20 Cost estimation of several integrated system configurations (Seawater)

Cost	UF-RO		UF-NF-RO		MD only		UF-NF-RO-MC_NF-MD_RO		UF-NF-RO-MC_NF-MC_RO		UF-NF-RO-MD_NF-MD_RO	
	Without ER	With ER	Without ER	With ER	Without HR	With HR	Without ER+HR +GLMC	With ER+HR +GLMC	Without ER+HR +GLMC	With ER+HR +GLMC	Without ER+HR +GLMC	With ER+HR +GLMC
Total capital cost (M $)	23.37	25.55	28.66	30.47	22.79	24.19	27.05	28.32	27.84	28.76	26.10	27.44
Annual fixed charge ($/m^3)	*0.24*	*0.26*	*0.29*	*0.31*	*0.23*	*0.25*	*0.28*	*0.28*	*0.28*	*0.29*	*0.27*	*0.28*
Membrane replacement (M $/year)	0.61	0.61	0.91	0.91	1.60	1.60	1.53	1.53	1.73	1.73	1.29	1.29
Electricity (M $/year)	1.24	0.70	1.35	0.90	0.01	0.01	1.35	0.90	1.35	0.90	1.35	0.90
Cost of steam (M $/year)	0	0	0	0	5.47	4.80	2.71	2.55	2.57	2.55	2.87	2.70
Cost of Na_2CO_3 (M $/year)	0	0	0	0	0	0	3.55	0	3.38	0	3.76	0
Cost of NaOH (M $/year)	0	0	0	0	0	0	0	2.15	0	2.04	0	2.28
Total annual O&M costs (M $/year)	2.50	1.95	2.91	2.45	7.71	7.05	9.78	7.77	9.67	7.86	9.92	7.81
Annual O&M charges ($/m^3)	*0.32*	*0.25*	*0.37*	*0.31*	*0.98*	*0.89*	*1.24*	*0.99*	*1.23*	*1.00*	*1.26*	*0.99*
Total water cost ($/m^3)	**0.56**	**0.51**	**0.66**	**0.62**	**1.21**	**1.14**	**1.52**	**1.27**	**1.51**	**1.29**	**1.53**	**1.27**
Performance ratio: PR	-	-	-	-	10.1	11.5	20.4	21.6	21.5	21.6	19.2	20.4
Specific heat consumption (kJ/kg)	-	-	-	-	193.5	170.1	95.9	90.3	91.1	90.4	101.6	95.6
Primary energy PE (MW)	-	-	-	-	92.1	81.0	45.6	43.0	43.4	43.0	48.3	45.5
NaCl ($/m^3)	0	0	0	0	0	0	0.39	0.39	0.84	0.84	0	0
$MgSO_4$ ($/m^3)	0	0	0	0	0	0	0.94	0.94	0.89	0.89	0	0
$CaCO_3$ ($/m^3)	0	0	0	0	0	0	0.04	0.04	0.04	0.04	0.04	0.04
Profit from crystallized salts ($/m^3)	*0*	*0*	*0*	*0*	*0*	*0*	*1.37*	*1.37*	*1.77*	*1.77*	*0.04*	*0.04*
Final water cost ($/m^3)	**0.56**	**0.51**	**0.66**	**0.62**	**1.21**	**1.14**	**0.15**	**-0.10**	**-0.26**	**-0.48**	**1.49**	**1.23**

Table 5.21 Cost estimation of several integrated system configurations (Brackish water)

Cost	UF-RO		UF-NF-RO		MD only		UF-NF-RO-MC_NF-MD_RO		UF-NF-RO-MC_NF-MC_RO		UF-NF-RO-MD_NF-MD_RO	
	Without ER	With ER	Without ER	With ER	Without HR	With HR	Without ER+HR +GLMC	With ER+HR +GLMC	Without ER+HR +GLMC	With ER+HR +GLMC	Without ER+HR +GLMC	With ER+HR +GLMC
Total capital cost (M $)	13.81	14.35	18.14	18.55	22.79	24.19	22.15	22.73	22.95	23.29	21.28	21.88
Annual fixed charge ($/m^3)	**0.14**	**0.15**	**0.18**	**0.19**	**0.23**	**0.25**	**0.23**	**0.23**	**0.23**	**0.24**	**0.22**	**0.23**
Membrane replacement (M $/year)	0.25	0.25	0.40	0.40	1.60	1.60	1.03	1.03	1.20	1.20	0.85	0.85
Electricity (M $/year)	0.32	0.19	0.42	0.32	0.10	0.10	0.42	0.32	0.42	0.32	0.42	0.32
Cost of steam (M $/year)	0	0	0	0	5.47	4.80	1.83	1.72	1.77	1.75	1.90	1.79
Cost of Na_2CO_3 (M $/year)	0	0	0	0	0	0	5.22	0	5.04	0	5.42	0
Cost of NaOH (M $/year)	0	0	0	0	0	0	0	3.16	0	3.05	0	3.28
Total annual O&M costs (M $/year)	1.22	1.08	1.46	1.36	7.71	7.05	9.14	6.86	9.05	6.95	9.22	6.87
Annual O&M charges ($/m^3)	**0.15**	**0.14**	**0.19**	**0.17**	**0.98**	**0.89**	**1.16**	**0.87**	**1.15**	**0.88**	**1.17**	**0.87**
Total water cost ($/m^3)	**0.29**	**0.29**	**0.37**	**0.36**	**1.21**	**1.14**	**1.39**	**1.10**	**1.38**	**1.12**	**1.39**	**1.10**
Performance ratio: PR	-	-	-	-	10.1	11.5	30.1	32.1	31.2	31.5	29.0	30.9
Specific heat consumption (kJ/kg)	-	-	-	-	193.5	170.1	64.8	60.9	62.5	62.1	67.3	63.2
Primary energy PE (MW)	-	-	-	-	92.1	81.0	30.9	29.0	29.8	29.5	32.0	30.1
NaCl ($/m^3)	0	0	0	0	0	0	0.04	0.04	0.14	0.14	0	0
$MgSO_4$ ($/m^3)	0	0	0	0	0	0	0	0	0	0	0	0
$CaCO_3$ ($/m^3)	0	0	0	0	0	0	0.06	0.06	0.06	0.06	0.06	0.06
Profit from crystallized salts ($/m^3)	***0***	***0***	***0***	***0***	***0***	***0***	***0.10***	***0.10***	***0.20***	***0.20***	***0.06***	***0.06***
Final water cost ($/m^3)	**0.29**	**0.29**	**0.37**	**0.36**	**1.21**	**1.14**	**1.29**	**1.00**	**1.18**	**0.92**	**1.33**	**1.04**

The estimated water cost of desalination plants obtained by this study was similar to the one reported in literature recently. Table 5.22 shows the estimated water cost obtained by different researchers.

Table 5.22 Estimated water cost for different MD plants

Year	Water Cost $/m^3	Note	Ref
2008	0.56	UF-RO without ERD	This work
	0.51	UF-RO with ERD	
	0.66	UF-NF-RO without ERD	
	0.62	UF-NF-RO with ERD	
	1.21	MD without HR	
	1.14	MD without HR	
	1.52	UF-NF-RO-MC_NF-MD_RO without ERD&HR	
	1.27	UF-NF-RO-MC_NF-MD_RO with ERD&HR	
	1.51	UF-NF-RO-MC_NF-MC_RO without ERD&HR	
	1.29	UF-NF-RO-MC_NF-MC_RO with ERD&HR	
	1.53	UF-NF-RO-MD_NF-MD_RO without ERD&HR	
	1.27	UF-NF-RO-MD_NF-MD_RO with ERD&HR	
2006	0.26	MD with cheap industrial waste heat	[26]
2007	0.56	NF+RO with ERD* and MD with available heat energy	[17]
	0.80	NF+RO without ERD* and MD with available heat energy	
	0.73	NF+RO with ERD* and MD without available heat energy	
	0.97	NF+RO without ERD* and MD without available heat energy	
2004	1.25	RO+MD	[27]
	1.32	MD only	
2003	1.40	MSF	[28]
2003	1.00	MED	[28]
2007	0.50	RO	[29]
2002	0.22-0.37	UF+RO for brackish water	[30]

* ERD: Energy Recovery Device, HR: Heat Recovery systems

5.4.3 Sensitivity study

The sensitivity of changing different variables of the desalination plant on the product water cost was studied in order to identify the most sensitive parameters on water cost and to establish optimal conditions for minimizing the total water cost. The same water production capacity of 1,000 m^3/h was assumed in all cases.

i) Water recovery (Yield)

The effects of changing the water recovery on the total water cost for the UF-RO, UF-NF-RO and MD plants was considered and the results are discussed below.

RO recovery in UF-RO plants

The first system considered in the study was the commonly used UF-RO desalination plant. The effect of changing the RO water recovery on the total water cost was investigated and the results are shown in Figure 5.18.

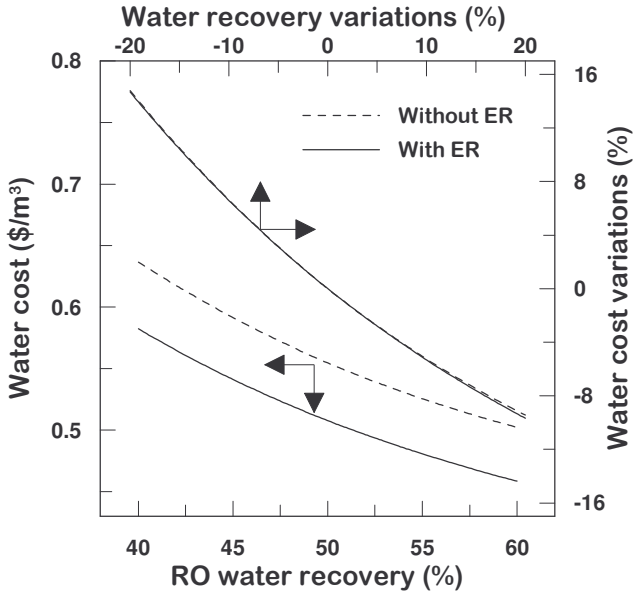

Figure 5.18 Effects of the RO water recovery on the total water cost of UF-RO plants

The results showed that when increasing the RO recovery from 40% to 60%, the total water cost decreased from 0.58 to 0.46 $/m^3 in case of using the energy recovery system and from 0.64 to 0.50 $/m^3 in case not using the energy recovery system. Since an RO recovery of 50% typically used, it has been taken as a reference value. An increment of 20% in this value will contribute to an average reduction of 10% in the total water cost for both cases with and without energy recovery system as obtained from the slope of the water cost variations graph in Figure 5.18.

RO recovery in UF-NF-RO plants

In this case, higher RO recovery values can be achieved at lower osmotic pressure since most of the bivalent ions were removed by the NF membranes. As shown in Figure 5.19, the RO recovery was changed within the range 48%-72% and the results showed that the total water cost decreased from 0.71 to 0.56 $/m^3 and decreased from 0.75 to 0.59 $/m^3 for systems with and without energy recovery devices, respectively.

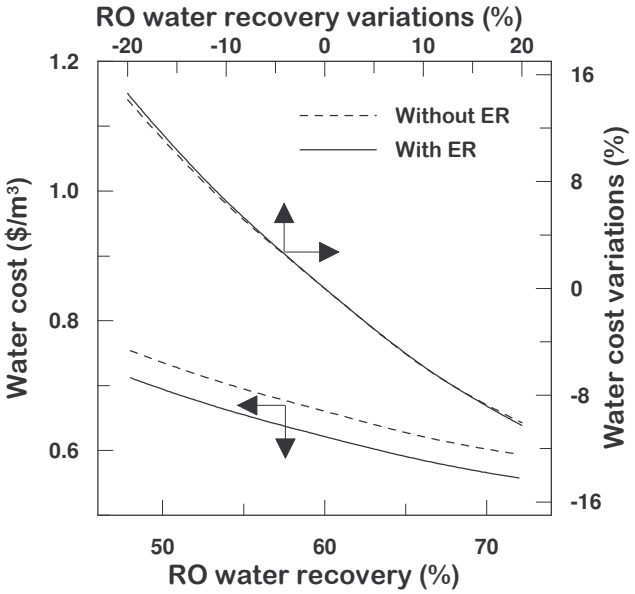

Figure 5.19 Effects of the RO water recovery on the total water cost of UF-NF-RO plants

Considering a recovery value of 60% as a reference, the total water cost was reduced by an average value of 10% as the RO recovery was increased by 20% for both cases with and without energy recovery systems as deduced from the slope of the water cost variations graph in Figure 5.19.

NF recovery in UF-NF-RO plants

The NF recovery was varied from 56% to 84% and the results showed that total water cost was reduced from 0.69 to 0.57 $/m^3 in case of the plant with the energy recovery system; and reduced from 0.73 to 0.61 $/m^3 in case of the plant without energy recovery system as shown in Figure 5.20. Taking a reference recovery value of 70%, an increase of 20% in this value will result in an average reduction of 7.9% and 7.6% in the total water cost for the plants with and without energy recovery system, respectively as given from the slope of the water cost variations graph in Figure 5.20.

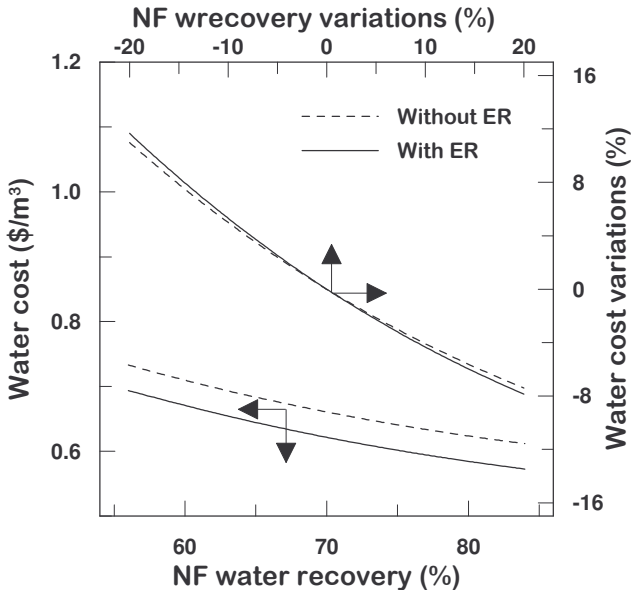

Figure 5.20 Effects of the NF water recovery on the total water cost of UF-NF-RO plants

MD recovery in MD plants

High MD recovery values can be achieved since the MD plant is a thermal process and not limited by the osmotic pressure. The MD recovery was increased from 64% to 96% and the total water cost was reduced from 1.24 to 1.08 $/m^3 and from 1.39 to 1.09 $/m^3 for both cases with and without heat recovery systems, respectively as illustrated in Figure 5.21. The difference in the water cost between MD with and without heat recovery was high (12%) when operating MD at low recovery values. However, at high water recovery values, the water cost of MD without heat recovery system became very close to the one of MD with heat recovery with difference of about 1% only. This was due to the fact that as the recovery was increased, the amount of hot brine was reduced and hence the amount of heat that can be recovered using the heat recovery system was reduced too. Increasing the MD recovery value by 20%, based on a reference recovery value of 80%, will lead to a reduction of 5.6% and 10.1% in the total water cost for cases with and without heat recovery systems, respectively as taken from the slope of the water cost variations graph in Figure 5.21.

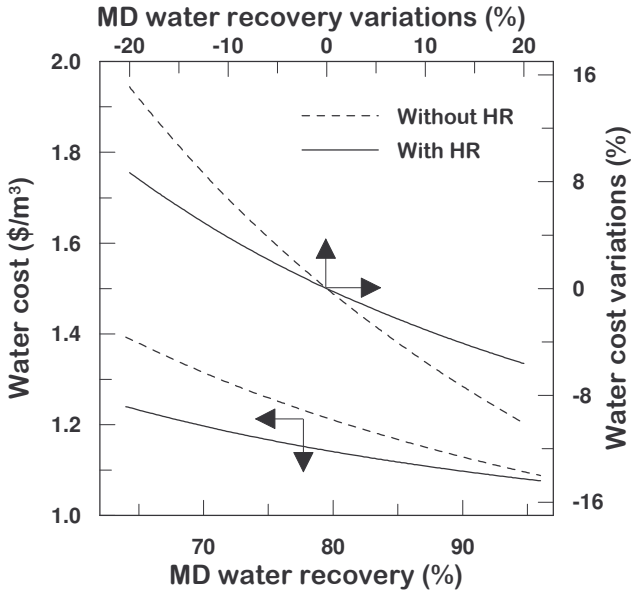

Figure 5.21 Effects of the MD water recovery on the total water cost of MD plants

Generally, the total water cost decreased as the water recovery was increased in all cases. This was due to the fact that smaller intake/discharge facilities and lower membrane surface area were required since higher flux values were obtained at higher recoveries. The pressure-driven membrane desalination plants showed similar sensitivity to the changes in the water recovery values for both cases with and without energy recovery systems. However, in case of MD, the sensitivity of the MD plant without heat recovery system was higher than the one with heat recovery system especially at low recovery values. This was due the dependency of the amount of heat to be recovered by the heat recovery system on the amount of the rejected brine which was varying with the recovery value.

ii) Temperature optimization in MD

An increase in the temperature difference (the driving force in membrane distillation) enhances the permeate flux per unit area, so decreasing the required membrane area and, therefore, the capital cost. On the other hand, a higher temperature difference requires more heat energy input which in turns increases the O&M costs. Consequently, an optimization between the membrane costs and the heating costs must be considered while increasing the operating temperatures of MD in order to obtain the best performance with minimum total unit cost of product water.

Figure 5.22 shows the results of this optimization. Considering MD without HR, the minimum water cost was 1.21 $/m^3 obtained when operating at a feed inlet temperature of 55 ^{o}C and a temperature gradient of 25°C. In case of MD with HR, the best condition was obtained when operating at a feed (inlet) temperature close to 60 ^{o}C and temperature gradient of 30^{o}C, with a total water cost of 1.14 $/m^3.

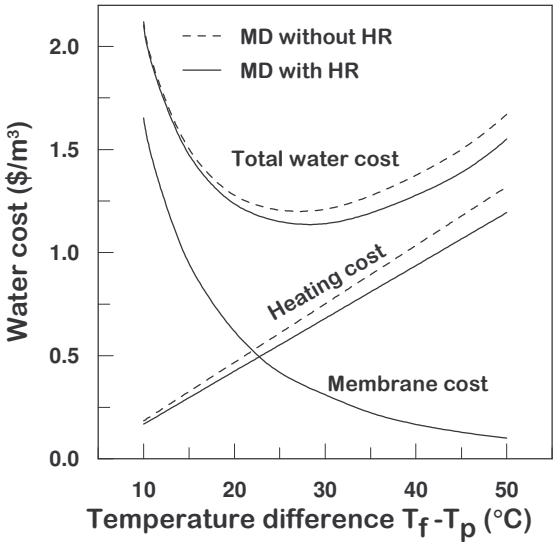

Figure 5.22 Effects of temperature difference on the product water cost for MD without HR system (dotted line) and for MD with HR system (solid line)

iii) Feed water concentration

The desalination plants were evaluated at situations where the feed concentration might vary. The total water cost was considered when the feed concentration changed between 10 to 25 g/L for brackish water and between 30 to 50 g/L for seawater.

UF-RO plants

The results showed that when the concentration was increased from 10 to 25 g/L in case of brackish water, the water cost increased from 0.34 to 0.39 $/m^3 for plants with energy recovery system and increased from 0.35 to 0.41 $/m^3 for plants without energy recovery system as shown in Figure 5.23. In case of seawater plants, the concentration was increased from 30 to 50 g/L and accordingly the water cost increased from 0.47 to 0.53 $/m^3 and from 0.51 to 0.58 $/m^3 in case of plants with and without energy recovery systems, respectively as shown in Figure 5.23.

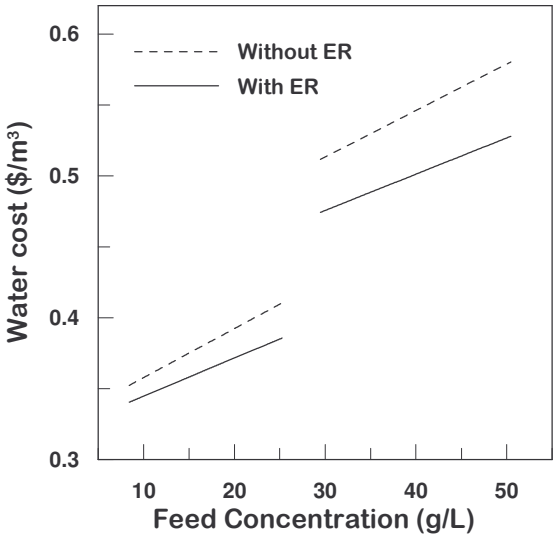

Figure 5.23 Effects of the feed concentration on the total water cost of UF-RO plants

UF-NF-RO plants

In this case, the results showed that when increasing the concentration from 10 to 25 g/L for brackish water plants, the water cost increased from 0.34 to 0.41 $/m^3 for plants with energy recovery system and increased from 0.35 to 0.42 $/m^3 for plants without energy recovery system as shown in Figure 5.24.

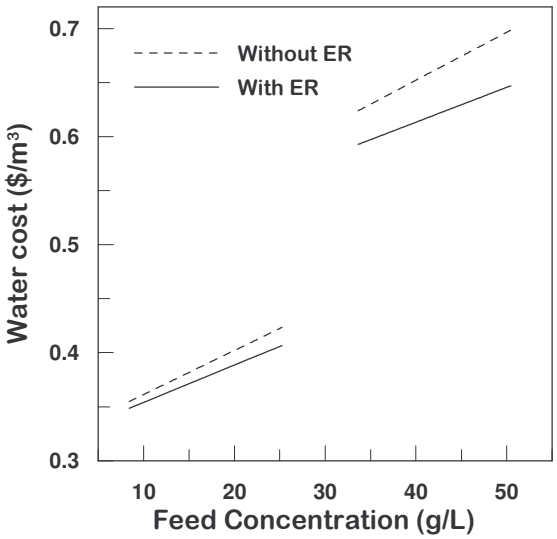

Figure 5.24 Effects of the feed concentration on the total water cost of UF-NF-RO plants

The water cost increased from 0.59 to 0.65 $/m^3 and increased from 0.62 to 0.70 $/m^3 for seawater plants with and without energy recovery systems, respectively as shown in Figure 5.25.

MD plants

In case of thermal processes, the total water cost was not affected by the change in the feed concentration for brackish and seawater plants as shown in Figure 5.25. The water cost was 1.13 $/m^3 and 1.20 $/m^3 for brackish water plants with and without heat recovery system, respectively. For seawater plants, the water cost was 1.14 $/m^3 and 1.21 $/m^3 for plants with and without heat recovery system, respectively.

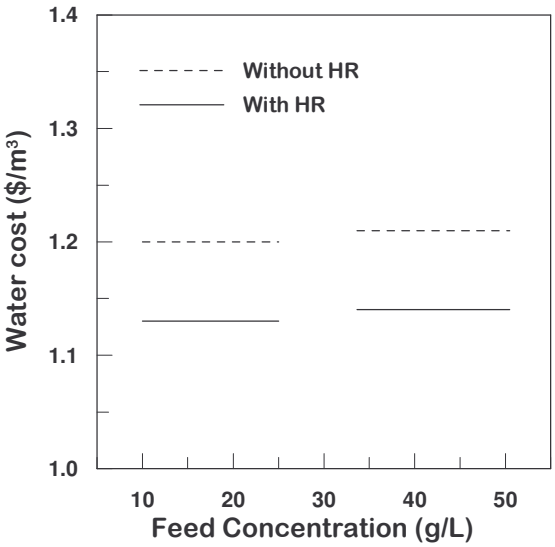

Figure 5.25 Effects of the feed concentration on the total water cost of MD plants

UF-NF-RO-MC_NF-MD_RO plants

These plants consisted of the integrated system which includes a membrane crystallization unit operated in the rejected stream of the NF unit and a membrane distillation unit operated in the brine stream of the RO unit. In this case, the results showed that when increasing the concentration from 10 to 25 g/L for brackish water plants, the water cost increased gradually from 1.09 to

1.13 $/m^3 for plants with energy recovery system and increased steadily from 1.38 to 1.42 $/m^3 for plants without energy recovery system as shown in Figure 5.26. The water cost increased slowly from 1.26 to 1.29 $/m^3 and increased from 1.50 to 1.53 $/m^3 for seawater plants with and without energy recovery systems, respectively as shown in Figure 5. 26.

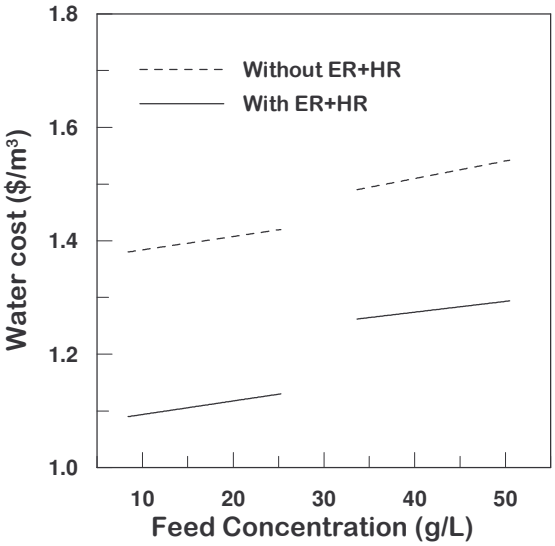

Figure 5.26 Effects of the feed concentration on the total water cost of UF-NF-RO-MC_NF-MD_RO plants

As shown above, the total water cost was increasing when the feed concentration increased in case of pressure-driven membranes. This raise in the total water cost was related to the additional requirement of membrane surface area due to the flux reduction as well as the additional power requirement due to higher pressure operations to overcome the additional resistance of osmotic pressure at higher concentration. On the other hand, MD plants were not greatly affected by the feed concentration. This was expected due to the fact that MD plants are thermal processes and they are not limited by osmotic pressure or concentration polarization phenomena. In case of integrated plants which contain pressure-driven membrane operations and membrane contactors (MD and MC), the total water cost was less sensitive to the changes in the feed concentration than the other cases.

iv) Membrane cost

The sensitivity of changing the membrane cost on the total water cost of desalination plants was studied. The reference values of the membrane cost was taken as 90 $/m^2 for UF membranes [11] and 30 $/m^2 for NF and RO membranes [17]. For study purposes, the membrane cost was changed by a factor of ±20% of these reference values in all cases.

UF-RO plants

An increase of 20% in the membrane cost contributed to an increase of 4.8% and 4.4% in the total water cost for plants with and without energy recovery system as shown in Figure 5.27.

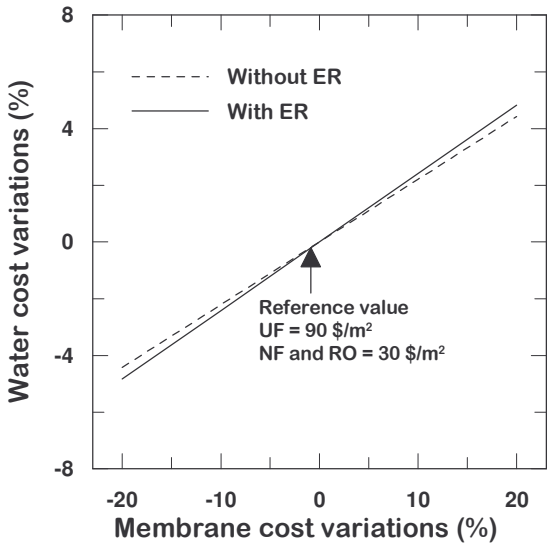

Figure 5.27 Effects of the membrane cost on the total water cost of UF-RO plants

UF-NF-RO plants

In this case, the results showed that the total water cost was increased by 4.8% for plants with energy recovery system and increased by 5.6% for plants

without energy recovery system when the membrane cost was increased by 20% as shown in Figure 5.28.

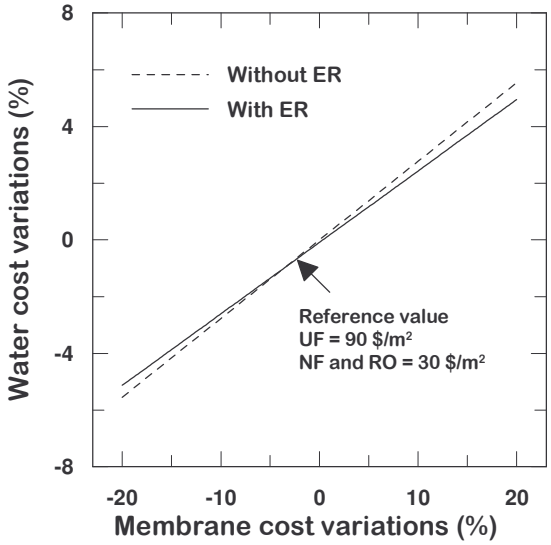

Figure 5.28 Effects of the membrane cost on the total water cost of UF-NF-RO plants

MD plants

In case of MD processes, the total water cost was increased by 5.6% and 5.4% for plants with and without heat recovery system, respectively when the MD membrane cost was increased by 20% as shown in Figure 5.29.

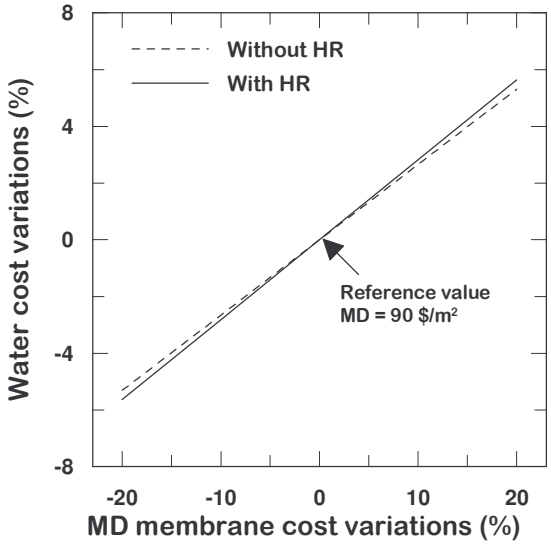

Figure 5.29 Effects of the membrane cost on the total water cost of MD plants

UF-NF-RO-MC_NF-MD_RO plants

In case of the integrated system, the changes in the total water cost were less evident than the other cases. The total water cost was increased only by 1.5% and 1.6% for plants with and without energy and heat recovery systems, respectively when the membrane cost was increased by 20% as shown in Figure 5.30.

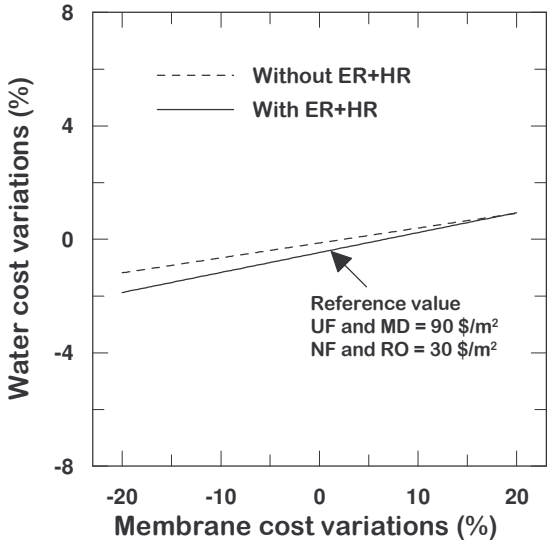

Figure 5.30 Effects of the membrane cost on the total water cost of UF-NF-RO-MC_NF-MD_RO plants

The results showed that when increasing the membrane cost per unit area by 20%, the total water cost was increased within the range 4.4-5.6% in all cases except the plant with the integrated systems. The plants with integrated systems showed better cost stability for the changes in the total water cost.

v) Electricity cost

The effects of the variations in the electricity cost were studied. The reference value was taken as 0.03 $/kWh [11]. The electricity cost was varied by a factor of ±20% of this reference value in all cases.

UF-RO plants

The total water cost was increased by 3.4% and 5.6% for plants with and without energy recovery system, respectively when the electricity cost was increased by 20% as shown in Figure 5.31.

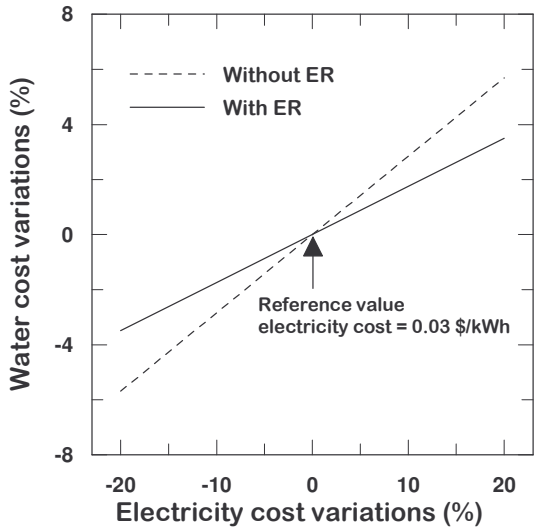

Figure 5.31 Effects of the electricity cost on the total water cost of UF-RO plants

UF-NF-RO plants

An increase of 20% in the electricity cost will result in increasing the total water costs by 3.6% and 5.2% for plants with and without energy recovery systems as shown in Figure 5.32.

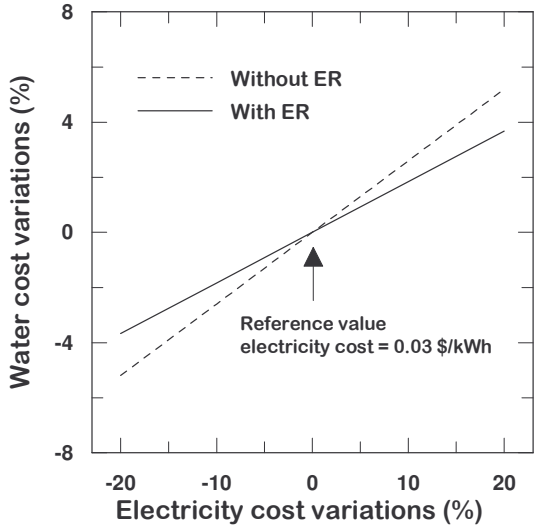

Figure 5.32 Effects of the electricity cost on the total water cost of UF-NF-RO plants

MD plants

In case of MD processes, the total water cost was not affected by the change in the electricity costs since the electricity power was used only as an auxiliary power supply for running the circulation pumps. The main energy input was the thermal energy provided as hot steam for heating the feed water. The total water cost was constant at 1.14 and 1.21 $/m^3 for plants with and without heat recovery systems, respectively.

UF-NF-RO-MC_NF-MD_RO plants

In case of the integrated system, the total water cost was increased only by 2.0% and 2.4% for plants with and without energy and heat recovery systems, respectively when the membrane cost was increased by 20% as shown in Figure 5.33.

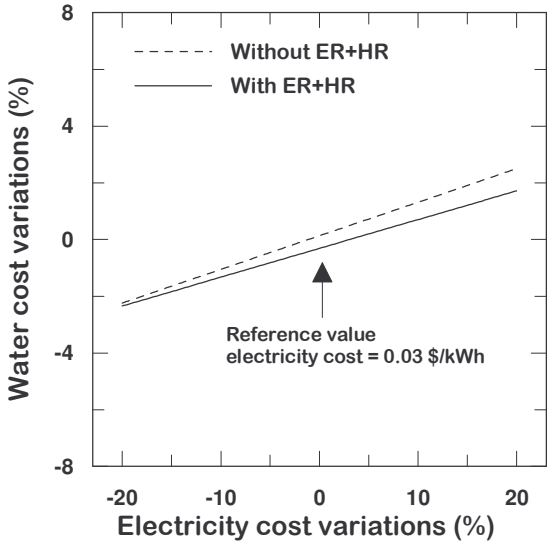

Figure 5.33 Effects of the electricity cost on the total water cost of UF-NF-RO-MC_NF-MD_RO plants

The results showed that the plants with energy recovery systems showed less sensitivity to the changes in the electricity cost than the ones without energy recovery systems in case of pressure-driven membrane operations. This means that the energy recovery system was useful in making the plants less sensitive to the changes in the electricity cost. The thermal process (MD) showed constant

water costs against the changes in the electricity costs since the electrical power was used only to operate auxiliary pumps and systems. Again, the integrated membrane system showed better stability to the changes in the electricity cost than the pressure-driven membrane operations alone.

vi) Steam cost

The cost of energy has a very wide variation among different countries and it might be even different in the same country depending on the location of the plant. In Thermal plants the main energy input is heat in the form of steam. This is applicable only for the cases where the steam was used as the heat energy input like in MD plants and the integrated system when using MD and MC processes. The reference value of the steam was taken as 7 $/ton [20]. The steam cost was varied by a factor of ±20% of this reference value in all cases.

MD plants

In case of operating MD process as a stand alone desalination plant, the total water cost increased by 10.6% for plants with heat recovery system and 11.4% for plants without heat recovery system when the steam cost was increased by 20% as shown in Figure 5.34.

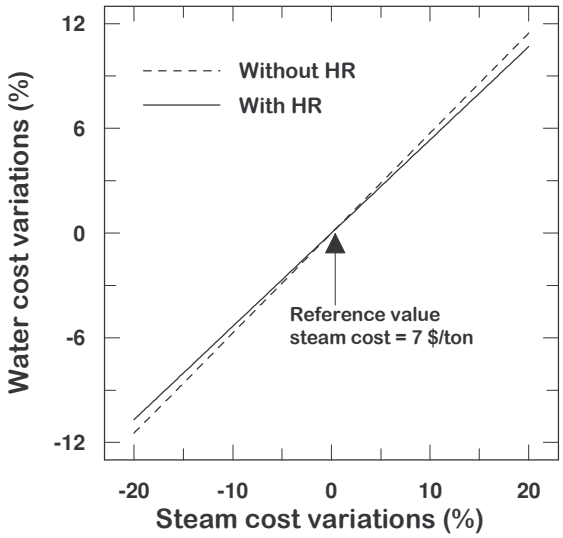

Figure 5.34 Effects of the steam cost on the total water cost of MD plants

UF-NF-RO-MC_NF-MD_RO plants

The integrated system showed less sensitivity to the changes in the steam cost. The total water cost increased by 4.7% for plants with energy and heat recovery systems and by 4.1% for plants without energy and heat recovery systems when the steam cost was increased by 20% as shown in Figure 5.35.

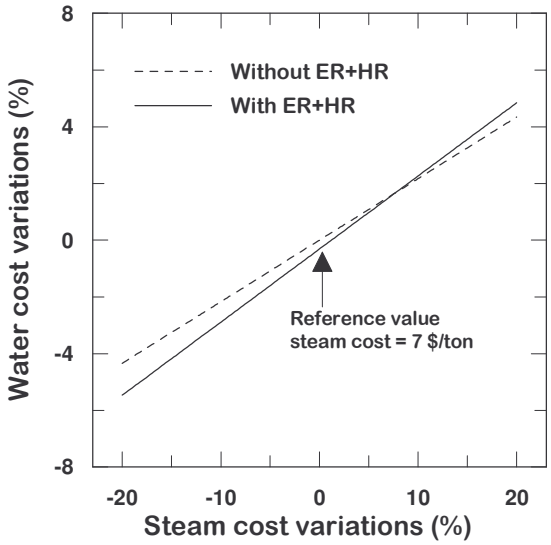

Figure 5.35 Effects of the steam cost on the total water cost of UF-NF-RO-MC_NF-MD_RO plants

The results showed that the MD process was very sensitive to any changes in the steam costs when operated as a stand alone desalination plant. However, when integrating MD and MC plants with the pressure-driven membrane operations, the system confirmed better stability against the changes in the steam costs.

vii) Membrane life

The operating life time of the membrane is a very important factor on the total water cost of desalination plants. In this study, the shortest life time was considered as 2 years and the longest life time was 8 years. The total water cost was evaluated when changing the life time of the membrane between these values for all cases. The results showed that the pressure-driven membranes had lower dependency on the membrane life than the thermal and integrated

processes. The total water cost was reduced from average values of about 0.8 $/m^3 at membrane life of 2 years to reach average values of about 0.5 $/m^3 at membrane life of 8 years for pressure-driven membrane operations as shown in Figure 5.36. The MD plants showed similar dependency on the membrane life as the integrated system. In this case, the total water cost decreased from 1.75 to 1.15 0.5 $/m^3 at membrane life time of 2 and 8 years, respectively. The total water cost showed higher sensitivity for the change in the membrane life time for values less than 4 years and the sensitivity started to be lower at membrane life time more than 4 years as shown in Figure 5.36.

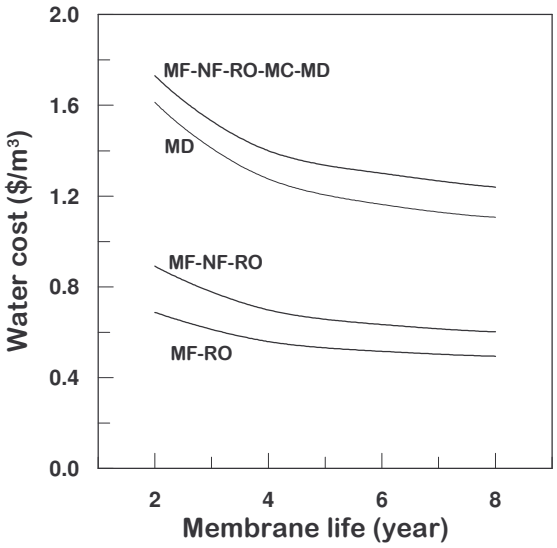

Figure 5.36 Effects of membrane life time on the total water cost of desalination plants

5.5 Conclusions

Exergy analyses were conducted to evaluate the performance of the desalination plants. The results showed that the exergy efficiency of the pressure-driven membrane operations was generally higher than of the thermal processes due to the high heat energy input in the thermal processes. The energy recovery device enhanced the exergy efficiency of the pressure-driven membranes from 22.6% before installation to 29.2% after installation of the energy recovery device.

Similarly, the exergy efficiency of the MD plant was improved after the utilization of the heat recovery system.

The integrated membrane system which contains pressure-driven membrane operations and membrane distillation/crystallization processes has great potentials to achieve the zero-liquid discharge goal since the amount of the rejected brine was very limited. Consequently, this leads to minimizing the environmental impact of desalination processes due to brine disposal.

Economical study and cost evaluation for several configurations of the integrated system were considered in order to estimate the total water cost. The lowest water cost was 0.51 $/m^3$ obtained when using the pressure-driven membrane operations (UF-NF-RO) with energy recovery device. In case of the integrated system which contained both pressure and thermal processes, the best combination was obtained when using the pressure-driven membranes combined with a membrane crystallization unit operating on the NF concentrated stream and a membrane distillation unit operating on the RO brine stream. The total water cost in this case was 1.27 $/m^3$ and 1.10 $/m^3$ for seawater and brackish water, respectively. Moreover, the combination of membrane crystallization units is very attractive especially if the salt crystals produced by the crystallization process are considered. This means that the desalination plant will produce both water and salt crystals. In this case, the price of the salts can cover the whole expenses of the desalination process.

Additionally, the total cost of water produced by the integrated system can be significantly reduced when using waste heat streams, as well as the use of alternative energy sources (solar, wind or geothermal).

The sensitivity analysis revealed that the pressure-driven membrane operations were very sensitive to the feed concentration and the cost of electricity

consumption. On the other hand, MD processes were not sensitive to the variation on the feed concentration or the electricity costs. The most sensitive parameter in the total water cost of the MD plant was the cost of steam which contributed to values as high as high as 5.8% in case of MD without heat recovery system. The best tolerance to the variation of these parameters was obtained when using the integrated membrane system of pressure-driven membranes and MDC processes.

Accordingly, it was demonstrated that combining several membrane processes in an integrated membrane system will offer essential improvements in efficiency, water cost and environmental impact which maintain the process sustainability and growth meeting the process intensification targets.

REFERENCES

[1] Drioli, E. and F. Macedonio, D 1.1.1 Report on raising public participation and awareness. MEDINA (2007).
[2] S. Al-Obeidani, H. Al-Hinai, M. Goosen, S. Sablani, Y. Taniguchi and H. Okamura, Chemical cleaning of oil contaminated polyethylene hollow fiber microfiltration membranes, Journal of Membrane Science 307 (2008) 299.
[3] R. Semiat, Desalination: Present and Future. IWRA, Water International 25 (2003) 54.
[4] N. Voutchkov, Desalination - water for the next generation. Filtration & Separation 42(2) (2005) 14.
[5] IDA Desalination yearbook, Water desalination report (2007-2008).
[6] R. Borsani, S. Rebagliati, Fundamentals and costing of MSF desalination plants and comparison with other technologies, Desalination 182 (2005) 29.
[7] K. Wangnick, 2000 IDA Worldwide Desalting Plants Inventory. 16 (2000).
[8] O.K. Buros, The ABCs of Desalting. The International Desalination Association, Topsfield, Massachusetts, USA, Second Edition (2000).
[9] Economic and Technical Assessment of Desalination Technologies in Australia, Project report (2002).
[10] U. Atikol, H.S. Aybar, Estimation of water production cost in the feasibility analysis of RO systems, Desalination 184 (2005) 253.

[11] H.M. Ettouney et al., Evaluating the Economics of Desalination Chemical Engineering Progress 98(12) (2002) 32.
[12] I. Dincer, The role of exergy in energy policy making, Energy Policy 30 (2002) 137.
[13] H. Mehdizadeh, Membrane desalination plants from an energy-exergy point of view, Desalination 191 (2006) 200.
[14] Y. Cerci, Exergy analysis of a reverse osmosis desalination plant in California, Desalination 142 (2002) 257.
[15] H.S. Choi et al., Performance improvement of multiple-effect distiller with thermal vapor compression system by exergy analysis, Desalination 182 (2005) 239.
[16] A. Criscuoli, E. Drioli, Energetic and exergetic analysis of an integrated membrane desalination system, Desalination 124 (1999) 243.
[17] F. Macedonio, E.C., E. Drioli, Integrated membrane systems for seawater desalination: energetic and exergetic analysis, economic evaluation, experimental study, Desalination 203 (2007) 260.
[18] I. Dincer, M.M. Hussain, I. Al-Zaharnah, Energy and exergy use in the utility sector of Saudi Arabia, Desalination 169 (2004) 245.
[19] A. Malek, M.H., J.C. Ho, Design and economics of RO desalination, Desalination 105 (1996) 245.
[20] A.M. Helal, A.M.E.-N., E. Al-Katheeri, S. Al-Malek, Optimal design of hybrid RO/MSF desalination plants Part I: Modeling and algorithms, Desalination 154 (2003) 43.
[21] http://matche.com/EquipCost/Exchanger.htm. 2007.
[22]http://dh-crystal.en.alibaba.com/product/50388538/51668258/Inorganic_Salt/Sodium_chloride_NaCl_.html.
[23]http://www.ecplaza.net/tradeleads/seller/2484891/sell_magnesium_sulphate.html.
[24] http://www.alibaba.com/catalog/10362154/CaCo3.html.
[25] http://www.chemistrystore.com/sodium_carbonate.htm.
[26] J.H. Hanemaaijer, J. van Medevoort, A.E. Jansen, C. Dotremont and E. van Sonsbeek, Memstill membrane distillation - a future desalination, Desalination 199 (2006) 175.
[27] A.M. Alklaibi and N. Lior, Membrane-distillation desalination: Status and potential, Desalination 171 (2005) 111.
[28] B. Van der Bruggen, Desalination by distillation and by reverse osmosis – trends towards the future, Membrane Technology, February/2 (2003) 6
[29] C. Fritzmann, J. Löwenberg, T. Wintgens and T. Melin, State-of-the-art of reverse osmosis desalination, Desalination 216 (2007) 1.
[30] A. Amulla et. al., Developments in high recovery brackish water desalination plants as a part of the solution to the water quantity problems, Desalination 153 (2002) 237.

CHAPTER 6
REALIZATION OF THE SEMI-PILOT PLANT OF THE INTEGRATED MEMBRANE SYSTEM

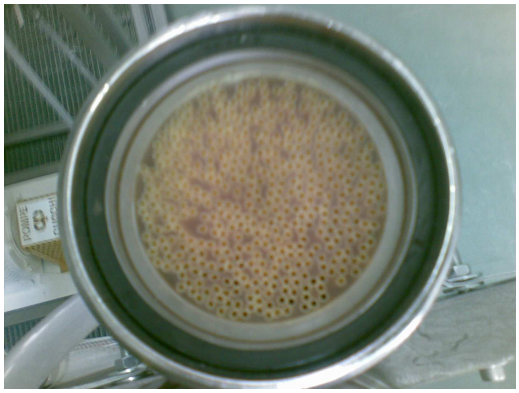

A semi-pilot plant of the integrated membrane system was designed and assembled based on the results obtained by the computer simulations and the preliminary experiments done for each unit individually in the previous chapters. The integrated plant consisted of the following subsystems:

6.1 The UF pretreatment unit

The ultrafiltration unit contains a vessel of 100 L capacity. The UF membrane element is submerged in the vessel as shown in Figure 6.1. The feed solution is introduced to the UF vessel using a feed pump. The filtration is done using a filtrate suction pump to obtain the required permeate flow rate. Air blower is used to introduce air bubbles in the UF vessel tank to prevent suspended contaminant adhesion to the membrane surface by shaking the membrane fibers. The UF unit was operated at 95% recovery.

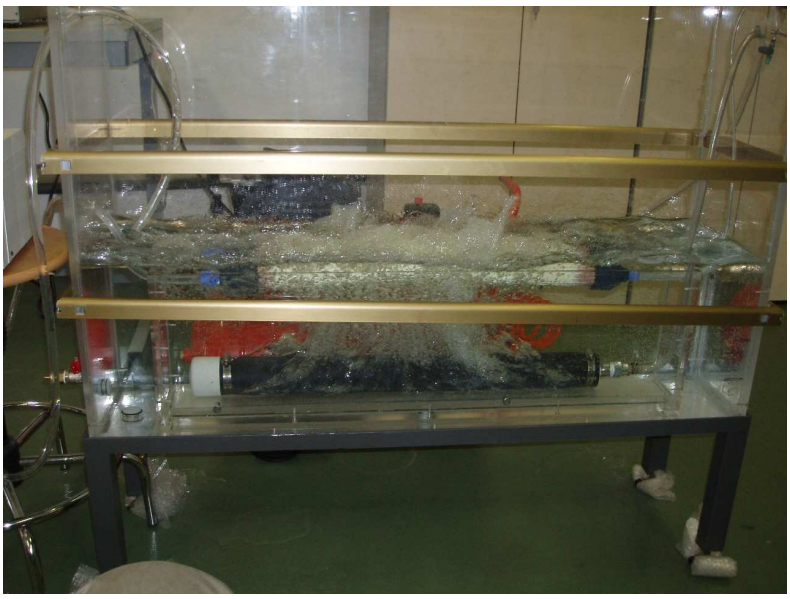

Figure 6.1 The UF pretreatment unit

6.2 The NF/RO plant

The NF/RO plant was made by MATRIX DESALINATION INC as shown in Figure 6.2. This plant can be used as an NF or as an RO plant depending on the installed membranes inside the vessels. The plant contains three vessels connected in series and each vessel can have one membrane module. The maximum operating flow and pressures are 270 L/h and 65 bars, respectively.

Figure 6.2 The NF/RO plant

The NF membrane elements used in the pilot plant were made by APPLIED MEMBRANES INC. and the RO membrane elements were made by OSMONICS DESAL. The specifications of these elements are shown in Table 6.1.

Table 6.1 NF and RO membrane element specifications

	NF elements	RO elements
Model	MN 2540 A9	AD 2540 FF
Size (Diameter×Length)	2.5×40 (inch)	2.5×40 (inch)
Surface area	2.4 m2	2.4 m2
Average rejection	97 %	99.6 %

The high pressure pump of the NF/RO plant is a plunger pump CP 1221 made by CAT PUMPS. The maximum feed flow is 16 L/min and a pressure range 7-

140 bars. The NF and RO were operated at water recovery rates of 70% and 60%, respectively.

6.3 The MD/MDC plant

The membrane distillation/crystallization plant is designed and assembled in the laboratory. It consists of the MD membrane module, the feed and permeate pumps, the feed and permeate tanks, the feed heating system and the permeate weighting balance as shown in Figure 6.3.

Figure 6.3 The MD/MDC plant

The membrane module was built at the laboratory (home-made) using polypropylene hydrophobic hollow fibers provided by Membrana (Accurel S6/2). The specifications of this home-made module are shown in Table 6.2.

Table 6.2 MD home-made MD/MDC module specifications

Module length	1 m
Module Inner diameter	85 mm
Casing material	Stainless steel 316
Number of fibers	100
Fiber inner diameter	1800 µm
Fiber outer diameter	2700 µm
Nominal pore size	0.2 µm
porosity	75%

The feed was recirculated inside the hollow fibers using a recirculation pump of a variable speed made by POMPE CUCCHI model NBX 24. This pump was connected to a variable frequency driver MC Series made by AC Tech. The purpose of this driver was to vary the speed of the feed pump (i.e. varying the feed flow rate) by changing the electric current frequency. In addition, it has the possibility to be connected to a workstation computer through a serial communication RS-485 cable. The heating system was used to heat the feed solution before entering the membrane fibers. It consisted of an immersion heater and a heat exchanger. The immersion heater was made by VWR model 1122S with a digital controller and a serial communication connectivity option. The heat exchanger was a tube-and-shell exchanger made of stainless steel 316L material. The permeate solution is recirculated through the shell side of the membrane module in counter-current configuration using LOWARA BG recirculation pump. The transmembrane flux was estimated by measuring the weight variations with time in the distillate tank using the weighting balance. The weighting balance was made by HEDW with accuracy of ±0.01 kg and a serial communication connectivity option. The flow meters were F-400 series made by BLUE WHITE INDUSTRIES with measuring capacity up to 15 L/min. The temperature was monitored using 4-channel datalogging thermometers type 800024 with RS-232 connectivity feature.

6.4 Semi-pilot plant experimental tests

Synthetic seawater was prepared according to the same composition of the Oman Gulf Sea [1]. This composition is shown in Table. 6.3.

Table 6.3 Oman Gulf Seawater composition [1]

Ion	Concentration (g/L)
Ca	0.499
Mg	1.554
Na	12.902
K	0.468
CO_3	0.000
HCO_3	0.174
SO_4	3.241
Cl	23.214
TDS	42.052

6.4.1 MDC operation on NF concentrate

The feed seawater was first introduced to the UF unit which was operated at a water recovery of 95% before introducing it to the NF unit. The filtrated stream from the UF was then introduced to the NF unit which was operated at water recovery of 70%. The concentrated stream from the NF unit was used as the feed solution in the MD/MDC unit. The GLMC unit (discussed in chapter 2) was used to precipitate calcium ions as $CaCO_3$ before transferring the concentrated stream to the MD/MDC unit. The initial concentration of this solution was 69.5 g/L and its chemical composition is shown in Table 6.4.

Table 6.4 The chemical composition of the NF concentrate

Ion	Concentration (g/L)
Ca	0.1
Mg	4.8
Na	21.2
K	0.7
CO_3	2.1
HCO_3	0.4
SO_4	10.0
Cl	30.1
TDS	69.5

The feed was collected in the MD/MDC feed tank and then recirculated inside the fibers of the membrane using the feed recirculation pump. The feed inlet and outlet temperatures were 52 ^{o}C and 47 ^{o}C, respectively. The permeate inlet and outlet temperatures were 27 ^{o}C and 32 ^{o}C, respectively.

In this case the MD/MDC was operated as an MDC unit since the feed was recirculated inside the fibers allowing its concentration to increase with time until it reached the supersaturation level when crystals started to appear.

The results showed that the first crystal appeared after 135 minutes at feed concentration of 273 g/L (based on NaCl concentration) as shown in Figure 6.4. The MD transmembrane flux remained stable at values around 1.1 kg/h.m^2 with minimum decrease due to the reduction in the activity coefficients at higher feed concentrations.

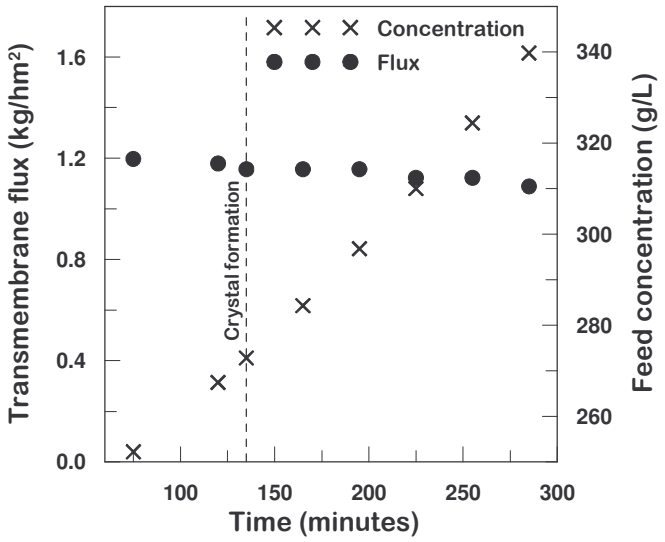

Figure 6.4 Transmembrane flux and feed concentration versus operation time of MDC operated on the NF retentate

The crystal size distribution (CSD) was estimated by collecting crystal samples at time interval of 30 minutes from the first appearance and the results are shown in Figure 6.5.

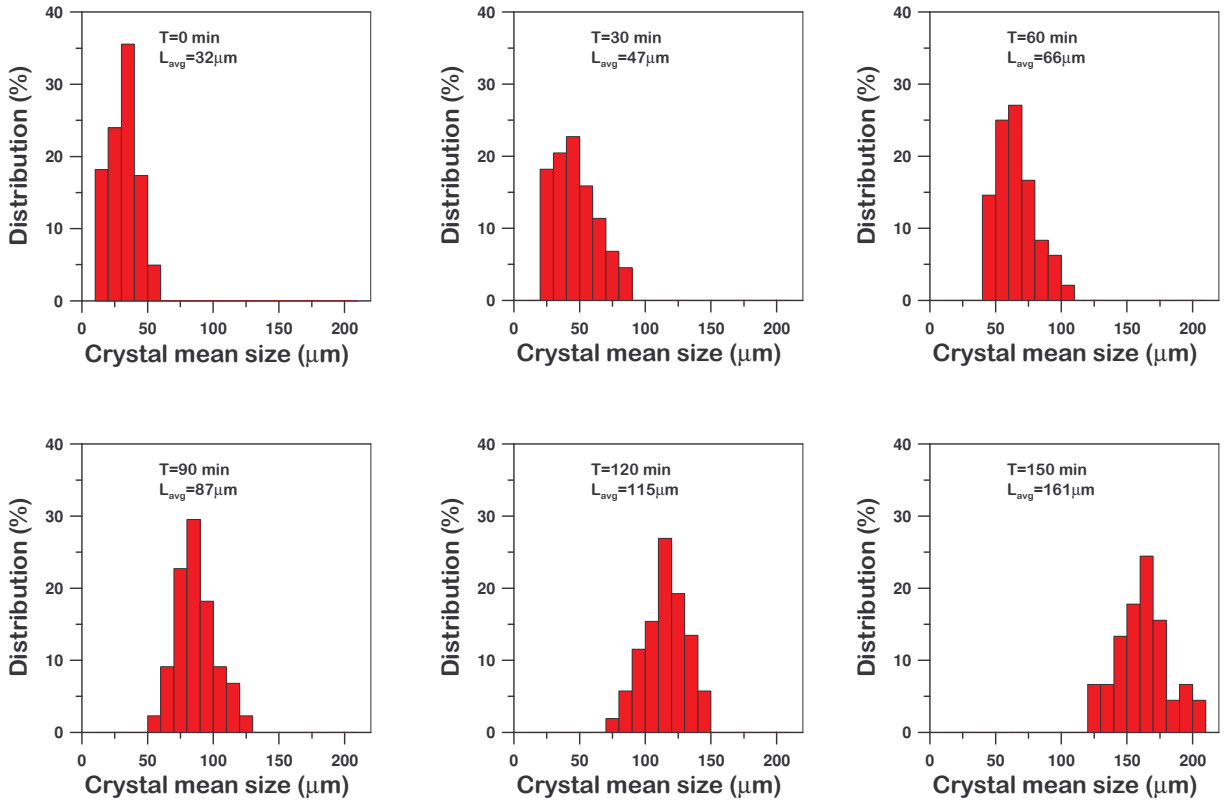

Figure 6.5. CDS of the crystals obtained by the MDC operated on NF retentate

The CSD results showed that the mean crystal size was increasing with elapsed time due to crystal growth process having the same trend as in the preliminary experiments discussed in chapter 4. The mean crystal length was 32, 47, 66, 87, 115 and 161 μm at elapsed time of 0, 30, 60, 90, 120 and 150 minutes, respectively. The values of the coefficient of variation (CV) varied from 12 to 34%.

6.4.2 MDC operation on RO brine

In this case, the brine stream from the RO plant was used as the feed solution in the MDC plant. The initial concentration of this stream was 77.7 g/L and its chemical composition is shown in Table 6.5.

Table 6.5 The chemical composition of the RO brine

Ion	Concentration (g/L)
Ca	0.1
Mg	0.4
Na	25.0
K	0.9
CO_3	0.0
HCO_3	0.2
SO_4	0.8
Cl	50.3
TDS	77.7

The plant was operated at feed inlet temperature of 52 ^oC and outlet temperature of 47 ^oC. The permeate inlet and outlet temperatures were 27 ^oC and 32 ^oC, respectively. The results showed that the first NaCl crystals started to show up after 100 minutes at feed concentration of 305 g/L as shown in Figure 6.6.

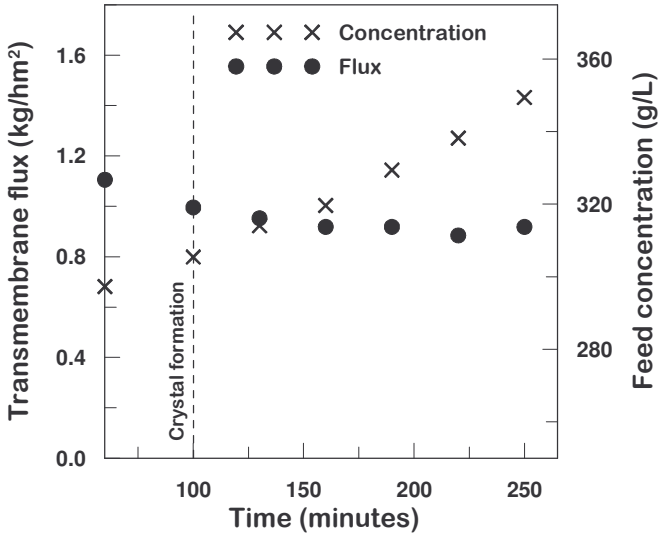

Figure 6.6 Transmembrane flux and feed concentration versus operation time of MDC operated on the RO brine

Once more, the transmembrane flux remained almost constant at values around 0.95 kg/h.m^2 and started to decrease gradually as the feed concentration

increasing which caused feed activity coefficient to decrease and hence creating this minor flux reduction.

The CSD of the crystals obtained by the MDC operated on the RO brine showed sharper distribution trends than the ones obtained from the NF retentate as shown in Figures 6.7. The mean crystal length was 26, 32, 51, 73, 99 and 139 μm at elapsed time of 0, 30, 60, 90, 120 and 150 minutes, respectively. The values of the coefficient of variation (CV) varied from 10 to 22%.

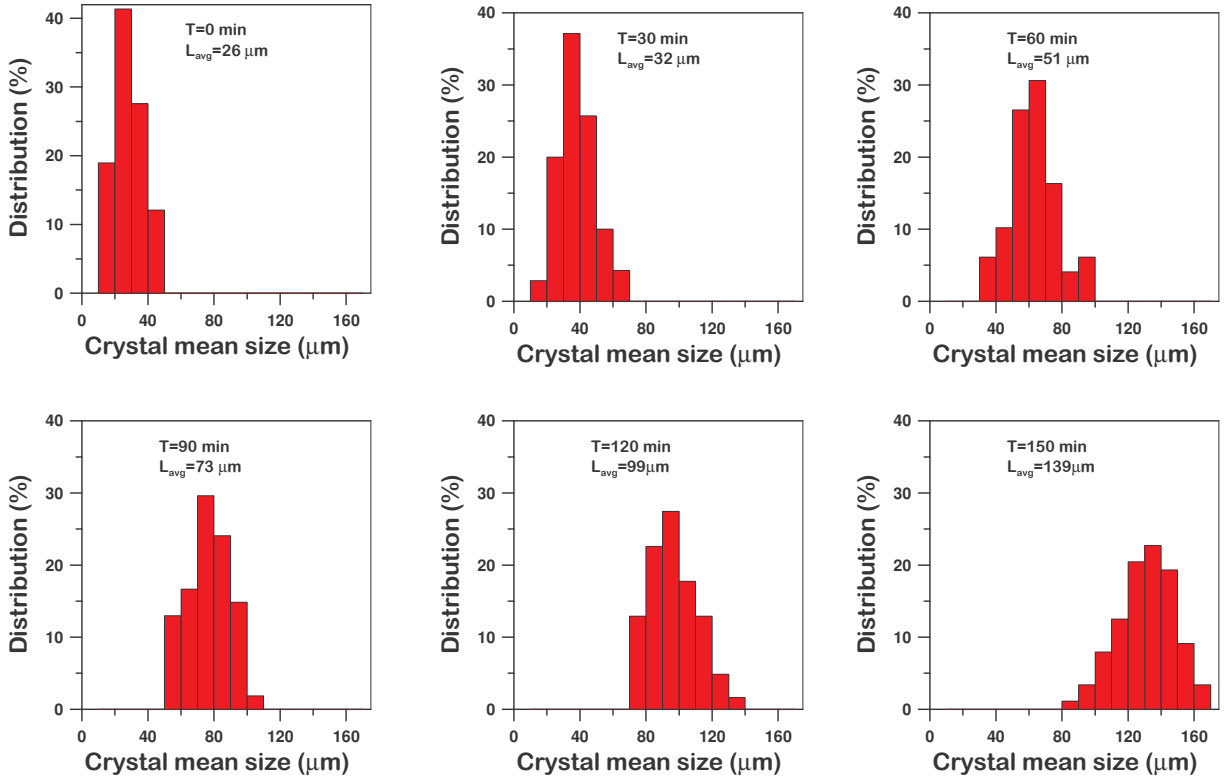

Figures 6.7 CDS of the crystals obtained by the MDC operated on RO brine

The growth was increasing as the supersaturation of the feed solution was increased. There was existing a linear relationship between the plot of $ln(G_r)$ versus $ln(S-1)$ as shown in Figure 6.8 in accordance with the results found in the literature [2, 3].

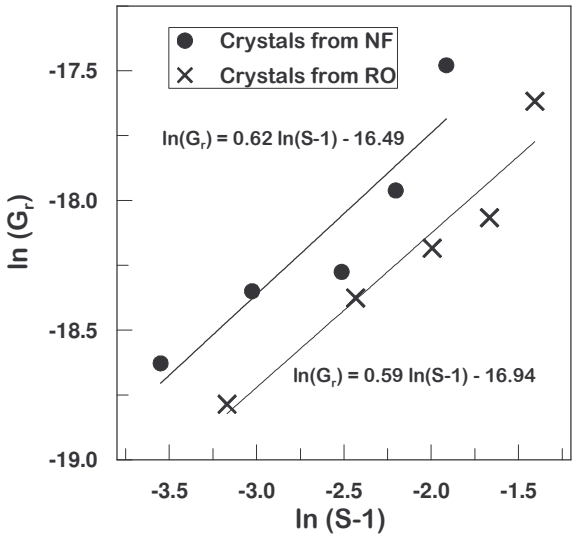

Figure 6.8 *ln(G_r)* versus *ln(S-1)*

In addition, the growth rate in case of the crystals obtained by the MDC operated on the RO brine was less than the growth rate of the crystals obtained by MDC when operated at the NF retentate as shown from the CSD plots as well as from the plot of *ln(G_r)* versus *ln(S-1).* This was due the presence of other salt crystals which embodied as impurities that induced a heterogeneous nucleation at lower critical supersaturation and resulted in higher growth rate in case of NF retentate. However, since most of the bivalent salts have be already rejected by the NF membranes, NaCl was the major salt in the RO brine and there was lower impurities compared to the NF retentate and therefore the growth rate in this case showed lower values and sharper distributions than the case of NF retentate. Furthermore, the crystals have cubic block-like geometry which corresponded with the characteristics of the NaCl crystals in case of RO brine, but these crystals have been stretched out in case of NF retentate as shown from the images obtained using the optical microscope (Figure 6.9 a. and b.).

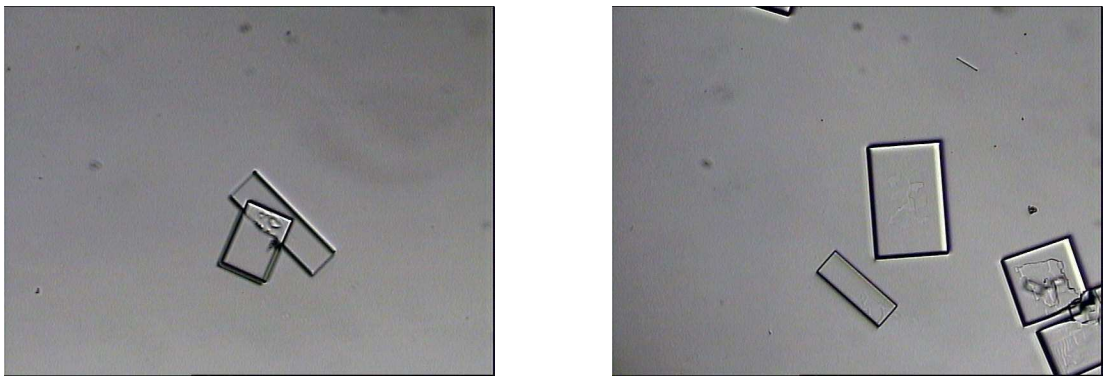

(a) Crystals from NF retentate

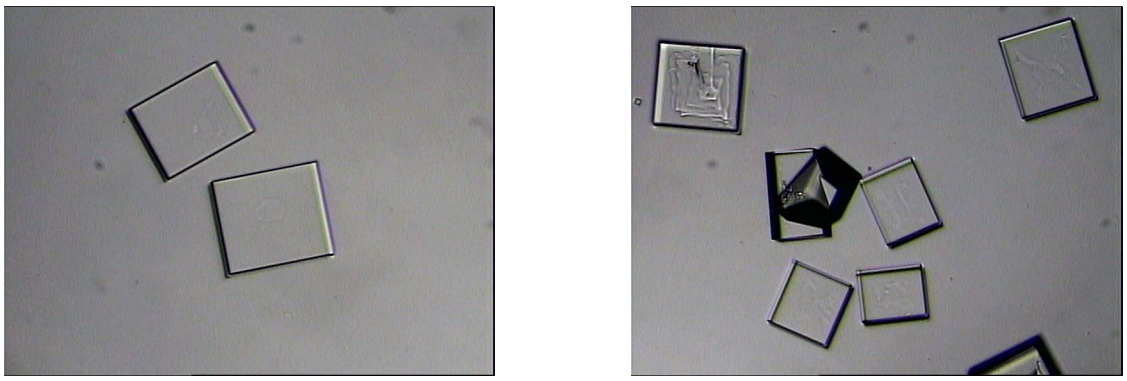

(b) Crystals from RO brine

Figures 6.9 Morphology of the crystals (magnification ×10)

6.4.3 MD operations on real seawater as a stand-alone desalination plant

MD was operated as a stand-alone desalination plant using real seawater in order to ensure its performance and stability. The feed seawater was collected from Amantea (Mediterranean Sea Italy) and its composition was analyzed using 861 Advanced Compact ion chromatography made by Metrohm and the results are shown in Table 6.6.

Table 6.6 The Amantea seawater composition

Ion	Concentration (g/L)
Ca	0.354
Mg	1.414
Na	11.906
K	0.411
CO_3	0.000
HCO_3	0.208
SO_4	3.244
Cl	26.566
TDS	44.103

The plant was operated continuously at the same temperatures and flow rates with feed recirculation. The transmembrane flux variation with time and concentration were measured and the results are shown in Figure 6.10.

The results showed that the transmembrane flux was steady and there was trivial decline due to the reduction in the activity coefficient due to the increase in the feed concentration.

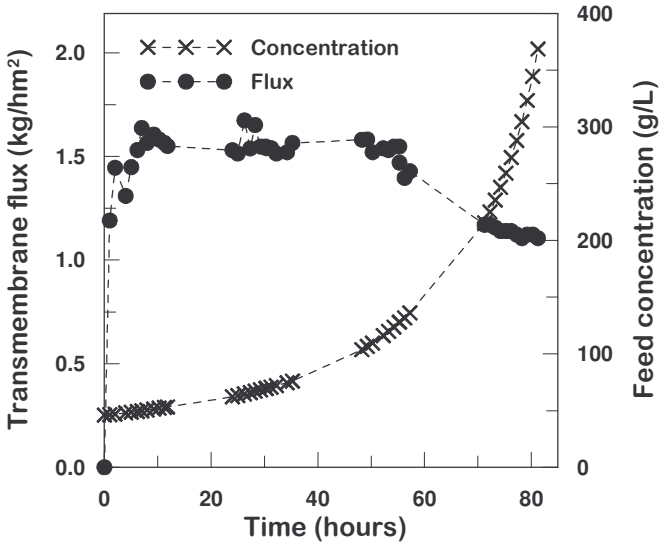

Figure 6.10 MD performance in seawater desalination

The conductivity of the permeate was measured during the test in order to confirm the stability of the membranes and make sure that they do not loss their

hydrophobicity during operation. The results proved that the conductivity of the permeate was not only constant throughout the test run, but also it was reducing which prove that only pure water was allowed to pass through the membrane which caused further dilution to the permeate and therefore reducing its conductivity as shown in Figure 6.11. This demonstrate that the MD can be operated for seawater desalination application since it showed steady flux and it did not loss hydrophobicity even at high concentration feeds. Moreover, in case of performance detritions, it was found that washing the MD membranes using citric acid solution (0.2% weight ratio) and pH around 3.5 was sufficient to retain the original performance of the MD.

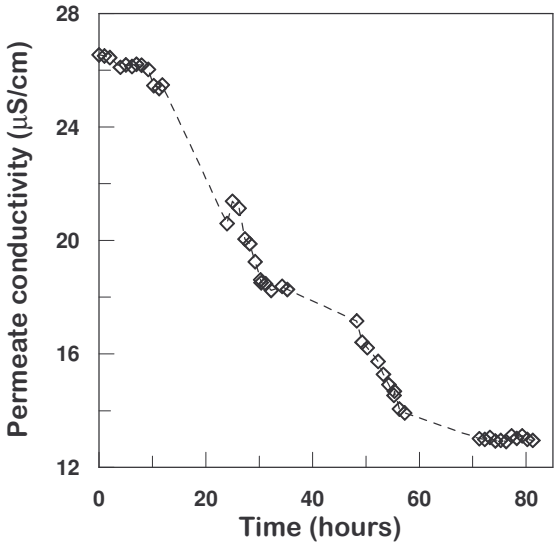

Figure 6.11 Permeate conductivity versus operation time

6.5 Conclusions

The semi-pilot desalination plant of the integrated membrane system was operated using synthetic and real seawater in order to confirm the performance and process stability. The transmembrane flux was stable during the operation.

The MDC was able to produce salt crystals from the NF retentate and the RO brine streams. The CSD of the crystals obtained by the MDC operating on the

RO brine showed sharper distribution trends than the ones obtained from the MDC when operating on the NF retentate.

In addition, the MD unit was operated as a stand-alone desalination process using real seawater and the results showed that it was stable and the membrane did not loss it's hydrophobicity during the operation.

PROSPECTIVE APPLICATIONS AND RESEARCH ASPECTS

- Designing a compact version of the integrated membrane system in a small package that can be installed in remote areas or small tourism resorts.
- Coupling the integrated membrane system with the renewable energy sources like wind, solar, geothermal, etc. in order to reduce the operating costs.
- Studying the possibility of applying MD contactors in oil removal from production water in the oil industry
- Develop the costing approach and software to estimate the total and operation costs of installing such plants or the costs of introducing the system for an existing water desalination plants.

REFERENCES

[1] S. Al-Obeidani, H. Al-Hinai, M. Goosen, S. Sablani, Y. Taniguchi and H. Okamura, Chemical cleaning of oil contaminated polyethylene hollow fiber microfiltration membranes, Journal of Membrane Science 307 (2008) 299.
[2] E. Drioli E, A. Criscuoli A, E. Curcio, Membrane Contactors: Fundamentals, Applications and Potentialities. Elsevier, Amsterdam (2006).
[3] E. Curcio, G. Di Profio, E. Drioli, Recovery of fumaric acid by membrane crystallization in the production of L-malic acid, Separation and Purification Technology 33 (2003) 63.

APPENDIX 1
PROGRAMMING CODE OF GLMC SIMULATION

```
Dk=(2*porerad/3)*(8*RR*(T+273)/(pi*MWG))^0.5
km=Dk*(eps/(delta*tau))
%km=DA*(eps/(delta*tau))
%km=1e-2
%%%%%%
%%%%%% Liquid phase mass transfer Coeff. kL  %%%%
Gz=(vL*dfiberin^2)/(DA*L)
%Gz=(vL*dfiberin)/(DA)
%Sh=(3.67^3+1.62^3*Gz)^(1/3)   %% for 10<Gz<20
Sh=3.67                        %% for Gz<10
Sh=1.62*Gz^(1/3)               %% for Gz>20
%Sh=0.85*((dfiberin/dfiber)^0.45)*((dh_L/L)^0.25)*Reyn_L^(1/3)*(mu/(ro*DA))^(1/3)
%Sh=0.9*Reyn_L^(1/2)*(mu/(ro*DA))^(1/3)
%
%
kL=(DA/dfiberin)*Sh

%%%%%%%%%%%%%%%%%%%%%%
%Gz=1000
%vL=Gz*L*DA/dfiberin^2
%Q_L=vL*area_L
%%%%%%%%%%%%%%%%%%%%%%%%%%%% Enhancement factor E %%%%%%%%%%%%%%%%%%%%%%%%
%%%%%%%%%%%%%%%%%%%%%%%%%%%%NOREACTION %%%%%%%%%%%%%%%%%%%%%%%%%%%%%%%%
E=1;H=1;m=1;
%%%%%%%%%%%%%%%%%%%%%%%%%%%%%%%%%%%%%%%%%%%%%%%%%%%%%%%%%%%%%%%%%%%%%%%%%%%
%%%%%%%%%%%%%%%%%%%%%%%%FIRST ORDER REACTION  %%%%%%%%%%%%%%%%%%%%%%%%%%%%%
%%% CHECK Gz NUMBER > 1000 BULK CONCE. CAN BE NEGLECTED
%%% CHECK Ha NUMBER > 2 HIGH REACTION REGIME ===> E=Ha renewal theory
m=1; % 0.1<m<1
k1=1000;  % 0.01<k1<10000
%Ha=((k1*DA)^0.5)/kL
%E=Ha %%%% HIGH REACTION REGIME
%
%%%%%%%%%%%%%%%%%%%%%%% SECOND ORDER REACTION  %%%%%%%%%%%%%%%%%%%%%%%%%%%%
%
DB=1e-9;  %%%(m2/s)  Diffusion Coeff. of Liquid phase reactant
v_B=1; %%% stoichiometric coeefficent
CB_0=.1; % Concentration of Liquid phase reactant [mol/m3]
m=1; % 0.1<m<1
k1_1=1000;  % 0.01<k1<10000
Ha=((k1_1*CB_0*DA)^0.5)/kL
%E=Ha %%%% HIGH REACTION REGIME Gz NUMBER > 1000 ((surface renewal theory))
%
%%%% For Low Gz Number
%
E_inf=(1+(CB_0*DB)/(v_B*CA_gas*DA))*(DA/DB)^(1/3)  %%Modified enhancement factor
%E=-(Ha^2)/(2*(E_inf-1))+((Ha^4/(4*(E_inf-1)^2))+(E_inf*Ha^2/(E_inf-1))+1)^0.5 %%DeCoursey solution
%
%%%%%%%%%%%%%%%%%%%%%%   Overall mass transfer Coeff.  K  %%%%%%%%%%%%%%%%%%
K=((1/km)+(1/(m*kL*E)))^-1
%
%K=m*E*kL    % for reactive absorption
%%%%%%%%%%%%%%%%%%%%%%%%%%%%%%%%%%%%%%%%%%%%%%%%%%%%%%%%%%%%%%%%%%%%%%%%%%%
%%%%%%%%%%%% Initialization %%%%%%%%
f=E/1.8;  %%% f=E/1.8 without reaction and f=E/2 with reaction
CA_z=CA(1)
CA_liquid=(CA(1)+CA_z)/2
delta_CA=(CA_gas-CA_liquid)
n_A=K*delta_CA  %%% [mol/m2.s]
```

```
CA_z_new=CA(1)+(n_A/Q_L)*pi*dfiber*nf*delta_z
pi*dfiber*nf*delta_z;
%CA_z_new=CA(1)+(n_A/Q_L)*dA
%%%%%%%%%%%%%%%%%%%%%%%%%%%%%%%%%%%%%%%%%%%%%%%%
for i=1:k,
    %CA_z=CA(1);
    while ((abs(CA_z-CA_z_new)) > 1e-5)
        CA_z=CA(i)+(n_A/Q_L)*pi*dfiber*nf*delta_z;
        %CA_z=CA(i)+(n_A/Q_L)*dA;
        CA_liquid=(CA(i)+CA_z)/2;
        delta_CA=(CA_gas-CA_liquid);
        n_A=K*delta_CA;   % [mol/m2.s]
        CA_z_new=CA(i)+(n_A/Q_L)*pi*dfiber*nf*delta_z;
        %CA_z_new=CA(i)+(n_A/Q_L)*dA;

    end

    %SS(i)=(n_A/Q_L)*pi*dfiber*nf*delta_z;
    N_A(i)=n_A;
    Flow_co2(i)=n_A*pi*dfiber*nf*delta_z;
    CA(i+1)=CA_z_new;
    CA_z=CA(i);
    SS(i)=n_A*pi*dfiber*nf;

end
%FLUX=(N_A)*f*3600
%CA
%CA_average=mean(CA)
%NN_A_sum=sum(N_A)  %*3600
%NN_A_mean=mean(N_A) % [mol/m2.s]
Flux=mean(N_A)*f*3600 % [mol/m2.h]
%Flow_co2_in=Flux*area %[mol/h]
%Flow_co2_in=sum(Flow_co2)*3600   %[mol/h]
%Flow_mean=mean(Flow_co2)
%Flux_co2_in=Flow_co2_in/pi*dfiber*nf*L*3600
%Flux_mean=mean(Flow_co2)/pi*dfiber*nf*L*3600
%Flow_mean=mean(Flow_co2)*3600
%aa=pi*dfiber*nf*L
%area
%SS
%VV=sum(SS)*L
%XX=mean(SS)*L*3600
%NNN_A=XX/(pi*dfiber*nf*L)
sulaiman
Gas_in=NN_A*area*3600*44       %%% Gas in flow rate [g/h]
Gas_in=Gas_in/Gas_density      %%% Gas in flow rate [L/h]
plot(CA)
pause
plot(N_A)
pause
peaks(CA)
pause
z=peaks(CA)
surf(CA)
colormap hsv
colorbar
```

APPENDIX 2
PROGRAMMING CODE OF MD SIMULATION

```
%%%%%%%%%%%%%%%%%%%%%%%%%%     INITIALIZATION   %%%%%%%%%%%%%%%%%%%%%%%%%%
k=100; %%%%%%% number of differential areas %%%%
A=[0];
TTF=repmat(A,k+1,1);
TTP=repmat(A,k+1,1);
TT1=repmat(A,k+1,1);
TT2=repmat(A,k+1,1);
TPC=repmat(A,k+1,1);
CC=repmat(A,k,1);
CCm=repmat(A,k,1);
QQF=repmat(A,k+1,1);
CPC=repmat(A,k,1);
NN=repmat(A,k,1);
Qf=repmat(A,k,1);
Qp=repmat(A,k,1);
Qc=repmat(A,k,1);
Qv=repmat(A,k,1);
Q_Total=repmat(A,k,1);
%DA=repmat(A,k+1,1);
DL_L=repmat(A,k,1);
%%%%%%%%%%%%%%%%%%%%%  PROCESS CONSTANTS  %%%%%%%%%%%%%%%%%%%%%%%%%%%%%%%%
P=1.01325e5; % total pressure= atmospheric pressure
MWW=18; %Moleculare weight of water (g/mole)
MWZ=23+35.5; %%% %Moleculare weight of NaCl (g/mole)
R=8287.05; % J/K*kmole
dens_w=980;  % pure water density
Dsw=25.7e-6;  %1.15e-9; % %%(m2/s)  Diffusion Coeff. of water vapor
%%%%%%%%%%%%%%%%%%%%%%%     INPUTS      %%%%%%%%%%%%%%%%%%%%%%%%%%%%%%%%%%%
%%%%%%%%%%%%%%%%%%%%  MEMBRANE MODULE PROPERTIES   %%%% %%%%%%%%%%%%%%%%%%%%
prompt1={'Pore radius:','Fiber Outer diameter:','Fiber Inner diameter:','Membrane thickness:','Shell
      diameter:','Length:','Number of fibers:','Number of modules:','Surface area per module:'};
name='MEMBRANE MODULE PROPERTIES';
numlines=1;
defaultanswer={'1e-7','2.8e-3','1.5e-3','6.5e-004','2.1e-2','0.45','40','2','0.1'};
answer1=inputdlg(prompt1,name,numlines,defaultanswer);
porerad=str2num(answer1{1,1});  %pore raduis
dfiber=str2num(answer1{2,1});   % fiber OUTER diameter
dfiberin=str2num(answer1{3,1}); % fiber INNER diameter
delta=str2num(answer1{4,1}); % membrane thickness
dshell=str2num(answer1{5,1}); % Shell diameter
l=str2num(answer1{6,1});  % Length of fibers
nf=str2num(answer1{7,1}); % number of fibers
nm=str2num(answer1{8,1}); % number of modules
area_m=str2num(answer1{9,1}); % membrane surface area per module
%%%%%%%%%%%%%%%%%%%  MEMBRANE PHYSICAL PROPERTIES   %%%%%%%%%%%%%%%%%%%%%%%
prompt2={'Porosity:','Tortoucity:','Thermal conductivity:'};
name='MEMBRANE PHYSICAL PROPERTIES';
numlines=1;
defaultanswer={'0.70','1.4','0.22'};
answer2=inputdlg(prompt2,name,numlines,defaultanswer);
eps=str2num(answer2{1,1}); % membrane porosity
tau=str2num(answer2{2,1}); % membrane pore tortuosity
ks=str2num(answer2{3,1});  % thermal conductivity [W/m K] of polypropalene
%%%%%%%%%%%%%%%%%%%%%%%  OPERATING CONDITIONS   %%%%%%%%%%%%%%%%%%%%%%%%%%%%%%%%
prompt3={'Feed flow rate (L/h):','Permeate flow rate (L/h):','Feed Inlet temperature Tf_in  (oC):','Permeate
      Outlet temperature Tp_out  (oC):','Feed Concentration (g/L):'};
name='OPERATING CONDITIONS';
numlines=1;
defaultanswer={'400','400','35','15','0.00'};
```

```
answer3=inputdlg(prompt3,name,numlines,defaultanswer);
QF=str2num(answer3{1,1}) % Feed flow rate (L/h)
QP=str2num(answer3{2,1}) % Permeate flow rate (L/h)
TFin=str2num(answer3{3,1});  % Feed Inlet temperature (oC)
TPout=str2num(answer3{4,1}); %Permeate Outlet temperature (oC)
C=str2num(answer3{5,1});     %Feed Concentration (g/L) Standard Seawater
%
QF=(QF/1000)/3600; % feed flow rate m^3/s
QP=(QP/1000)/3600;% distillate flow rate m^3/s
Co=C;
C=C/1000; % to change from g/L to wait ratio
%%%%%%%%%%%%%%%% CALCULATION OF GEOMETRICAL CONFIGURATIONS  %%%%%%%%%%%%%%%%
PF=nf*(dfiber/2)^2/(dshell/2)^2   % PACKING FACTOR
area_shell=pi*(dshell/2)^2
areaP=(area_shell-PF*area_shell)   % cross-section area of distillate
vP=QP/(areaP*nm); % distillate velocity in each module m/s
dhP=4*areaP/(nf*pi*dfiber) % hydrulic diameter of permeate
areaF=((pi/4)*(dfiberin)^2)*nf % cross-section area of feed
vF=QF/(areaF*nm); % feed velocity m/s
dhF=dfiberin % hydrulic diameter of feed
%
% ReynP=1000*vP*dhP/mu
%dhP=4*((pi/4)*dshell^2-(nf*(pi/4)*dfiber^2))/(nf*pi*dfiberin);
%ReynP=1000*vP*dhP/mu
%area=pi*dfiber*nf*l   % membrane surface area
%area=area*0.633*nm    %% area correction =contact area/membrane surface area (0.1/area)
%area_m=0.1; % membrane surface area per module
area=nm*area_m; % total membrane surface area
dA=area/k;
delta_l=l/k;
%%%%%%%%%%%%%%%%%%% AREA CORRECTION %%%%%%%%%%%%%%%%%%%%%%%%%%%%%%%%%%%%%%
%ReynF_avg=980*vF*dhF/6.6256e-4;
%ReynP_avg=980*vP*dhP/6.6256e-4;
%%% Feed Side
%vFdhF=2.89e-4  % Flow =100 L/h
%vFdhF=5.78e-4  % Flow =200 L/h
%vFdhF=8.68e-4  % Flow =300 L/h
%vFdhF=1.16e-3  % Flow =400 L/h
%vFdhF=1.45e-3  % Flow =500 L/h
%%%  Permeate Side
%vPdhP=1.09e-4  % Flow =100 L/h
%vPdhP=2.18e-4  % Flow =200 L/h
%vPdhP=3.27e-4  % Flow =300 L/h
%vPdhP=4.36e-4  % Flow =400 L/h
%vPdhP=5.44e-4  % Flow =500 L/h
QQF(1)=QF;        % Feed flow rate at the first diff. area
%CC(1)=Co;     % concentration at feed side in the first diff. area
%CCm(1)=Co;   % concentration  at membrane surface in the first diff. area
ts=Co*QF;     % Total amount of salt flow kg/s
%%%%%%%%%%
for j=1: nn
TF=TFin+273;
TTF(1)=TF;
TP=TPout+273;
TTP(1)=TP;
t1=TF; %%% Tentative value of T1
t2=TP; %%% Tentative value of T2
T1=0;
T2=0;
for i=1:k,
    xiF=1-(C/MWZ)/((C/MWZ)+((1-C)/MWW)); % molar frction of water in feed side
    xiP=1; % molar fraction of water in permeate side
```

```
xis=(C/MWZ)/((C/MWZ)+((1-C)/MWW)); % molar fraction of solute
%CCC=xis*MWZ/(MWW-xis*(MWW-MWZ));  % kg NaCl/kg H2O
gammas=1-0.5*xis-10*xis^2; % activity coefficient of NaCl solution Schofield Desalination 77 (1990)
gamma=1.0; % activity coefficient of water
dens=980+1950*xis; % NaCl solution feed density Schofield Desalination 77 (1990)
mu=(8.7e-4-6.3e-6*(t1-273))*(1+12.9*xis); % viscocity of NaCl solution Schofield Desalination 77 (1990)
CP=4180-8370*xis; % Heat capacity [J/kg] for NaCl solution Schofield Desalination 77 (1990)
ktF=(0.608+7.46e-4*(t1-273))*(1-0.98*xis); % thermal conductivity Schofield Desalination 77 (1990)
ReynF=dens*vF*dhF/mu;
PrandF=CP*mu/ktF;
GzF=dens*QF*CP/(nm*ktF*l);
ktP=(0.608+7.46e-4*(t2-273))*(1-0.98*xis); % thermal conductivity Schofield Desalination 77 (1990)
ReynP=dens*vP*dhP/mu;
PrandP=CP*mu/ktP;
GzP=dens*QP*CP/(nm*ktP*l);
hF=ktF/dhF*(4.36+((0.036*ReynF*PrandF*(dhF/l))/(1+0.0011*(ReynF*PrandF*(dhF/l))^0.8))); %feed side heat
  transfer coe [W/m2 K]
hP=ktP/dhP*(4.36+((0.036*ReynP*PrandP*(dhP/l))/(1+0.0011*(ReynP*PrandP*(dhP/l))^0.8))); %permeate side heat
  transfer coe [W/m2 K]
%hF=ktF/dhF*(3.66+((0.067*GzF)/(1+0.04*GzF^(2/3))))
%hP=ktP/dhP*(3.66+((0.067*GzD)/(1+0.04*GzP^(2/3))))
NuF=hF*dhF/ktF;
NuP=hP*dhP/ktP;
%%%%%%%%%%%%%%%%%%%%%%%%%%%%%%%%%%%%%%%%%%%%%%%%%%%%%%%%%%%%%%%%%%%%%%%%%%%%%%%
Tavg=(t1+t2)/2;
%D=0.32;
%D=0.45;
D=50; %3.85*tau/eps; %0.61;   %0.775;
Do=eps/tau*4.46e-6*Tavg^2.334;  %Lawson 1996 and Bird
Dk=D*(2/3)*(eps*porerad/tau)*(8*R*Tavg/(pi*MWW))^0.5;
pvF=exp(23.1964-(3816.44/(t1-46.13))); % Antoine Equation
pvP=exp(23.1964-(3816.44/(t2-46.13))); % Antoine Equation
%pvF=(10^(8.07131-(1730.63/(233.42+(t1-273)))))*P/760;
%pvD=(10^(8.07131-(1730.63/(233.42+(t2-273)))))*P/760;
pF=pvF*xiF*gammas;
pP=pvP*xiP*gamma;
Pavg=P-(pF+pP)/2;
N=(-1/(R*Tavg))*(Dk*Do/(Do+Pavg*Dk))*((pP-pF)/delta)*MWW; %Lawson 1996 Flux [kg/m2 s]
kv=2.72e-3+5.71e-5*Tavg; % transporting vapor conductivity [W/m K] Schofield Desalination 77 (1990)
ktm=kv*eps+(1-eps)*ks; %heat conduction coefficient of membrane (0.04 - 0.06)[W/m K]  Tomaszewska JMS 1998
a=exp(-1*N*CP*delta/ktm);
Hv=1000*(1.7535*t2+2024.3); %heat of vaporization [J/kg]  Perry Handbook

while ((abs(T1-t1)) > 1e-3) & ((abs(T2-t2)) > 1e-3)
        t1=(hF*TF*(1-a)+N*CP*((hF/hP)*TF+TP)-N*Hv*(1-a))/(hF*(1-a)+N*CP*(1+(hF/hP)));
        t2=(hP*TP*(1-a)+N*CP*((hP/hF)*TP+TF)+N*Hv*(1-a))/(hP*(1-a)+N*CP*(1+(hP/hF)));
        Tavg=(t1+t2)/2;
        Do=eps/tau*4.46e-6*Tavg^2.334;
        Dk=D*(2/3)*(eps*porerad/tau)*(8*R*Tavg/(pi*MWW))^0.5;
        xiF=1-(C/MWZ)/((C/MWZ)+((1-C)/MWW)); % molar frction of water in feed side
        xiP=1; % molar fraction of water in permeate side
        xis=(C/MWZ)/((C/MWZ)+((1-C)/MWW)); % molar fraction of solute
        CCC=xis*MWZ/(MWW-xis*(MWW-MWZ));  %
        gammas=1-0.5*xis-10*xis^2; % activity coefficient of NaCl solution Schofield Desalination 77 (1990)
        gamma=1.0; % activity coefficient of water
        dens=980+1950*xis; % NaCl solution feed density Schofield Desalination 77 (1990)
        mu=(8.7e-4-6.3e-6*(t1-273))*(1+12.9*xis); % viscocity of NaCl solution Schofield Desalination 77
  (1990)
        CP=4180-8370*xis; % Heat capacity [J/kg K] for NaCl solution Schofield Desalination 77 (1990)
        ktF=(0.608+7.46e-4*(t1-273))*(1-0.98*xis); % thermal conductivity [W/m K]of water Schofield
  Desalination 77 (1990)
        ReynF=dens*vF*dhF/mu;
```

```
      PrandF=CP*mu/ktF;
      GzF=dens*QF*CP/(ktF*l);
      ktP=(0.608+7.46e-4*(t2-273))*(1-0.98*xis); % thermal conductivity [W/m K]of water Schofield
 Desalination 77 (1990)
      ReynP=dens*vP*dhP/mu;
      PrandP=CP*mu/ktP;
      GzP=dens*QP*CP/(ktP*l);
      hF=ktF/dhF*(4.36+((0.036*ReynF*PrandF*(dhF/l))/(1+0.0011*(ReynF*PrandF*(dhF/l))^0.8)));
      hP=ktP/dhP*(4.36+((0.036*ReynP*PrandP*(dhP/l))/(1+0.0011*(ReynP*PrandP*(dhP/l))^0.8)));
      %hF=ktF/dhF*(3.66+((0.067*GzF)/(1+0.04*GzF^(2/3))));
      %hP=ktP/dhP*(3.66+((0.067*GzP)/(1+0.04*GzP^(2/3))));
      %%%%%%%%%%%%%%%%%%%%%%%%%%%%%%%%%%%%%%%%%%%%%%%%%%%%%%%%%%%%%%%
      pvF=exp(23.1964-(3816.44/(t1-46.13)));
      pvP=exp(23.1964-(3816.44/(t2-46.13)));
      pF=pvF*xiF*gammas;
      pP=pvP*xiP*gamma;
      Pavg=P-(pF+pP)/2;
      N=(-1/(R*Tavg))*(Dk*Do/(Do+Pavg*Dk))*((pP-pF)/delta)*MWW; %Lawson 1996 Flux [kg/m2 s]
      kv=2.72e-3+5.71e-5*Tavg; % transporting vapor conductivity [W/m K] Schofield Desalination 77 (1990)
      ktm=kv*eps+(1-eps)*ks; %heat conduction coefficient Through membrane (0.04   - 0.06)  Tomaszewska JMS
 1998
      a=exp(-1*N*CP*delta/ktm);
      Hv=1000*(1.7535*t2+2024.3); %heat of vaporization [J/kg]  Perry Handbook
      T1=(hF*TF*(1-a)+N*CP*((hF/hP)*TF+TP)-N*Hv*(1-a))/(hF*(1-a)+N*CP*(1+(hF/hP)));
      T2=(hP*TP*(1-a)+N*CP*((hP/hF)*TP+TF)+N*Hv*(1-a))/(hP*(1-a)+N*CP*(1+(hP/hF)));

end
%%%%%%%%%%%%%%%%%
HF(i)=hF;
HP(i)=hP;
pFF(i)=pF;
pPP(i)=pP;
PPavg(i)=Pavg;
%%%%%%%%%%%%%%%%%
NN(i)=N;
TT1(i)=T1;
TT2(i)=T2;
TPC(i)=(TT1(i)-TT2(i))/(TTF(i)-TTP(i));
Qf(i)=hF*(TTF(i)-TT1(i));            % Feed side heat transfer [W/m2]
Qp(i)=hP*(TT2(i)-TTP(i));            % Permeate side heat transfer [W/m2]
Qc(i)=(ktm/delta)*(TT1(i)-TT2(i));   % Conduction heat transfer [W/m2]
Qv(i)=NN(i)*(Hv+CP*(TT1(i)-TT2(i))); % Vaporization heat transfer [W/m2]
Q_Total(i)=Qc(i)+Qv(i);
dTF=(hF*(TTF(i)-TT1(i))*dA)/(CP*(dens*QF-NN(i)*dA));
dTP=(hP*(TT2(i)-TTP(i))*dA)/(CP*(dens*QP-NN(i)*dA));
TTF(i+1)=TTF(i)-dTF;
TTP(i+1)=TTP(i)-dTP;
%dxF=(NN(i)*dA*(1-xiF))/(dens*QF-NN(i)*dA)
%CC(i+1)=CC(i)+dxF
%CC(i+1)=CC(i)/(dens*QF-NN(i)*dA)
TF=TTF(i+1);
TP=TTP(i+1);
t1=TTF(i+1);
t2=TTP(i+1);
%DL(i)=i*dA/area;
DL_L(i)=i*delta_l/l;
%
%%%%%%%%%%%%%%%%%%%% MASS TRANSFER CALCULATION%%%%%%%%%%%%%%%%%%%%%%%%%%%%% %%%%%%%%%
%vF=1
%RR=8.314e3; % [Pa.m3/kmol.K]
%Dk=(2*porerad/3)*(8*RR*(Tavg)/(pi*MWW))^0.5
%kmm=(Dk*Do/(Do+Pavg*Dk))/delta %%% membrane mass transfer coefficent
```

```
    %Rm=1/kmm;
    Dk=D*(2/3)*(eps*porerad/tau)*(8*R*Tavg/(pi*MWW))^0.5;
    kmm=Dk*(eps/(delta*tau));   %masss transfer coef. at the membrane [m/s]
    Rmm=1/kmm;
    %Gz=(vF*dfiberin)/(Dsw);
    Gz=(vF*dfiberin^2)/(Dsw*l);
    %Sh=(3.67^3+1.62^3*Gz)^(1/3);   %% for 10<Gz<20
    %Sh=3.67;                        %% for Gz<10
    Sh=1.62*Gz^(1/3);               %% for Gz>20
    %Sh=0.85*((dfiberin/dfiber)^0.45)*((dh_L/L)^0.25)*Reyn_L^(1/3)*(mu/(ro*Dsw))^(1/3);
    %Sh=0.9*Reyn_L^(1/2)*(mu/(ro*Dsw))^(1/3);
    kfm=(Dsw/dhF)*Sh;  %masss transfer coef. at the Feed side [m/s]
    %kfm=0.0197;
    %kfm=0.0125;
    Rf=1/kfm;
    CPC(i)=exp(NN(i)/(kfm*dens_w)); % CPC along the module
    QQF(i+1)=QQF(i)-((NN(i)*dA)/dens_w); % CPC along the module
    CC(i)=ts/QQF(i+1); % feed concentration along the module
    CCm(i)=CC(i)*CPC(i); % concentration on the membrane surface along the module
end
TF=TTF(i+1);
TP=TTP(i+1);
TT1(i+1)=(hF*TF*(1-a)+N*CP*((hF/hP)*TF+TP)-N*Hv*(1-a))/(hF*(1-a)+N*CP*(1+(hF/hP)));
TT2(i+1)=(hP*TP*(1-a)+N*CP*((hP/hF)*TP+TF)+N*Hv*(1-a))/(hP*(1-a)+N*CP*(1+(hP/hF)));
TPC(i+1)=(TT1(i+1)-TT2(i+1))/(TF-TP);
%%%%%%%%%%%%
Flux(j)=mean(NN); % Flux after time interval
%CPC_t(j)=mean(CPC);
%CPC_t(j)=exp(Flux(j)/(kfm*dens_w)); % CPC after time interval
%C_t(j)=(V*Co)/(V-Flux(j)*area*j*n/dens_w); % feed concentration (g/L) after time interval
%C=C_t(j)/1000; % feed concentration (wt%) after time j
%Cm_t(j)=C_t(j)*CPC_t(j); % concentration (g/L) at the membrane surface after time interval
%Dt(j)=j*30; % time interval = 30 minutes
end
%TFin
%TPout
%C=C*1000
%delta
%Dlta_T=TFin-TPout
%QF
%ReynF
%ReynP
%ks
%eps
%tau
%l
%area_m
QF=QF*1000*3600
vF
ReynF
vFdhF=ReynF*mu/dens
QP=QP*1000*3600
vP
ReynP
vPdhP=ReynP*mu/dens
%ks
%TTF
%TTP
FF=mean(NN)*3600
Flux=Flux*3600
%flux=NN*3600
qf=mean(Qf);
```

```
qp=mean(Qp);
qc=mean(Qc); % Conduction heat transfer [W/m2]
qv=mean(Qv); % Vaporization heat transfer [W/m2]
q_total=qc+qv;
effeciency=qv/q_total*100
% tpc=mean(TPC)
% cpc=mean(CPC)
%gammas
%pF
%pP
%kmm
%kfm
%TPC
%
sssssssssssssssssssssssssssssssssssssssssssssssssssssssssssssssss
a3='DL_L';
b3='Flux';
xlswrite('md.xls', a3, 'MD1', 'A3:A3')
xlswrite('md.xls', DL_L, 'MD1', 'A4')
xlswrite('md.xls', b3, 'MD1', 'B3:B3')
xlswrite('md.xls', NN*3600, 'MD1', 'B4')
sssssssssssssssssssssssssssssssssssssssssssssssssssssssssssssssssssssssssssssssss

%%%
xlswrite('md.xls', Flux, 'MD1', 'E3')
xlswrite('md.xls', effeciency, 'MD1', 'E4')
xlswrite('md.xls', qv, 'MD1', 'E5')
xlswrite('md.xls', qc, 'MD1', 'E6')
xlswrite('md.xls', tpc, 'MD1', 'E7')
xlswrite('md.xls', cpc, 'MD1', 'E8')
xlswrite('md.xls', kmm, 'MD1', 'E9')
xlswrite('md.xls', kfm, 'MD1', 'E10')
%%%
%%%
xlswrite('md.xls', DL_L, 'MD2', 'A5')
xlswrite('md.xls', TTF, 'MD2', 'B4')
xlswrite('md.xls', TT1, 'MD2', 'C4')
xlswrite('md.xls', TTP, 'MD2', 'D4')
xlswrite('md.xls', TT2, 'MD2', 'E4')
xlswrite('md.xls', TPC, 'MD2', 'F4')
%%%
%%%
xlswrite('md.xls', DL_L, 'MD3', 'A4')
xlswrite('md.xls', CC, 'MD3', 'B4')
xlswrite('md.xls', CCm, 'MD3', 'C4')
xlswrite('md.xls', CPC, 'MD3', 'D4')
msgbox('Resluts are ready in MD.xls file', 'Successful Operation', 'help')
winopen('D:\MATLAB7\work\md.xls')
%
%CC
%CCm
%CPC_t
%C_t
%Cm_t
%plot(DL,CC,'ro-',DL,CCm,'rx-')
%pause
%plot(C_t)
%plot(Dt,C_t,'ro-',Dt,Cm_t,'rx-')
%pause
%plot(DL,TTF,'ro-',DL,TT1,'rx-',DL,TTP,'bo-',DL,TT2,'bx-')
%vF
%vP
```

```
%ReynF=dens*vF*dhF/mu
%ReynP=dens*vP*dhP/mu

%%%%%%%%%%%%%%%%%%

ReynF=dens*vF*dhF/mu
Gz_m
Sh_m
kmm
Rm
kfm
Rf
flux=mean(NN)
cpc=mean(CPC)
Cm=cpc*C*1000
S=cpc*1000*C/361.5    %%% Supersaturation
tpc=mean(TPC)
%%%%%%%%%%%%%%%%%%%%%% EFFECTS OF TPC and HEAT FLUX %%%%%%%%%%
xlswrite('mdc.xls', C*1000, 'Sheet1', 'B5')
xlswrite('mdc.xls', QF*3600, 'Sheet1', 'C5')
xlswrite('mdc.xls', Gz_m, 'Sheet1', 'D5')
xlswrite('mdc.xls', Sh_m, 'Sheet1', 'E5')
xlswrite('mdc.xls', kfm, 'Sheet1', 'F5')
xlswrite('mdc.xls', Rf/Rm, 'Sheet1', 'G5')
xlswrite('mdc.xls', flux*3600, 'Sheet1', 'H5')
xlswrite('mdc.xls', cpc, 'Sheet1', 'I5')
xlswrite('mdc.xls', Cm, 'Sheet1', 'J5')
xlswrite('mdc.xls', S, 'Sheet1', 'K5')
xlswrite('mdc.xls', ReynF, 'Sheet1', 'L5')
%%%%%%%%%%%%%%%%%%%%%% EFFECTS OF MODULE LENGTH %%%%%%%%%%
%xlswrite('md2.xls', l, 'Sheet5', 'B5')
%xlswrite('md2.xls', flux, 'Sheet5', 'C5')
%xlswrite('md2.xls', deltaT, 'Sheet5', 'D5')
%xlswrite('md2.xls', TPCavg, 'Sheet5', 'E5')
%xlswrite('md2.xls', Qfavg, 'Sheet5', 'F5')
%xlswrite('md2.xls', Qpavg, 'Sheet5', 'G5')
%xlswrite('md2.xls', Qcavg, 'Sheet5', 'H5')
%xlswrite('md2.xls', Qvavg, 'Sheet5', 'I5')
%xlswrite('md2.xls', hf, 'Sheet5', 'J5')
%xlswrite('md2.xls', hp, 'Sheet5', 'K5')

%%%%%%%%%% EFFCT OF MEMBRANE THICKNESS %%%%%%%%%%%%%%%%%
%xlswrite('md3.xls', delta*1000, 'Sheet4', 'B5')
%xlswrite('md3.xls', dfiber, 'Sheet4', 'C5')
%xlswrite('md3.xls', dfiberin, 'Sheet4', 'D5')
%xlswrite('md3.xls', flux, 'Sheet4', 'E5')
%xlswrite('md3.xls', deltaT, 'Sheet4', 'F5')
%xlswrite('md3.xls', TPCavg, 'Sheet4', 'G5')
%xlswrite('md3.xls', Qfavg, 'Sheet4', 'H5')
%xlswrite('md3.xls', Qpavg, 'Sheet4', 'I5')
%xlswrite('md3.xls', Qcavg, 'Sheet4', 'J5')
%xlswrite('md3.xls', Qvavg, 'Sheet4', 'K5')
%xlswrite('md3.xls', hf, 'Sheet4', 'L5')
%xlswrite('md3.xls', hp, 'Sheet4', 'M5')


%xlswrite('md.xls', TTF-273, 'Sheet1', 'C2')
%xlswrite('md.xls', TT1-273, 'Sheet1', 'D2')
%xlswrite('md.xls', TTP-273, 'Sheet1', 'E2')
%xlswrite('md.xls', TT2-273, 'Sheet1', 'F2')
```

APPENDIX 3
PROGRAMMING CODE OF MDC SIMULATION

```
%%%%%%%%%%  MEMBRANE PROPERTIES   %%%%%%%%
dfiber=2.8e-3 % fiber OUTER diameter
dfiberin=1.5e-3 % fiber INNER diameter
delta=(dfiber-dfiberin)/2 % membrane thickness
dshell=2.1e-2;  % Shell diameter
%%%%%%%%%%%%%%%%%%%%MEMBRANE THICKNESS EFFECTS %%%%%%%%%%%%%%%%%%%%%%%%%%%%%%
%dfiber=dfiber*1.2
%dfiberin=dfiberin*1.2
%delta=(dfiber-dfiberin)/2
%%%%%%%%%%%%%%%%%%%%%%%%%%%%%%%%%%%%%%%%%%%%
%delta=6.5e-4; % membrane thickness
%dfiber=dfiberin+2*delta;
%dfiberin=dfiber-2*delta;
%%%%%%%%%%%%%%%%%%%%%%%%%%%%%%%%%%%%%%%%%%%%%%%%%%%%%%%%%%%%%%%%%%%%%%%%%%%%%%%
l=0.45; % Length of fibers
eps=0.70; % membrane porosity
tau=1.4; % membrane pore tortuosity
nf=40; % number of fibers
nm=2; % number of modules
porerad=1e-7; %pore raduis
ks=0.22; % thermal conductivity of polypropalene
P=1.01325e5; % total pressure= atmospheric pressure
MWW=18; %Moleculare weight of water (g/mole)
MWZ=23+35.5; %%% %Moleculare weight of NaCl (g/mole)
R=8287.05; % J/K*kmole
dens_w=980;  % pure water density
k=10; %%%%%%% number of differential areas %%%%
%%%%%%%%%%%%%%%%%%%%%%%%%%%%%%%%%%%%%%%%%%%%%%%%%%%%%%%%%%%%%%%%%%%%%%%%%%%%%%%
area_m=0.1; % membrane surface area per module
area=nm*area_m; % total membrane surface area
dA=area/k;
delta_l=l/k;
%dA=pi*dfiber*nf*nm*delta_l;
%area=dA*l;
%%%%%%%%%%%%%%%%%%%%%%%%%%%%%%%%%%%%%%%%%%%%%%%%%%%%%%%%%%%%%%%%%%%%%%%%%%%%%%%
A=[0];
TTF=repmat(A,k+1,1);
TTP=repmat(A,k+1,1);
TT1=repmat(A,k+1,1);
TT2=repmat(A,k+1,1);
TPC=repmat(A,k+1,1);
CC=repmat(A,k,1);
CCm=repmat(A,k,1);
QQF=repmat(A,k+1,1);
CPC=repmat(A,k,1);
NN=repmat(A,k,1);
Qf=repmat(A,k,1);
Qp=repmat(A,k,1);
Qc=repmat(A,k,1);
Qv=repmat(A,k,1);
DA=repmat(A,k+1,1);
DL=repmat(A,k,1);
%%%%%%%%%%%%%%%%%%%%%%%%% INPUTS %%%%%%%%%%%%%%%%%%%%%%%%%%%%%%%%%%%%%%%%%%%
QF=0.25/3600; % feed flow rate m^3/s
QP=0.1/3600; % distillate flow rate m^3/s
TFin=40.0; % Feed inelt temp (oC)
TPin=14.0; % Distilat inelt temp (oC)
TPout=20.0; %(TPin+TFin)/2; %%% Tentative value of TP out
C=33.51;  % feed concentration g/L
```

```
Co=C; % initial concentration in g/L
%%%%%%%%%%%% Initialization %%%%%%%%
TF=TFin+273;
TTF(1)=TF;
TP=TPout+273;
TTP(1)=TP;
t1=TF; %%% Tentative value of T1
t2=TP; %%% Tentative value of T2
T1=0;
T2=0;
C=C/1000; % to change from g/L to wait ratio
%%%%%%%%% Calculation of constants  %%%%%%
dhF=dfiberin; % hydrulic diameter of feed
areaF=nm*nf*(pi/4)*(dfiberin)^2; % cross-section area of feed
vF=QF/areaF; % feed velocity m/s
dhP=4*((pi/4)*dshell^2-(nf*(pi/4)*dfiberin^2))/(nf*pi*dfiberin); % hydrulic diameter of distillate
areaP=nm*((pi/4)*dshell^2-nf*(pi/4)*dfiber^2); % cross-section area of distillate
vP=QP/areaP; % distillate velocity m/s
%%%%%%%%%%%%%%%%%%%%%%%%%%%%%%%%%%%%%%%%%%%%%%%%%%%%%%%%%%%%%%%%%%%%%%%%%%%%%%%
QQF(1)=QF;        % Feed flow rate at the first diff. area
%CC(1)=Co;     % concentration at feed side in the first diff. area
%CCm(1)=Co;   % concentration  at membrane surface in the first diff. area
ts=Co*QF;     % Total amount of salt flow kg/s

%%%%%%%%%%%%%%%%%%%%%%%%%%%%%%%%%%%%%%%%%%%%%%%%%%%%%%%%%%%%%%%%%%%%%%%%%%%%%%%
V=5;  % initial water volume (Liter)
%V=V/1000;  % water volume in m3

%%%%%%%%%%%%%%%%%%%%%%%%%%%%%%%%%%%%%%%
total_time=16; % total experiment hours
%%%%%%%%%%%%%%%%%%%%%%%%%%%%%%%%%%%%%%%
time_interval=10; % measuring time interval  min
n=time_interval*60;  % time interval seconds
nn=total_time*60/time_interval; % total elapsed time
C_t=repmat(A,nn,1); % feed concentration after time interval
Flux=repmat(A,nn,1); % Flux after time interval
CPC_t=repmat(A,nn,1); % CPC after time interval
Cm_t=repmat(A,nn,1); %  concentration at membrane susface  after time interval
Dt=repmat(A,nn,1);
VP_t=repmat(A,nn,1); %  permeat volume  after time interval
VP=repmat(A,nn,1); %  total permeat volume  after time interval
%%%%%%%%%%%%%%%%%%%%%%%%%%%%%%%%%%%%%%%%%%%%%%%%%%%%%%%%%%%%%%%%%%%%%%%%%%%%%%%
for j=1: nn
TF=TFin+273;
TTF(1)=TF;
TP=TPout+273;
TTP(1)=TP;
t1=TF; %%% Tentative value of T1
t2=TP; %%% Tentative value of T2
T1=0;
T2=0;
for i=1:k,
    xiF=1-(C/MWZ)/((C/MWZ)+((1-C)/MWW)); % molar frction of water in feed side
    xiP=1; % molar fraction of water in permeate side
    xis=(C/MWZ)/((C/MWZ)+((1-C)/MWW)); % molar fraction of solute
    %CCC=xis*MWZ/(MWW-xis*(MWW-MWZ));  % kg NaCl/kg H2O
    gammas=1-0.5*xis-10*xis^2; % activity coefficient of NaCl solution Schofield Desalination 77 (1990)
    gamma=1.0; % activity coefficient of water
    dens=980+1950*xis; % NaCl solution feed density Schofield Desalination 77 (1990)
    mu=(8.7e-4-6.3e-6*(t1-273))*(1+12.9*xis); % viscocity of NaCl solution Schofield Desalination 77 (1990)
    CP=4180-8370*xis; % Heat capacity for NaCl solution Schofield Desalination 77 (1990)
    ktF=(0.608+7.46e-4*(t1-273))*(1-0.98*xis); % thermal conductivity Schofield Desalination 77 (1990)
```

```
ReynF=dens*vF*dhF/mu
PrandF=CP*mu/ktF;
GzF=dens*QF*CP/(nm*ktF*l);
ktP=(0.608+7.46e-4*(t2-273))*(1-0.98*xis); % thermal conductivity Schofield Desalination 77 (1990)
ReynP=dens*vP*dhP/mu
PrandP=CP*mu/ktP;
GzP=dens*QP*CP/(nm*ktP*l);
hF=ktF/dhF*(4.36+((0.036*ReynF*PrandF*(dhF/l))/(1+0.0011*(ReynF*PrandF*(dhF/l))^0.8)));
hP=ktP/dhP*(4.36+((0.036*ReynP*PrandP*(dhP/l))/(1+0.0011*(ReynP*PrandP*(dhP/l))^0.8)));
%hF=ktF/dhF*(3.66+((0.067*GzF)/(1+0.04*GzF^(2/3))))
%hP=ktP/dhP*(3.66+((0.067*GzD)/(1+0.04*GzP^(2/3))))
NuF=hF*dhF/ktF;
NuP=hP*dhP/ktP;
%%%%%%%%%%%%%%%%%%%%%%%%%%%%%%%%%%%%%%%%%%%%%%%%%%%%%%%%%%%%%%%%%%%%%%%%%%%%
Tavg=(t1+t2)/2;
%D=0.38;
%D=0.775;
D=0.4;
Do=eps/tau*4.46e-6*Tavg^2.334;  %Lawson 1996 and Bird
Dk=D*(2/3)*(eps*porerad/tau)*(8*R*Tavg/(pi*MWW))^0.5;
pvF=exp(23.1964-(3816.44/(t1-46.13))); % Antoine Equation
pvP=exp(23.1964-(3816.44/(t2-46.13))); % Antoine Equation
%pvF=(10^(8.07131-(1730.63/(233.42+(t1-273)))))*P/760;
%pvD=(10^(8.07131-(1730.63/(233.42+(t2-273)))))*P/760;
pF=pvF*xiF*gammas;
pP=pvP*xiP*gamma;
Pavg=P-(pF+pP)/2;
N=(-1/(R*Tavg))*(Dk*Do/(Do+Pavg*Dk))*((pP-pF)/delta)*MWW*nm; %Lawson 1996 Flux (kg/m2 s)
kv=2.72e-3+5.71e-5*Tavg;
ktm=kv*eps+(1-eps)*ks; %heat conduction coefficient of membrane (0.04 - 0.06)
a=exp(-1*N*CP*delta/ktm);
Hv=1000*(1.7535*t2+2024.3);

while ((abs(T1-t1)) > 1e-3) & ((abs(T2-t2)) > 1e-3)
        t1=(hF*TF*(1-a)+N*CP*((hF/hP)*TF+TP)-N*Hv*(1-a))/(hF*(1-a)+N*CP*(1+(hF/hP)));
        t2=(hP*TP*(1-a)+N*CP*((hP/hF)*TP+TF)+N*Hv*(1-a))/(hP*(1-a)+N*CP*(1+(hP/hF)));
        Tavg=(t1+t2)/2;
        Do=eps/tau*4.46e-6*Tavg^2.334;
        Dk=D*(2/3)*(eps*porerad/tau)*(8*R*Tavg/(pi*MWW))^0.5;
        xiF=1-(C/MWZ)/((C/MWZ)+((1-C)/MWW)); % molar frction of water in feed side
        xiP=1; % molar fraction of water in permeate side
        xis=(C/MWZ)/((C/MWZ)+((1-C)/MWW)); % molar fraction of solute
        CCC=xis*MWZ/(MWW-xis*(MWW-MWZ));  %
        gammas=1-0.5*xis-10*xis^2; % activity coefficient of NaCl solution Schofield Desalination 77 (1990)
        gamma=1.0; % activity coefficient of water
        dens=980+1950*xis; % NaCl solution feed density Schofield Desalination 77 (1990)
        mu=(8.7e-4-6.3e-6*(t1-273))*(1+12.9*xis); % viscocity of NaCl solution Schofield Desalination 77
  (1990)
        CP=4180-8370*xis; % Heat capacity for NaCl solution Schofield Desalination 77 (1990)
        ktF=(0.608+7.46e-4*(t1-273))*(1-0.98*xis); % thermal conductivity Schofield Desalination 77 (1990)
        ReynF=dens*vF*dhF/mu;
        PrandF=CP*mu/ktF;
        GzF=dens*QF*CP/(ktF*l);
        ktP=(0.608+7.46e-4*(t2-273))*(1-0.98*xis); % thermal conductivity Schofield Desalination 77 (1990)
        ReynP=dens*vP*dhP/mu;
        PrandP=CP*mu/ktP;
        GzP=dens*QP*CP/(ktP*l);
        hF=ktF/dhF*(4.36+((0.036*ReynF*PrandF*(dhF/l))/(1+0.0011*(ReynF*PrandF*(dhF/l))^0.8)));
        hP=ktP/dhP*(4.36+((0.036*ReynP*PrandP*(dhP/l))/(1+0.0011*(ReynP*PrandP*(dhP/l))^0.8)));
        %hF=ktF/dhF*(3.66+((0.067*GzF)/(1+0.04*GzF^(2/3))));
        %hP=ktP/dhP*(3.66+((0.067*GzP)/(1+0.04*GzP^(2/3))));
        %%%%%%%%%%%%%%%%%%%%%%%%%%%%%%%%%%%%%%%%%%%%%%%%%%%%%%%%%%%%%%%%%%%%%%%%%%%%
```

```
        pvF=exp(23.1964-(3816.44/(t1-46.13)));
        pvP=exp(23.1964-(3816.44/(t2-46.13)));
        pF=pvF*xiF*gammas;
        pP=pvP*xiP*gamma;
        Pavg=P-(pF+pP)/2;
        N=(-1/(R*Tavg))*(Dk*Do/(Do+Pavg*Dk))*((pP-pF)/delta)*MWW*nm; %Lawson 1996
        kv=2.72e-3+5.71e-5*Tavg;
        ktm=kv*eps+(1-eps)*ks; %heat conduction coefficient of membrane (0.04 - 0.06)
        a=exp(-1*N*CP*delta/ktm);
        Hv=1000*(1.7535*t2+2024.3);
        T1=(hF*TF*(1-a)+N*CP*((hF/hP)*TF+TP)-N*Hv*(1-a))/(hF*(1-a)+N*CP*(1+(hF/hP)));
        T2=(hP*TP*(1-a)+N*CP*((hP/hF)*TP+TF)+N*Hv*(1-a))/(hP*(1-a)+N*CP*(1+(hP/hF)));

end
%%%%%%%%%%%%%%%%%
HF(i)=hF;
HP(i)=hP;
pFF(i)=pF;
pPP(i)=pP;
PPavg(i)=Pavg;
%%%%%%%%%%%%%%%%%
NN(i)=N;
TT1(i)=T1;
TT2(i)=T2;

TPC(i)=(TT1(i)-TT2(i))/(TTF(i)-TTP(i));
Qf(i)=hF*(TTF(i)-TT1(i));
Qp(i)=hP*(TT2(i)-TTP(i));
Qc(i)=(ktm/delta)*(TT1(i)-TT2(i));
Qv(i)=NN(i)*(Hv+CP*(TT1(i)-TT2(i)));
dTF=(hF*(TTF(i)-TT1(i))*dA)/(CP*(dens*QF-NN(i)*dA))
dTP=(hP*(TT2(i)-TTP(i))*dA)/(CP*(dens*QP-NN(i)*dA))
TTF(i+1)=TTF(i)-dTF
TTP(i+1)=TTP(i)-dTP
%dxF=(NN(i)*dA*(1-xiF))/(dens*QF-NN(i)*dA)
%CC(i+1)=CC(i)+dxF
%CC(i+1)=CC(i)/(dens*QF-NN(i)*dA)
TF=TTF(i+1)
TP=TTP(i+1)
t1=TTF(i+1)
t2=TTP(i+1)
%DL(i)=i*dA/area;
DL(i)=i*delta_l;

%%%%%%%%%%%%%%%%%%%% MASS TRANSFER CALCULATION
%vF=1
vF=QF/areaF;

kmm=(Dk*Do/(Do+Pavg*Dk))/delta; %%% membrane mass transfer coefficent
Rm=1/kmm;
Dsw=1.15e-9;
Gz_m=(vF*dfiberin^2)/(Dsw*l);
Sh_m=(3.67^3+1.62^3*Gz_m)^(1/3);
%Sh_m=1.62*Gz_m^(1/3)
kfm=(Dsw/dhF)*Sh_m;
%kfm=0.0197
%kfm=0.0125
Rf=1/kfm;
CPC(i)=exp(NN(i)/(kfm*dens_w)); % CPC along the module
QQF(i+1)=QQF(i)-((NN(i)*dA)/dens_w); % CPC along the module
CC(i)=ts/QQF(i+1); % feed concentration along the module
CCm(i)=CC(i)*CPC(i); % concentration on the membrane surface along the module
```

```
end
TF=TTF(i+1);
TP=TTP(i+1);
TT1(i+1)=(hF*TF*(1-a)+N*CP*((hF/hP)*TF+TP)-N*Hv*(1-a))/(hF*(1-a)+N*CP*(1+(hF/hP)));
TT2(i+1)=(hP*TP*(1-a)+N*CP*((hP/hF)*TP+TF)+N*Hv*(1-a))/(hP*(1-a)+N*CP*(1+(hP/hF)));
TPC(i+1)=(TT1(i+1)-TT2(i+1))/(TF-TP);
%%%%%%%%%%%%%%
Flux(j)=mean(NN); % Flux after time interval
%CPC_t(j)=mean(CPC);
CPC_t(j)=exp(Flux(j)/(kfm*dens_w)); % CPC after time interval
VP_t(j)=Flux(j)*area*n*(1000/dens_w); % permeate volume L after time interval
VP(j)=sum(VP_t);
C_t(j)=(V*Co)/(V-VP(j)); % feed concentration (g/L) after time interval
C=C_t(j)/1000; % feed concentration (wt%) after time j
Cm_t(j)=C_t(j)*CPC_t(j); % concentration (g/L) at the membrane surface after time interval
Dt(j)=j*time_interval; % elapsed time interval

end
Flux=Flux*3600   %kg/m2 h
%VP_t
%flux=NN*3600
%CPC
%CC
%CCm
Dt
CPC_t
C_t
Cm_t
VP=VP*1000      %mL
plot(DL,CC,'ro-',DL,CCm,'bx-')
pause
plot(C_t)
plot(Dt,C_t,'ro-',Dt,Cm_t,'bx-')
pause
plot(Dt,Flux*1000,'ro-',Dt,VP,'bx-')

%%%%%%%%%%%%%%%%%%
ReynF=dens*vF*dhF/mu
Gz_m
Sh_m
kmm
Rm
kfm
Rf
flux=mean(NN)
cpc=mean(CPC)
Cm=cpc*C*1000
S=cpc*1000*C/361.5    %%% Supersaturation
tpc=mean(TPC)
```

LIST OF CONTRIBUTIONS

1. **S. Al-Obaidani**, E. Curcio and E. Drioli "The Role of Membrane Distillation/Crystallization Technologies in the Integrated Membrane System for Seawater Desalination". Submitted to Desalination Journal (2008).

2. **S. Al-Obaidani**, E. Curcio and E. Drioli "The Role of Membrane Distillation/Crystallization Technologies in the Integrated Membrane System for Seawater Desalination". EUROMED 2008: Desalination Cooperation among Mediterranean Countries of Europe and the MENA Region. Dead Sea (Jordan) November 9-13 (2008).

3. **S. Al-Obaidani**, E. Curcio, G. DiProfio, F. Macedonio, H. Al-Hinai and E. Drioli, "Potential of Membrane Distillation in Seawater Desalination: Thermal Efficiency, Sensitivity Study and Cost Estimation", Journal of Membrane Science 323(1) (2008) 85.

4. **S. Al-Obaidani**, E. Curcio and E. Drioli "Approaching the Zero-Liquid-Discharge (ZLD) Goal by Integrated Membrane System for Seawater Desalination: Exergy analysis and Economical Considerations". Proceedings 5th Chemical Engineering Conference for Collaborative Research in Eastern Mediterranean Countries. Cetraro (Italy) May 24-29 (2008).

5. Curcio E. , **Al Obaidani S.** , Macedonio F. , Di Profio G. , Drioli E. , " Membrane Distillation as a Viable Option for Seawater Desalination". Proceedings "Asian Conference on Desalination & Water Reuse 2007". Qingdao (China) July 4-6 (2007) 147.

6. Curcio E. , **Al Obaidani S.** , Macedonio F. , Di Profio G. , Gualtieri S. , Drioli E. , "Advanced membrane systems for seawater desalination. Kinetics of salts crystallization from RO brines promoted by polymeric membranes". Korean Membrane Journal 17 (2007) 93.

7. Curcio E. , Drioli E. , Di Profio G. , **Al Obaidani S**. , Macedonio F. , " Advanced Membrane Systems for Seawater Desalination". Proceedings "5th Italy-Korea Workshop on "Membranes and Membrane Processes for Clean Environment". Giardini Naxos (Italy) September 29-30 (2006) 46.

8. **S. Al-Obaidani**, "Modeling and Simulation of Membrane Distillation for Seawater Desalination". Network Young Membrains, 8th meeting. Rende (Italy) September 21-23 (2006).

9. **S. Al-Obaidani**, E. Curcio, G. DiProfio and E. Drioli, "Optimization and Control of Integrated Membrane System for Brackish and Seawater Desalination: Modeling and Simulation of Membrane Distillation Contactors". Advance Membrane Technology III: Membrane Engineering for Process Intensification. Cetraro (Italy) June 11-15 (2006).

ACKNOWLEDGMENTS

First of all would like to thank my GOD "Allah" for giving me the strength and knowledge to proceed with my study. I am grateful to the Middle East Desalination Research Center (MEDRC) for providing the financial support and for revising the periodic reports with thoughtful comments and suggestions. I would like to express my gratitude to my supervisor Prof. Enrico Drioli for his continuous support and valuable advices. I am also thankful to my Co-supervisor Dr. Hilal Al-Hinai for his efforts, encouragements and endless support. I will never forget the help of my tutor and my friend Dr. Efrem Curcio throughout the period of the study. Also, I would like to thank my colleague Dr. Alessio Caravella for helping me in completing the bureaucratic items required for my stay here in Italy. In addition, I am thankful to my friends and colleagues with whom I felt like at home: Francesco, Adele, Francesca, Gianluca, Enrica, Carmella, Maria Giovanna Adolfo, Antonella and Ji.

Finally, I would like to thank my father and mother and all my family for taking care of my wife and children while I am abroad. In addition, I am appreciative to my wife for her patient and motivations.